Development of Smart Anticorrosion Coatings from Biomass Extracts

Thesis Submitted to AcSIR for the award of the degree of

DOCTOR OF PHILOSOPHY
in
CHEMICAL SCIENCES

By

Ulaeto, Sarah Bill

Registration No: 10CC15A39007

Under the guidance of

Dr. T.P.D. Rajan

CSIR-National Institute for Interdisciplinary Science and Technology
Thiruvananthapuram-695019, Kerala, India

September, 2019

Dedicated to my Loving Parents,
Pastor & Deaconess (Mrs) Samuel & Iquo Bill
Ulaeto (Late)

DECLARATION

I hereby declare that the Ph.D. thesis entitled **"Development of Smart Anticorrosion Coatings from Biomass Extracts"** is an independent work carried out by me at Materials Sciences and Technology Division, CSIR-National Institute for Interdisciplinary Science and Technology (CSIR-NIIST), Thiruvananthapuram under the supervision of Dr. T. P. D. Rajan and it has not been submitted anywhere else for any other degree, diploma or title.

Sarah Bill Ulaeto
(CSIR-TWAS SRF)

Thiruvananthapuram
September, 2019
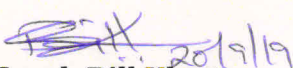
CERTIFICATE

This is to certify that the work embodied in the thesis entitled **"Development of Smart Anticorrosion Coatings from Biomass Extracts"** has been carried out by **Ms. Sarah Bill Ulaeto** under my supervision and guidance at Materials Science and Technology Division, CSIR-National Institute for Interdisciplinary Science and Technology (CSIR-NIIST), Trivandrum and the same has not been submitted elsewhere for any other degree. Research materials obtained from other sources has been duly acknowledged in the thesis. Any text, illustration, table etc., used in the thesis from other sources, has been duly cited and acknowledged. It is also certified that this work done by the scholar, under my supervision, is plagiarism free.

Sarah Bill Ulaeto
(CSIR-TWAS SRF)

Dr. T. P. D. Rajan
Principal Scientist
CSIR-NIIST
Trivandrum

Trivandrum
20th September, 2019

ACKNOWLEDGEMENTS

CONTENTS

Chapter 2 Biomass Derived Corrosion Inhibitors and Coatings for Aluminium Alloys – Role of *Azadirachta indica* Extract Phytochemicals

Chapter 3 Smart Anticorrosive Bio-Coatings: Evaluation of Quercetin for Corrosion Protection of Al6061

Chapter 4 Biogenic Ag Nanoparticles of Neem Leaves Extract; its Structural Evaluation and Antimicrobial Investigations

Chapter 5 Smart Core-Shell Hybrid Nanocomposite Coatings with Multifunctional Characteristics

Chapter 6 Summary and Future perspectives

List of Tables

List of Figures

xiii

List of Abbreviations

cm	Centimetre
A	Ampere
ATR-FTIR	Attenuated total reflection-Fourier transform infrared
BE	Binding energy
C	Capacitance
°C	Degree Celsius
CPE	Constant phase element
d	Diameter
DGEBA	Diglycidyl ether of bisphenol-A
E_{corr}	Corrosion potential
EDS	Energy-dispersive X-ray spectroscopy
EIS	Electrochemical impedance spectroscopy
eV	Electron volt
f	Frequency
FTIR	Fourier transform infrared
FWHM	Full width at half maximum
g	Gram
HY951	Araldite HY951 hardener
Hz	Hertz
i	Current density
i_{corr}	Corrosion current density
L	Litre
min	Minute
mm	Millimeter
mM	Millimolar
n	CPE constant

nm	Nanometer
OCP	Open circuit potential
R_{ct}	Charge transfer resistance
R_p	polarization resistance
R_s	solution resistance
s	Second
SCE	Standard calomel electrode
SEM	Scanning electron microscopy
V	voltage
wt.%	Weight percentage
XPS	X-ray photoelectron spectroscopy
XRD	X-ray diffraction
Z	Impedance
μm	Micrometer
Ω	Ohm
MS/MSN	Mesoporous silica nanoparticles
EP	epoxy
EENL/NLE	Ethanol extract of neem leaves
PDP/PP	Potentiodynamic polatization
TG	Thermogravimetry
TEM	Transmission electron microscope
DLS	Dynamic light scattering
Al6061	Aluminium alloy 6061
CTAB	Cetyltrimethylammonium bromide
NaCl	Sodium chloride
NaOH	Sodium hydroxide
TEOS	Tetraethyl orthosilicate
HCl	Hydrochloric acid
NBCs	Neem bionanocomposites

HRTEM	High-resolution transmission electron microscope
FFT	Fast fourier transform
SERS	Surface-enhanced Raman spectroscopy
AgNO$_3$	Silver nitrate
NPs	Nanoparticles
ANCs	core-shell silver nanoparticles
ANCCs	core-shell silver nanoparticles/nanocomposites coatings

Preface

Chapter 1 describes the overview of smart coatings and their relevance for corrosion inhibition. It also discusses the role of nanodispersoids in anticorrosive coatings. With the unique properties of nanomaterials being size and shape-dependent with respect to the high surface area, surface activity, etc. The uniqueness of smart coatings is related to phenomenal innovations and its developments continue to accelerate. In addition, phytochemicals from plant matter were reviewed as corrosion inhibitors. The efficiency of the biomass-derived phytochemicals in coating formulations was also considered. The presence of a variety of active organic compounds in readily available biomass species has made them compelling candidates for eco-friendly corrosion inhibition of metals and alloys.

Chapter 2 describes the surface preparation of aluminum and its alloys prior to corrosion inhibition studies which influence the efficiency of the inhibitors used as well their adsorption phenomenon. The influence of surface pretreatments (degreasing and etching) on the corrosion behavior and interaction with inhibiting neem biomolecules on aluminium alloy 6061 were investigated. Immersion test and potentiodynamic polarization were employed as corrosion monitoring techniques. Surface morphology, chemistry and crystalline nature of both corrosion and inhibition products of the treated surfaces were characterized using scanning electron microscopy/energy dispersive spectroscopy (SEM/EDS) and X-ray diffraction spectroscopy (XRD).

Furthermore, a new contribution to the development of self-healing anticorrosive primers using natural organic inhibitors is described. Neem leaves extract (NLE) loaded silica nanocomposite was prepared to obtain organic-inorganic hybrid self-healing coatings utilizing neem biomass extract for the first time in such coating formulations. The smart hybrid coating formulated and used in the study for protecting aluminum alloy 6061 contained 2 wt.% of the natural inhibitor loaded silica nanocontainers using two different solvents; ethanol and hexane for the loading process. The anticorrosive performance of the newly synthesized coatings was evaluated with electrochemical impedance spectroscopy (EIS) and potentiodynamic

polarization (PP) techniques when exposed to 3.5 wt.% NaCl solutions with varying pH. Through monitoring the corrosion around artificial scratches, it was observed that ethanol loaded nanocomposite coating displayed the satisfactory self-healing effects. This was attributed to the smart nanocontainers and the biomolecules responding efficiently to alkaline pH triggers, sealing the defect to control further damage to the coatings. The novel active coatings revealed enhanced corrosion protection in comparison with the unmodified epoxy coating film.

Chapter 3 investigates the corrosion inhibiting efficiency of Quercetin (QCT) a known secondary metabolite of plants, loaded in silica nanocontainers to obtain self-healing coatings. QCT, hosts five electroactive hydroxyl groups in addition to carboxylic, carbonyl and aromatic groups etc., which participates in the interaction with the silica nanocontainers and the coating matrix. The hybrid coating developed and used in the study for protecting aluminum alloy 6061 displayed both active and passive anticorrosive properties. The storage of QCT in the nanocontainers was investigated using UV-visible spectroscopy and TGA while the pH triggered release of QCT from the nanocontainers and its subsequent reactions were determined with UV-visible spectroscopy and further confirmed with FTIR.

The anticorrosion performances of the nanocomposite and the formulated coatings on aluminum alloy 6061 surfaces were systematically evaluated by electrochemical impedance spectroscopy (EIS) and potentiodynamic polarization (PP) techniques. With an artificial defect induced on the epoxy nanocomposite coating and subsequent corrosion reactions, a self-healing action was triggered in comparison with the unmodified epoxy coating at pH 10. The corrosion protection offered by QCT was due to the chemical transformation experienced by QCT with pH influence involving possible autoxidation and polymerization processes. Furthermore, a primary investigation was conducted to assess the antibacterial property of the epoxy-based coatings which offered manifold antibacterial protection to the aluminium alloy surfaces by inhibiting the growth of the biofilm-forming bacteria *Pseudomonas nitroreducens*.

Chapter 4 describes the successful fabrication of silver nanocrystals by the bioreduction route using the ethanolic extract of *Azadirachta indica* (Neem) leaves as the reducing and capping agent without the solvent interference. The silver nanocrystals were grown in a single-step method, at room temperature, and without the influence of external energy or surfactants. The nanoparticles were roughly spherical and polydispersed with diameters less than 40 nm as determined with High-resolution transmission electron microscopy. The SERS activity of the Ag nanoconstruct was explored using 30 μM solution of Rhodamine B as the Raman probe molecule. It was possible to detect the SERS spectral pattern of the probe molecules on the Ag nanoconstruct without the use of any aggregating analytes. Thus, the formation of probable intra and inter-particle hot-spots is attributed to evaporation-induced aggregation. Furthermore, the effect of stirring and precursor salt concentration influenced the kinetics involved in the fabrication process. The lyophilized nanoparticles prepared from 0.1 M AgNO$_3$ inhibited the growth of biofilm-forming bacteria like *Pseudomonas nitroreducens*, and fungi *Aspergillus niger.* This provides a promising contribution to material science for the fabrication of active bionanocomposite coatings.

Chapter 5 describes the evaluation of silver nanocomposites for both anticorrosive and antimicrobial performances in fabricated epoxy-based coatings. Neem biomass extract was utilized as the reducing agent in the preparation of the silver nanoparticles via a one-pot synthesis protocol. The one-pot synchronous process produced stable, near-spherical silver-core nanocomposites. The mesoporous silica shell allowed the incorporation of the neem inhibitor within its pores. A combination of Tetraethylorthosilicate and Octyltriethoxysilane were used as surface modifiers to impart stability, control surface reactivity through functionalization, and improve the dispersibility of the nanoparticles in the epoxy matrix. The presence of the bio-based corrosion inhibitor in the nanocomposite provided enhanced anticorrosion performance compared to the unloaded epoxy coatings. The antimicrobial effect of silver nanoparticles in the core was influenced by the confinement of the silver nanoparticles restricting its release in sufficient amounts. Directly spiking of silver

nanoparticles in the epoxy matrix without functionalization resulted in poor anticorrosion performance due to promoted conductivity from the silver particles in the epoxy resin. A hybrid of the silver nanoparticles with the bio-based corrosion inhibitor leveraged the anticorrosion performance of the coatings positively and improved the antimicrobial performance of the nanocomposite coatings by inhibiting the growth of *Pseudomonas nitroreducens* and *Aspergillus unguis* species.

Chapter 6 summarizes the entire thesis work and also includes a number of future perspectives.

Chapter 1

Introduction to Smart Coatings

Abstract

Smart coatings are innovative coatings that can react spontaneously due to stimuli-responsive mechanisms. These class of coatings has gained recognition in material sciences, colloidal chemistry, biomedical sciences, and polymer chemistry due to the characteristic properties and chemistry they possess on fabrication. The functionality obtained from these class of coatings at the metal-solution interface in aggressive environments has led to advances in anticorrosion studies and applications. Smart coatings are creatively prepared for diverse applications and desirability is in being able to respond to several cycles and spanning over many years. Smart coatings respond to several external stimuli and in response have demonstrated outstanding, barrier properties which have resulted in the extended service life of the coatings and protection for metallic materials. Many smart coatings contain diverse dispersants which provide various functional properties and enhanced performances. Ranging from the use of micro to nanoparticle formulations, as well as combinations of organic and inorganic phases. Smart coatings have exhibited superior properties in comparison to many classical coatings. The use of materials at the nanoscale has contributed immensely to the enhanced performances of smart inhibiting materials compared to the micro and macroparticles. Smart anticorrosive coatings are formulated to contain both passive and active components so that on application the benefits of its prompt response based on the required stimuli can be achieved. The utilization of smart coatings in complex, real-time conditions is aimed at effectively controlling the triggers of metallic degradation, structural failures, and resource depletion.

1.1 Introduction

Smart coatings also known to as "intelligent," coatings provide a spontaneous response to changes in the microenvironment such as heat, light irradiation, mechanical induction, wettability, temperature, pressure, ion exchange, pH variation, aggressive

corrosive ions, etc.[1–4] They are designed to maintain a passive feature, provide superior performance and recover the functional performance of coatings by exhibiting stimuli-responsive behavior when the need arises. The stimuli-responsive characteristic of smart coatings enhances the efficiency of the coated system. The driving force in developing smart coating technologies is the continuous demand for higher performance, extending product lifetimes and significantly reducing maintenance cost. Enhancing energy efficiency for both cost and environmental reasons, as well as coping with the change in substrates towards new and lightweight materials like composites and lightweight metals such as aluminium and its alloys etc. Examples of smart coatings include but are not limited to anti-inflammatory, antimicrobial and antifouling coatings; corrosion, degradation, and defect sensing coatings; self-healing and pressure-sensing paints; reversible thermochromic, piezoelectric paint, hydrophilic/hydrophobic switching, self-cleaning, pH-responsive, light-sensing coatings, self-erasing inks, smart window coatings, photochromic and electrochromic coatings, radio frequency identification coatings, antibacterial, anti-icing, intumescent coatings etc.[1,2,5–7]

Shifting demand towards nano-based coatings instead of conventional polymer coatings and other microparticle-based coatings due to superior properties and low Volatile Organic Contents (VOC) emissions are expected to be the major mainspring for the nanocoatings market. But with the growing preference for advanced materials in sectors such as medical and automotive industry, there is a surge in nanotechnology research and development, expected to boost market growth. Nanotechnology-based coatings are embraced by the nanocoatings market due to its superior properties such as abrasion resistance, ductility, hardness, lubricity and transparency to mention a few as compared to other conventional coatings. A boost in market demand is expected from the application of anti-microbial and self-cleaning coatings in mechanical and aerospace applications for extending the durability of parts. Nanostructured coatings, however, provide key functions such as protection from ice, pollutant, UV, fire, heat, bacteria, marine foulants, touch, and corrosion. Due to the fact that properties such as anti-microbial action, product longevity, thermal insulation, anti-graffiti, self-cleaning,

moisture absorbing, gloss retention, dirt and water repellency, hardness, corrosion resistance, flame retardancy, ultraviolet radiation stability, improved energy efficiency, chemical and mechanical properties to mention a few are significantly improved with nanostructured materials.[8]

Being increasingly used in a variety of applications in the medical, textile, transport, construction, military, electronics, aviation and several other industries for providing varying functionalities alongside protecting against corrosion. Smart coatings have been considered as pragmatic candidates without manual intervention. The goal of smart coatings is therefore directed at improving a system's efficiency by reducing inspection times, significantly reduce the maintenance costs and equipment downtime in many industrial applications. It is a class of coatings capable of impacting on the society in a significant way.[1,2,4,7,9] This chapter aims to provide a concise perspective on smart coatings and its developments as its utilization cuts across various aspect of science.

1.2 Classification of smart coatings

Smart coatings may be classified based on application, function, responsiveness, material types, level of complexity,[10] functional ingredients and fabrication methods etc.[11] The functional ingredient within these intelligent coatings can be the resin or from a variety of additives such as pigments, bioactive species, enzymes, microencapsulated agents, nanomaterials, inhibitors, radiofrequency identification devices, microelectromechanical devices etc., [12]. Triggers for the required responses come from both internal and external stimuli. When applied to the surfaces of the desired substrates these smart coatings contribute to decoration in their functionality. These chemically active coatings exhibit their various functionality either on film-substrate interfaces, air-film interfaces or in the bulk of the film. In the various sectors of application, multifunctionality of smart coatings is an advantage.[1,2,4,6,9] The selected smart coatings discussed herein are categorized based on the functions exhibited by the coatings. Self-healing coatings are discussed under smart repair coatings. Active sensing coatings include corrosion-sensing and pressure-sensing coatings. Flame-retardant coatings are intumescent and non-intumescent coatings. Antifouling and anti-

bacterial coatings are referred to as bioactive coatings. Easy-to-clean coatings include self-cleaning and anti-graffiti coatings. Smart window coatings are optically active coatings. Others are anti-fingerprint, anti-reflective, anti-icing, and anti-fogging coatings.

1.2.1 Smart repair coatings

1.2.1.1 Self-healing coatings

The concept of self-healing is a key property of biological materials and has drawn considerable research interest in the medical sector and pharmaceutical industries and is now very relevant in the development of corrosion-resistant coatings. [13] The self-healing effect is modeled after the biological wound healing process and the functional nature of the self-healing coating depends on its chemical composition and structure. [4] The self-healing concept was first proposed in 1979 by Jud and Kausch through molecular inter-diffusion across crack interfaces and later advanced by White and co-workers in 2001 by embedding microcapsules containing healing liquid and catalyst particles into the matrix material.[14,15] Self-healing materials are known to provide the following advantages over the conventional coating: (i) automatic repair process upon damage; (ii) auto-preservation of aesthetics of surface appearance of coatings, plastic, and films; (iii) restoration of mechanical integrity of load-bearing materials such as composites etc. [13].

Self-healing materials are generally classified into non-autonomous and autonomous systems. Non-autonomous self-healing (or stimuli-assisted) can be induced and controlled by heat, light, mechanical forces, chemical reactions, pH, etc. while autonomous self-healing does not require any external intervention because the damage itself triggers repair processes. Autonomous systems, therefore, behave as smart, adaptive materials and the autonomous self-healing process can either be intrinsic or extrinsic. Intrinsic involves mending mechanical failures since it is based on the formation of either covalent or non-covalent chemical bonds between cracked interfaces. Although, engineering intrinsic processes is quite hard for most of the materials. Extrinsic requires the presence of some externally loaded healing agents, responding when triggered by mechanical damage.[16] Amongst the different

approaches for self-healing coatings, the use of nanocontainers has been the most widely accepted and employed due to the versatility of nanocontainer fabrication and the variety of possible applicable healing agents[17] Nanocontainers such as halloysite clay, mesoporous silica,[3,18] cyclodextrins[19], layered double hydroxide, polyelectrolyte multilayers and mesoporous zirconia, exist and are being utilized.[3,6] Various self-healing mechanisms in polymeric materials have been described in Fig. 1.1.[20] The illustration explains self-healing based on the actions of healing agents in enclosed micro or nanocapsule embedded in polymer matrices.
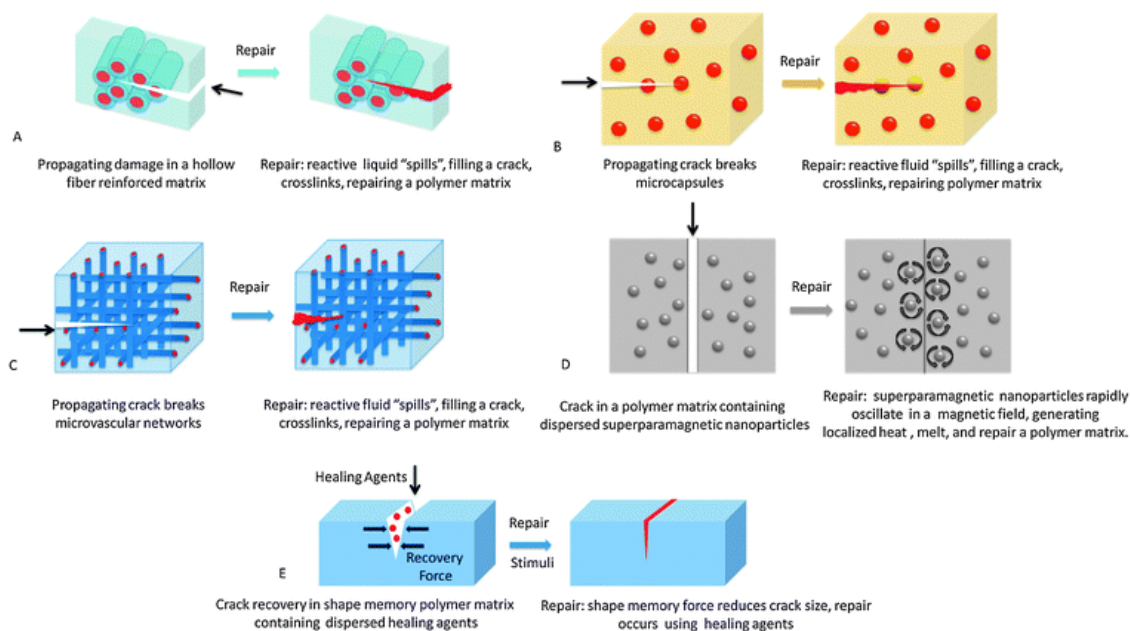
Fig. 1.1: (A-E) Self-healing of different enclosed micro or nanocapsule healing agents in polymeric matrices.[20]

The self-healing ability of coatings has become a treasured and desirable effect of protective coatings. This is due to the considerable delay in corrosion when they are in use and a subsequent reduction upon final occurrence. Smart self-healing coatings provide a protective film build-up via adsorption on the exposed area of the metal or alloy. Physisorption and strong covalent bonds are involved in the attachment of the nanoparticles to the polymer molecules as well as with other functional molecules of small sizes [4]. It is best to design and establish such a stimuli-responsive release system (self-healing system) that entrap corrosion inhibitors in containers with a high uptake

capacity and releases only in response to certain stimuli. Hence, nanocontainer-based coatings serve as the solution for the challenge of self-healing for corrosion inhibition processes. The nanoparticles, in addition to occupying minor defects and holes formed during the curing process of the coating also ensures interconnection of the molecules through its bridging effect. By incorporating the inhibitor-loaded nanocontainers into the coating, further corrosion occurrence is suppressed by the long-term self-healing effect derived from the high inhibitor uptake and release capacity and response to local changes resulting from corrosion.[17,18,21]

1.2.2 Active sensing coatings

1.2.2.1 Corrosion-sensing coatings

Corrosion sensing coatings are used to monitor the corrosion risk of the material at the early stages of deterioration. It is well-known that when corrosion occurs, the anodic region possesses an acidic pH and the cathodic region has an alkaline pH. pH-triggered release of corrosion indicators and healing agents from the microcapsules or nanocapsules is one of the active research areas. The corrosion sensing indicators can be color or fluorescent dyes. The size and pH sensitivity of the microcapsule or nanocapsules can be controlled by adjusting the preparation method and time.

1.2.2.2 Pressure-sensing coatings

Pressure-sensing coatings have been applied on wind tunnel models and flight vehicles to quantify the surface pressures for aerodynamic and acoustic investigations. It determines surface pressure distributions by measuring changes in the intensity of emitted light. Mainly, luminescent coatings are painted on the surface which will be excited by light of appropriate wavelength and imaged with digital cameras.[22] Another category is the porous pressure-sensitive paint (PSP) which contains a binder (porous material with the large surface area to hold luminophores directly) with a response time in the order of 1 µs. The response time is due to the feasibility of oxygen molecules in the test gas directly quenching luminescence without having to permeate into the binder layer as shown in Fig. 1.2. Anodized aluminum, anodized titanium, polymer/ceramic, thin-layer chromatography (TLC) plate etc. have been used as porous materials[23]
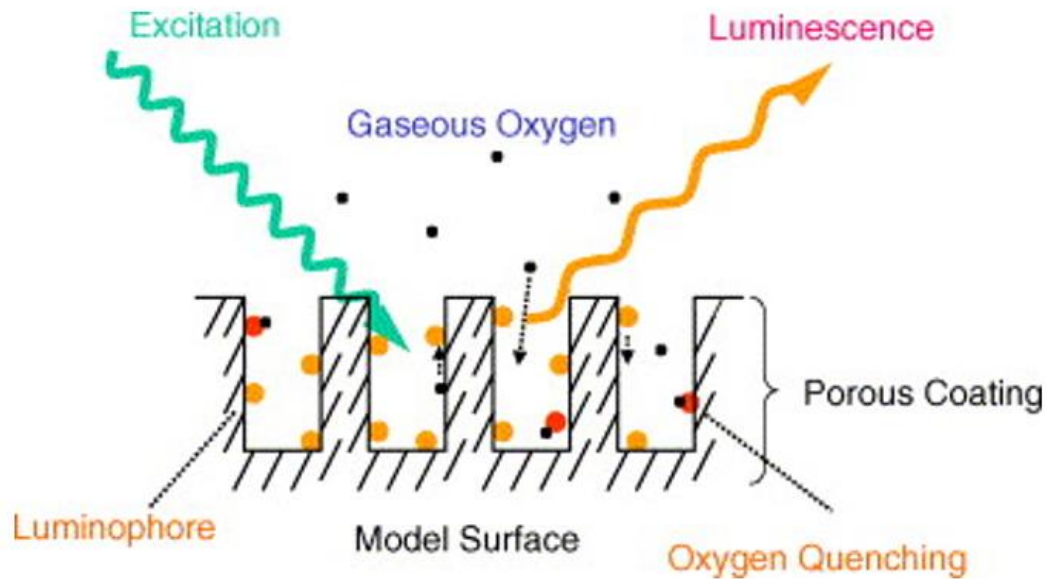
Fig. 1.2: Schematic illustration of porous pressure-sensitive paint (PSP).[24]

Fast pressure-sensitive paint is an extension applicable to unsteady flows and acoustics. Majority of the fast PSP formulations are associated with porous binders that allow rapid oxygen diffusion and interaction with the chemical sensor. Calibrations of their dynamic response have shown a flat frequency response to a minimum of 6 kHz, with some paint formulations exceeding a response of 1 MHz[23]

1.2.3 Optically-active coatings

1.2.3.1 Smart window coatings

These are thin films with spectrally selective properties on the surface of glass. They are characterized by their ability to regulate the amount of radiant energy between wide limits. These coatings are commonly referred to as Energy Efficient Window Coatings.[25–27] Smart window coatings are required to impede inbound infrared radiation from the sun's rays during warm weather conditions but provide heat retention inside a room during cold seasons. Since the active materials in these coatings obstruct both near-infrared (NIR) light and visible light, this allows customization of the window settings to maximize energy efficiency. Thus, energy-consuming processes are greatly eliminated. Smart window coatings can be fabricated

from any of the following; photochromic coatings, thermochromic coatings, suspended particle devices (SPD), polymer dispersed liquid crystal devices (PDLC), electrochromic coatings etc.[26,28,29]

SPD or electrochromic windows seem really encouraging for dynamic daylight and solar energy applications in buildings based on the achieved transmittance modulation ranges. However, SPDs consume higher energy due to the electric field which is a key requirement for controlling the transparent mode of the glass.[28] A notable study by Li et al. described an approach where a single nanoparticle structure (VO$_2$@TiO$_2$ core-shell nanorods) with both thermochromic and photocatalytic properties offered significant potential for creating a multifunctional energy-saving smart coating. With the vanadium dioxide (VO$_2$) nanorod core, a remarkable modulation ability for solar infrared light was achieved while the anatase titanium dioxide (TiO$_2$) shell displayed significant photocatalytic degradation of organic dye.[27] Another interesting study by Liu et al. was based on the synergistic effect of potassium-doped tungsten bronze (K$_x$WO$_3$) powder and surface-fluorinated TiO$_2$ (F-TiO$_2$), to obtain FT-KWO nanocomposite films for windows. With the fabricated films, strong near-infrared, ultraviolet light-shielding ability, good visible light transmittance, superior photocatalytic activity, and exceptional hydrophilic capacity were achieved. The proposed multifunctional NIR shielding-photocatalytic nanocomposite window film is meant to solve the energy crisis and deteriorating environmental issues. The working model is described in Fig. 1.3 [30].
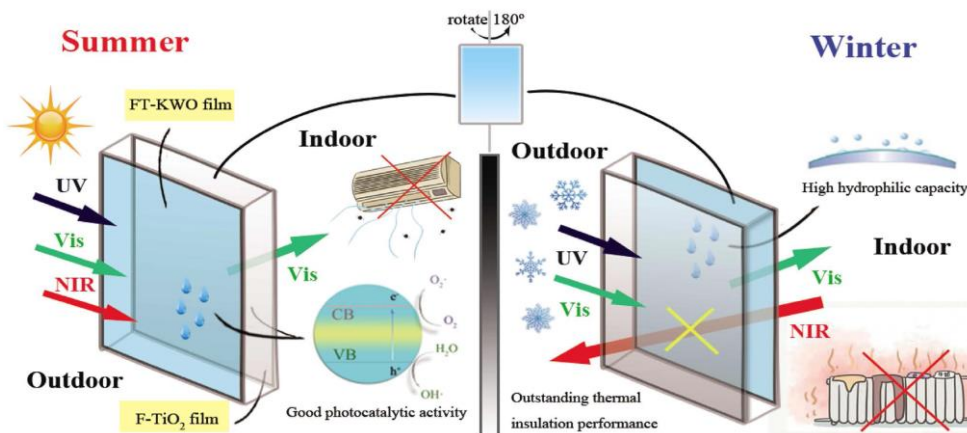
Fig. 1.3: Schematic of the FT-KWO and F-TiO$_2$ coated window applied to dissimilar conditions.[30]

1.2.4 Easy-to-clean coatings

1.2.4.1 Self-cleaning coatings

Self-cleaning coatings inspired by nature and centered on surface contact angles ensures an independent action of dirt removal from a surface by either hydrophilic or hydrophobic techniques. The first approach involves the application of a photocatalytic coating to the substrate surface, where the effect of the sun's ultraviolet rays catalytically breaks down organic dirt. Simultaneously, the surface becomes superhydrophilic spreading the water evenly over the surface and less drying traces are formed by dripping. In the other approach, a self-cleaning (bionic) surface is achieved in congruence with the Lotus effect phenomenon in which the surface becomes super-hydrophobic. The extent of hydrophobicity is determined by the contact angle of water. Contact angles greater than 90° are regarded as hydrophobic. While contact angles of 150° or higher yield surfaces that are superhydrophobic and repel water droplets completely.[4,8] Superhydrophobic surfaces are obtained from roughened hydrophobic surfaces. The effects of both, the contact and the sliding angle are important in defining a superhydrophobic surface with a self-cleaning effect. This is because, for self-cleaning in addition to the high contact angle, the water drop should slide off the surface.[31] Fig. 1.4 illustrates self-cleaning related actions such as (i) natural self-cleaning surfaces and corresponding SEM micrographs. (ii) hydrophilic action of self-cleaning coating via photocatalysis reaction of titanium dioxide coating on a pre-painted aluminium surface. (iii) Lotus effect (a) self-cleaning and (b) wetting based on contact angle differences (iv) hydrophobic/superhydrophobic action of self-cleaning coatings made of organosilane-coated alumina particles deposited via electrospraying.
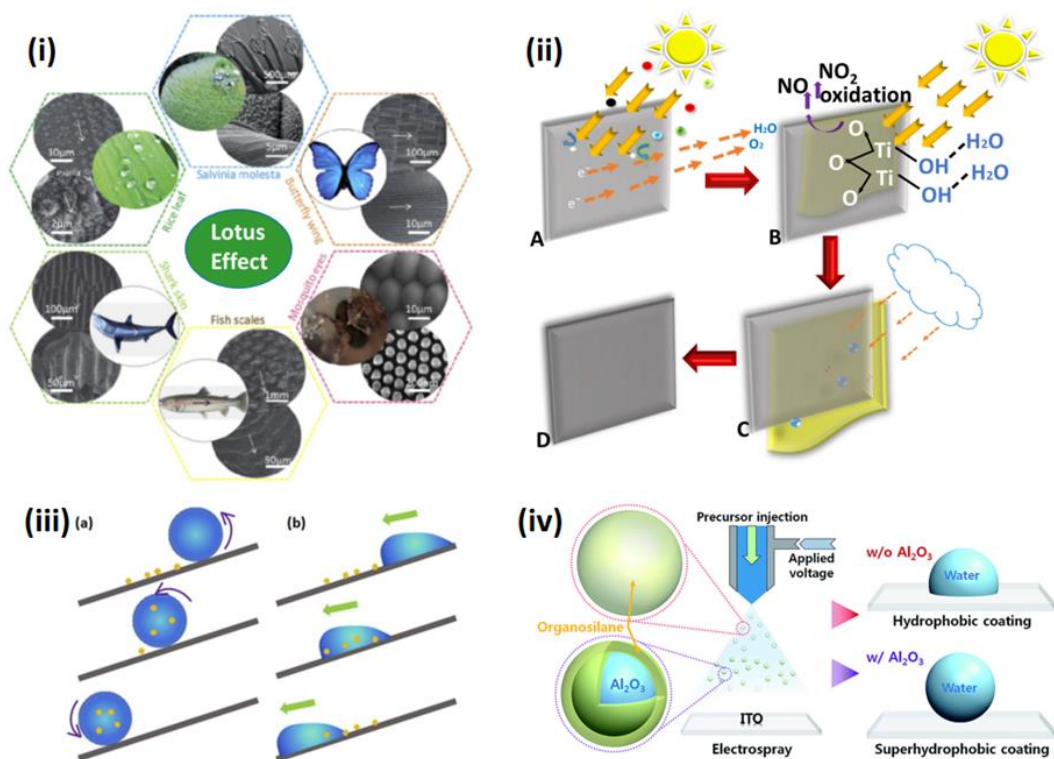
Fig. 1.4: (i) Natural self-cleaning surfaces and corresponding SEM micrographs.[32] (ii) Hydrophilic action of a self-cleaning coating. Schematic shows photocatalysis reaction of titanium dioxide coating on a pre-painted aluminium surface. (A) UV light energizes the electrons in TiO_2 which transfer energy to oxygen and water in the air forming free radicals like *OH. (B) The free radicals attack organic matter by oxidation as hydroxyls accumulate on the surface. (C) The hydroxyls collapse water molecules on the surface in the cleansing action. [4] (iii) Lotus effect (a) self-cleaning and (b) wetting based on contact angle differences.[32] (iv) Hydrophobic/superhydrophobic action of self-cleaning coatings made of organosilane-coated alumina particles deposited via electrospraying.[33]

1.2.4.2 Anti-graffiti coatings

Graffiti is a major challenge to architectural heritage materials. Graffiti affects a wide variety of surfaces and the cleaning is very expensive and quite often, the penetration into the pores contained in the substrate material induces an irreparable effect onto the painted surface. Anti-graffiti coatings have been developed by functionalizing nanoparticles and polymers to form a coating repellent to both water

and oil simultaneously. As a result, the coated surface can be a non-stick surface, an easy to clean surface, and also able to withstand repeated graffiti attacks.[8,34] To enable hassle-free cleaning of the substrates fluorinating agents have been used to lower surface energy of the coating by migrating onto the coating surface. This offers good hydrophobicity reducing the adherence of staining agent to substrates. Also, outstanding thermal and oxidative stability, low coefficient of friction and good chemical resistance is achieved with its use.[35] Fluoropolymers exhibit a great deal of oleophobicity since the high extent of electronegativity and low polarizability of fluorine atom in the backbone or side chains induces hydrophobic and oleophobic properties to the coatings synthesized from them [36]. Furthermore, most commercially available anti-graffiti paints are siloxane/silicone-based formulations. They repel most of the water-based paints and markers [37].

1.2.5 Bioactive coatings

1.2.5.1 Antifouling coatings

Biofouling occurs when microorganisms in water adhere to wet surfaces, multiply and gradually cover the surface with biofilm. Effects of biofouling costs marine, shipping, and other global industries billions of dollars every year.[38] Fouling basically occurs in two categories: micro and macro-fouling. Antifouling coatings are meant to reduce biofouling and its attendant effects and are categorized into biocide-free coatings and biocide containing coatings [4]. Specifically, antifouling coatings can be further categorized into chemically active self-polishing coatings (SPC) with booster biocides, silicone- and fluorine-based fouling release coatings (FRC), based on physicochemical and mechanical effects. The efficacy of SPC is connected to biocidal effects, while for the biocide-free FRC, the adhesion between foulant and the surface is minimized due to the low surface energy and elastic modulus. This ensures that biofouling can be removed by hydrodynamic stress during movement or mechanical cleaning. However, FRCs fail to prevent the colonization of biofilm but inhibit the adhesion of most macrofouling under dynamic conditions. The biofilms predominantly consist of diatoms which adhere tenaciously to hydrophobic surfaces and are not

released from FRC, even on vessels operating at high speeds such as >30 knots.[39–41] Fig. 1.5 illustrates the marine antifouling coating approaches.
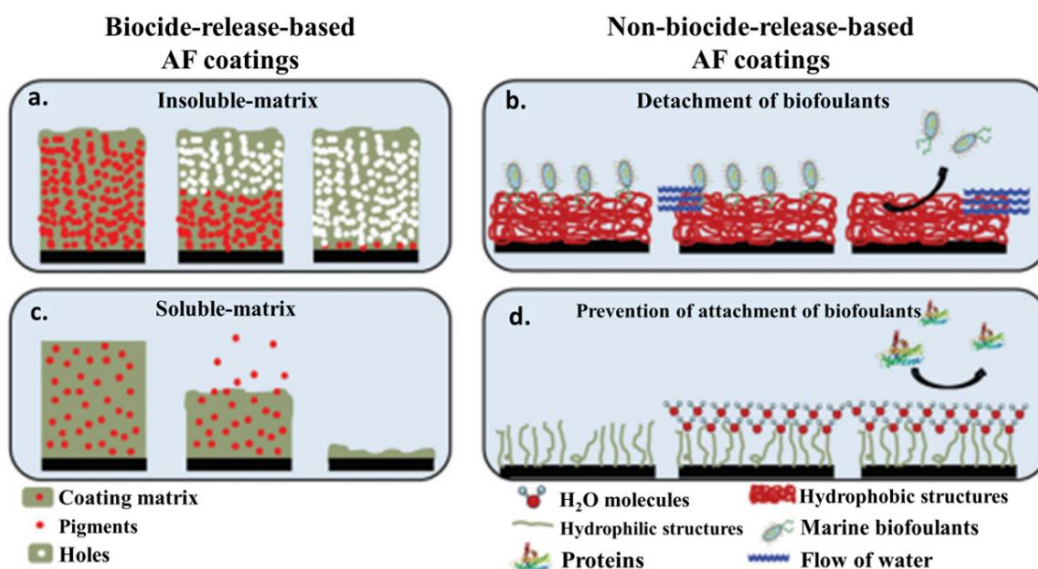
Fig. 1.5: (a-d) Marine antifouling coating approaches.[42]

Marine biofouling is of great concern to the maritime sector due to its related huge economic losses since substrates are rapidly colonized by both micro- and macro-organisms when immersed in seawater. This process is accountable for important economic and ecological effects, related to shipping hulls which result in the increase of fuel consumption and dry-docking operations. This further leads to significant increases in pollution and economic burden. Thus, antifouling coatings are meant to reduce biofouling and its attendant effects.[41,43] An effective antifouling coating should exhibit antifouling properties, durability, good adhesion, corrosion inhibition, smoothness. It should be easy to apply, fast-drying, economical, and accessible etc. [44] Over time, Tributyltin (TBT) has been the most widely used chemical antifoulant compound. To avoid the known adverse effect of TBT and its derivatives on marine environments, rigorous studies have been ongoing towards obtaining eco-friendly antifouling coatings able to withstand the rigors of practical applications such as shipping. Furthermore, eco-friendly antifouling paints containing natural biodegradable compounds have been reported. This involves the use of bacteria

isolated from living surfaces in the marine environment to produce chemicals that are potential antifoulants.[43]

1.2.5.2 Anti-bacterial coatings

Bacterial interactions are dominated by several factors and one of such is the surface charge. The bacterial surface charge varies depending on the species, the containing medium, the age of the bacteria and the rod or round surface structure.[45] Generally, bacteria survive by attaching to solid substrates via biofilms, where they can persist for extended periods, acting as a reservoir of pathogens and multiplying their pathways of transmission. In the biofilms, they are drastically more resistant to antibiotics and external forces and can withstand host immune responses. In-dwelling devices and implants, as well as surfaces in the near-patient environment, they play a major role in the spread of hospital-acquired (nosocomial) infections. These nosocomial infections can be attributed to Gram-negative bacterial pathogens, for which there is a dwindling supply of antibiotics. The need for antibacterial coatings is strongly stimulated by the increasing urgency of identifying alternatives to the traditional administration of antibiotics. Hence, the development of controlled release strategies is vital to optimizing therapeutic effects.[46] A study demonstrated by Su et al. revealed that a shaking condition applied to the self-polymerization of dopamine in an alkaline solution can facilitate the formation of roughened polydopamine (rPDA) coatings which remarkably enhanced antibacterial activities against gram-positive *S. aureus*, and gram-negative *E. coli* and *P. aeruginosa*. The cell membranes of the bacteria incubated with the rPDA coatings were damaged by the contact-kill mechanism.[47] The gradual release of antibacterial agents, contact-killing, and anti-adhesion/bacteria-repelling approaches are the three major strategies for designing antibacterial coatings[46,48] as demonstrated in Fig. 1.6 (a-c).
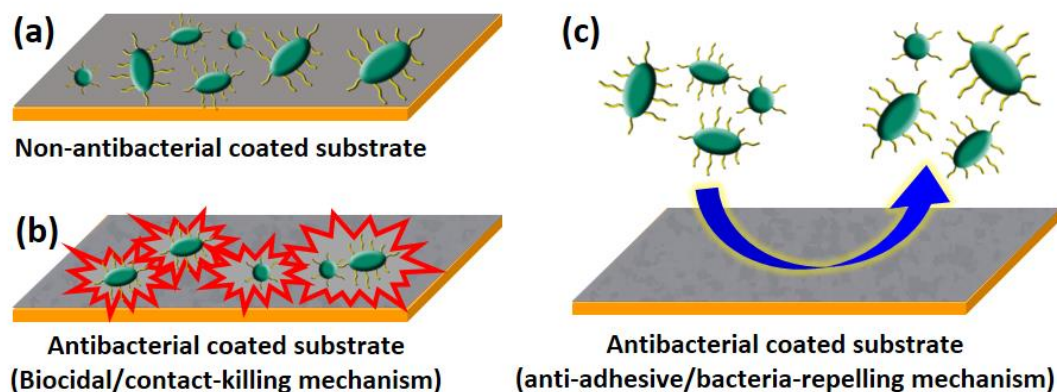
Fig. 1.6: Schematic of bacterial action in contact with (a) non-antibacterial coating (b) antibacterial coating featuring contact-killing mechanism (c) antibacterial coating featuring anti-adhesive mechanism.

1.2.6 Fire-retardants coatings

1.2.6.1 Intumescent coatings

Intumescent coatings decrease heat transfer to the substrate structure hence, are used as protective fire-resistant materials. An intumescent coating swells on heat exposure, thus increase in volume and decrease in density will occur. They can be applied to structural members as fireproofing paint. Intumescent paint contains many ingredients such as acid source, charring agent, blowing agent, binder etc. The binder acts as a carbon source and also impacts on the foaming process.[49] The selection of appropriate of flame-retardant fillers strongly influences the physical and chemical properties of the coatings. Intumescent coatings made of acrylic binder and flame-retardant ingredients on steel substrates showed better fire protection as well as mechanical properties. It is reported that the combination of aluminium hydroxide $(Al(OH)_3)$ and titanium dioxide (TiO_2) has significantly improved the fire protection, thermal stability and water resistance.[50]

Intumescent coatings made of epoxy resin as a binder with variable concentrations of coconut fiber (CCN), wood waste (MDP) and peach stones (PEA) biomasses were studied. The optimum dry mass percentage of CCN and MDP was 9%, while 6% is ideal for PEA. The determined total expansion of the coatings after fire

resistance testing was more than 600% for CCN9, 1300% for MDP9 and 1600% for PEA6 and 1500% for the blank coating. The biomass-based intumescent coatings showed better thermal insulation. Also, the maximum temperatures on the back of the coated substrates were 120°C and 474°C for uncoated steel.[51] Intumescent flame-retardant coatings with incorporated chicken eggshell (CES) waste as a filler in addition to the flame-retardant additives; ammonium polyphosphate phase II, pentaerythritol and melamine in the acrylic binder has been proven to be efficient in the protection of plywood against fire.[52] Furthermore, epoxy resin coatings prepared with vegetable compounds such as ginger powder and coffee husk as a carbon source showed better flame resistance [53].

1.2.6.2 Non-intumescent coatings

Active non-intumescent coatings release fire-retarding species such as gas-phase radicals from the formulations of water-soluble salts containing phosphate, nitrate, halides sulfate, sulfamate, boric acid, and borax.[54] Methacrylated phenolic melamine (MAPM) incorporated epoxy acrylate has been reported to have superior flame retardancy. It was found that decomposition of melamine released non-flammable nitrogen volatiles like ammonia has no increase in char formation.[55] Çakmakçi et al. prepared flame retardant epoxy acrylate coatings with the incorporation of phosphate-containing allyldiphenylphosphine oxide (ADPPO).[56] Likewise, phosphorus-containing UV cured hyperbranched polyurethane acrylate showed a limiting oxygen index of 27.0. The synergistic effect of phosphorus at 0.7 wt.% and nitrogen provided an enhancement. The P-O-P bonds were formed by the breaking of P-O-C bonds. The presence of phosphorus in coating supported the char formation and reduced the flame attack of underlying polymeric materials.[57]

1.2.7 Other smart coatings

1.2.7.1 Anti-fingerprint coatings

These smart coatings provide a fingerprint-hiding effect. Anti-fingerprint coatings are widely used for touch screens in consumer electronic devices. With the release of surfactants or enzymes in response to surface contact, the deposited fingerprints become faded.[7] Furthermore, anti-fingerprint surfaces should have low

energy, for the formation of an oleophobic weak boundary layer. Low energy surfaces are known to reduce intermolecular attractive forces.[58] The fingerprint problem on a touch screen surface is a pressing issue requiring anti-fingerprint coatings. This can be resolved by the development of protective coating materials with amphiphobic (water and oil repellent) properties. The amphiphobic property can be achieved by the construction of the morphological structure with re-entrant curvature in combination with the chemical composition and roughness on surfaces. Derived from a nano-scaled concave structure consisting of cavities, in which the capillary force produced at the liquid-air interface inside the re-entrant is able to repel liquid (water or oil) from entering the void. In a study by Siriviriyanun and Imae, an attempt to make anti-fingerprint properties from non-fluorinated organosiloxane self-assembled monolayer-coated glass surfaces was achieved. The substrate with non-fluorinated (methyl terminated) organosiloxane (TMS-glass) provided both amphiphobic and anti-fingerprint properties on the surfaces. Also, the hybrid with both hydrophobic and non-fluorinated moieties (octadecyltrimethoxysilane, ODS, and trimethoxymethylsilane, TMS) imparted the same properties evaluated by the contact angle of oleic acid. It was concluded that anti-fingerprint is related to amphiphobicity [59].

Furthermore, the use of fluoride films on glass substrates of electronic panel devices providing anti-fingerprint effects experiences adhesion problems. To overcome the aforementioned, a thin SiO_2 layer should be inserted between the fluoride film and the glass. An attempt to realize an enhanced mechanical durability of an anti-fingerprint coating by further incorporation of silver nanoparticles has been reported. For strong adhesion, the SiO_2 layer was inserted between the silver nanoparticles and the glass substrate and the fluoride/SiO_2 films deposited on that composition. An effective anti-fingerprint property based on a wetting angle of about 116° was achieved.[60] Recently, both anti-fingerprinting and anti-bacterial effects from 30 nm thick ZnO thin films without an additional protective layer for smart phone panel application has been achieved. As a result of a simple annealing treatment of the film, high transmittance (~91.3%) comparable to that of a glass substrate at a wavelength of 550 nm was realized.[61]

1.2.7.2 Anti-reflective coatings

The idea of anti-reflective coatings in physical sciences dates back to Lord Rayleigh (John Strutt) in the 19th century when he observed the tarnishing on a glass increasing its transmittance rather than reducing it. However, Fraunhofer in 1817 actually produced anti-reflective coatings when he noticed that reflection was reduced due to etching a surface in an atmosphere of sulphur and nitric acid vapours. The quest for ways to maximize light collection efficiency has encouraged countless investigations for anti-reflective coatings to cater for the growing demand of optical and optoelectronic equipment in diverse areas of application.[62] There is increased performance of optical components in anti-reflection coatings fabricated from glass-based optical materials and a reduction in reflective losses at interfaces. Thus, anti-reflective coatings on flat-panel displays in electronics, eliminate the effects of spurious images or veiled glares originating from stray and multiple reflections from optical surfaces. High-efficiency anti-reflection coatings fabricated from phase-separated polyelectrolyte multilayer films that undergo a reversible pH-induced swelling transition have been realized.[63] Li and Shen 2011 reported a double-layer coating based on a $\lambda/4$-$\lambda/4$ index-gradient design wavelength system. Prepared with both dense and porous silica films as high and low index layers separately. When coated on a glass substrate, a satisfactory broadband anti-reflective performance was realized for the demand of the amplifier blast-shields used in high power laser systems. With a subsequent NH_3-heat treatment and trimethylchlorosilane (TMCS) post-treatment, weak mechanical property and optical instability of the coating were overcome.[64]

1.2.7.3 Anti-icing coatings

Icing is a source of a variety of problems. The icing on the wings and surfaces of aircraft could cause crash accidents. During flights, aircraft intercept supercooled water droplets through clouds or encounter freezing rain. The impacting water freezes rapidly to form deposits of ice. The ice accretion results in drag increase and sometimes may lead to dangerous loss of lift force, which may cause tragic aircraft crash accidents. Similarly, frost and ice accumulation in heat exchangers and refrigerators often results in a decrease of heat transfer efficiency up to 50-75% due to the frost formation.[65] Icing

can result in major electrical outages, interrupt offshore oil and gas production and decrease the efficiency of wind power generation.[66] The need for anti-icing strategies and coatings cannot be overemphasized. Anti-icing coatings are coatings with properties that can prevent or delay freezing of the impacting and condensed water as well as decrease the ice adhesion on its surface. The condensed water droplets can spontaneously jump away before freezing due to its superhydrophobicity. In another scenario, the coating can be impregnated with anti-freeze lubricants.[65,66]. Anti-icing properties of coatings may depend on the following: (i) the state of the solid surface if colder than the air/vapor, (ii) how large the temperature gradient is, and (iii) if a thin film of water tends to form on the solid surface due to capillary effects, disjoining pressure etc. (CORDIS). An ideal superhydrophobic surface does not allow frost formation due to the coalescence induced self-removal of condensed water but in reality, most of the superhydrophobic surfaces have been susceptible to frosting and the initiation of any defect on the coating surface further encourages frost formation.[65,66]

To improve the anti-icing performance of aircraft, the superhydrophobic anti-icing coatings should be effectively deposited on the aluminium and copper substrates. In a contribution to overcoming the shortcomings of anti-icing coatings, projects such as ICECOAT project have developed new types of coating matrices, new nanoparticles for nanocomposites and a new method for coating surface modification to produce anti-icing coating with superior hardness and erosion resistance (CORDIS). Similarly, Zheng et al. have fabricated anti-icing coatings with low ice adhesion strength and higher contact angles for aluminium substrates in contribution to overcoming ice accumulation on aluminium surfaces at low temperatures.[67] Furthermore, the focus on bio-inspired strategies for anti-icing is ongoing. A blend of icing-prevention by antifreeze dispensing and by repelling impinging drops has been developed. The fabricated bio-inspired anti-icing coating was aimed at reducing the need for antifreeze liquid by dispensing antifreeze only when required and directed towards having significant economic and environmental benefits. The semi-passive coating consisted of a porous superhydrophobic epidermis and wick-like underlying dermis that was

infused with antifreeze liquid. The outer layer served as a barrier between the antifreeze and the environment. The coating was designed to respond remarkably when eventually iced over by releasing stored antifreeze liquid amongst other factors.[66]

1.2.7.4 Anti-fogging coatings

Fogging relates to the formation of water droplets on transparent solid surfaces which scatters light and reduces optical transmission. Fogging is a major challenge for the everyday use of eyeglasses, goggles, and windshields. Additionally fogging reduces the efficiency of solar energy panels, medical/analytical instruments, etc. In anti-fogging research, superhydrophilic surfaces with very low θ_S (<5°) are well known to prevent water droplets by promoting the formation of a continuous thin film of water condensed from the air and this has gained significant attention. However, these rely on external stimulation by UV-light. Highly transparent superhydrophilic anti-fogging coatings were prepared and coated on various substrates such as glass slides, silicon, copper and Poly(methyl methacrylate) (PMMA). The anti-fogging coatings fabricated with polyvinylpyrrolidone (PVP) and aminopropyl-functionalized, nanoscale clay platelets exhibited 90% transmission of visible light. The chemical/physical properties of the coated surface remained almost unchanged after several antifogging tests and exposure to humid air for 30 days.[68]

Similarly, the improvement of water repellency by designing a micro- or nanostructure onto a low surface-energy material surface, with a water contact angle (CA) greater than 150° and a low sliding-off angle of less than 10°, enhances anti-fogging abilities. Anti-fogging coatings are therefore relevant for surfaces in cold and humid environments. Anti-fogging coatings with icing-delay properties have been investigated using poly(vinylidenedifluoride) (PVDF) polymer together with zinc oxide (ZnO) which produced ZnO-on-PVDF micro/nanostructure (ZP-MN) composite. On the ZP-MN surface, condensed water droplets were easily shed from at -5°C for ~1600 s via a slight wind or tilting. Interestingly, the droplets did not completely freeze on the ZP-MN surface at -10°C until ~7360 s.[69]

1.3   Developments in smart anticorrosive coatings

1.3.1 Self-healing coatings

Qian et al. synthesized a novel superhydrophobic coating that exhibited good self-healing properties in their anticorrosion studies of Q235 carbon steel in 3.5 wt.% NaCl. The fabricated coating contained benzotriazole (BTA) as the corrosion inhibitor. The self-healing induced by the shape memory effect of the damaged epoxy coating was investigated under two conditions; (i) heating in an oven at 60°C for 20 min and (ii) exposure to sunlight for different durations. Healing through thermally triggered shape memory effect of the epoxy polymers is an entropically driven process. The inspiring practicality presented for use in actual outdoor environments was the self-healing achieved under sunlight (Fig. 1.7) revealing a potential for long-term corrosion protection from an external damage. The 45° straight line in the Bode plot of the Impedance investigation indicated that the anticorrosion performance was already fully repaired after 1 day and the recovered surface maintained after 7 days of exposure. [70]
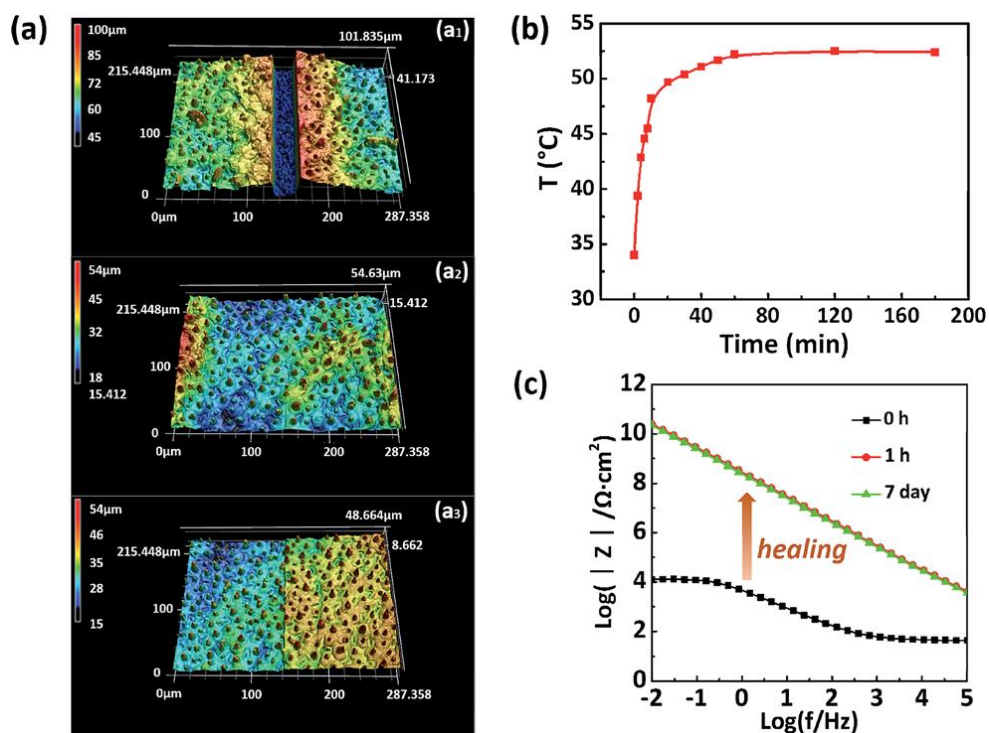
Fig. 1.7: (a) Confocal laser scanning microscopy (CLSM) images of the scratched coating surface containing BTA-5% after (a$_1$) 0 h, (a$_2$) 1 h and (a$_3$) 7 days of exposure to sunlight under an outdoor environment. (b) Temperature evolution of the superhydrophobic coating surfaces with time during the outdoor exposure. (c) Bode plots of the healed BTA-5% coatings after 0 h, 1 h and 7 days of exposure to sunlight in the outdoor environment.[70]

In another significant study, Light-responsive and self-healing anticorrosive coatings were investigated by Chen et al. The incorporation of hollow mesoporous nanocontainers (HMSs) loaded with benzotriazole (BTA) having smart molecular switches (photoresponsive azobenzene molecular switches) denoted as BTA@Azo-HMSs were used in the fabrication of the smart coating to protect the aluminium alloy AA2024. Exposure of the modified water-borne alkyd coating to visible light illumination had a reverse effect. The cis-isomer of the azobenzene molecules grafted in the mesopores of hollow nanocontainers transformed into the trans-isomer closing the pores (Fig. 1.8 (i)). Such that the residual corrosion inhibitors were not sequentially released/wasted but remained encapsulated within the nanocontainers to prevent the next corrosion occurrence. Thus, the reversible light-responsive release system achieved in the self-healing coating was aimed at providing flexibility and avoiding the excess release of the corrosion inhibitors after repairing the initial corrosion affected area. The nanocontainers possessed a high loading capacity and could also control the entrance and release of trapped active molecules on the basis of the dynamic motion of azobenzene molecules. With the scanning vibration electrode technique (SVET), local current density measurements around the artificial scratches were performed to verify the active anticorrosion performance of the light-sensitive nanocontainers in 0.1 M NaCl aqueous solution represented in Fig. 1.8 (ii).[71]
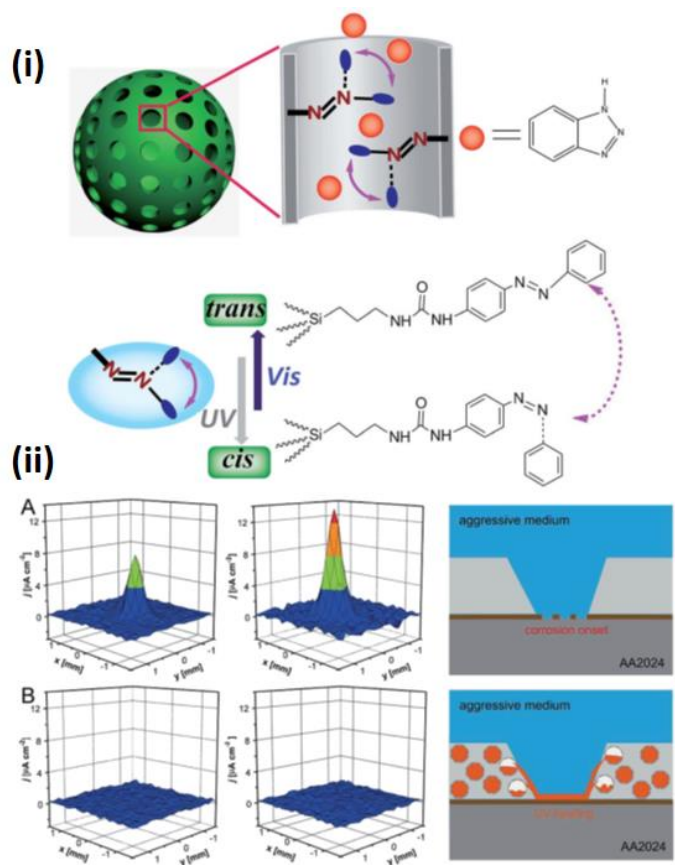
Fig. 1.8: (i) Schematic of reversible release system by utilizing trans-cis photoisomerization of azobenzene molecules grafted in the mesopores of HMSs. UV irradiation at 365 nm converts azobenzene to the cis form, resulting in pore opening. The cis isomer of the azobenzene molecules transforms into the trans isomer under visible light irradiation (450 nm), leading to pore closing. (ii) SVET current density maps of aluminium coated with the alkyd coating without (A) and with (B) the BTA@Azo-HMSs nanocontainers obtained after 1 h (left column) and 10 h (middle column) immersion in 0.1 M NaCl. The passive protection performance of the pure coating and the active self-healing performance of the coating containing BTA@Azo-HMSs was compared when the scratches were exposed to the UV light (right column).[71]

1.3.2 Corrosion-sensing coatings

A corrosion-sensing fluorescent coating made of phenylfluorone (PF) in acrylic paint was prepared for monitoring corrosion of aluminum alloys. This system was

sensitive to underlying corrosion processes through reacting with the Al^{3+} produced by the anodic reaction. The corroded areas were found under the fluorescence quenching spots by an optical microscope. The anodic reaction sensitivity associated with corrosion was determined by applying constant charge current and measuring the charge, where the fluorescence quenching was detected in the coating.[72] A carbon nanotube (CNT)-polyelectrolyte composite multilayer thin film has been made for measuring both strain and corrosion processes. The layer-by-layer fabrication exhibited changes in the electrical properties to strain and pH.[73] The corrosion-sensing compounds with color-change or fluorescing to the pH increase associated with the cathodic reaction were also used by applying constant cathodic current and measuring the charge at which color change or fluorescence occurred. The color change of modified acrylic coating systems was controlled by the sensitivity of the coating to pH increase.[74]

1.3.3 Self-cleaning/superhydrophobic coatings

Anticorrosive self-cleaning coatings with superhydrophobic surfaces are particularly attractive candidates for achieving enhanced anticorrosive performances. In the study led by Li et al.[75] a hierarchical structured superhydrophobic coating with nanoflakes was formulated via electrodeposition and solution-immersion processes. The water contact angle was about 157° and sliding angle around 3° after fluorination modification. The prepared self-cleaning superhydrophobic coating was investigated for anticorrosive properties. The fabricated coating had higher E_{corr} (-0.346 V) and lower I_{corr} (4.128 x 10^{-6}A/cm^2) values compared to the bare steel substrate (E_{corr} = -0.684 V, I_{corr} = 7.270 x 10^{-6}A/cm^2).

The superhydrophobic coating was also investigated for anti-scaling property and this was confirmed when $CaCO_3$ crystals on the superhydrophobic coating had needle-like features compared to the rhombohedral $CaCO_3$ crystals on the surface of the bare steel substrate. The superhydrophobic coating maintained good long-term stability in air, mechanical and thermal stability under certain environment. After the polarization test, the aggressive NaCl solution did not destroy the robust

superhydrophobic coating which had dandelion-like hierarchical structures. An illustration of the coating properties is presented in Fig. 1.9.[75]
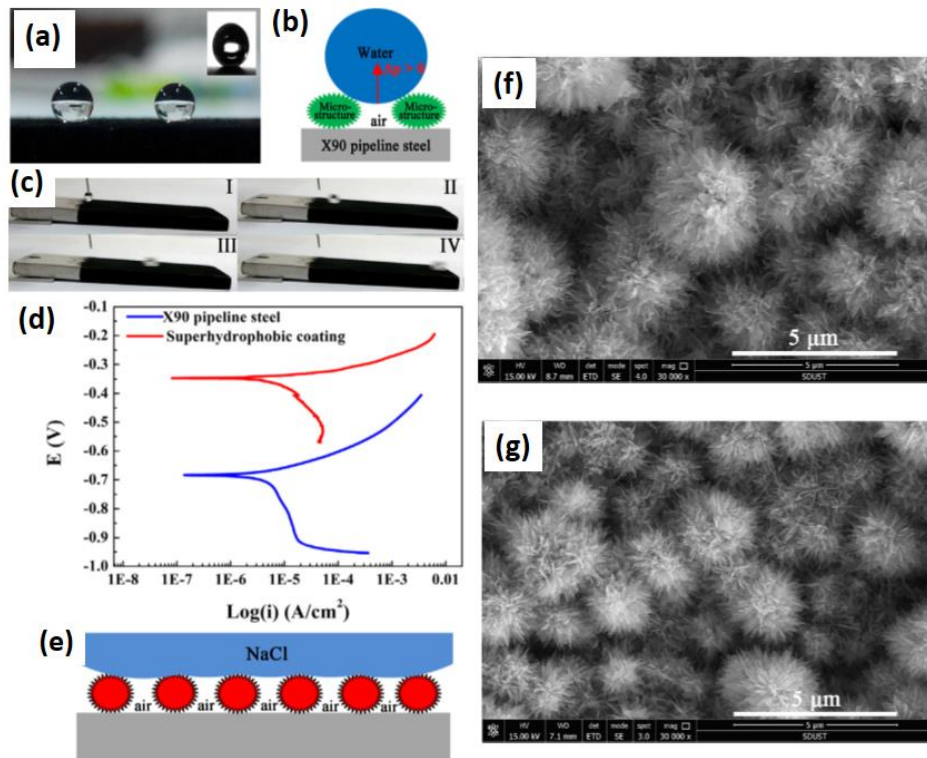
Fig. 1.9: (a) Photos of water droplets on the superhydrophobic coating surface, (b) the superhydrophobic coating can sustain the water droplet due to intrusion pressure (Δp) > 0, (c) sliding process of the water droplet on the superhydrophobic coating. (d) Tafel plots of the bare pipeline steel and the superhydrophobic coated pipeline steel, (e) schematic mechanism of the anticorrosion process, (f & g) SEM micrographs of the superhydrophobic coating before and after the potentiodynamic polarization test.[75]

In another study, a self-cleaning superhydrophobic coating with a contact angle of 155.2 ± 0.5° and a sliding angle of 3.5 ± 1.3° was fabricated by Zheng et al.[67] using a facile low-cost method and investigated for anticorrosive protection on aluminium surfaces. Myristic acid modified samples were denoted as MA-*x* and the reference was anodized Al samples without surface modification denoted as AAO-*x*, where *x* represents the value of anodization voltage. In Fig. 1.10 samples a, b, c representing hydrophilic aluminium (Al), superhydrophilic (AAO-20) and superhydrophobic coating

(MA-20) were immersed in a dirty solution and dried. Dirt accumulated on Al (d) and AAO-20 (e) surfaces, but a little dirt was observed on MA-20 coating (f). After spraying water on the studied surfaces, the MA-20 coating (i) was as clean as before, in comparison to both Al (g) and AAO-20 (h) surfaces which were still covered with a large amount of dirt. The findings revealed that it is difficult for dirt to attach to a superhydrophobic surface and if any, can be easily cleaned by spraying water. This is due to the joint action of high capillary forces induced by water droplets and weak adhesion of dirt to the superhydrophobic surface. The anticorrosive performance of the coatings was investigated using potentiodynamic polarization technique in comparison with the uncoated Al substrate (Fig. 1.10 (j)). The E_{corr} of the superhydrophobic MA-20 coating was 59 mV more positive than the bare Al substrate and 39 mV higher than the hydrophobic MA-0 coating. The corresponding J_{corr} (1.527×10^{-9} Acm^{-2}) was reduced by 2 orders of magnitude compared to the bare Al substrate. Meanwhile, the MA-20 superhydrophobic coating showed higher polarization resistance (R_p), 408 times that of the bare Al substrate and 147 times that of the hydrophobic MA-0 coating. In comparison with other previously reported superhydrophobic anticorrosive coatings, the results showed a remarkable corrosion resistance on Al and its alloy.[67]
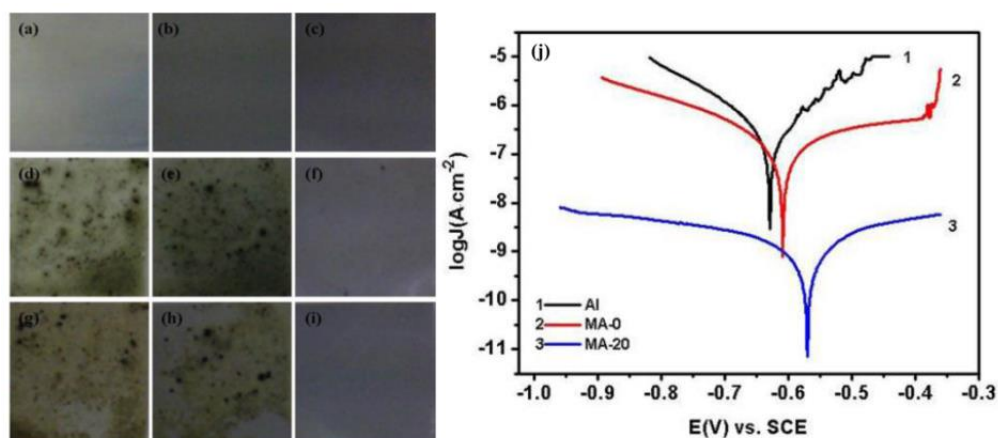
Fig. 1.10: The self-cleaning process of (a) Al (b) AAO-20 (c) MA-20 pristine samples before the test. (d) Al (e) AAO-20 (f) MA-20, samples after immersion in a dirty solution for 1 min and (g) Al (h) AAO-20 (i) MA-20 cleaned samples after water spray and drying. (j) Potentiodynamic polarization curves of Al, MA-0, and MA-20.[67]

Another study by Li et al. on superhydrophobic multiwalled carbon nanotubes dispersed in a thermoplastic elastomer (MWCNT/TPE) smart coating revealed the development of a high-performance coating with sensing ability toward stretching, bending, and torsion. The smart coating could be easily fabricated under ambient conditions with no special requirements for cleaning or activation of the substrate. The superhydrophobicity of the coating was maintained irrespective of the substrate (glass, plastic, cloth, and metals) for self-cleaning, drag reduction, or other related applications. The coating showed excellent stability to UV radiation, acid/alkali stress, repetitive bending and kneading, and extreme repellency to acidic/alkaline droplets. The smart coating can be exploited as a flexible, high-performance, and multifunctional wearable sensor in human healthcare and human-machine interface applications, and being superhydrophobic can be used under wet and corrosive conditions.[76]

1.3.4 Antifouling coatings

Self-cleaning foul release coatings have been developed by Selim et al.[77] in a recent study and the anticorrosive performance was investigated through salt spray test. Low-surface free energy, low micro-roughness, and ultra-smooth topology of self-cleaning surfaces prevent fouling settlements. Amongst the concentrations investigated, the addition of well-dispersed 0.5% $ZnO-SiO_2$ nanospheres minimized the surface tension inside the polymer matrix, leading to enhanced surface inertness against fouling adhesion alongside excellent mechanical and anticorrosive properties in aqueous salt fog environments. Foulants investigated for biofilm formation were gram-positive (*Micrococcus* sp.), gram-negative (*Pseudomonas putida*) strains of bacteria and the fungi (*Aspergillus niger*) which are widely used in the evaluation of the antifouling performance of marine paints. In a nutshell, the nanocomposite coating demonstrated inert and superhydrophobic properties with a contact angle of 165° ± 2°. Superior physical characteristics, lotus effect, thermal stability, long-term durability under UV radiation, and resistance against a wide range of pH solutions was observed making them promising as efficient eco-friendly fouling release self-cleaning coatings for ship hulls without biocides.[77] Biodegradability measurements of the studied nanocomposites against the different foulant are presented in Fig. 1.11(a) and a

comparison of the prepared nanocomposite smart coating with some commercial fouling release coatings is presented in Fig. 1.11(b).
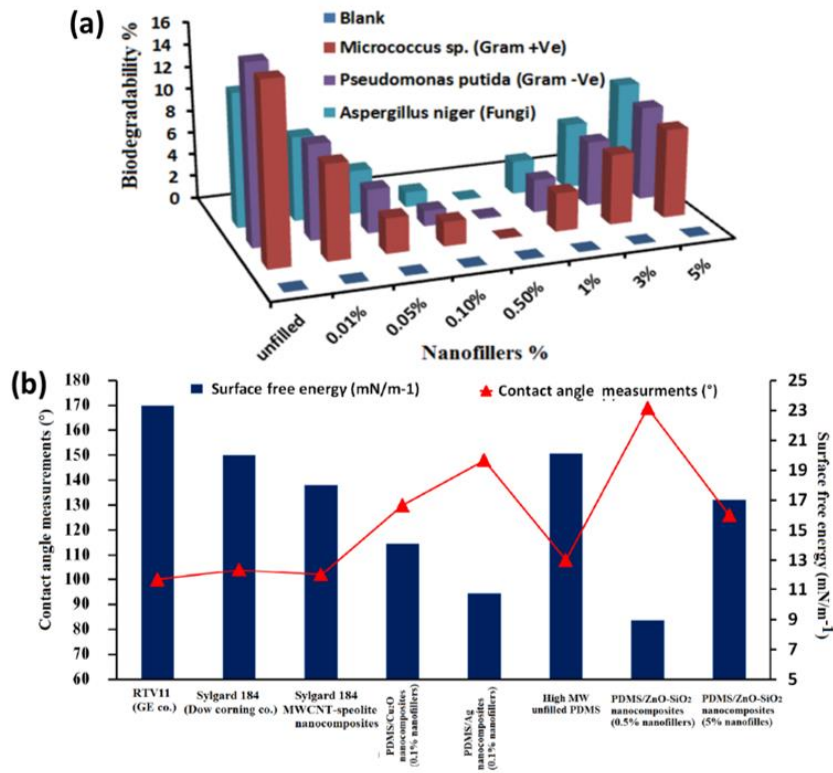
Fig. 1.11: (a) Represents biodegradability measurements of the virgin polydimethylsiloxane (PDMS) and filled ZnO-SiO$_2$/PDMS nanocomposites against different foulant. (b) A comparison of the prepared PDMS/ZnO-SiO$_2$ nanocomposites with some commercial fouling release coatings.[77]

Furthermore, antifouling coatings developed by incorporating butenolide derived from marine bacteria into biodegradable poly(ε-caprolactone) based polyurethane were investigated by Ma et al. Mass loss measurements revealed that the polymer degraded in seawater and the degradation rate increased in the presence of marine organisms or enzymes. Butenolide was released from the biodegradable polymer for at least 3 months and the release rate depended on both the concentration of butenolide and temperature. With the incorporation of a naturally occurring resin (rosin) into the biodegradable polymer, the self-renewal rate increased and the later

release rate of butenolide improved. A field test indicated that the system had excellent antifouling properties.[78]

1.4 Mechanism of smart anticorrosive coatings

Anticorrosion mechanisms of these engineered smart coatings vary for different systems. The major concern here is barrier creation, sustenance between substrates and immediate environment, sacrificial coating, and corrosion inhibition. Amongst the variations to mention a few are:

i) Capsule-based healing mechanism such as the Ring Opening Metathesis Polymerization (ROMP) of Dicyclopentadiene (DCPD) usually stimulated by Grubbs catalyst[14,79] as shown in Fig. 1.12.
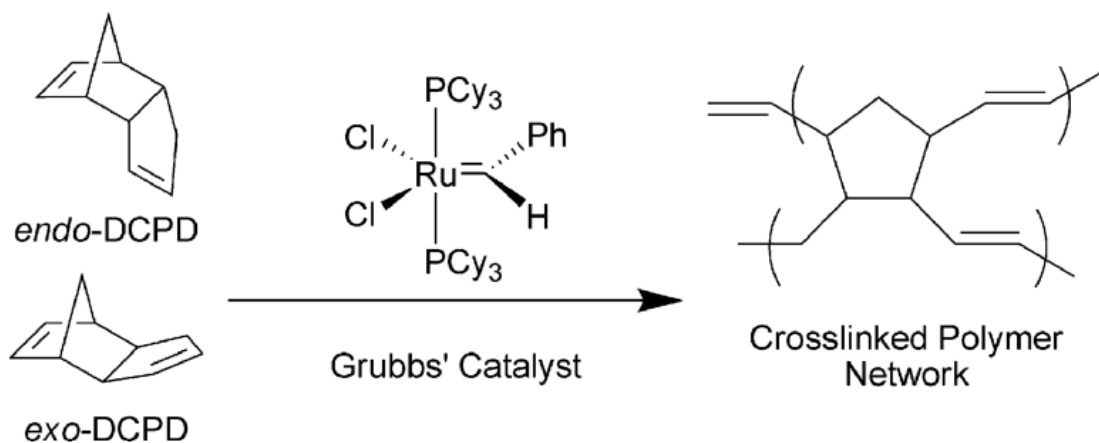
Fig. 1.12: ROMP reaction mechanism of DCPD as stimulated by Grubbs catalyst.[14]

ii) The Zipper-like mechanism by Zhang *et al*. was synthesized poly 2, 2, 3, 4, 4, 4-hexafluorobutyl methacrylate-co-isocyanate triethylene glycol methacrylate [Poly(HFBMA-co-ITEGMA)] copolymer directly was applied as a coating on aluminium alloys.[80] Upon damage, isocyanate groups present reacted with water molecules in the air forming a stable urea cross-link. Schematic illustration of the mechanism is shown in Fig. 1.13.
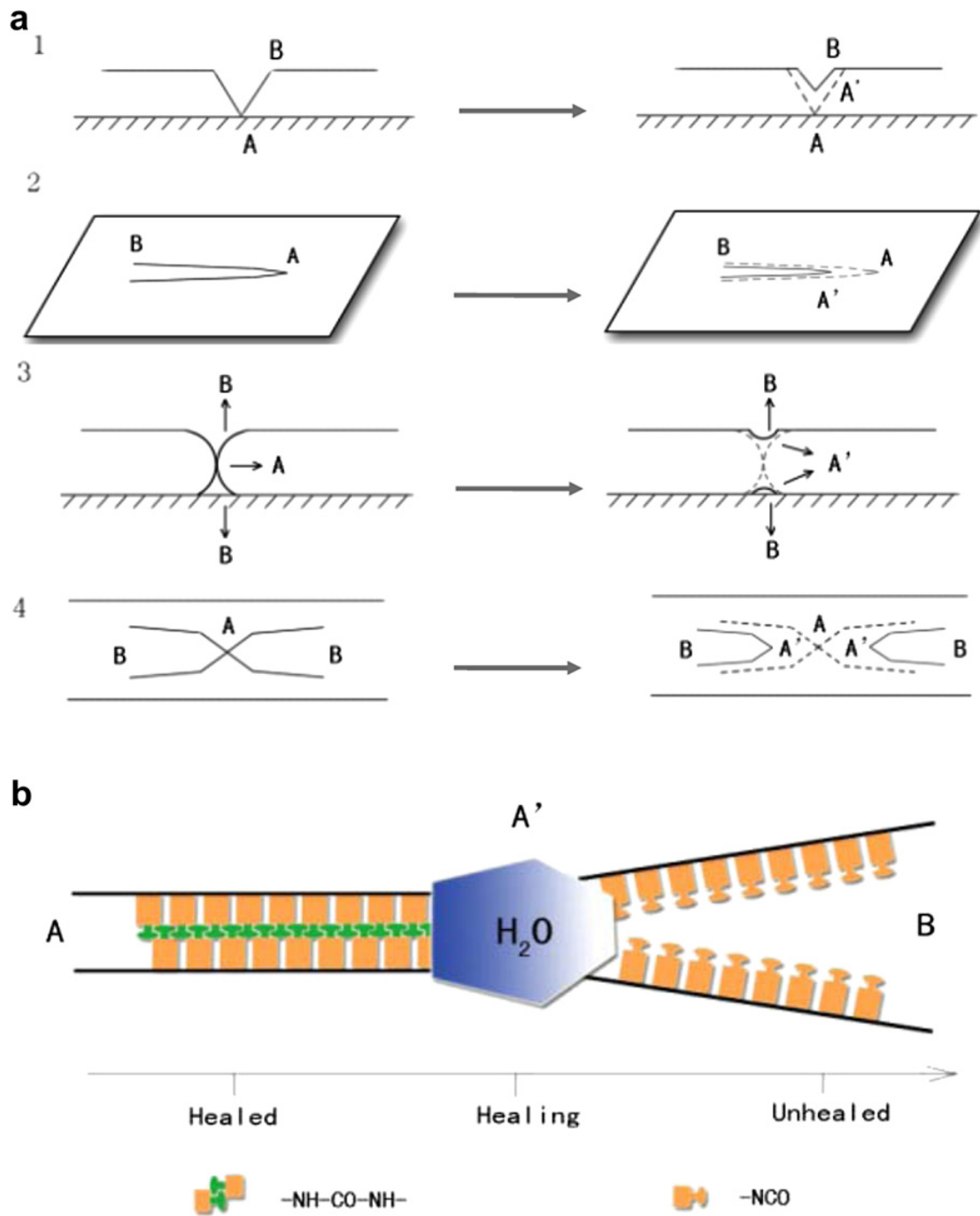
Fig. 1.13: (a) Illustration of self-healing via zipper model mechanism. 1A) crack bottom; 2A) the ends of the crack; 3A, 4A) Contact areas between the two sides of the crack; B: number of contact areas. (b) Zipper model.[80]

iii)   Polycondensation as seen in hydroxy end-functionalized polydimethylsiloxane (HOPDMS) and polydiethoxysiloxane (PDES) phases separated in the vinyl ester matrix in the presence of polyurethane encapsulated di-n-butyltin dilaurate catalyst released only upon mechanical damage.[81] The equation of the reaction is shown in Fig. 1.14.
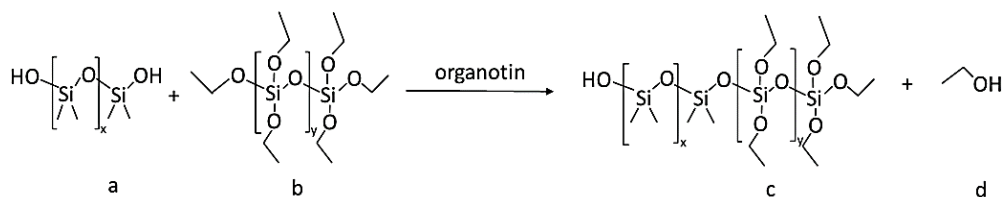
Fig. 1.14: Polycondensation of silanol-functionalized PDMS catalysed by organotin. (a) PDMS chain with hydroxyl terminals, (b) (PDES), (c) cross-linked product and (d) released ethanol from the condensation product.[82]

iv)   An epoxy-based system where the epoxy matrix and amine inhibitor were separately encapsulated. The epoxy solution was encapsulated by in-situ polymerization of urea and formaldehyde in an oil-in-water emulsion while the amine solution was filled and etched by vacuum-assisted method.[83]

v)   The active-passive mechanism which involves the formation of a passive layer responsible for retarding corrosion reactions (as the active mechanism) and a resulting barrier at the interface referred to as the 'Schottky barrier' depleting resultant electrons. While the responsive coating as the other barrier layer does not allow the penetration of corrosive ions to the metal surface (passive mechanism) etc.[84]

1.5   Processing, formulation and deposition of smart coatings

Anticorrosive smart coating formulations are composites made up of thermoset, thermoplastic or elastomeric polymer matrix resins,[85] and reinforcements which can either be particulates or fibrous in composition. The reinforcements are usually as particles, capsules or tubes in micro or nanometer dimensions containing active agents with either porous, layered or core-shelled structure. The efficiency of these coatings is related to the containers for inhibitor loading. The containers differ in size, structure, shape, and chemical nature which also influences coating design.[14,86,87] In a nutshell,

the process of smart coating formulation involves inhibitor preparation, inhibitor/pigment loading into micro/nanocontainers, embedding in the appropriate coating layer, catalyst addition in some cases to trigger a response on coating interaction with environmental factors. Embedding encapsulated inhibitor and catalyst separately into the polymer coating is another encouraging possibility. But when using polymers with intrinsic responsive qualities or UV-sensitive agents in coating formulations the use of a catalyst may not be required.

The functionality of a smart coating is dependent on factors such as constituents of the coating solution, preparation techniques, and coating deposition methods. Formulation constituents of coating solution include polymer matrix, curing agent, inhibitor host (micro or nano-sized), inhibitor type and catalyst where necessary etc. all of which should be ecologically acceptable with zero toxicity where possible. Smart coatings are a combination of organic-inorganic constituents and can be formulated via several approaches of which we will feature sol-gel method, self-assembly method, and encapsulation.[1,2] The sol-gel method involves hydrolysis and condensation processes in the coating formulation. It is polymerization of inorganic metal alkoxides/organo-functional metal alkoxides with a regular polymer. The following reactions were observed:

$$M(OR)n + xH_2O \rightarrow [M(OR)n - x(OH)x] + xR - OH \qquad (1.1) \text{ (Hydrolysis)}$$

$$M - OH + RO - M \rightarrow M - O - M + ROH \qquad (1.2) \text{ (Condensation)}$$

$$M - OH + HO - M \rightarrow M - O - M + HOH \qquad (1.3) \text{ (Condensation)}$$
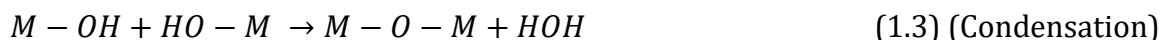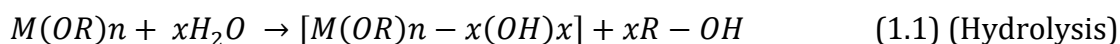
Equation (1.1) represents the first step in the process, (1.2) and (1.3) represents the second step. M is for the inorganic elements (Si, Zr, Ti, etc.), R is the organic moiety, $M(OR)n$ represents the metalloid alkoxide precursor or the monomeric material (metal). M-OH stands for the hydroxylated metal centers and M-O-M stands for oxo-polymers. Thereafter the sol undergoes gelation and converts to a coating film. This method is used to prepare both inorganic sol-gel coatings and inorganic-organic hybrid based sol-gel coatings. It is a widespread and low-temperature technique and yields eco-friendly coatings that are more resistant to oxidation, wear and corrosion-erosion than most metals. Amongst the inorganic precursors, coatings prepared with

alkoxysilane are most preferred since it is mild and can be easily controlled.[1,88] Self-assembly method is a layer by layer molecule deposition approach. It is required for preparation of thin coating films layered by adsorption of oppositely charged particles in a sequential manner from the aqueous suspensions. It involves three other processes which are; Evaporation Induced Self-assembly process (EISA), Self-assembled Nanophase Particle coating process (SNAP), and Electrostatic Self-assembly process (ESA). EISA involves an initial substrate dip coating into a solution mixture of silica, surfactant, organic monomers, water, and ethanol.

During the evaporation and drying stage, micelles are formed in a partition of organic constituents in its interior and silica in its exterior. This is followed by a self-assembly of the micelle species (silica-surfactant-monomer) and subsequent polymerization. It is a rigorous process and is only applied on very smooth surfaces like glass and silicon wafer which obviously hinders its widespread applicability. SNAP consists of sol-gel processing (hydrolysis and condensation reactions controlled by pH and water content), SNAP solution mixing (addition of crosslinking agents to improve the barrier and film forming properties and other additives to the solution), coating application (substrate dip-coating) and cure. While in ESA, firstly polyelectrolytes are layered on the substrates, then oppositely charged nanoparticles are electrostatically deposited on the polyelectrolyte surface forming another layer. This layered electrostatic assembly can control the coating thickness depending on the number of self-assembly cycles done. However, it is a time-consuming process, rarely used for nanocomposite coatings preparation rather mainly for formulating hollow capsules, spheres, and core-shell materials.[1,89]

The encapsulation method is concerned with embedding nanoparticles and inhibitors within capsules which are incorporated into the polymer matrix. It is now one of the key steps for effective smart coating formulations. A viable technique to overcome the shortcomings of coating degradation, inhibitor deactivation, and leaching by functioning via a controlled release mechanism which contributes to sustaining coating integrity. The capsules in use for the encapsulation process have been developed by the following methods: emulsification, layer by layer assembly,

coacervation and internal phase separation illustrated in Fig. 1.15(a-d). The use of ultrasonic waves for fabricating hollow composite and inorganic nanospheres is also reported. These capsules have been reportedly filled in different ways with successful results. These are agitation of the suspension of capsules and active agents, soaking capsules in inhibitor solution under reduced pressure and also the layer by layer procedure. For effective results, quality of resultant coatings is determined by the compatibility and adhesion between the micro/nano containers and the coating materials. Also, the surfaces of the nano-reservoirs should provide colloidal stability and the encapsulated inhibitors should remain intact.[90–92]
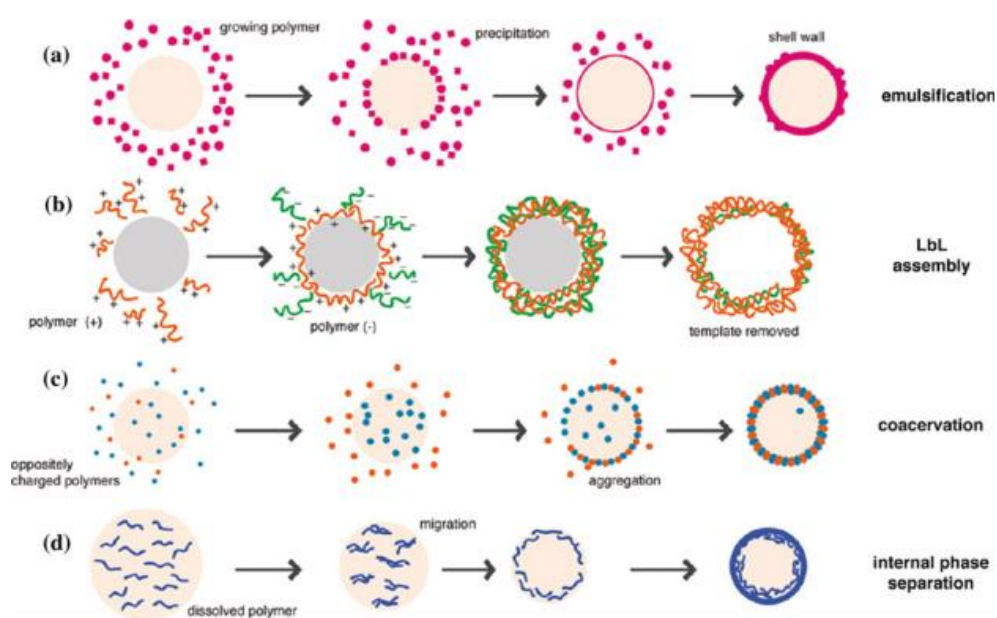
Fig. 1.15: (a-d) Capsule formation methods for encapsulation process.[91]

In coating application, most widely used deposition techniques include chemical solution deposition techniques such as dip coating, spin coating, and aerosol deposition technique of spray coating.[93–96] Amongst others like brush painting [88], chemical bath deposition techniques such as electroless deposition, liquid phase deposition and successive ion layer adsorption and reaction,[97] chemical vapor deposition,[98] physical vapor deposition such as vacuum deposition, arc vapor deposition, sputter deposition and ion plating,[99] inkjet and direct writing methods etc.[100] Other widely used coating

methods are roller coating, airless spraying, and air-assisted airless spraying techniques. A few of these techniques will be discussed herein.

a.   Dip coating: This is the oldest commercially used coating process amongst other processes. First applied in the sol-gel technology of 1939 to produce thin films. With dip coating, thin films can be deposited on cylinders, plates, and irregular objects. For the process, the substrate undergoes three stages: firstly, immersion and dwell time; secondly, deposition and drainage; lastly, evaporation which can be facilitated by heat drying. This process involves immersing a substrate in a solution bath for some time and once it is completely wetted it is removed vertically at some withdrawal speed from the bath as shown in Fig. 1.16(a). The withdrawal speed is dependent on the film thickness required. Therefore, the film thickness is a function of the withdrawal speed, solvent evaporation, matrix concentration, and viscosity. The viscous drag of the substrate in motion is proportional to the withdrawal speed.

Hence, on evaporation, a uniform solid film is seen on the surface of the substrate. The evaporation rate has been reported to be of little or no effect on the film thickness. The solvent evaporates on drying resulting in a well-defined drying line (boundary) made up of phases. Vapor-liquid-solid phase boundary upon which the entrained film assumes a wedge-like shape and the non-volatile species remain on the deposited layer which undergoes curing. It is a viable process for coating substrates irrespective of surface topography and shape.[93,101]

b.   Spray coating: This is an aerosol deposition technique. It is suitable for high aspect ratio structures and uneven surfaces. It is a commercially available technique and enables a wide range of materials to be coated. Varying spray coating processes exist and are widely used against corrosion, wear and for functional purposes. They are classified into thermal spray process and cold spray process. Coatings sprayed onto the substrates using this method are atomized forming a growing resisting film. Coating deposition stages and formation illustrated in Fig. 1.16(b). For film homogeneity, substrate and nozzle move laterally against each other. Coating film deposition on irregularly sized and shaped substrates is permissible. The coating is possible for both wet and dry conditions without any damage. For the cold spray process, about 60-90%

of the coating is retained on the substrate compared to other coating techniques. Films formed from this technique are characteristically intermediate of metal organic chemical vapor deposition and spin coating.[95,96,102–104]

Furthermore, airless spraying and air-assisted airless spraying are pressure-driven spray techniques. Airless spray coating utilizes a spray produced by forcing a fluid under high-pressure 500-5000 psi (34-340 bar) through a small precision orifice in a small nozzle (spray tip) to atomize the fluid. The fluid emerges as a tapered sheet at a high speed. The sheet is disrupted by friction between the fluid and air, breaking it initially into fragments and ultimately into droplets. Airless spray coating is clean and fast and the overspray fog or rebound associated with conventional spray is greatly reduced. Also, with airless spray, it is possible to apply heavy coating thickness more quickly than by any other method. It doesn't require the use of compressed air. Certain disadvantages also exist with this technique such as the potential risk of injection injury, the operator having no control over the amount of fluid flow, cost intensive since the high-pressure pump is required, coating quality is not as good as conventional coatings etc.[105,106]

For the air-assisted airless spray method, the coating substance reaches the gun at a lower pressure than traditional airless types and is partially atomized through the small tip. By adding a small amount of air (5-35 psi) to the edges of the spray fan full atomization is achieved. This also results in a softer pattern, more control, higher transfer efficiency, and less overspray. The air-assisted airless guns are similar to airless spray guns, but actually, a hybrid combining the features of airless and air spray guns. The guns in this technique provide the advantage of producing a finishing quality close to that of air spray guns due to the ability to operate at lower fluid pressures than the airless spray guns. This technique also has some disadvantages such as being much more cost intensive, provides room for operator error during the selection of an appropriate tip to control the fluid flow and adjust the air supply for optimal atomization. Also, the risk of skin injection injury exists.[105,107]

c.   *Spin coating:* This is another technique required to produce a uniform thin film. Emsile and colleagues in 1958 pioneered the first analysis with a mathematical model

of spin coating in his work on the flow of a viscous liquid on a rotating disk. The coating process is in stages made up of fluid dispense, spin-up, a spin-off (fluid flow out) and evaporation with drying. Fluid flow and solvent evaporation occur simultaneously and are responsible for the film thickness. Other parameters of importance responsible for film quality are coating solution concentration and viscosity, dispense volume and spin speed. Air bubbles and pin holes on film surface are likely to occur when dispense tip is uneven, swirl pattern, comets, chuk marks, radial thickness variation, striations, and streaks occur when spin bowl exhaust rate is too high while insufficient dispense volume results in some uncoated areas. Spin coating is referred to as the simplest technique in chemical solution deposition process and produces excellent coating qualities when solvent evaporation is not too quick. It is reproducible and fast but not quite suitable for substrates with non-circular and non-planar topography. Also, there is an extent of coating waste in the spin-off stage.[94,96,101,108,109] The process is illustrated in Fig. 1.16(c).
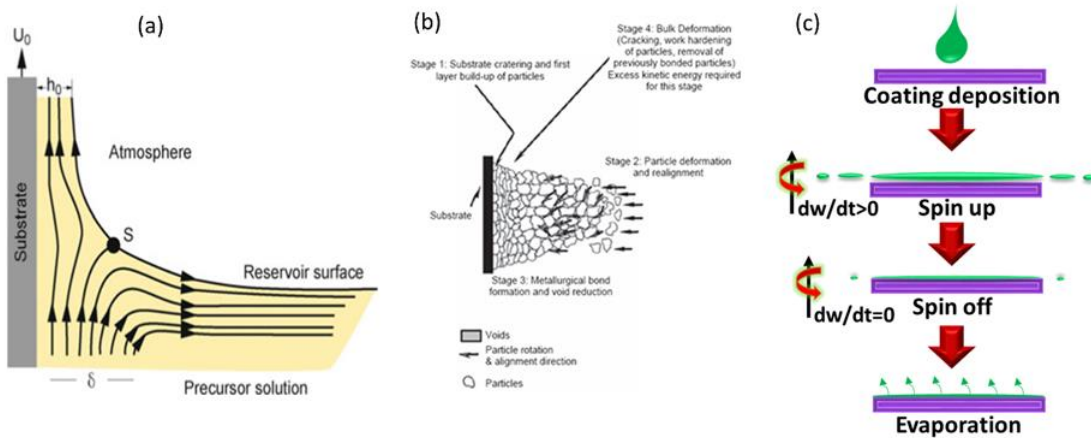
Fig. 1.16: (a) Schematic of dip-coating process with the flow patterns. Where U_0 is withdrawal speed, S is stagnation point, δ is boundary layer, and h_0 is the thickness of the film adhered on the substrate.[93] (b) Schematic showing stages of film formation by spray coating a substrate.[103] (c) Schematic of the stages in spin coating process.

d. *Brush painting:* This is the simplest method of applying a coating. It is slow, expensive but needful where spraying is impossible. It provides better wetting of the

surface, is necessary for coating restricted spaces and small areas with less wastage and contamination of the workspace. The brushing application is usually by up and down strokes, then crosswise and finally up and down strokes lightly. This pattern eliminates brush and lap marks and is called cross lapping. For an even flow of the coating material, it is necessary to stroke the brush at an angle of 45°. Light strokes produced at this angle ensures the flow.[106]

e.   *Roller coating:* This process is efficient for applying industrial coatings on broad flat surfaces. It is much quicker than brushing and the rheological properties of the paint must be suitable for the surface. For a successful application, selecting a roller cover with a smooth surface is important. The roller cover should be completely saturated with the coating until the point it's about to drip. The first coating strokes should be done in a "W" pattern within a space of approximately 0.75 m². Successive strokes fix the "W" pattern and for uniform film, thickness coating should be done from dry areas back into wet areas.[106]

1.6   The role of nanodispersoids

The idea of nanoparticles within a polymer resin has been well received as an important eco-friendly step expected to bring satisfaction, with respect to toughness and reliability of the coating. This is because polymeric nanocomposite coatings have been designed in such a way that combined effects of water resistance and elasticity; permeability and hardness of both the organic polymers and inorganic nanomaterials have been achieved.[110] The fine nanoparticles within fills the cavities in the organic coating, that results in crack bridging. Disaggregation during curing is thus encouraged with a reduced tendency for the coating to blister or delaminate. This experimental observation of nanoparticle/capsules reported has yielded better features than that of the bulk corrosion inhibitors; corrosion inhibitors only in a coating or microcapsules loaded with corrosion inhibitors in coatings.[111]

Particle behavior along with spatial distribution are greatly influenced by the interaction between ligands within the polymer molecules and the nanoparticles attached to them. These nanoparticles are also attached by electrostatic interactions and strong covalent bonds within the polymer molecules.[112] When applied to the

surfaces of the respective products they also account for decoration in their functionality. These chemically active smart coatings exhibit their functionality either on film–substrate interfaces, air–film interfaces or in the bulk of the film.[1,2,17,113] Table 1.1[114] presents a summary of multifunctionality of various smart coatings containing nano-additives for mostly automotive and construction sectors.

Table 1.1: Summary of multifunctionality of various smart coatings containing nano-additives.[114]

S/No.	Function	Nanomaterial (Examples)	Advantage/Effect	Industrial Branch
1.	Color brilliance, shade, color effects (flip-flop effect), reproducible paints, easily dispersible paints.	Carbon black; Oxides (TiO_2, Fe_2O_3, Fe_3O_4, SiO_2, Cr_2O_3) (on mica flakes or SiO_2 spheres, with metal pigments), ZnO.	Intensify effects of metal pigments; Stabilize pigments and fillers; Positive effects in dispersion paints; Prevent crack formation (Phyllosilicates/sheet silicates); Improve resistance to fading.	Automotive, consumer goods (furniture), construction.
2.	Self-cleaning (easy-to-clean).	Organic-inorganic hybrid polymers (organically modified ceramics), nano-silica/colloidal silica embedded in resin particles following polymerization; Silanes (silicon-based mixtures with other chemicals, e.g. fluorine compounds); TiO_2.	Dirt and water repellant, Protection against algae and fungi; Anti-graffiti protection: Easy removal of unwanted paint.	Automotive, construction (facades), glass .
3.	Switchable (electrochromic, photochromic, thermochromic).	Tungsten oxide (WO_3) (electrochromic).	Color effects	Automotive
4.	Self-Assembly	Polymer gel, specific organic-inorganic hybrid polymers.	Self-healing surfaces	Automotive, cosmetics
5.	Monolayer adhesive films	Polymers	Ultra-thin layers	Automotive, consumer goods
6.	Scratch resistance	Oxide (synthetic amorphous silica), SiO_2, Al_2O_3).	Improved scratch resistance	Automotive, information and

				communication, parquet flooring, consumer goods (furniture), optics (lenses).
7.	Optimized flow characteristics	Oxide (synthetic amorphous silica)	Generate new rheological properties (elasticity, flow characteristics, thixotropy).	Various
8.	Conductive coatings for electrostatic paint spraying	Carbon: Fullerenes, carbon nanotubes (CNT)	Enhanced spraying processes	Automotive
9.	Photocatalytic effect, antimicrobial effect	TiO_2, ZnO_6, Ag	Removal of grease, dirt, algae, bacteria, fungi, odorants and pollutants, transforma-tion of NOx and ozone from the atmosphere into harmless compounds.	Construction (facades, noise barriers, tiles), road surface, vehicles, wood preservation, glass
10.	Fire retardant	SiO_2	When a certain temperature is exceeded, a heat insulating carbon foam layer is created on the wood surface followed by a flame-resistant ceramic layer.	Construction, protection of wood against fire
11.	Corrosion protection, wood preservation	Zinc or aluminium coated with nano-TiO_2, nano-clay (like hydrotalcite $Mg_4Al_2(OH)_{12}CO_3xH_2O$)	Nano-clay coatings delay the fading of wood (which is a result of the bleeding of complex chemicals like tannins).	Construction, automotive, wood preservation

12.	Ultra violet protection, Infrared reflective or Infrared absorbing	TiO_2, ZnO, CeO_2, iron oxide pigments (transparent iron oxide; needle-shaped particles with a length of 50-100 nm and width of 2 nm).	Enhanced Ultra violet resistance, blocking of Infrared and visible light, indoor climate control.	Construction (facades), wood preservation, glass, plastics

1.7   Characterization of smart coatings

Coating film characterization includes an initial visual determination of coating texture and appearance particularly for viscosity and color, followed by detailed film characterization after curing. Several non-destructive techniques have been applied to analyze and characterize these engineered coatings in use, according to their film surface functionality. Extreme sensitivity and high magnification are involved due to the thin nature of films developed. Electron microscopy techniques such as Scanning electron microscopy (SEM) and Transmission electron microscopy (TEM) and the sensitive Atomic Force Microscopy (AFM) are mostly involved. AFM is a high-resolution imaging tool which measures and manipulates matter at a nanoscale. It shows significant changes on the metal and coating surfaces. It offers 3D visualization, qualitative and quantitative information on size, morphology, surface texture and roughness, statistical distribution, surface area and volume distributions. It characterizes in multi mediums such as ambient air, controlled environs, gas, solid and liquid dispersions of particle sizes between 1 nm to 8 μm in height and scan range up to 80 μm. The topography of films doped with nanocontainers can also be determined with it.[115-117] Also, its versatility has allowed its application in measuring nanoscale properties of natural bioadhesive materials and the substratum interface in natural conditions for the purpose of evaluating antifouling coatings.[118]

TEM involves a fraction of the incident beam penetrates the sample of study which must be very thin. TEM determines particle size and shape.[17] Also, histograms of TEM images can be employed to count individual particles formed.[119,120] Furthermore, TEM imaging has been employed to observe certain fabrication features between smart nanocontainers and inhibitors.[121] In SEM, the beam a resultant focus of high energy electrons is scanned across the surface of the sample. Particle size and shape and same can also be achieved with SEM. Morphology of additive to be loaded into the coatings, morphology of bare and coated metallic substrates, dimensions of coating thickness from the cross section of the coatings can also be achieved with SEM.[92,122] Environmental SEM (ESEM) is another useful tool which has revealed the presence of thin polymer films on a fractured surface studied.[123,124]

UV/Visible spectrophotometry is required for determining the reduction of metal ions to nanoparticles via surface plasmon resonance, which is also responsible for their unique colors upon reduction. Optical properties of the metallic nanoparticles are permissible.[119,125] Fourier Transform Infrared Spectroscopy (FTIR) identifies possible molecules responsible for the reduction, stabilization, and capping of micro and nanoparticles also, coatings formed by producing IR absorption spectra.[126]

X-ray Diffraction (XRD) determines particle crystallinity and nature of metallic particles[119,127] in the coating types. Also, phase structure of metal nanoparticles can be identified.[120] Estimation of coating performance in terms of coating degradation and corrosion kinetics, electrochemical techniques are usually employed. Scanning Vibrating Electrode Technique (SVET) provides information on corrosion reactions initiating in small areas and also examines the inhibitor action in the coatings by monitoring both the cathodic and anodic corrosion activities through measuring current density maps over the selected surface of the sample. This has been employed for self-healing evaluation.[128] Investigating chemical composition of mechanically damaged coating surfaces and providing information on migrating ions within the scratched area is executed with X-ray Photoelectron Spectroscopy (XPS) and Electron-probe Microanalysis (EPMA).[90,129] While Micro-Raman Spectroscopy determines the chemical composition and displays bands for specific compound formations.[130]

Mechanical characterization is an essential aspect when characterizing a smart coating. It also determines functional recovery in self-healing coatings. Static fracture testing, fatigue testing, tear testing, microcapsule induced toughening, micro-hardness test, scratch hardness test, pencil hardness test, and cross-hatch adhesion test etc. are amongst the relevant tests in use.[82,131] Electrochemical and salt spray tests are also relevant characterization techniques which give insight to how responsive and/or functional (in terms of anticorrosive properties) the smart coatings are when applied in practical situations.

1.8   Damage modes of smart coatings

Certain damage types occur in smart coatings and composites, and this is due to a combination of factors during formulation and service. Fig. 1.17 illustrates some

damage modes experienced by the smart composite coatings. Amongst existing damage patterns, the few illustrated show the effects of impact, corrosion, and fatigue. The extent of each damage and its outcome on the properties of the coating depends on the type of composite formulated, nature of the polymer matrix and loading rate of the secondary phase. Corrosion occurrence is the effect of barrier depletion due to environmental factors, as well as mechanical damage such as cuts and abrasion in the coating. Crazing can occur when there is extreme stress and propagates due to applied tension. Damage due to ablation may occur mostly in antifouling coatings after an effective release of antifoulant from the coating surface over time. There is surface cracking, opening crack, transverse and shear cracking which occur as a result of impact loading, and all these severely affects both mechanical and barrier properties. These will, in turn, affect physical and chemical properties of the coatings while in use.[79,82,113,132]

Delamination is due to poor adhesion, coating damage and/or crack propagation. When bonds break at the coating-metal interface resulting from the alkalinity of the cathodic reaction products, blistering ensues due to osmotic pressure, which develops as a result of high water solubility of the reaction products from the cathodic reaction. The blisters may be cathodic (consisting of highly alkaline liquid) or neutral. Blistering on coatings can also occur with no seeming defect, and this has been attributed to the following governing mechanisms: expansion due to swelling, gas inclusion, and osmotic processes.[133] It should be noted that blistering and delamination occur alongside each other during the failure of organic coatings. Blisters develop and expand forming dis-bonded areas in the coating which become sites for delamination to occur.
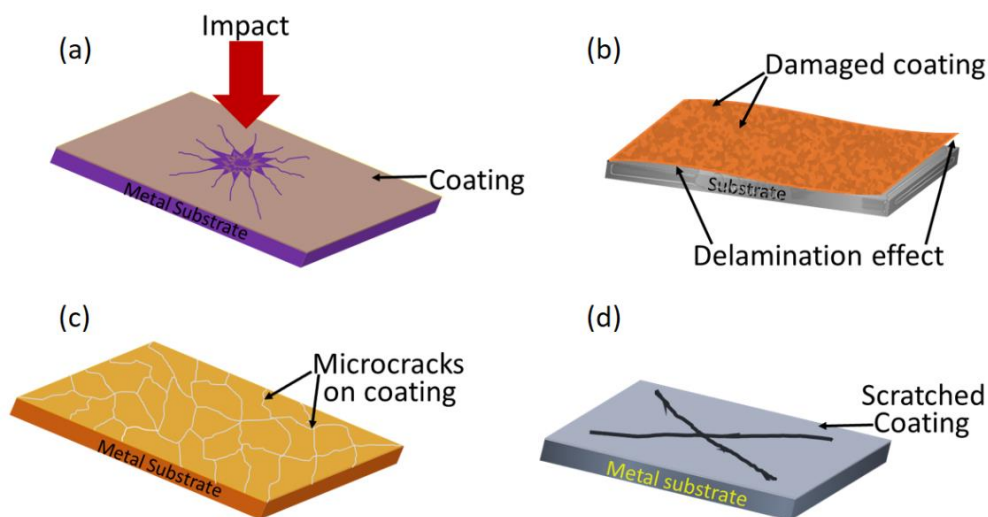
Fig. 1.17: (a-d) Schematic of possible damage types in smart coatings.

1.9 Bio-based inhibitors and coatings

1.9.1 Biomass-derived phytochemicals as corrosion inhibitors

Phytochemicals in vegetal extracts have been explored as corrosion inhibitors for various metals due to the adsorption process occurring on the metal surface that gives rise to a protective layer. These phytochemicals are environmentally friendly agents containing heteroatoms and aromatic rings etc. of inhibiting importance. The investigation of green compounds irrespective of origin as cheap and non-toxic corrosion inhibitors is still a strong consideration. Despite earlier criticisms, the use of phytochemicals are the current focus of studies in diverse corrosion fields. Their efficacy is attributable to adsorption on the metallic surface by heteroatoms such as N, O, S, P; polar functional groups such as $-OH$, $-NH_2$, $-NO_2$, $-CN$, etc.; π-electrons, planar and conjugated aromatic rings as adsorption centers. This is because of their capability to donate available lone pair of electrons or acceptance of electrons in their low energy empty orbitals. The retardation of metal corrosion by inhibitors adsorbed on metallic surfaces is also influenced by the molecular size of inhibitor, inhibitor concentration, nature of substituents, solution temperature, and nature of test solution.[134–137].

The general mechanism of corrosion inhibition by plant-based organic inhibitors are known to displace water molecules while adsorbing onto the metal surface. In this

scenario, corrosion inhibition occurs due to the transport of the inhibitor to the metal surface and metal-inhibitor interactions resulting in the formation of metal-organic inhibitor complex as a barrier to further corrosion. The resulting complex may be stable, inhibiting further corrosion or relatively soluble, thus catalyzing further metal dissolution depending on the nature of bonds formed during the adsorption process.[138–140] The number of water molecules displaced is determined by the size and orientation of the inhibitor molecule(s).[141] Apart from the influence of the molecular structure of the organic compounds, adsorption behavior of organic molecules on metals is accompanied by charge-transfer processes between the adsorbates and the substrate resulting in a change in physical and chemical properties of the molecules in comparison to when it's in the solution phase.[142] During adsorption of an organic inhibitor on a metal surface any of the following processes may occur; (i) Electrostatic interaction between the charged inhibitor molecules and charged metal surface, (ii) Interaction between unshared electrons of the inhibitor molecules and the metal surface, (iii) Interaction of pi-electrons present in the inhibitor compound and the metal surface, and (iv) A synergy of (i) and (iii).[140]

Table 1.2: Selected corrosion inhibitors of biomass origin.

S/N	Plant names (Common name)	Phytochemicals/ chemical compounds present	Mechanism of inhibition	Inhibition efficiency (%)	Substrate/ Corrosive media	Characteristics	References
1.	*Aloe vera (L.)*	Mannose-6-phosphate	Adsorption	98.0	Carbon steel/sea water	Aloe gel used. Contains hydroxyl groups, phosphate groups, and ring oxygen.	[143]
2.	*Areca catechu* (Betel nut)	Flavonols, tannins (polyphenols) arecoline, arecaidine, guvacoline and guvacine (alkaloids), carbohydrates, fats, proteins, crude fiber and mineral matters.	Adsorption	96.97	Mild steel/HCl	Powdered seeds were used in the study.	[144]
3.	*Aspidosperma album*	Alkaloids	Physical adsorption	91.0	C38 steel/HCl	Medicinal plant in South America.	[145]
4.	*Brassica oleracea*	-	Adsorption	99.63	Pipeline steel /H_2SO_4	Outer leaves were used.	[146]
5.	*Bucolzia coriacea*	Tannins, saponins, carbohydrates, proteins etc.	Physical adsorption	96.6	Aluminium pigment/ (H_2O/butyl alcohol)	-	[147]
6.	*Cocos nucifera L.* water (coconut water)	Sorbitol, ascorbic acid, methionine, malic acid, vitamin B1, fructose, glucose, phytohormone, auxin, cytokinin, gibberellin etc.	Physical adsorption	93.0	Aluminium/ HCl	Coconut water was used. –COOH and –OH etc. are the functional groups present.	[148]
7.	*Emblica officinalis*	Emblica A & B, phyllanthin, punigluconin and pedunculagin	Physical adsorption	92.6	Cu-27ZN/sea water	-	[151]
9.	*Guaterria ouregou*	Alkaloids	Physical adsorption	92.0	Low carbon steel/HCl	-	[150]

1.9.2 Biomass-derived phytochemicals in anticorrosive coatings

The involvement of bio-based components to complement existing coating formulation techniques is an interdisciplinary contribution to material science. Bio-based materials are strongly considered as cheap and non-toxic alternatives. The underlying idea for the use of these class of materials is to harness nature's abundant sustainable resources, by combination of the "green" characteristics of natural products and wherever possible the high performance rendered by nanomaterials for advanced functional applications in diverse areas such as drug delivery, medicine, sensing devices, flame retardancy, food packaging, gas diffusion barriers, protective coatings etc.[151]

These bio-based additives can be chemically the same as petrochemical-based products but produced from biomass instead of fossil resources. They can also be isolated compounds that provide a desired functionality with the potential to impart new properties to coatings or enhance desirable performance characteristics.[152] The development of protective coatings using renewable resources is a green processing approach and its investigations is significantly increasing especially with the aim of achieving smart and functional coatings.[153,154]

1.9.3 Commercial viability of selected bio-based coatings

In Table 1.3 a selection of bio-based coatings is presented. About 50-90% of renewable resources have been utilized in their fabrication to produce viable coatings that have been commercialized for wood protection, floor coatings, printing purposes and hardeners for automotive scratch resistant paints.

Table 1.3: Selected commercially viable bio-based coatings.

S/N	Brand	Properties	Application	References
1.	Ecopoxy Epoxy Coatings	50% bio-content in coating. Utilizes soyabean, cashew nut oil and recycled egg shells.	Any surfaces but excellent with wood.	www.ecopoxy.com
2.	TerraGreen Coatings	90% or above renewable resources in coatings. Resins and waxes from plants, trees and animals.	Printing purposes	www.actega.com/terra/products.terragreen coatings.htm
3.	Eco-tuff Coatings	Products from rapidly renewable, abundant, or low-impact/organic materials. Biobased technology	Non-skid coatings. High traffic floor coatings. Safety coatings.	www.dwellsmart.com
4.	Desmodur® eco N 7300	70% of its carbon content - renewable raw materials. First bio-based hardener for polyurethane coatings (clearcoat). Test bodies successfully coated under realistic production conditions	Scratch resistant, glossy etc. for the automotive industry. Collaboration between Audi, BASF and Covestro	www.coatings.covestro.com

www.ecopoxy.com, www.actega.com/terra/products.terragreen coatings.htm, www.dwellsmart.com, www.coatings.covestro.com

1.10 Applications and commercial viability of smart coatings

End-user application of smart coatings are in the following areas: medical and healthcare, military, aerospace, automotive, marine, energy, consumer electronics, construction, oil and gas, packaging, textiles and apparel industries etc. Smart coatings can be customized to meet specific consumers' requirements.[2] Self-cleaning thin nanofilms are applicable on household surfaces. They are safe for skin contact and protect the surfaces from dust or grease accumulation, scale deposition, and corrosion attack. From computer equipment to kitchen surfaces to shower screens these self-cleaning surfaces will minimize the use of detergents and time spent on cleaning [155]. Anti-fingerprint coatings have found application in optics, kitchens, cafes, restaurants, electronic display screens, textiles, floor sealants, automotive and HVAC (heating, ventilation, and air conditioning) systems etc.[8] Self-healing coatings for the aviation industry have been proposed by a team of researchers from the Centre for Research in Ceramics and Composite Materials (CICECO), University of Aveiro. When applied to the fuselage of the aircraft, it repairs, as a skin, small discontinuities resulting from mechanical and environmental impacts suffered by appliances during flight by releasing its embedded restorative molecules when required.[156] Likewise, an innovative nano-paint technology called Ultra-Ever Dry® a contribution to development in the world's first self-cleaning car has been tested by Nissan. It repels mud, rain, oil, sleet, dirt and everyday road spray minimizing the car wash trips. Although there are no current plans to apply the self-cleaning paint to Nissan's vehicle lineup as a standard feature, the technology is considered as a potential aftermarket option.[157]   A few commercialized products are presented in Table 1.2. The challenge of translating smart coatings concepts in academic fundamental research into practical coating systems with commercially viable industrial applications is still of great concern. This obviously requires a lot more dialogue and collaboration between academics and industrialists to bridge the gap between the technological progress and the market demand. Within the industry, there is continued product development and focus is on higher performance, not only to fulfill customer needs but also to comply with regulatory requirements. While the results from the academia with the aid of computer simulations may

contribute to providing some leverage to certain technical difficulties in the coatings industries. Furthermore, durability is a key challenge to advancing current smart coating technologies for external and internal applications in the different sectors where it is being utilized. Similarly, adding functionality to coatings often increases cost which is another challenge. But, effective multifunctional smart coatings in real-time service will boost market demands far beyond predictions.[7,158]

Table 1.4: Selected commercially available smart coatings.

S/No.	Products	Characteristics	Applications	Producers
1.	Deletum 5000 & 3000	Anti-graffiti paints	Coatings repellant to water and oil.	Victor Castaño
2.	2C Marine Sealant PRO	Antifouling coating	Intended for gel coat marine surfaces with no or only minimal sign of wear.	Nanosafeguard
3.	Burgundy Cukote™	Antifouling coating	Cuprous oxide self-polishing coating	Sea Hawk®
4.	Smart solution™	Copper free antifouling	Eco-friendly metal free bottom paint	Sea Hawk®
5.	Intercept® 8500 LPP	Antifouling coating	Biocidal antifouling for marine vessels	AkzoNobel
6.	ECONTROL®	Intelligent solar control glass	Provides shading in the glass	EControl-Glas GmbH & Co. KG

7.	NanoChar™	Fire protection coating, VOC-free epoxy intumescent coatings based on nanotechnology.	Protects steel amongst other non-metallic substrates.	Intumescent Associates Group
8.	SPD-SmartGlass	Smart window coating	Changes the tint of any window, sunroof or skylight.	Research Frontiers
9.	NANOMYTE®	Waterborne, solventborne, superhydrophobic, self-healing, anticorrosion, acid resistant etc.	Pretreatments, primers and topcoats	NEI Corporation
10.	Ultra-Ever Dry®	Self-cleaning, anti-icing, anti-wetting, anticorrosion etc.	Superhydrophobic and oleophobic coating that will repel most water-based and some oil-based liquids. For industrial use only.	UltraTech International, Inc.
11.	EcoShield® 386 Water Based Coating	Acrylic based formula with a complex mixture of nano sized non-toxic organic corrosion inhibitors that can provide protection against 1000 hours of salt spray performance.	For harsh, unsheltered outdoor applications where corrosion and UV protection are required on metals for long periods of time.	Cortec Corporation

12.	1K-Nano	Nano paint sealant	Coatings for automobile exterior	Koch-Chemie
13.	Nanotol®	Nano-based sealant that creates a durable water and dirt repellent protective layer and provides deep gloss on all surfaces of the vehicle. Contains nanopolymers that are activated by rubbing with a microfiber cloth during application.	Automobile exterior, wheels and disc.	CeNano GmbH & Co. KG
14.	NanoMate®5810/5820	Functional and decorative metal finishing with anticorrosive properties for metals. Eco-friendly finishing chemical.	Pre-painting and pre-bonding applications for metals, stone , ceramics, glass etc.	NanoMate Technology, Inc.

Victor Castano: http://www.nanotechproject.org, Nanosafeguard: http://www.nanotechproject.org, Intumescents Associates Group: http://www.advancedepoxycoatings.com, NEI Corporation: http://www.neicorporation.com/products/coatings/anticorrosion-paints-coatings/, Sea Hawk®: www.seahawkpaints.com, UltraTech International, Inc.: http://www.spillcontainment.com/, AkzoNobel: https://www.akzonobel.com, Research Frontiers: http://www.smartglass.com, EControl-Glas GmbH & Co. KG: www.econtrol-glas.de/en/company/, Cortec Corporation: http://www.cortecvci.com, Koch-Chemie: http://www.1k-nano.de/en/main.html, CeNano GmbH & Co. KG: www.nanotol.de, NanoMate Technology, Inc.: http://nanomatetech.com/2014/finishing.html

1.11 Summary and Outlook

This chapter highlights some of the functions exhibited by smart coatings with conceivable industrial relevance. With recent developments focused mainly on smart coatings for anticorrosive applications, one of the key approaches for self-healing coatings focused on the use of micro and nanocontainers capable of being loaded with active agents and having shells possessing controlled permeability specific to several triggers. Sustainability/durability was observed to be related to an effective healing action. Leading approaches for self-cleaning coatings involved high superhydrophobicity with extreme repellency to varying corrosive droplets which were maintained irrespective of the metal substrate and UV stability. Active corrosion-sensing coatings comprised the use of fluorescent or color indicators responsive to varying environmental triggers such as pH, ion or redox indicators. While approaches for enhancing antifouling coatings were concerned with self-cleaning, water resistant and superhydrophobic surfaces with low-surface free energy, low micro-roughness, and ultra-smooth topology to prevent fouling settlements when biocides are not utilized. Otherwise eco-friendly biocides were encouraged. With these considerations the objectives of the thesis were developed considering the use of biomass-based compounds.

1.12 Objectives of the investigation

- Evaluation of crude biomass extract as corrosion inhibitors.
- Synthesis and utilization of porous silica nanocontainers for loading the natural green inhibitors.
- Development of smart anticorrosive coatings based on biomass derived additives and its evaluation.
- Synthesis, characterization and functionalization of silver nanoparticles from biomass extracts.
- Formulation and evaluation of bioreduced Ag-based nanocomposite coatings for corrosion protection of aluminium alloys.
- Antimicrobial investigation of the biomass-derived nanoparticles and hybrid coatings.

References

[1] J. Baghdachi, In *Smart Coatings II, ACS Symposium Series*; T. Provder; Baghdachi, J., Eds.; American Chemical Society: Washington DC, 2009; Vol. 1002.

[2] A. S. H. Makhlouf, *Handbook of Smart Coatings for Materials Protection*; Woodhead Publishing Limited: Oxford, United Kingdom, 2014.

[3] H. Wei, Y. Wang, J. Guo, N. Z. Shen, D. Jiang, X. Zhang, X. Yan, J. Zhu, Q. Wang, L. Shao, H. Lin, S. Wei, Z. Guo, *J. Mater. Chem. A* **2015**, *3*, 469.

[4] S. B. Ulaeto, R. Rajan, J. K. Pancrecious, T. P. D. Rajan, B. C. Pai, *Prog. Org. Coatings* **2017**, *111*, 294.

[5] T. Provder, J. Baghdachi, *Smart Coatings*; Provder, T.; Baghdachi, J., Eds.; American Chemical Society: Washington, DC, 2007; Vol. 957.

[6] M. F. Montemor, *Surf. Coatings Technol.* **2014**, *258*, 17.

[7] C. Challener, *CoatingsTech*. 2017,.

[8] FutureMarkets, 2014, p. 200.

[9] M. Hosseini, A. S. Hamdy Makhlouf, *Industrial applications for intelligent polymers and coatings*; 2016.

[10] I. S. Cole, In *Handbook of Smart Coatings for Materials Protection*; Makhlouf, A. S. H., Ed.; Woodhead Publishing Limited: UK, 2014; pp. 29–55.

[11] J. O. Carneiro, V. Teixeira, S. Azevedo, M. Maltez-da costa, In *Handbook of Smart Coatings for Materials Protection*; Makhlouf, A. S. H., Ed.; Woodhead Publishing Limited, 2014; pp. 489–509.

[12] M. Chanda, *Plastics Technology Handbook*; Hudgin, D. E., Ed.; 5th ed.; CRC Press, Taylor & Francis Group: Boca Raton, FL, 2018.

[13] A. K. Guin, S. Nayak, M. K. Bhadu, V. Singh, T. K. Rout, *ISRN Corros.* **2014**, *2014*, 1.

[14] S. R. White, N. R. Sottos, P. H. Geubelle, J. S. Moore, M. R. Kessler, S. R. Sriram, E. N. Brown, S. Viswanathan, *Nature* **2001**, *409*, 794.

[15] H. Zhang, J. Yang, *Smart Mater. Struct.* **2014**, *23*, 065003.

[16] I. Alessandri, In *Self-Healing at the Nanoscale. Mechanisms and Key Concepts of Natural and Artificial Systems*; Amendola, V.; Meneghetti, M., Eds.; CRC Press: New York, 2012; pp. 163–198.

[17] H. Choi, K. Y. Kim, J. M. Park, *Prog. Org. Coatings* **2013**, *76*, 1316.

[18] Z. Zheng, M. Schenderlein, X. Huang, N. J. Brownbill, F. Blanc, D. Shchukin, *ACS Appl. Mater. Interfaces* **2015**, *7*, 22756.

[19] S. Amiri, A. Rahimi, *J. Polym. Res.* **2014**, *21*, 566.

[20] Y. Yang, M. W. Urban, *Chem. Soc. Rev* **2013**, *42*, 7446.

[21] M. L. Zheludkevich, D. G. Shchukin, K. A. Yasakau, H. Möhwald, M. G. S. Ferreira, *Chem. Mater.* **2007**, *19*, 402.

[22] J. H. Bell, E. T. Schairer, L. A. Hand, R. D. Mehta, *Annu. Rev. Fluid Mech* **2001**, *33*, 155.

[23] J. W. Gregory, H. Sakaue, T. Liu, J. P. Sullivan, *Annu. Rev. Fluid Mech.* **2014**, *46*, 303.

[24] H. Sakaue, T. Tabei, M. Kameda, *Sensors Actuators B Chem.* **2006**, *119*, 504.

[25] S. Babulanam, W. Estrada, M. O. Hakim, S. Yatsuya, a. M. Andersson, J. R. Stevens, J. S. E. M. Svensson, C. G. Granqvist, *Spie* **1987**, *823*, 64.

[26] M. Kamalisarvestani, R. Saidur, S. Mekhilef, F. S. Javadi, *Renew. Sustain. Energy Rev.* **2013**, *26*, 353.

[27] Y. Li, S. Ji, Y. Gao, H. Luo, M. Kanehira, *Sci. Rep.* **2013**, *3*.

[28] R. Baetens, B. P. Jelle, A. Gustavsen, *Sol. Energy Mater. Sol. Cells* **2010**, *94*, 87.

[29] J. S. E. M. Svensson, C. G. Granqvist, *Sol. Energy Mater.* **1985**, *12*, 391.

[30] T. Liu, B. Liu, J. Wang, L. Yang, X. Ma, H. Li, Y. Zhang, S. Yin, T. Sato, T. Sekino, Y. Wang, *Sci. Rep.* **2016**, *6*.

[31] H. Dodiuk, P. F. Rios, A. Dotan, S. Kenig, *Polym. Adv. Technol.* **2007**, *18*, 746.

[32] M. Zhang, S. Feng, L. Wang, Y. Zheng, *Biotribology* **2016**, *5*, 31.

[33] H. Yoon, H. Kim, S. S. Latthe, M. Kim, S. Al-Deyab, S. S. Yoon, *J. Mater. Chem. A* **2015**, *3*, 11403.

[34] W. Zhu, P. J. M. Bartos, A. Porro, *Mater. Struct. Constr.* **2004**, *37*, 649.

[35] G. N. Manvi, A. R. Singh, R. N. Jagtap, D. C. Kothari, *Prog. Org. Coatings* **2012**, *75*, 139.

[36] N. Kumar, G. Manik, *Polymer (Guildf).* **2016**, *100*, 194.

[37] I. Bayer, *Coatings* **2017**, *7*, 12.

[38] H. Venugopalan, *Laser Focus World*. 2016, pp. 28–31.

[39] C. Anderson, M. Atlar, M. Callow, M. Candries, A. Milne, R. L. Townsin, *J. Mar. Des. Oper.* **2003**, *B4*, 11.

[40] M. Lejars, A. Margaillan, C. Bressy, Fouling release coatings: A nontoxic alternative to biocidal antifouling coatings. *Chem. Rev.* **2012**, *112*, 4347–4390.

[41] M. Camps, A. Barani, G. Gregori, A. Bouchez, B. le Berre, C. Bressy, Y. Blache, J. F. Briand, *Appl. Environ. Microbiol.* **2014**, *80*, 4821.

[42] A. G. Nurioglu, A. C. C. Esteves, G. de With, *J. Mater. Chem. B* **2015**, *3*, 6547.

[43] E. Armstrong, K. G. Boyd, A. Pisacane, C. J. Peppiatt, J. G. Burgess, *Biofouling* **2000**, *16*, 215.

[44] Woods Hole Oceanographic Institute, *Chapter 18: Characteristics of Antifouling Coatings*; 1952.

[45] J. Chapman, F. Regan, T. Sullivan, *Nanoparticles in anti-microbial materials: Use and characterisation*; Royal Society of Chemistry: Cambridge, UK, 2012.

[46] M. Cloutier, D. Mantovani, F. Rosei, Antibacterial Coatings: Challenges, Perspectives, and Opportunities. *Trends Biotechnol.* **2015**, *33*, 637–652.

[47] L. Su, Y. Yu, Y. Zhao, F. Liang, X. Zhang, *Sci. Rep.* **2016**, *6*, 1.

[48] P. Thebault, T. Jouenne, In *The battle against microbial pathogens: Basic science, technological advances and educational programs*; Mendez-Vilas, A., Ed.; Formatex, 2006; Vol. 95, pp. 483–489.

[49] S. Duquesne, S. Magnet, C. Jama, R. Delobel, *Surf. Coatings Technol.* **2004**, *180–181*, 302.

[50] M. C. Yew, N. H. Ramli Sulong, M. K. Yew, M. A. Amalina, M. R. Johan, *Prog. Org. Coatings* **2015**, *78*, 59.

[51] M. M. de Souza, S. C. de Sá, A. V Zmozinski, R. S. Peres, C. A. Ferreira, *Ind. Eng. Chem. Res.* **2016**, *55*, 11961.

[52] M. C. Yew, N. H. Ramli Sulong, M. K. Yew, M. A. Amalina, M. R. Johan, *Prog. Org. Coatings* **2015**, *81*, 116.

[53] S. C. de Sá, M. M. de Souza, R. S. Peres, A. V. Zmozinski, R. M. Braga, D. M. de Araújo Melo, C. A. Ferreira, *Prog. Org. Coatings* **2017**, *113*, 47.

[54] S. Liang, N. M. Neisius, S. Gaan, *Prog. Org. Coatings* **2013**, *76*, 1642.

[55]   H. Liang, A. Asif, W. Shi, *Polym. Degrad. Stab.* **2005**, *87*, 495.

[56]   E. Çakmakçi, Y. Mülazim, M. V. Kahraman, N. K. Apohan, *React. Funct. Polym.* **2011**, *71*, 36.

[57]   S. W. Zhu, W. F. Shi, *Polym. Degrad. Stab.* **2002**, *75*, 543.

[58]   G. Wang, H. Wang, Z. Guo, *Chem. Commun.* **2013**, *49*, 7310.

[59]   A. Siriviriyanun, T. Imae, *Chem. Eng. J.* **2014**, *246*, 254.

[60]   S. Y. Heo, B. J. Park, J. R. Jeong, S. G. Yoon, *J. Alloys Compd.* **2014**, *602*, 255.

[61]   H. J. Choi, B. J. Park, J. H. Eom, M. J. Choi, S. G. Yoon, *ACS Appl. Mater. Interfaces* **2016**, *8*, 997.

[62]   H. K. Raut, V. A. Ganesh, A. S. Nair, S. Ramakrishna, *Energy Environ. Sci.* **2011**, *4*, 3779.

[63]   J. Hiller, J. D. Mendelsohn, M. F. Rubner, *Nat. Mater.* **2002**, *1*, 59.

[64]   X. Li, J. Shen, *Thin Solid Films* **2011**, *519*, 6236.

[65]   J. Lv, Y. Song, L. Jiang, J. Wang, Bio-inspired strategies for anti-icing. *ACS Nano* **2014**, *8*, 3152–3169.

[66]   X. Sun, V. G. Damle, S. Liu, K. Rykaczewski, *Adv. Mater. Interfaces* **2015**, *2*, 25.

[67]   S. Zheng, C. Li, Q. Fu, W. Hu, T. Xiang, Q. Wang, M. Du, X. Liu, Z. Chen, *Mater. Des.* **2016**, *93*, 261.

[68]   M. W. England, C. Urata, G. J. Dunderdale, A. Hozumi, *ACS Appl. Mater. Interfaces* **2016**, *8*, 4318.

[69]   M. Wen, L. Wang, M. Zhang, L. Jiang, Y. Zheng, *ACS Appl. Mater. Interfaces* **2014**, *6*, 3963.

[70]   H. Qian, D. Xu, C. Du, D. Zhang, X. Li, L. Huang, L. Deng, Y. Tu, J. M. C. Mol, H. A. Terryn, *J. Mater. Chem. A* **2017**, *5*, 2355.

[71]   T. Chen, R. Chen, Z. Jin, J. Liu, *J. Mater. Chem. A* **2015**, *3*, 9510.

[72]   S. LI, H. ZHANG, J. LIU, *Trans. Nonferrous Met. Soc. China* **2006**, *16*, s159.

[73]   K. J. Loh, J. Kim, J. P. Lynch, N. W. S. Kam, N. A. Kotov, *Smart Mater. Struct.* **2007**, *16*, 429.

[74]   J. Zhang, G. S. Frankel, *Corrosion* **1999**, *55*, 957.

[75]   H. Li, S. Yu, X. Han, Y. Zhao, *Colloids Surfaces A Physicochem. Eng. Asp.* **2016**, *503*,

43.

[76] L. Li, Y. Bai, L. Li, S. Wang, T. Zhang, *Adv. Mater.* **2017**, *29*.

[77] M. S. Selim, M. A. Shenashen, A. Elmarakbi, N. A. Fatthallah, S. ichi Hasegawa, S. A. El- Safty, *Chem. Eng. J.* **2017**, *320*, 653.

[78] C. Ma, W. Zhang, G. Zhang, P.-Y. Qian, *ACS Sustain. Chem. Eng.* **2017**, *5*, 6304.

[79] B. Blaiszik, S. L. B. Kramer, J. S. Moore, N. R. Sottos, B. J. Blaiszik, S. L. B. Kramer, S. C. Olugebefola, J. S. Moore, N. R. Sottos, S. R. White, *Annu. Rev. Mater. Res* **2010**, *40*, 179.

[80] Z. Zhang, Y. Hu, Z. Liu, T. Guo, *Polymer (Guildf).* **2012**, *53*, 2979.

[81] S. H. Cho, H. M. Andersson, S. R. White, N. R. Sottos, P. V. Braun, *Adv. Mater.* **2006**, *18*, 997.

[82] S. W. H. M. Andersson, M. W. Keller, J. S. Moore, N. R. Sottos, In *Self-Healing Materials. An Alternative Approach to 20 Centuries of Materials Science*; Zwaag, S. van der, Ed.; Springer Series in Materials Science; Springer Netherlands: Dordrecht, 2007; Vol. 100, pp. 19–44.

[83] H. Zhang, J. Yang, *Smart Mater. Struct.* **2014**, *23*, 065004.

[84] A. Popoola, O. Olorunniwo, O. Ige, In *Developments in Corrosion Protection*; InTech, 2014; pp. 241–270.

[85] Y. C. Yuan, T. Yin, M. Z. Rong, M. Q. Zhang, *Express Polym. Lett.* **2008**, *2*, 238.

[86] S. M. Bleay, C. B. Loader, V. J. Hawyes, L. Humberstone, P. T. Curtis, *Compos. Part A Appl. Sci. Manuf.* **2001**, *32*, 1767.

[87] D. Borisova, D. Akçakayıran, M. Schenderlein, H. Möhwald, D. G. Shchukin, *Adv. Funct. Mater.* **2013**, *23*, 3799.

[88] S. S. Pathak, A. S. Khanna, In *Corrosion Protection and Control Using Nanomaterials*; Elsevier, 2012; pp. 304–329.

[89] G. Decher, In *Multilayer Thin Films*; Wiley-VCH Verlag GmbH & Co. KGaA: Weinheim, Germany, 2012; pp. 1–21.

[90] A. Stankiewicz, I. Szczygieł, B. Szczygieł, *J. Mater. Sci.* **2013**, *48*, 8041.

[91] A. P. Esser-Kahn, S. A. Odom, N. R. Sottos, S. R. White, J. S. Moore, *Macromolecules* **2011**, *44*, 5539.

[92] M. F. Haase, D. O. Grigoriev, H. Möhwald, D. G. Shchukin, *Adv. Mater.* **2012**, *24*, 2429.

[93] C. J. Brinker, In *Chemical Solution Deposition of Functional Oxide Thin Films*; Springer Vienna: Vienna, 2013; Vol. 9783211993, pp. 233–261.

[94] D. P. Birnie, In *Chemical Solution Deposition of Functional Oxide Thin Films*; Springer Vienna: Vienna, 2013; pp. 263–274.

[95] M. ICHIKI, L. ZHANG, Z. YANG, T. IKEHARA, R. MAEDA, *Integr. Ferroelectr.* **2004**, *61*, 167.

[96] M. D. Brubaker, In *Chemical Solution Deposition of Functional Oxide Thin Films*; Springer Vienna: Vienna, 2013; Vol. 9783211993, pp. 275–302.

[97] M. R. De Guire, L. P. Bauermann, H. Parikh, J. Bill, In *Chemical Solution Deposition of Functional Oxide Thin Films*; Springer Vienna: Vienna, 2013; pp. 319–339.

[98] J. R. Creighton, P. Ho, In *Chemical vapor deposition*; Park, J.; Sudarshan, T., Eds.; ASM international, 2001.

[99] D. Mattox, *Handbook of physical vapor deposition (PVD) processing*; 2nd ed.; Elservier: Oxford, UK, 2010.

[100] P. G. Clem, N. S. Bell, In *Chemical Solution Deposition of Functional Oxide Thin Films*; Springer Vienna: Vienna, 2013; Vol. 9783211993, pp. 303–318.

[101] P. Yimsiri, M. R. Mackley, *Chem. Eng. Sci.* **2006**, *61*, 3496.

[102] A. Papyrin, V. Kosarev, S. Klinkov, A. Alkhimov, V. M. Fomin, *Cold spray technology*; 1st ed.; Elsevier: Oxford, UK, 2006.

[103] T. H. Van Steenkiste, J. R. Smith, R. E. Teets, *Surf. Coatings Technol.* **2002**, *154*, 237.

[104] R. Ghelichi, M. Guagliano, *Frat. ed Integrità Strutt.* **2009**, *3*, 30.

[105] GracoInc, *Airless spray coating technology: Concept and theory training. www.chreed.com/help_pages/airless_guns.pdf Accessed November 2016*; 1995.

[106] IMTMA, *Compendium of Industrial Painting & Coating Processes for Machine Tools. www.imtma.in/pdf/painting_manual.pdf Accessed November 2016*; 2015.

[107] GracoInc, *The basics of airless spraying. www.graco.com/content/dam/graco/ced/literature/misc/321132/321132EN-F.pdf Accessed November 2016*; 2014.

[108] S. Panigrahi, S. Waugh, S. K. Rout, A. K. Hassan, A. K. Ray, *Indian J. Phys.* **2004**, *78*, 823.

[109] N. Sahu, B. Parija, S. Panigrahi, *Indian J. Phys.* **2009**, *83*, 493.

[110] A. Salam Hamdy, *Recent Patents Mater. Sci.* **2010**, *3*, 258.

[111] X. Shi, T. A. Nguyen, Z. Suo, Y. Liu, R. Avci, *Surf. Coatings Technol.* **2009**, *204*, 237.

[112] A. C. Balazs, T. Emrick, T. P. Russell, *Science (80-.).* **2006**, *314*, 1107.

[113] A. Mathiazhagan, R. Joseph, *Int. J. Chem. Eng. Appl.* **2011**, *2*, 225.

[114] P. A. W. Dubbert, K. Schwirn, D. Völker, *Fact Sheet – Use of nanomaterials in coatings. https://www.umweltbundesamt.de/sites/default/files/medien/378/publikationen/use_of_nanomaterials_in_coatings_0.pdf Accessed September 2015*; Dessau-Roßlau, Germany, 2014.

[115] D. Féron, *Nuclear corrosion science and engineering*; Woodhead publishing limited: Cambridge, UK, 2012.

[116] J. Scalf, P. West, *Part I: Introduction to Nanoparticle Characterization with AFM*; Santa Clara, CA 95054, 2006.

[117] J. Telegdi, T. Szabó, L. Románszki, M. Pávai, In *Handbook of Smart Coatings for Materials Protection*; Elsevier, 2014; pp. 135–182.

[118] I. Phang, N. Aldred, A. Clare, G. Vancso, *NanoS* **2007**, 36.

[119] K. M. M. Abou El-Nour, A. Eftaiha, A. Al-Warthan, R. A. A. Ammar, *Arab. J. Chem.* **2010**, *3*, 135.

[120] E. A. D. and M. A. El. Maher A. El Sockary, Ashraf M. El-Saeed, Samya I. El Sherbiny, Fatma A. Morsy, *J. Eng. Res. Appl.* **2014**, *4*, 65.

[121] M. L. Zheludkevich, J. Tedim, M. G. S. Ferreira, *Electrochim. Acta* **2012**, *82*, 314.

[122] J. Carneiro, J. Tedim, S. C. M. Fernandes, C. S. R. Freire, A. Gandini, M. G. S. Ferreira, M. L. Zheludkevich, *ECS Electrochem. Lett.* **2013**, *2*, C19.

[123] H. Ashassi-Sorkhabi, D. Seifzadeh, M. G. Hosseini, *Corros. Sci.* **2008**, *50*, 3363.

[124] H. B. Wang, H. Shi, T. Hong, C. Kang, W. P. Jepson, In *Corrosion2001*; NACE International, 2001.

[125] L. Mulfinger, S. D. Solomon, M. Bahadory, A. V. Jeyarajasingam, S. A. Rutkowsky, C.

Boritz, *J. Chem. Educ.* **2007**, *84*, 322.

[126] T. R. K. Satyavani, S. Gurudeeban, V. Deepak, *Res. J. Chem. Environ.* **2013**, *17*, 27.

[127] G. Narasimha, B. Praveen, K. Mallikarjuna, B. Raju, B. Deva Prasad Raju, *Int. J. Nano Dimens.* **2001**, *2*, 29.

[128] S. Neema, M. Selvaraj, J. Raguraman, S. Ramu, *J. Appl. Polym. Sci.* **2013**, *127*, 740.

[129] D. V. Andreeva, D. G. Shchukin, *Mater. Today* **2008**, *11*, 24.

[130] T. H. Tran, A. Vimalanandan, G. Genchev, J. Fickert, K. Landfester, D. Crespy, M. Rohwerder, *Adv. Mater.* **2015**, *27*, 3825.

[131] P. Gupta, M. Bajpai, *Adv. Chem. Eng. Sci.* **2011**, *01*, 133.

[132] W. Feng, S. H. Patel, M.-Y. Young, J. L. Zunino, M. Xanthos, *Adv. Polym. Technol.* **2007**, *26*, 1.

[133] P. A. Sørensen, S. Kiil, K. Dam-Johansen, C. E. Weinell, *J. Coatings Technol. Res.* **2009**, *6*, 135.

[134] P. B. Raja, M. G. Sethuraman, *Mater. Lett.* **2008**, *62*, 113.

[135] S. K. Saha, A. Dutta, P. Ghosh, D. Sukul, P. Banerjee, *Phys. Chem. Chem. Phys.* **2015**, *17*, 5679.

[136] C. Verma, L. O. Olasunkanmi, E. E. Ebenso, M. A. Quraishi, I. B. Obot, *J. Phys. Chem. C* **2016**, *120*, 11598.

[137] K. Xhanari, M. Finšgar, M. Knez Hrnčič, U. Maver, Ž. Knez, B. Seiti, *RSC Adv.* **2017**, *7*, 27299.

[138] J. Buchweishaija, *Tanzania J. Sci.* **2009**, *35*.

[139] B. E. A. Rani, B. B. J. Basu, *Int. J. Corros.* **2012**, *2012*, 1.

[140] V. S. Sastri, *Green corrosion inhibitors : theory and practice*; 1st ed.; John Wiley & Sons, Inc.: Hoboken, New Jersey, 2011.

[141] S. Papavinasam, Revie, R. W., Ed.; John Wiley & Sons, Inc.: Hoboken, New Jersey, 2011.

[142] R. Otero, A. L. Vázquez de Parga, J. M. Gallego, *Surf. Sci. Rep.* **2017**, *72*, 105.

[143] V. Sribharathy, S. Rajendran, P. Rengan, R. Nagalakshmi, *Eur. Chem. Bull* **2013**, *2*, 471.

[144] K. P. Vinod Kumar, M. Sankara Narayanan Pillai, G. Rexin Thusnavis, *J. Mater. Sci.*

2011, *46*, 5208.

[145] M. Faustin, M. Lebrini, F. Robert, C. Roos, T. Biran, F. Guiana, *Corrosion Studies of C38 Steel by Alkaloids Extract of a Tropical Plant Type*; 2011; Vol. 6.

[146] N. C. Ngobiri, E. E. Oguzie, Y. Li, L. Liu, N. C. Oforka, O. Akaranta, *Int. J. Corros.* **2015**, *2015*, 1.

[147] C. O. Akalezi, C. K. Enenebeaku, C. E. Ogukwe, E. E. Oguzie, *Environ. Pollut.* **2012**, 1.

[148] O. K. Abiola, Y. Tobun, *Chinese Chem. Lett.* **2010**, *21*, 1449.

[149] P. Rani, S. Selvaraj, *Arch. Appl. Sci. Res.* **2010**, *2*, 140.

[150] A. Lecante, F. Robert, P. A. Blandinires, C. Roos, *Curr. Appl. Phys.* **2011**, *11*, 714.

[151] E. Sharmin, O. ur Rahman, F. Zafar, D. Akram, M. Alam, S. Ahmad, *RSC Adv.* **2015**, *5*, 47928.

[152] S. N. Joghand, *Current status of bio-based chemicals*; 2015.

[153] M. R. Shaik, M. Alam, N. M. Alandis, *J. Nanomater.* **2015**, *2015*, 1.

[154] M. Izadi, T. Shahrabi, B. Ramezanzadeh, *Appl. Surf. Sci.* **2018**, *440*, 491.

[155] C. Ngô, M. H. de Voorde, *Nanotechnology in a Nutshell: From Simple to Complex Systems*; Atlantis Press, 2014.

[156] CICECO, *CICECO creates smart coatings to protect aircrafts. http://www.ciceco.ua.pt/index.php?menu=255&language=eng&tabela=geral_article&id_article=40 Accessed 18-01-18*; 2015.

[157] nissanusa.com, 2014,.

[158] S. Jiang, A. Van Dyk, A. Maurice, J. Bohling, D. Fasano, S. Brownell, *Chem. Soc. Rev.* **2017**, *46*, 3792.

Chapter 2

Biomass Derived Corrosion Inhibitors and Coatings for Aluminium Alloys – Role of *Azadirachta indica* Extract Phytochemicals
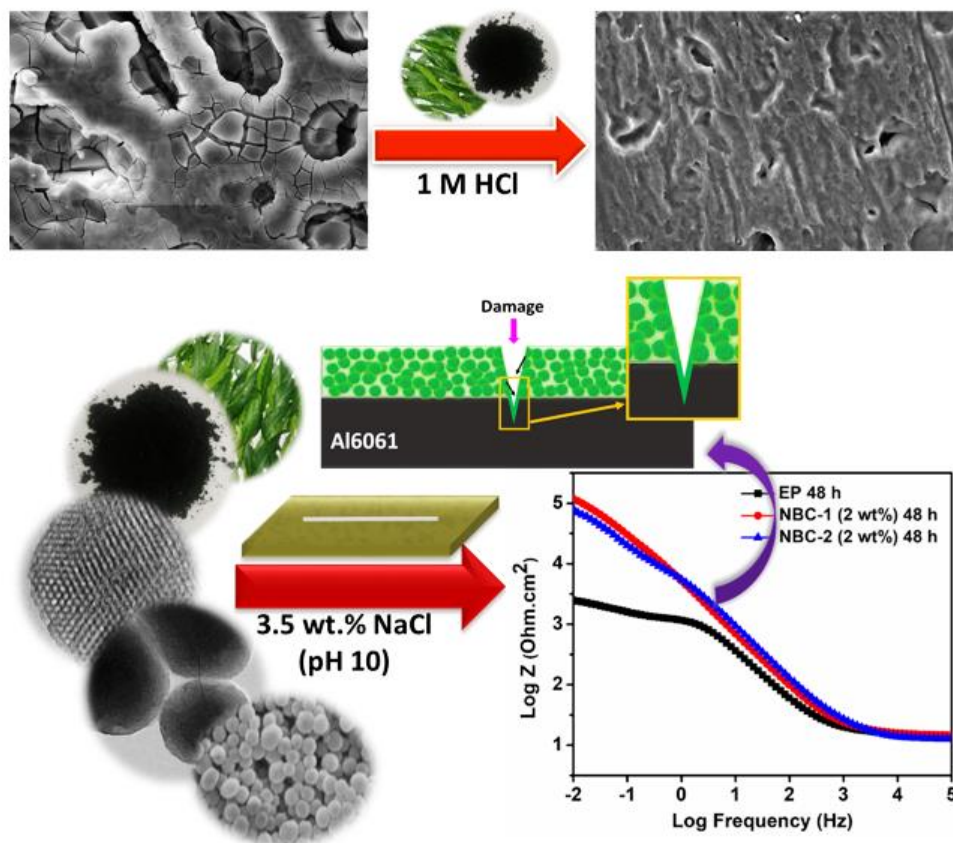
Abstract

This study describes the effectiveness of the ethanolic extract of neem (Azadirachta indica) leaves as a corrosion inhibitor. The influence of surface pretreatments (degreasing and etching) on the corrosion behaviour of aluminium alloy 6061 and their interaction with the inhibiting biomolecules were evaluated in 1 M HCl. Subsequently, the neem leaves extract (NLE) loaded mesoporous silica nanoparticles yielded a bionanocomposite for fabricating smart active hybrid coatings. The loading in mesoporous silica nanoparticles was achieved using two different solvents: ethanol and

hexane. The solvents influenced the amount of the natural product inhibitor loaded in the silica nanoparticles. The organic compounds in the crude neem extract host hydroxyl, carboxylic, carbonyl, aromatic groups etc., which participated in the interaction with the silica nanocontainers and the coating matrix. With 2.0 wt.% of the bionanocomposite in the coating and monitoring the corrosion process around artificial scratches, pH-dependent self-healing effects were observed in 3.5 wt.% NaCl. This was attributed to the response of the smart coatings to external triggers releasing NLE biomolecules to control corrosion propagation in the damaged coatings. The anticorrosive performance of the inhibitor and coatings were evaluated with electrochemical techniques. The bio-based inhibitor provided corrosion protection for Aluminium alloy 6061 via extrinsic healing in comparison with the unmodified defective epoxy coating film. The fixed amount of the corrosion inhibitor investigated although small compared to the defect size showed active corrosion protection. The epoxy-based coatings inhibited the growth of Pseudomonas nitroreducens and Aspergillus unguis species.

2.1   Introduction

The properties of protective films on metal alloy surfaces differ according to the preparation procedures applied. Changes in morphological properties occur in corrosion inhibition processes. Non-toxic corrosion inhibitors are key requirements for green contributions in corrosion inhibition. In the 1930s, dried stems, leaves and seeds of Celandine (*Chelidonium majus*) and other plants were used in H_2SO_4 pickling baths for corrosion prevention purposes. Later on an additive, ZH-1 consisting of finely divided oil cake, a by-product formed in the phytin manufacture was developed for the control of corrosion. Then, animal proteins consisting of by-products of meat and milk industries were interestingly utilized for retarding acid corrosion.[1] In 2017, a survey reported by Xhanari et al. stated that amongst the natural products used as corrosion inhibitors for aluminium and its alloys in the last two decades, about 68% of the green corrosion inhibitors were obtained from plant extracts while the remaining 32% was shared between drugs, gums, natural oils, and other products.[2]

In order to achieve effective adsorption of corrosion inhibitors on the metal substrates, the pretreatment step is a key factor. Pretreatment removes impurities,

conditions the surface for optimum adhesion of the inhibiting film, and ensures uniformity throughout the entire treated surface of the substrate. This provides a matte finished surface with higher surface energy between the metal surface and organic layer and is expected to facilitate the achievement of better corrosion protection. The structural, mechanical, and chemical characteristics of the adsorbed layers formed are hinged on the electronic structure of the inhibitor, nature of the metal surface and environmental conditions etc.[3,4] Several studies have been conducted on the corrosion of steel in chloride media in the presence of natural product-based corrosion inhibitors.[5–7]

However, the effect of surface preparation has not yet been systematically investigated. As the aluminium alloy surface is altered by changing the surface preparation method, one may expect an impact of the surface reactivity towards inhibiting compounds. In the 6xxx series, Al6061 is of relevance in this work. It is known to contain Al-Mg-Si with proven strength, suitable for varying applications in marine, aerospace and industrial sectors.[6] The passivity typically related to aluminium comes from the highly adherent amphoteric oxide film of Al_2O_3 on its surface. In aqueous environments, this protective oxide becomes thicker due to the presence of oxygen and it will continue to re-passivate if defects occur. However, this is known to yield to corrosion in the presence of chloride ions (Cl^-), or when the concentration of the aggressive environment is high exposing the substrate to series of electrochemical reactions as it dissolves giving rise to uniform, pitting and sometimes galvanic corrosion.[5,6,8] Therefore, protecting them is without a doubt, a necessity for their efficiency and durability.

The most significant challenge in bio-composite coating fabrication is to finally obtain bio-composites with superior performance, by precise and notable management of the individual properties of their components. The cost-effectiveness, non-toxicity, biocompatibility and biodegradability characteristics of natural products coupled with the mechanical and thermal properties of the inorganic components bridge the gap between functional and structural/reinforcing materials, introducing synergism into the final product. When mesoporous silica (MS) is modified with

organic compounds, the organic groups become integral parts of the framework. The organic groups implanted in the pore walls is readily achieved through functionalization as a post-treatment.[9] The nature of the container and its response to the external stimulations greatly influence the required protective action of the coating.[10] The inhibitor storage containers in nanometer are more advantageous than in the microscale as uniform dispersion in the coating is not a challenge[11,12]

The neem plant, amongst its other outstanding functionalities such as being an effective therapeutic source,[13,14] insecticide/pesticide,[15,16] and antimicrobial activities[17,18] has shown great efficiency in the area of corrosion protection of metals.[19–23] The neem plant contains several chemical compounds responsible for its various activities.[24–26]

In the area of coatings for metal protection, Toliwal and Patel investigated modified neem oil as a curing agent for acrylic copolymer resin as an anticorrosive coating for the protection of mild steel and tin panels.[27] Chaudhari et al. synthesized neem oil fatty amides based polyurethanes coatings for protecting mild steel plates[28] Also polyurethane from neem oil polyesteramides for self-healing anticorrosive coatings for mild steel panels based on polyurea microcapsules loaded with linseed oil.[29] Marathe et al. investigated Neem acetylated polyester polyol as a renewable source-based smart polyurethane coating containing quinoline as corrosion inhibitor encapsulated in polyurea microcapsules for protection of mild steel panels in 0.5 M HCl and 3.5 wt. % NaCl solutions.[30] But there is a gap concerning the loading of neem compounds in porous silica nanostructures for corrosion inhibiting purposes.

With these considerations, it is observed that the neem oil is mostly utilized for coating purposes. This work describes the use of the neem leaves extracts to design corrosion protecting bionanocomposite coatings. In this study, the inhibitive property of neem leaves extract was integrated with the excellent delivery and biocompatible attribute of MS to build an interesting composite (inhibitor delivery) system, which provided active corrosion inhibition influenced by pH changes on defective coatings. Prior to the evaluation of the coatings, the influence of the ethanolic extracts of Neem leaves as a corrosion inhibitor (referred to as NLE hereafter) on the surface chemistry

of different pretreated aluminum alloy 6061 surfaces in 1M HCl solution will be investigated.

2.2   Materials and methods

2.2.1   Materials

Cetyltrimethylammonium bromide (CTAB) were purchased from SD Fine Chemicals, Mumbai, India and tetraethyl orthosilicate (TEOS) reagent grade 98% from Sigma Aldrich, Germany. Ethanol 95% available in our laboratory and 99.9% purchased from Changshu Hongsheng Fine Chemicals Co., Ltd, and HCl 36% (Avantor Performance Materials India Ltd). NaOH pellets purified (SD Fine Chemicals, Mumbai, India), n-Hexane (SD Fine Chemicals, Mumbai, India), 1-Butanol anhydrous 99.8% (Signa-Aldrich, USA) and NaCl was purchased from Merck Specialties Private Limited, Mumbai, India. Ultrapure water of 18.2 MΩ·cm resistivity at 25°C (Evoqua water technologies, Inexus Biotech Pvt. Ltd. India) and distilled water was used in the study. Diglycidyl ether of bisphenol A (DGEBA) with molecular weight 340.42 g/mole was purchased from Thermofisher scientific, India and commercially available hardener, HY951 was obtained from Vantico, India.

2.2.2   Methods

2.2.2.1 Bio-inhibitor Extraction

Fresh neem leaves collected from within the institute (CSIR-NIIST) were washed thoroughly with distilled water and dried under shade for about two weeks. The dried leaves were crushed using a mechanical blender and 50 g was taken and the crude vegetal extract was obtained using absolute ethanol (500 mL) under magnetic stirring for 24 h at room temperature. The extract was filtered thrice with Whatman No. 1 filter paper and the solvent was removed using a rotovap, oven-dried at 60°C and stored in an airtight analytical container at 4°C prior to its use.

2.2.2.2 Substrate preparation and surface pretreatment

Aluminium alloy 6061 of the same composition described elsewhere [31] was used as the working electrode in the study. The test specimens were cut and polished with different grades of emery papers up to 1000 grit size. The surface pretreatment methods were carried out by applying reported procedures.[32,33] The surfaces were

prepared by three methods (a-c); the samples after polishing and degreasing will be referred to as "degreased" and the samples after polishing, degreasing and chemical etching will be denoted "etched-1" and "etched-2" respectively. A brief description is as follows:

a.   *Degreased:* Degreasing by ultra-sonication in acetone twice for 10 min each. Washing thoroughly with distilled water thereafter dry in a warm air oven at 60°C.

b.   *Etched-1:* After degreasing with acetone, ultra-sonicate in 0.1 M NaOH at room temperature for 5 min. Rinse ultrasonically in de-ionized water twice for 5 min to stop the reaction of NaOH with aluminum and then dry for more than 16 h in an oven at 60 °C to remove any excess water. This is an alkaline etching procedure.

c.   *Etched-2:* After degreasing with acetone, alkaline etch for 60 seconds and rinse, acid etch or dismutting for 60 seconds and rinse thoroughly with distilled water. Dry in oven at 60°C. To avoid prolonged exposure to the atmosphere, the specimens were tested immediately after the drying process.

Immersion test was carried out by immersing freshly pretreated aluminium alloy 6061 specimens of the dimension 35 x 15 x 2 mm in aggressive solutions of I M HCl and 3.5 wt.% NaCl solutions. Crevice corrosion was avoided by suspending samples in the solution using a plastic string. The nature of corrosion products on sample coupons was determined after 72 h exposure to test solutions. When taken out of the test solutions, the coupons were dried and the products scraped off lightly for further analysis. Only 1 M HCl solution was used for the bio-inhibitor evaluation in the study of the differently pretreated aluminium alloys.

2.2.2.3 Synthesis of mesoporous silica nanoparticles (MS)

Mesoporous silica nanocontainers were prepared following a published procedure[34] with slight modification. The surfactant cetyltrimethylammonium bromide (CTAB) was utilized as the template in alkaline conditions. That is, 1.0 g of CTAB was dissolved in 480 mL of deionized water and 3.5 mL of 2.0 M NaOH was introduced into the CTAB solution at room temperature under constant stirring. The temperature of the stirred mixture was raised to 80°C in an oil bath and 5.0 mL of TEOS was added drop-wise. The solution was allowed to react while stirring for 2 h at

the same temperature giving rise to a white precipitate during the process. The precipitate was washed with ethanol and deionized water and freeze-dried to obtain the free-flowing powder. The as-synthesized nanoparticles were calcined at 550°C for about 6 h to remove the template. The nanoparticles served as the nanocarriers for loading the corrosion inhibitor.

2.2.2.4 Encapsulation of neem leaves extract into mesoporous silica nanocontainers

Ethanol and n-hexane were utilized as the loading solvents. The ethanol extract of neem leaves (NLE) was dissolved in the respective solvents at 40 mg/mL following a published protocol[35] with slight modification. Hence, 0.5 g mesoporous silica nanoparticles (MS) was added into 25 mL NLE-solvent solution at room temperature. The conical flask was sealed to prevent the evaporation of the solvent and the mixture was gently stirred for 24 h in order to equilibrate the suspensions. MS adsorbed with NLE was separated from this suspension by centrifugation at 10000 rpm for 10 min and dried under vacuum at 60°C for about 16 h. Neem leaves loaded in mesoporous silica nanoparticles using ethanol as the solvent is designated as MS-NLE-E and with n-hexane as the solvent, MS-NLE-H.

2.2.2.5 Substrate and coating preparation

Polished alloy strips 40 x 25 x 3 mm in dimension was cleaned by ultrasonic decreasing in acetone for 10 min (twice), alkaline and acid etching 60 sec each, thorough rinsing and dried in a hot air oven at 60°C. The alloy strips were allowed to cool before coating. 3.5 wt.% NaCl of analytical grade was used throughout the study. The proportion of the incorporated smart nanocontainers (NLE-loaded MS) added to a known weight of epoxy (DGEBA) was fixed at 2 wt.% of the total mass of the hardener and the resin and the epoxy to hardener ratio used for the study was 2:1. Firstly, the nanocomposite was sonicated in 1-butanol for 15-20 min. This was added to the epoxy coatings (10 g) and stirred with a magnetic stirrer at 1000-1500 rpm for about 20 min for the entire mixture to be well-homogenized. Thereafter, 5 g of HY951 (diluted with 1-butanol in a 1:1 ratio) was added as the curing agent. This was further stirred and sonicated within 6 min. It is worth mentioning that stirring for a long time after addition of the curing agent will result in the curing of the coating. The pretreated

alloy substrates were dip-coated at 700 mm/min using Spectrodip Instruments dip coater (Chennai, India). After application, the freshly coated strips were left for room temperature curing process for 24 h, and post cured for 48 h at 50°C and preserved in a desiccator prior to its use. Coating samples containing the crude extract in the as-synthesized MS with ethanol as the loading solvent are designated as NBC-1 (neem-bionanocomposite-1), with hexane as the loading solvent as NBC-2 (neem-bionanocomposite-2). The unloaded epoxy coating was designated as EP.

2.2.3 Characterizations

UV-Visible spectrophotometer model UV-2401PC (SHIMADZU) was used for UV-Vis analysis from 200-800 nm wavelength. The SEM Micrographs were recorded using Zeiss EVO 18 cryo SEM Special Edition with variable pressure detector attached with EDS working at 10-30 kV after sputtering with gold/Palladium. TEM micrographs were recorded using JEOL 2010 transmission electron microscope operating at 300 kV. Dynamic light scattering and zeta potential measurements were performed using Anton Paar particle size analyzer, Litesizer 500, Germany. TGA/DTA was determined using STA7300 Thermal Analysis System, Hitachi, under argon atmosphere.

N_2 adsorption-desorption analysis was adopted to characterize the mesoporous structure, pore size and volume and specific surface area of MS and MS-NLE using Micromeritics, Tristar II, USA. The test temperature was 77 K and the samples were degassed at 60-80°C for 2 h before the test. The specific surface area of the sample was calculated by Brunauer-Emmett-Teller (BET) method based on the adsorption data when the relative pressure (P/P_o) was within the range of 0.02-0.50. The pore size distribution was calculated by Barrent-Joyner-Halenda (BJH) model based on the adsorption isotherm. The pore volume was calculated by the adsorption capacity at P/P_o=0.98. Polyphenols in NLE, MS-NLE-E and MS-NLE H were determined using HPLC. The analysis was performed by injecting a loop of 20 μL volume on a Prominence UFLC system (Shimadzu, Japan) containing LC-20AD system controller, Phenomenex Gemini C18 column (250 x 4.6 mm, 5 μm), a column oven (CTO-20A), and a diode array detector (SPD-M20A).

The presence of functional groups in the studied systems were determined using Perkinelmer FTIR, Model 2, Perkinelmer Singapore PTE LTD in transmittance mode. The amorphous/crystalline nature of the composites were examined by X-ray diffraction (XRD) PANalytical, Netherlands with Cu Kα radiation at 2θ range of 5-90°. Dip coating was done using Spectrodip Instruments dip coater (Chennai, India). Electrochemical impedance spectroscopy (EIS) and Potentiodynamic polarization (PP) studies were conducted with a conventional three-electrode cell using CH Instruments electrochemical workstation (CHI608E, CH Instruments Inc.). The three-electrode electrochemical system comprised of the working electrodes (test substrate), counter electrode (platinum wire), and reference electrode (saturated calomel electrode, SCE). Alloy test substrates of 1 cm^2 exposure dimensions were used for the study. Before starting the corrosion evaluation experiments on the bare aluminium alloy 6061, the electrochemical system was stabilized for 30 min to attain steady open circuit potential.

Potentiodynamic polarization curves were recorded by sweeping the electrode potential ±0.250 V away from the operating corrosion potential (E_{corr}) at 1.0 mV/s scan rate. Tafel extrapolations were used to obtain corrosion current density (i_{corr}) values. The inhibition efficiency was determined by using equation (2.1):[36,37]

$$\eta\% = \frac{i^o_{corr} - i^i_{corr}}{i^o_{corr}} \times 100 \hspace{3cm} (2.1)$$

where i^o_{corr} and i^i_{corr} are corrosion current densities without and with NLE.

EIS measurements were performed using the AC signal with an amplitude perturbation of 5 mV at OCP in the frequency range 100 kHz to 0.01 Hz. All potentials were measured against SCE. EIS spectra obtained was fitted with ZsimpWin software. Dip coating was done using Spectrodip Instruments dip coater (Chennai, India). Before the coatings analysis, the coating on one side of the sample was removed and the metal substrate functioned as the working electrode. pH of the NaCl solution were adjusted with dilute HCl or NaOH and monitored using a pH meter during the adjustments. The average thicknesses of EP, NBC-1 and NBC-2 were estimated from the cross-sectional scanning electron microscopy images after the coated samples

were vertically mounted in the acrylic polymer and polished to a mirror finished surface. All corrosion related experiments were carried out in triplicates.

2.2.4 Antimicrobial evaluation

The epoxy-based coatings were tested for both antibacterial and antifungal activities by the inhibition zone method against the test bacteria; *Pseudomonas nitroreducens* and fungus; *Aspergillus unguis* - NII 08123. The culture media (Luria Bertani Broth and LB Agar) and glasswares were autoclaved at 121°C, 15 psi for 15 min, before the bacterial culturing experiments. When cooled, a loop of *Pseudomonas nitroreducens* strain was inoculated in 100 mL Luria Bertani Broth under sterile conditions and incubated at 37°C, overnight. After the incubation and using a sterile L-rod, 100 µL of the culture was uniformly plated on the Luria Bertani Agar Petri plates. The sterilized coated samples were placed in the center of the Petri plates in contact with the culture. Bare sterilized Al6061 (uncoated) was used as the control. The plates were examined for possible clear zone formation after 24 h incubation at 37°C. The halo formation observed as the zone of inhibition was measured. The experiments were carried out in duplicates.

The fungus culture media (Potato Dextrose Agar) and glass wares were also autoclaved at 121°C, 15 psi for 15 min, and prior to the experiments. *Aspergillus unguis* - NII 08123 was cultured on Potato Dextrose Agar slants for 72 h. The sporulated culture was treated with sterile 0.85% NaCl solution to dislodge the spores to form a spore suspension according to the modified protocol of De Lira Mota[38] 75 µL of the spore suspension was uniformly plated on sterile Potato Dextrose Agar plates using sterile L-rod. The sterilized coated samples were placed in the center of the Petri plates in contact with the culture and uncoated sterilized Al6061 was used as the control. The plates were examined for possible clear zone formation after 48 h incubation at 30°C. The zone of inhibition was observed and measured. The experiment was done in duplicates.

2.3 Results and discussion

Aluminium and its alloys are popularly referred to as corrosion-resistant alloys because they rely on their passive films to gain corrosion-resisting properties. These

passive film may be formed naturally by reacting with their environment or as a result of some intentional pretreatment process to enhance the protective properties of the film by modifying the nature of existing films. The passive film forms a kinetic barrier that isolates the metal from the surrounding corrosive media controlling the rate of the reaction.[39]

Generally, when the protective film over a metallic substrate is broken down, corrosion occurs. Equations (2.2) – (2.5) explains the redox processes in electrochemical corrosion reactions in different corroding environments. Basically, anodic reactions are generally expressed as:

$$M(s) \rightarrow M^{n+} + ne^{-} \tag{2.2}$$

M represents the metal, n+ is the valency charge of n electrons. The value of n is dependent on the nature of the metal which could be either univalent or multivalent. Cathodic reactions occur in different forms. These include oxygen reduction and hydrogen evolution depending on the type of metal affected and the corrosive environment encountered. These cathodic reactions are represented as:

$$O_2 + 4H^+ + 4e^- \rightarrow 2H_2O \tag{2.3}$$

For oxygen reduction in acid solution;

$$O_2 + 2H_2O + 4e^- \rightarrow 4OH^- \tag{2.4}$$

For oxygen reduction in neutral or basic solutions;

$$2H^+ + 2e^- \rightarrow H_2(g) \tag{2.5}$$

For hydrogen evolution reactions in acid solutions.[40]

The basic anodic reaction in acidic medium is metal dissolution such that in this acidic range, Al is oxidized by forming Al^{3+} while the cathodic reaction is hydrogen reduction due to aluminium ion hydrolysis. Hence, in acidic medium, the passive continuity of the passive film is disrupted as the film becomes soluble facilitating the rapid dissolution of the alloy. Thus, in solutions containing halide ions especially chlorides as the most common, aluminium and its alloys are susceptible to pitting corrosion. This occurs because in the presence of oxygen, the metal is readily polarized to its pitting potential and since chlorides contribute to the formation of

soluble chlorinated aluminium hydroxide which interferes with the formation of a stable oxide on the metal surface.[41]

2.3.1 FTIR analysis of NLE

It is well established that FTIR spectrophotometer is a powerful tool that can be used to identify the type of bonding particularly functional group(s) present in organic compounds. The IR spectrum of NLE is presented in Fig. 2.1 and from the spectrum, it is observed that the broad band within 3300 and 3550 cm^{-1} is a superposition of N-H stretching and O-H vibrations. The stretching vibration of the methylene (CH_2) band occurred at 2920.23 and 2859.79 cm^{-1}. The band at 1735.93 cm^{-1} corresponds to C=O vibration. 1448.54 cm^{-1} for C-H bending vibration. 1236.37 and 1168.86 cm^{-1} for C-O stretching vibrations in C-O-C and O-C-C. C-O stretching vibrations of alcohols and phenols occurred at 1058.92 cm^{-1}. C-O bending vibrations of alkenes are at 952.84 cm^{-1}. C-N stretching occurs within the bands at 1563-700 cm^{-1}.
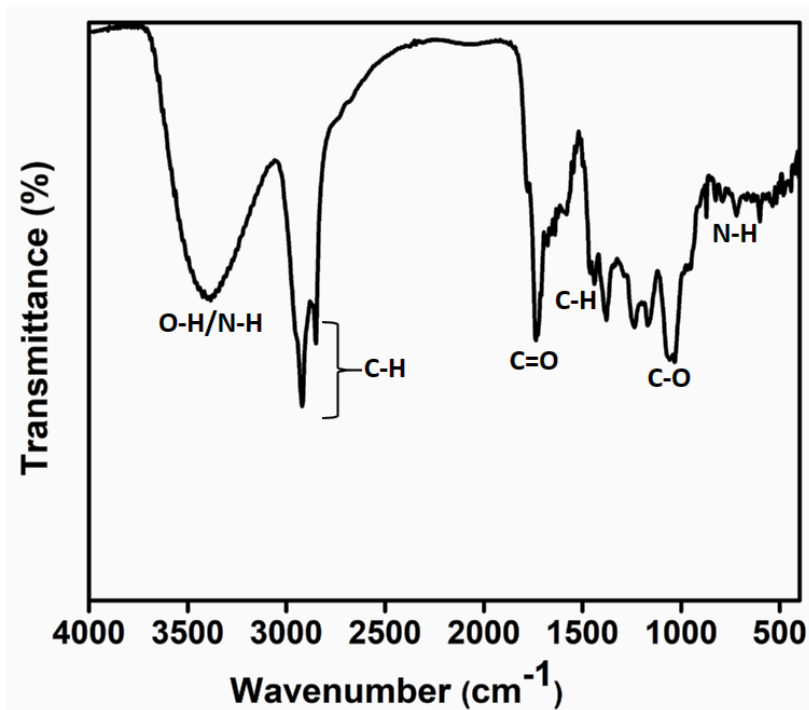
Fig. 2.1: FTIR spectrum of Neem leaves crude extract (NLE).

2.3.2 Effects of pretreatments

Surface preparation involves mechanical removal of oxides, salt contaminants, and other debris. Pretreatment is usually applied to the substrate in order to provide a

consistent surface that is free of contamination and deleterious phases. From the surface chemistry of the alloy 6061, alloying elements are added to aluminium for various reasons, for which improving mechanical properties is the principal reason. These elements introduce heterogeneity into the microstructure, which is the main cause of localized corrosion that initiates in the form of pitting. Each alloying element has a different effect on the corrosion of aluminium. Mg in 6xxx alloys, however, forms precipitates with other alloying elements to strengthen the alloy. The addition of Si in conjunction with Mg, which is typical in 6xxx series Al alloys, allows Mg_2Si particles to precipitate. This particle is beneficial in terms of increasing strength but renders the alloy prone to localized corrosion. The electrochemical behavior of Mg_2Si is more 'anodic' (less noble) than the matrix in aluminium alloys. As a consequence of this, Mg_2Si undergoes selective dissolution in the aluminium matrix.[41]

The morphology and EDS analysis of the different pretreated surfaces (a) degreased (b) etched-1 and (c) etched-2 is presented in Fig. 2.2. From SEM analysis, roughness in morphology varies with the alloy substrate preparation. The EDS analysis reveals a higher percentage of oxygen in the degreased alloy sample compared to the etched-1 and etched-2 alloy samples indicative of the presence of a thicker oxide layer in the degreased sample surface. The aggressive alkaline solution in etched-1 produces increased surface roughening and pit depths. This surface morphology occurred due to the extensive treatment time (5 min) compared to etched-2. The pretreatment involving immersion in alkaline and acidic baths is meant to reduce the heterogeneous nature of the metal surface such as removing the near-surface deformed layer (NSDL) etc.[41]
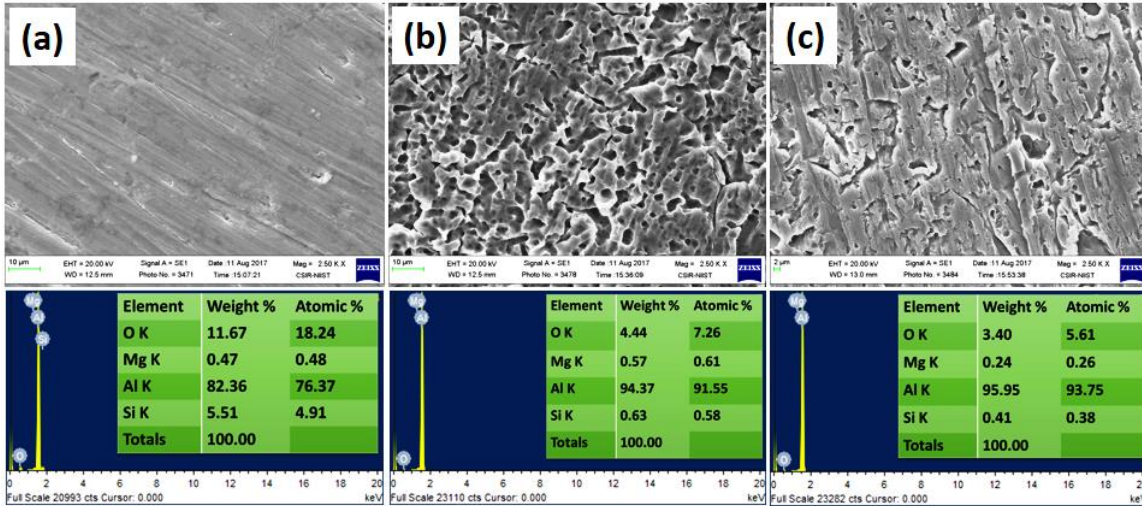
Fig. 2.2: SEM micrographs and EDS spectra of pretreated surfaces (a) degreased, (b) etched-1, (c) etched-2.

2.3.3 Surface preparation effect in chloride media

Exposing the treated aluminium alloys to the aggressive solutions results in positively charged metal ions passing from the metal into the solutions. This leaves electrons on the metal illustrated in equation (2.2). In neutral solutions, the concentration of the hydrogen ions generated is very low to allow reaction (2.5) to proceed at a significant rate, rather the electrons in the metal reacts with oxygen molecules, adsorbed on the metal surface from air dissolved in the solution, yielding hydroxyl ions as described in equation (2.4). But in acid solutions, the electrons can react with hydrogen ions, adsorbed on the metal surface from the solution, to produce hydrogen gas (equation 2.5). This continual loss of an equivalent quantity of metal ions in acidic solution leads to significant corrosion of the alloy.[40] The SEM/EDS analysis shown in Fig. 2.3, confirms the formation of more corrosion products for etched-1 in 3.5 wt.% NaCl. Also, more corrosion products for degreased in 1 M HCl. Pits are evident in the treated alloys after acid corrosion indicative of a significant loss of the metal in acid solution.
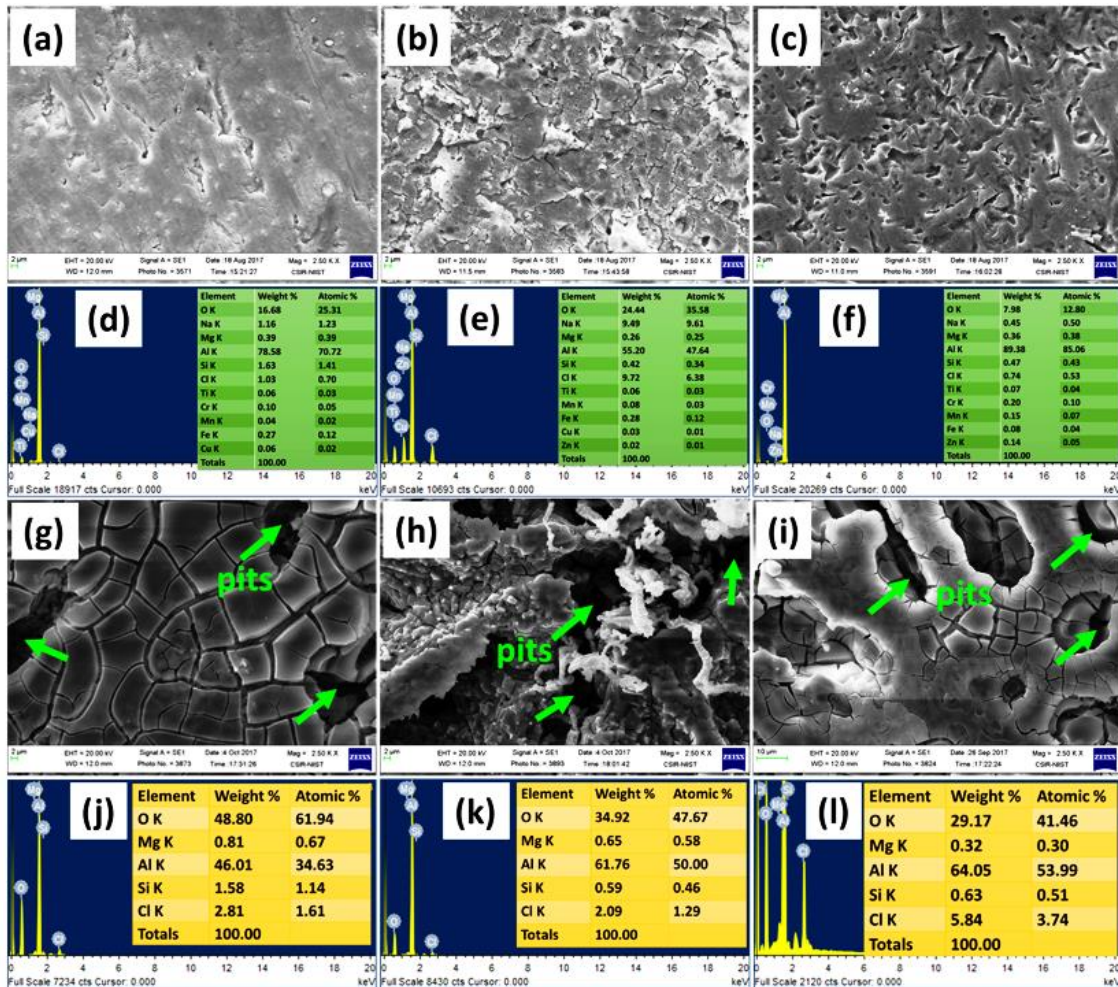
Fig. 2.3: SEM micrographs and EDS spectra of (a,d) degreased, (b,e) etched-1, (c,f) etched-2 after exposure to 3.5 wt.% NaCl and (g,j) degreased, (h,k) etched-1, (i,l) etched-2 after exposure to 1 M HCl solutions.

Fig. 2.4 presents XRD diffractogram of aluminium alloy 6061 corrosion products after exposure to (a) 3.5 wt.% NaCl and (b) 1 M HCl solutions without the corrosion inhibitor. The peaks from the crystalline nature of the corrosion products in the diffractograms were auto indexed using X'Pert Highscore plus software. In 3.5 wt.% NaCl solution as the corrosive medium, the XRD pattern of the corrosion products from the degreased surface (Fig. 4(a)) reveals the presence of the oxides $Al(OH)_3$ and AlO. The peaks at $2\theta = 18.92^\circ$, 20.41°, 27.95°, 40.72°, 56.55°, 64.16°, and 75.35° correspond to (001), (020), (021), (131), (051), (060), and (260) planes for

peaks of Aluminium hydroxide, Al(OH)$_3$ related to monoclinic crystal phase (JCPDS No. 01-074-1119), while the peaks at $2\theta = 31.79^o$, 45.54^o, and 53.31^o correspond to (200), (220) and (311) planes of Aluminium (II) oxide, AlO cubic crystal phase (JCPDS No. 01-075-0278). No phase for chloride ion-containing compounds was observed in the corrosion product. Corrosion products of Al in saline environments consists mainly of Al(OH)$_3$ which is protective in nature and its presence on the surface of the alloy impedes the penetration of the corrosive species to the surface.[42]

In 1 M HCl solution, the products were obtained after immersion in the acidic solution for 72 h. The peaks at $2\theta = 38.42^o$, 44.69^o, 65.02^o, and 78.16^o in Fig. 2.4(b) correspond to (111), (200), (220), and (311) planes for Aluminium related to cubic crystal phase (JCPDS No. 01-071-4624). This also confirms the significant loss of the alloy in the acidic solution without the presence of a corrosion inhibitor. Thus, the corrosion behavior of metals in neutral solutions differs significantly from that in acids solutions.
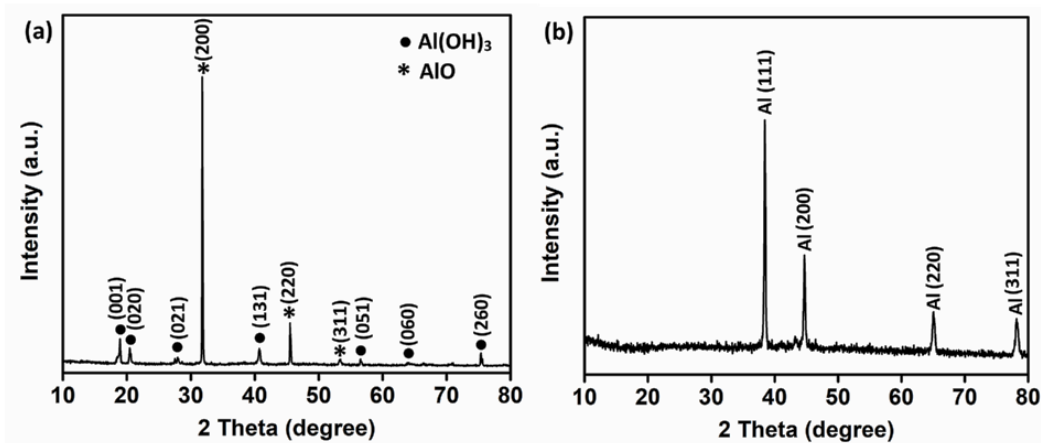
Fig. 2.4: XRD diffractograms of aluminium alloy 6061 corrosion products after 72 h immersion in (a) 3.5 wt.% NaCl and (b) 1 M HCl solution in the absence of the corrosion inhibitor.

The potentiodynamic polarization test is used to characterize the corrosion performance of metals and alloys from an instantaneous test route. This method provides vital kinetic information such as current density over a range of potentials, pitting potential (if it exists), corrosion potential, passive current density and

information in reverse scans, etc. Thus factors affecting corrosion can be evaluated with much higher confidence. Comparison of substrate behavior and dominant reactions can be made quantitatively. The anodic branch of the polarization curve gives information related to the anodic/dissolution reactions while the cathodic branch represents the reduction reactions.[43,44]

Fig. 2.5 presents the potentiodynamic polarization curves of the treated 6061 alloy surfaces in different chloride media; 3.5 wt.% NaCl (Fig. 2.5(a)) and 1 M HCl (Fig. 2.5(b)) without the inhibitor. In the NaCl medium, etched-2 exhibited greater suppression of the cathodic current observed with the I_{corr} value (1.823 x 10^{-6}) compared to the degreased I_{corr} (3.126 x 10^{-6}) and etched-1 I_{corr} (3.414 x 10^{-6}) as shown in Table 2.1. In 1 M HCl medium, etched-1 exhibited greater suppression of the cathodic current observed with the I_{corr} value (1.033 x 10^{-3}) compared to the degreased I_{corr} (1.637 x 10^{-2}) and etched-2 I_{corr} (1.392 x 10^{-2}) as shown in Table 2.2. This may be attributed to the stability of the oxide layer in the different aqueous media.
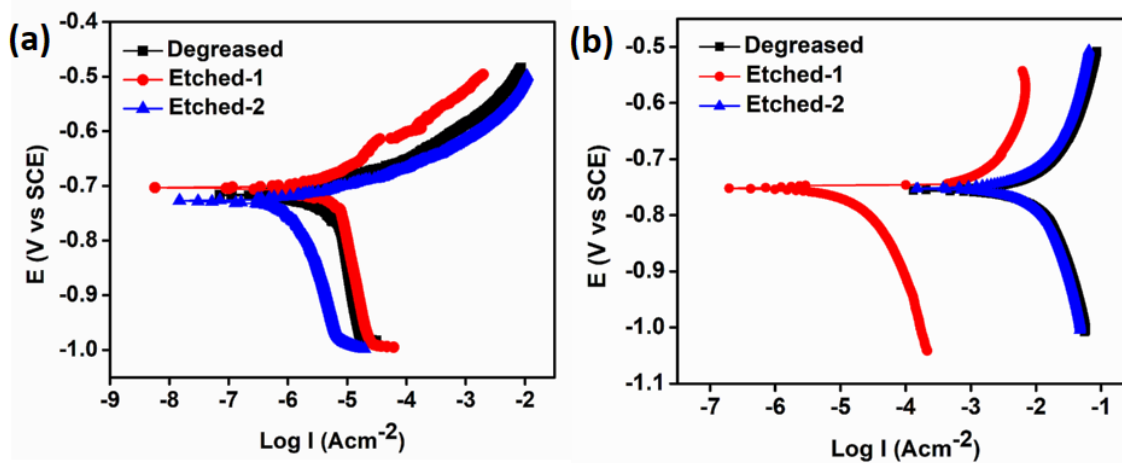
Fig. 2.5: Representative potentiodynamic polarization curves for the treated 6061 alloy in (a) 3.5 wt.% NaCl and (b) 1 M HCl.

Table 2.1: Potentiodynamic polarization parameters obtained for the differently treated 6061 aluminium alloy in 3.5 wt.% NaCl solution.

Substrates	E_{corr} (V)	I_{corr} (A cm^{-2})
Degreased	-0.717	3.126×10^{-6}
Etched-1	-0.703	3.414×10^{-6}
Etched-2	-0.727	1.823×10^{-6}

Table 2.2: Potentiodynamic polarization parameters obtained for the differently treated 6061 aluminium alloy in 1 M HCl solution.

Substrates	E_{corr} (V)	I_{corr} (A cm^{-2})
Degreased	-0.756	1.637×10^{-2}
Etched-1	-0.752	1.033×10^{-3}
Etched-2	-0.753	1.392×10^{-2}

2.3.4 Inhibitor efficiency in 1 M HCl

The presence of inhibitor molecules in the aggressive environment competes with the chloride anions as well as water molecules in getting adsorbed on the substrate surface to form a more protective film which may comprise aluminum hydroxide, oxide and salts or complexes of the corrosion inhibitor anions.[32] The corrosion inhibiting nature of plant extracts is generally accredited to the synergistic effect of different functional groups adsorbed on the metal surface, and the formation of a stable plant extract-metal complex.[45] The inhibitive characteristics of the complexes formed are derived from the adsorption potentials of their molecules. In the process, the polar groups act as the reaction centers and the resulting adsorbed film acts as a barrier separating the metal from the corrosive medium and the corresponding metal oxides formed will enhance the stability of passivation.[46,47] The inhibition efficiency depends on the mechanical, structural and chemical characteristics of the adsorption layers formed under the particular condition.[46]

Fig. 2.6 shows typical polarization curves recorded in the presence of the neem inhibitor (0.5 g/L). Table 2.3 contains the corrosion potential (E_{corr}), corrosion current

density (I_{corr}) values and inhibition efficiency (η%). The formation of a protective surface film of inhibitor on the electrode surfaces was further confirmed by SEM analysis after the exposure in inhibited HCl solution, as shown in Fig. 2.7. EDS survey spectra (Fig. 2.7) was used to assess the elements present in the alloy surface before and after exposure to the working solutions. The calculated inhibition efficiency using equation (1) gives a 99.9% inhibition in the presence of the neem extract irrespective of the treated surface.
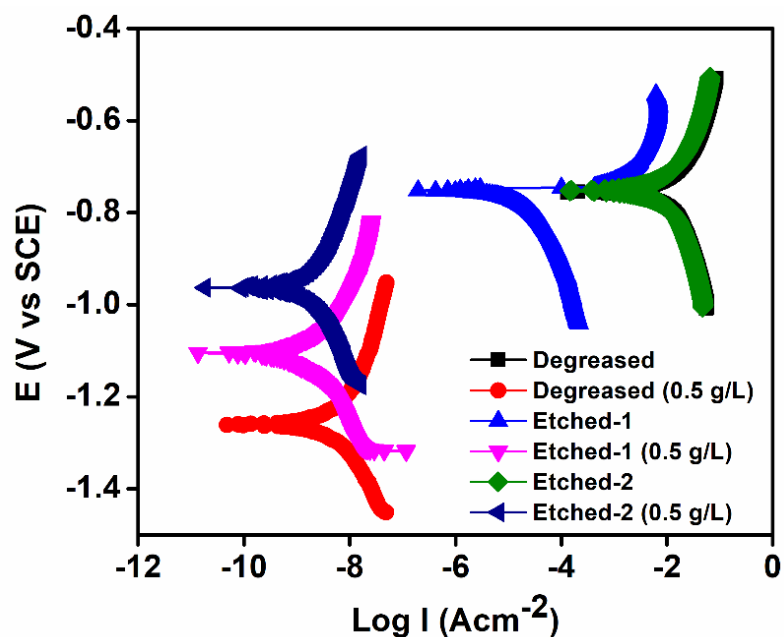
Fig. 2.6: Potentiodynamic polarization curves for the treated 6061 aluminium alloys in uninhibited and inhibited 1 M HCl.

Table 2.3: Potentiodynamic polarization parameters obtained for the differently treated 6061 aluminium alloy in 1 M HCl solution in the presence of neem extract inhibitor.

Substrates	E_{corr} (V)	I_{corr} (A cm^{-2})	η%
Degreased	-0.756	1.637×10^{-2}	-
Degreased (0.5 g/L)	-1.261	5.453×10^{-9}	99.9
Etched-1	-0.752	1.033×10^{-3}	-
Etched-1 (0.5 g/L)	-1.105	1.836×10^{-9}	99.9

Etched-2	-0.753	1.392×10^{-2}	-
Etched-2 (0.5 g/L)	-0.963	2.118×10^{-9}	99.9

(a)

(b)

(c)

10kV   X2,500   10μm   1102 NIIST SEM

2μm   EHT = 20.00 kV   Signal A = SE1   Date :26 Jul 2019   Mag = 2.50 K X   ZEISS   WD = 11.5 mm   Photo No. = 1785   Time :15:20:28   CSIR - NIIST

10kV   X2,500   10μm   1102 NIIST SEM

(d)

Element	Weight %	Atomic %
C K	13.31	21.98
N K	1.39	1.96
O K	28.26	35.03
Mg K	0.20	0.16
Al K	50.86	37.39
Si K	0.83	0.59
Cl K	5.15	2.88
Totals	100.00	

Full Scale 2120 cts Cursor: 0.000   keV

(e)

Element	Weight %	Atomic %
C K	8.73	15.81
N K	0.44	0.68
O K	19.32	26.28
Mg K	0.40	0.36
Al K	68.30	55.09
Si K	0.31	0.24
Cl K	2.51	1.54
Totals	100.00	

Full Scale 2120 cts Cursor: 0.000   keV

(f)

Element	Weight %	Atomic %
C K	7.97	14.05
N K	0.94	1.42
O K	25.64	33.90
Mg K	0.38	0.33
Al K	60.76	47.64
Si K	0.51	0.38
Cl K	3.80	2.27
Totals	100.00	

Full Scale 2120 cts Cursor: 0.000   keV

Fig. 2.7: SEM micrographs and corresponding EDS spectra of (a,d) degreased, (b,e) etched-1, (c,f) etched-2 after analysis in inhibited 1 M HCl solution.

The strength of adsorption depends on the charge on the anchoring group (atoms other than carbon including nitrogen, oxygen, sulfur etc.). The structure of the rest of the molecules influences the charge density on the anchoring group.[48] Hence water molecules initially adsorbed on the metal surface immersed in an aqueous phase is replaced by the organic molecules in the inhibitor. The EDS spectra showed signals for the existence of C and N (due to the carbon atoms and nitrogen atoms of the neem extract inhibitor). The O signal is less compared to the uninhibited samples. These show that a carbonaceous material containing these atoms covered the electrode surface which is undoubtedly due to the inhibitor. This suggests that a surface film inhibited the dissolution of the alloy and retarded hydrogen evolution reactions at cathode sites. The inhibitor surface film acts as a barrier reducing the passage of metal ions into solution (reduced the anodic dissolution reactions). Therefore, NLE acts as a cathodic type inhibitor deduced from the more negative E_{corr} values.

84

In practice, inhibitors are not often pure substances, but mixtures that may be by-products of some industrial chemical processes. While the commercial inhibitor packages may contain, in addition to the active ingredients for inhibition, other chemicals, including surfactants, de-emulsifiers, carriers (e.g., solvents) and biocides. With the presence of heteroatoms in the active ingredients of organic inhibitors, anchoring onto the metal surface is possible. These functional groups are attached to a parent chain, which increases the ability of the inhibitor molecule to cover a large surface area. Common repeating units of the parent chain are usually methyl and phenyl groups. Furthermore, the backbone may contain additional molecules, or substituent groups, which enhances the electronic bonding strength of the anchoring group on the metal resulting in enhanced surface coverage. The presence of electron-donating substituents increases inhibition by increasing the electron density of the anchoring group while electron-withdrawing, substituents decrease inhibition by decreasing the electron density. The percentage of inhibition is a function of substituents present in the corrosion inhibitor molecule(s).[49]

2.3.5 Effect of solvent in loading NLE onto MS

The preferred method for the extraction of plant constituents in its concentrated form is through alcohol extraction and the yield obtained is usually 50 times more concentrated than the yield obtained through water extraction. Most active ingredients present in plants have very high solubility in alcoholic solvents and less solubility in water.[16] To evaluate the feasibility of MS to load the hydrophobic NLE, different solvents ethanol and hexane were chosen. The polarity parameters of ethanol and hexane are different. Ethanol is polar and hexane is non-polar. Hence, the polarity parameter increases with increase in solubility parameter. The corrosion inhibitor loading capacity increased with the decrease of the solvent polarity. MS-NLE-H had the highest inhibitor loading content observed from the decrease in the surface area measurement (Fig. 2.12(b)) as well as the higher percentage of carbon in the EDS analysis (Fig. 2.11(f)) which will be discussed in sections 2.3.7 and 2.3.8. Most likely because the less polar solvent did not compete with the highly hydrophobic compounds in NLE to adsorb onto MS, hence inhibitor loading content was

significantly increased. However, when ethanol is used as the solvent, there is a direct competition of the alcohol molecules with the silanol groups resulting in lesser loading and a loss in the functionalization process[50]

The main interaction between the neem leaves extract and the silica surface is thought to be from hydrogen bonding between the carboxylic acid groups of the neem extract with surface silanol groups of the hydrophilic silica nanoparticles. The silanol groups act as the anchoring points for the organic functionalization[51,52] In ethanol, hydrogen bonds are possible at different points within the system allowing for more interaction within the solvent. With hexane, the intermolecular attractions are entirely due to dispersion forces there is no dipole interactions and no hydrogen bonding contribution.

HPLC analysis (Fig. 2.8) provided identification of the following compounds from 10 mg/mL ethanolic extract in comparison with 13 available standards[53] LC LabSolutions software was used for data acquisition and analysis. Eleven polyphenols were identified in the ethanolic extract of neem leaves. These are; (1) Chlorogenic acid, (2) Caffeic acid, (3) Syringic acid, (4) *P*-coumaric acid, (5) Ferulic acid, (6) Ellagic acid, (7) Myercetin, (8) Cinnamic acid, (9) Quercetin, (10) Kaemferol, (11) Apigenin at the following retention times 23.066, 25.107, 26.918, 28.052, 28.809, 31.135, 31.625, 33.901, 34.554, 37.143, 39.809 respectively. According to Pandey et al.[26] β-sitosterol, lupeol, rutin, ellagic acid, quercetin, and ferulic acid have been identified from the ethanol extract of the neem leaves, and this is in support with our findings. Phytochemicals present in ethanolic extract of neem leaves are known to consist of flavonoids, phenols and tannins, saponins, alkaloids, glycosides, proteins, triterpenoids, and carbohydrates etc.[25,26] The polyphenols present in MS-NLE-E include: (2) Caffeic acid, (3) Syringic acid, (4) P-coumaric acid, (5) Ferulic acid, (6) Ellagic acid, (7) Myercetin, (8) Cinnamic acid, (9) Quercetin while those present in MS-NLE-H include: (1) Chlorogenic acid, (2) Caffeic acid, (3) Syringic acid, (4) P-coumaric acid, (5) Ferulic acid, (6) Ellagic acid, (7) Myercetin, (8) Cinnamic acid, and (9) Quercetin.
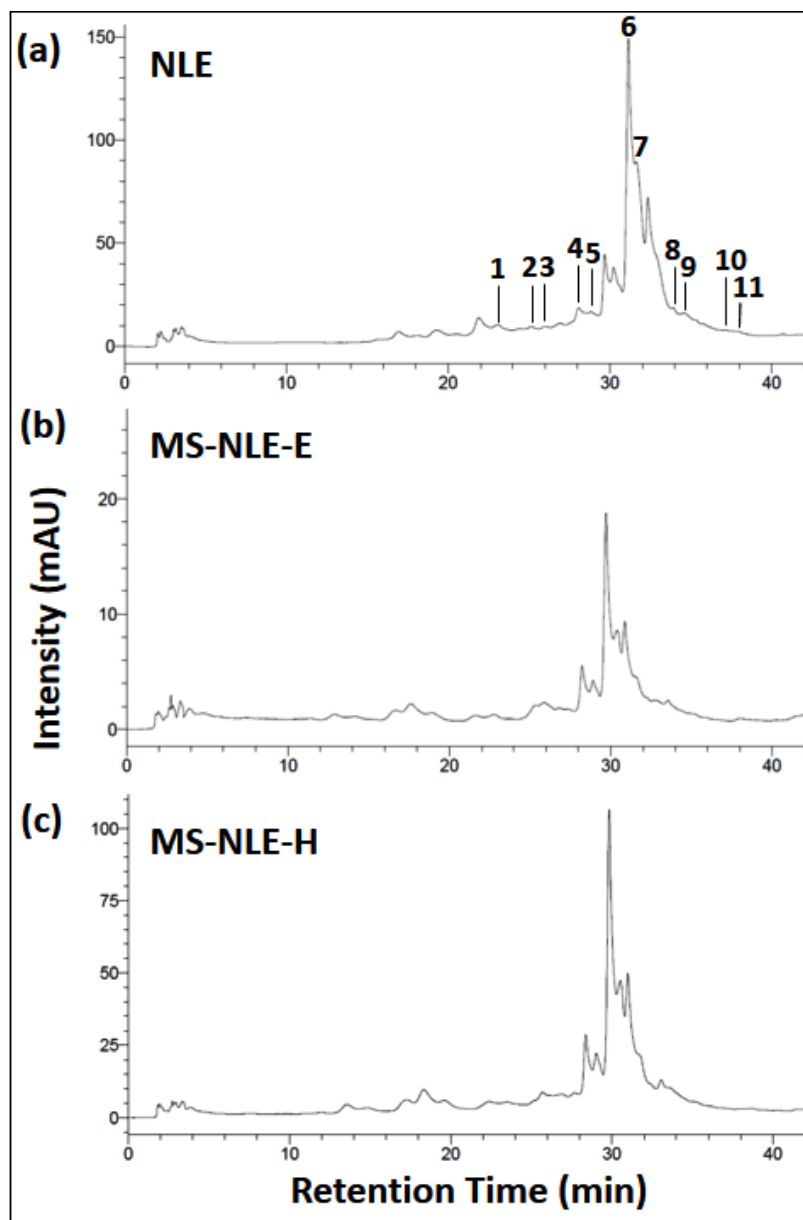
Fig. 2.8: HPLC chromatogram of (a) NLE, (b) MS-NLE-E, and (c) MS-NLE-H. The numbers represents the identified polyphenols mentioned in the text at the various retention times.

2.3.6 UV-Visible analysis of the bionanocomposites

Neem leaves crude extract was successfully loaded onto MS by mixing the MS with a 2:1 ratio of NLE:MS. Firstly, 1.0 g NLE was dissolved in 25 mL of the solvent by sonication. Thereafter, 0.5 g MS was added while stirring and allowed to mix for 24 h

in an air-tight vial. Fig. 2.9(a) presents the UV-Vis spectra of NLE/solvent before and after the interactions with MS. A spectrum scan from 200 to 800 nm at 1 nm intervals showed that the leaf extracts and nanoccomposite absorb strongly throughout the visible and ultraviolet regions. The UV-visible spectra showed that the absorption maxima for NLE/solvent were decreased after the interaction of NLE molecules with MS. With ethanol as the solvent, there were no new absorption bands and the position of the peaks was not changed. While with hexane as the solvent, the decreased absorption intensity of NLE after the interaction with MS also confirmed the decrease of the NLE concentration in the solution as well as the successful loading and adsorption of the vegetal extract within and onto MS. A not so noticeable peak at 298 nm became evident after the loading process.
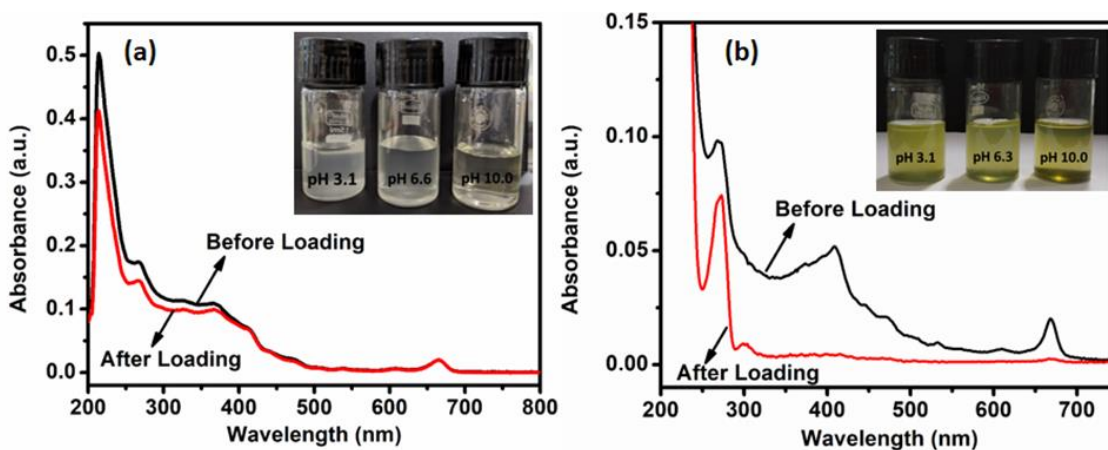
Fig. 2.9: Absorption spectra of (a) NLE/Ethanol and (b) NLE/Hexane before and after interaction with MS.

The response of NLE entrapped in MS to pH changes was determined by UV-visible analysis. 5 mg of MS-NLE was dispersed in 50 mL of 3.5 wt.% NaCl at pH values within 2.50-10.50 at room temperature. This was stirred at 350-500 rpm using a magnetic stirrer. Acidic pH was obtained by adding microliter drops of dilute HCl to the mixture while alkaline pH was obtained by adding microliter drops of dilute NaOH to the mixture. The pH adjustments were monitored with a pH meter. At time intervals of 2, 24 and 48 h an aliquot of each sample was taken, centrifuged at 5000 rpm for 5 min and 3 mL of the supernatant was used for the analysis and returned back to the

sample beakers. The gradual dissolution of MS-NLE in the aqueous medium at varying pH values were observed (not shown) from the turbidity changes of the solution from acidic to alkaline pH while stirring. The absorbance curves over time provided insight regarding the response of the bionanocomposite in different pH (Fig. 2.10).
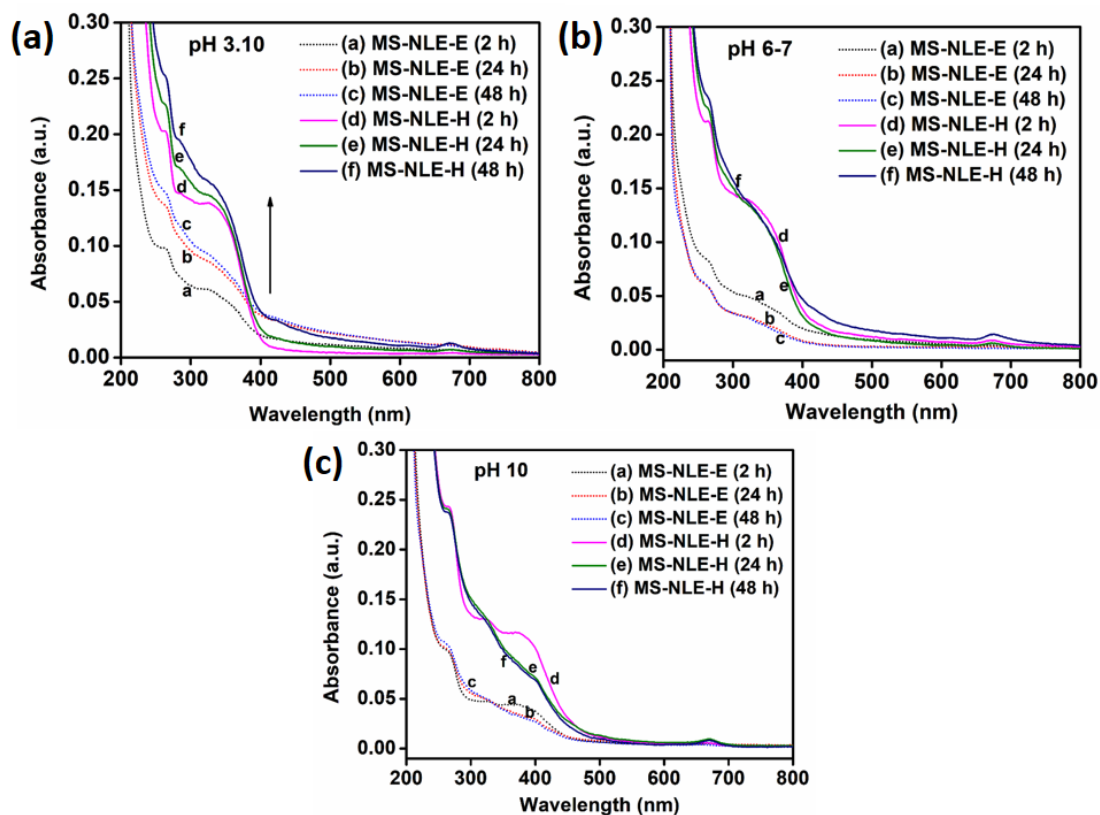
Fig. 2.10: pH response of MS-NLE-E and MS-NLE-H in 3.5 wt.% NaCl (Concentration 0.5 g/L). (a) pH 3.1, (b) pH 6-7, (c) pH 10 during 48 h.

With the passage of time and with continuous stirring turbid systems (acidic pH) gradually became less turbid exhibiting hyperchromic effects. The less turbid (near neutral and alkaline) systems became colorless. From the study, when the releasing medium had infiltrated into the pores and channels of MS nanocontainers, the inhibitor molecules (NLE) gets dissolved in the medium and diffuses through the pores along the aqueous pathways. Hence, the release of NLE through the absorbance measurements with time revealed a slower response at acidic pH and a faster response at alkaline pH. This stimuli-responsive releasing property of MS

nanocontainers loaded with NLE is shown by the dependency of inhibitor release on pH. At higher pH, the nucleophilic character of the inhibitor molecules is high. The reaction occurs between OH^- and the inhibitor molecules disrupting the existing conjugation.

2.3.7 Morphology and size analysis of the nanoparticles

The TEM micrographs in Fig. 2.11 (a-c) represents the morphologies of the studied nanoparticles in the order; mesoporous silica nanoparticles (MS), neem extract loaded MS using ethanol as the solvent (MS-NLE-E) and neem extract loaded MS using hexane as the solvent (MS-NLE-H). The porous nature of MS allowed for the entrapment of the inhibiting molecules into the siloxane matrix. The SEM micrographs in Fig. 2.11 (d-f) represents the surface morphologies of the studied nanoparticles. The shape of the nanoparticles was not significantly altered by the presence of the loaded organic moiety but appeared to be dense. The corresponding EDS analysis reveals higher carbon percentages after loading the crude neem extract using hexane as the solvent compared to using ethanol as the solvent. The hydrodynamic sizes of the nanoparticles measured with the dynamic light scattering technique were 212.6 nm, 228.1 nm and 291.5 nm for MS, MS-NLE-E, and MS-NLE-H. The corresponding zeta potential of the nanoparticles was, -26.7 ± 1.0 mV, -12.2 ± 0.6 mV, and -36.9 ± 1.7 mV for MS, MS-NLE-E, and MS-NLE-H respectively.
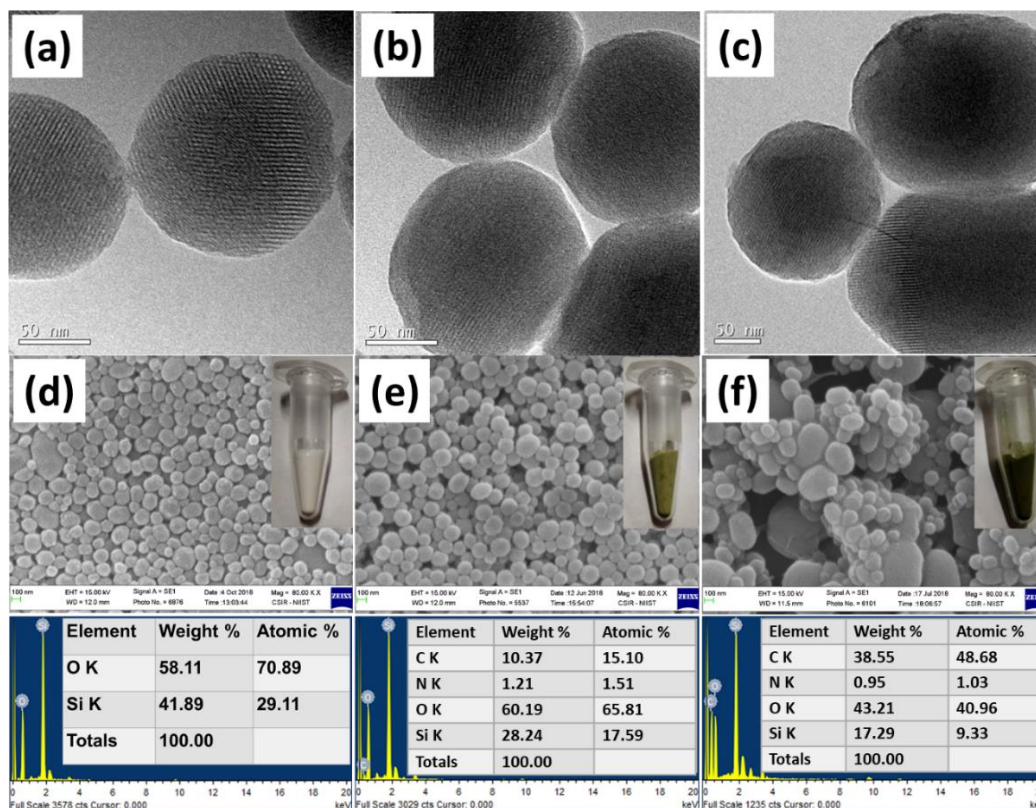
Fig. 2.11: TEM micrographs of (a) MS (b) MS-NLE-E and (c) MS-NLE-H. SEM micrographs/EDS analysis of (a) MS, (b) MS-NLE-E, and (c) MS-NLE-H.

2.3.8 TG analysis

The amount of natural organic inhibitor loaded into the mesoporous material and its thermal stability were determined through this technique under inert conditions. Fig. 2.12(a) shows the TGA curves of the studied samples within the temperature range of 25-600°C. Table 2.4 is the evaluation of percentage weight losses of the studied samples within the temperature range of 25-600°C. The weight losses occurred in distinct regions and the steps involve the thermo-desorption of physisorbed water and the decomposition of organic components which varies according to the samples. The residual masses were considered at 600°C. The decomposition of organic moieties in MS-NLE-E and MS-NLE-H between 150-600°C indicates that the biomolecules of NLE had been successfully grafted onto MS and filling its pores.

Furthermore, a lower percentage of mass loss is observed for MS-NLE-E between 150-600°C compared to MS-NLE-H at the same temperature range. This implies that for MS-NLE-E, a lesser quantity of NLE was adsorbed resulting in a slight decrease of the free hydroxyl groups present on its surface while for MS-NLE-H more NLE was adsorbed. Since hexane is a non-polar solvent, functionalization of MS with NLE in hexane promoted a non-polar silica scale and a lower percentage weight loss for MS-NLE-H at 25-150°C was observed. The decreased value of weight loss in this region (25-150°C) indicates a hydrophobic character of the material and a decrease in the effective silanol concentration[54] A slight decomposition between 150-600°C in MS is observed indicative of the presence of possible low carbon concentration. This may be due to some residual carbon of the organic template and/or adventitious environmental carbon contamination after the thermal treatment.[55]

Table 2.4: TG analysis of MS, loaded MS, and NLE.

Samples	Weight Loss (%w/w)		Residues (% w/w)
	25-150°C	150-600°C	600°C
(a) MS before calcination	7.4	41.4	51.2
(b) MS after calcination	27.0	1.5	71.5
(c) NLE	4.1	80.6	15.3
(d) MS-NLE-E	17.2	12.7	70.1
(e) MS-NLE-H	3.3	55.7	41.0

2.3.9 Nitrogen adsorption/desorption analysis

The pore volume, pore sizes and specific surface area (physical properties) of the nanoparticles were determined by N_2 adsorption-desorption technique. The N_2 sorption provides an estimate on the loading efficiency by observing a reduction in the total pore volume and the change in the porosity of the nanoparticles. A decreased

pore volume usually represents the loaded inhibitor molecules within the mesopores of the silica network.[56] The aforementioned parameters are shown in Table 2.5.

Table 2.5: N$_2$ adsorption-desorption analysis of MS and the obtained nanocomposites.

Samples	BET surface area (m^2/g)	Total pore volume at P/Po = 0.981 (cm^3/g)	Pore Diameter by BJH (nm)
MS	867.389	0.491	2.98
MS-NLE-E	351.337	0.300	4.75
MS-NLE-H	1.797	0.003	41.26*

* Significant increase in pore diameter after loading NLE with a non-polar solvent

The hysteresis loop was completely lost and surface area sharply reduced indicating the maximum filling of spaces in MS-NLE-H (Fig. 2.12(b)) and changes in the mesoporous structure characteristics when the non-polar solvent was used for loading the corrosion inhibitor into the mesoporous nanocontainer. Increase in the average pore diameter of the matrix after inhibitor loading has been reported.[34,56]
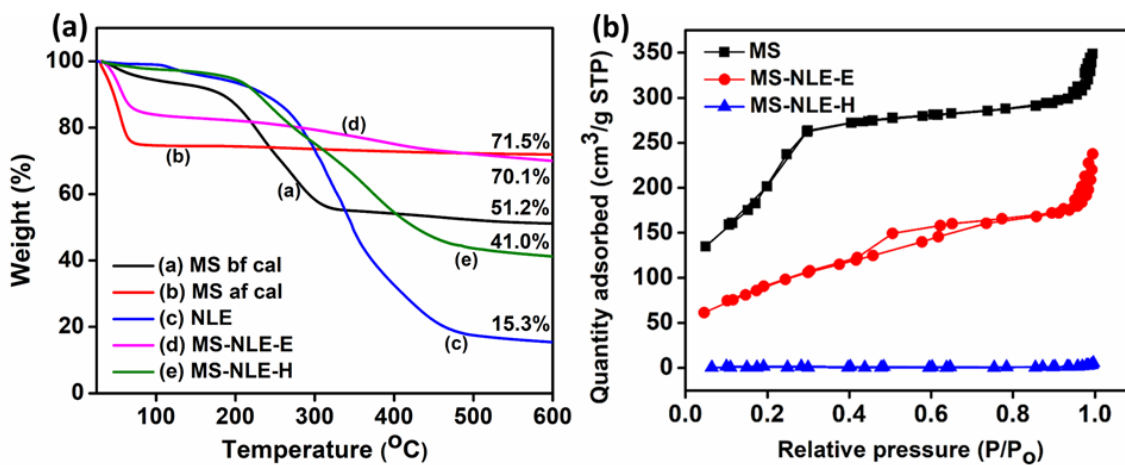
Fig. 2.12: (a) TGA curves obtained at a heating rate of 10°C/min under argon atmosphere for MS (a-b), NLE (c), MS-NLE-E (d), and MS-NLE-H (e). (b) N$_2$ adsorption-desorption isotherms of MS, MS-NLE-E, and MS-NLE-H.

2.3.10 ATR-FTIR analysis

The ATR-FTIR spectra of NLE and MS-NLE (Fig. 2.13(a)) were recorded in order to investigate possible chemical interactions between the natural product inhibitor and the mesoporous silica nanoparticles. This was achieved by identifying the functional groups present in the crude extract and nanocomposites. In Fig. 2.13(a-d), hydroxyl groups occur within 3550-3200 cm^{-1} in the spectra. While in Fig. 2.13(a-c) the bands at 1228 cm^{-1} represent Si-CH$_2$, 962 cm^{-1} for the silanol group (Si-OH), Si-O-Si shows very strong infrared bands in the region of 1130-1000 cm^{-1} and in the region of 452 cm^{-1} for Si-O rocking.[57] The band at 1630 cm^{-1} in Fig. 2.13(a-c), represents water bending vibration. It occurs due to a more hydrophilic silanol-containing surface after template depletion as well as indicative of the presence of adsorbed water. In SiO$_2$ containing materials, bands within 620 cm^{-1} and 810 cm^{-1} are regarded as useful for identifying the kind of SiO$_2$.[57]

In NLE, Fig. 2.13(d), the broad band within 3300 and 3550 cm^{-1} is a superposition of N-H stretching and O-H vibrations. The stretching vibration of the methylene (CH$_2$) band occurs at 2924 and 2854 cm^{-1}. The band at 1732 cm^{-1} is assigned to C=O vibration. 1442 cm^{-1} for C-H bending vibration. 1239 and 1153 cm^{-1} for C-O stretching vibrations in C-O-C and O-C-C band of esters at 1031 cm^{-1}. Bands within 1563-700 cm^{-1} can also be attributed to vibrations involving C-N stretching. Furthermore, N-H out of plane wagging is observed at 788 and 719 cm^{-1}. Similar bands are featured in MS-NLE-E and MS-NLE-H in combination with bands present in MS demonstrating the incorporation of NLE into MS. However, there is an additional band at 1153 cm^{-1} in MS-NLE-H.

2.3.11 XRD analysis

The broad hump, commonly called amorphous halo is an amorphous characteristic of silica nanoparticles usually centered at 23, 2θ degree[58] was observed in Fig. 2.13(b). A slight shift to 21, 2θ degrees occurred upon modification from the NLE loading step with hexane as the loading solvent (MS-NLE-H). Hexane loading retained some of the crystalline peaks of NLE in the nanocomposite while ethanol loading remained amorphous after the loading step. The amorphous halo is

also a feature in XRD of biomass extract when the compounds in the extract are not completely crystalline. This was observed at 17, 2θ degree in NLE alongside crystalline peaks at 21.60°, 28.55°, 40.66°, 50.35°, 66.52°. Similar combinations of amorphous and crystalline peaks for powdered x-rays of biomass extracts have been reported.[59] The amorphous halo in biomass and its extract is due to the presence of amorphous organic matter (e.g cellulose, hemicelluloses and lignin etc.).[60]
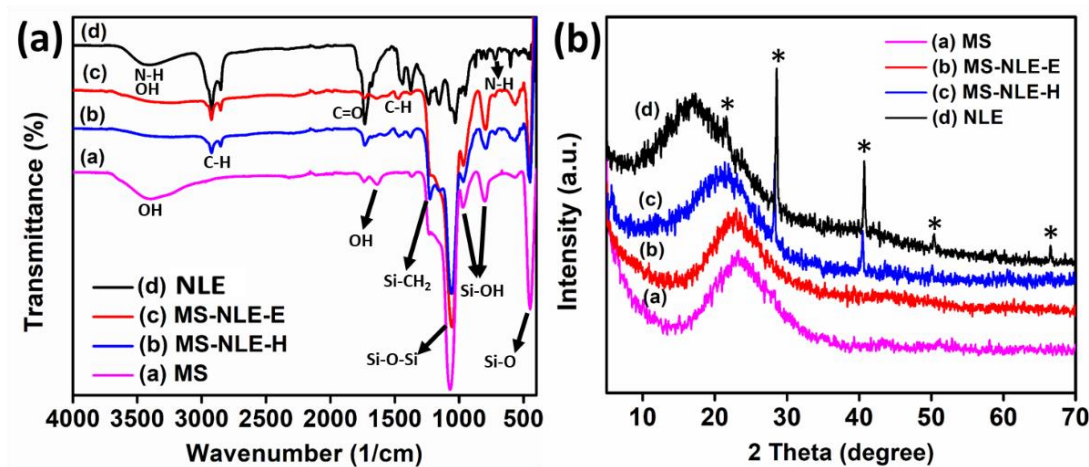
Fig. 2.13: (a) ATR-FTIR spectra of (a) MS, (b) MS-NLE-H, (c) MS-NLE-E, (d) NLE. (b) XRD spectra of MS, MS-NLE-E, MS-NLE-H, NLE.

2.3.12 Surface analysis of the bionanocomposites by XPS

The chemical composition of the modified silica surfaces after loading the corrosion inhibitor with different solvents was determined by X-ray photoelectron spectroscopy (XPS) measurements (Fig. 2.14 & 2.15). The binding energy was calibrated by referencing the C 1s peak at 284.6 eV using XPS data. The survey scan spectra of both MS-NLE-E and MS-NLE-H is presented in Fig. 2.14 confirming the presence of O, Si, and N in addition to C with the conclusion that the bio-inhibitor had been grafted onto the silica nanoparticles. Apart from giving evidence of functionalization, the identity of the functional groups is provided. Fig. 2.15(a-d) shows the deconvoluted C 1s, O 1s, Si 2p, and N 1s core-level spectra of MS-NLE-E which allowed the identification of the different species on the surface. MS-NLE-E shows a C 1s main component with binding energies at 284.77 eV and 284.37 eV corresponding to C-C of SP^2 carbon, other components at 288.38 eV assigned to the

carboxyl group in O=C-OH and 286.48 eV assigned to C-N bonds of C–NH(C=O). The energy range of adsorbed nitrogen within 398-404 eV can be related to different nitrogen configurations. The deconvolution of the N 1s core level spectra presented spectral components at a binding energy of 399.4 eV assigned to –C-NH$_2$ of aromatic amines and 400.68 eV assigned to -N-C=O of amide groups. The deconvolution of O 1s core-level spectra showed components at 534.33 eV for Si-OH, 532.89 eV for Si-O-Si and 531.09 eV for C=O. The deconvolution of Si 2p core-level spectra presented Si components at a binding energy of 104.63 for SiO$_2$, 103.47 for Si(O)$_4$ and 101.38 for Si-O respectively.

While Fig. 2.15(e-h) represents the deconvoluted C 1s, O 1s, Si 2p, and N 1s core-level spectra of MS-NLE-H. The spectral components at a binding energy of 399.82 eV are attributed to adsorbed nitrogen from –C-NH$_2$ of aromatic amines and 398.05 eV for the nitride in HN-Si-O-Si. The deconvolution of C 1s core-level spectra showed components at 284.67 and 284.44 eV for C-C of SP^2 carbon, 288.53 eV for carboxyl in O-C=O and 286.13 eV for C-N bonds of C–NH(C=O). The deconvolution of O 1s core-level spectra showed components for 532. 70 and 532.21 eV for Si-O-Si and 534.7 eV for Si-OH. The deconvolution of Si 2p core-level spectra presented Si components at binding energy of 103.1 eV and 101.20 eV for Si(O)$_4$ and Si-O respectively.
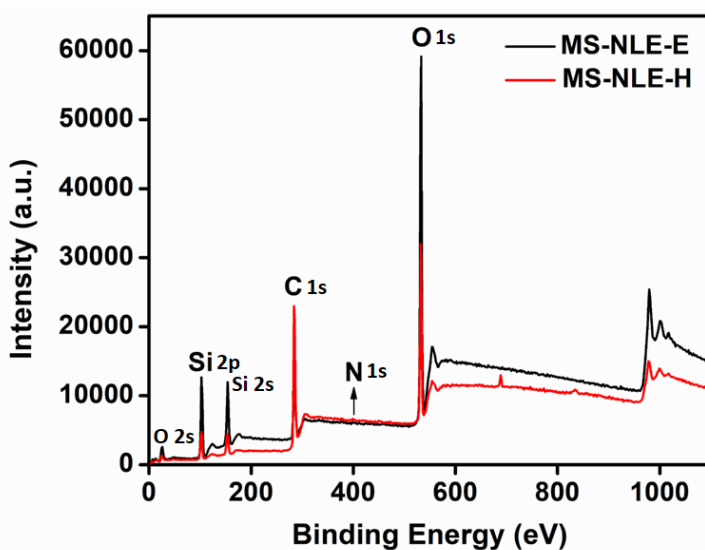
Fig. 2.14: XPS survey spectra of Neem bionanocomposites MS-NLE-E and MS-NLE-H.
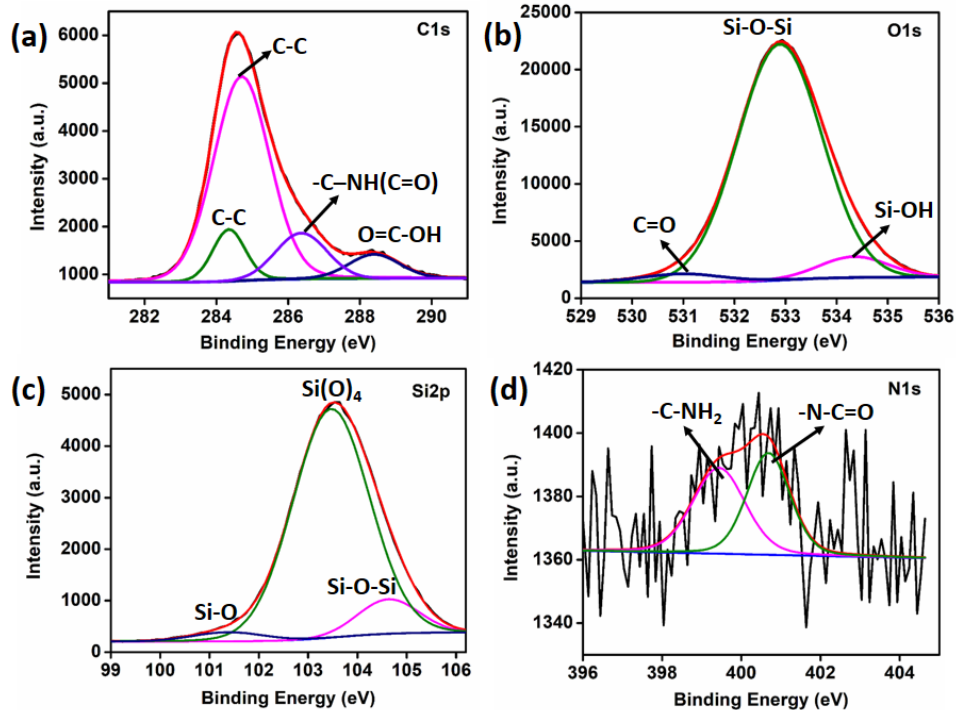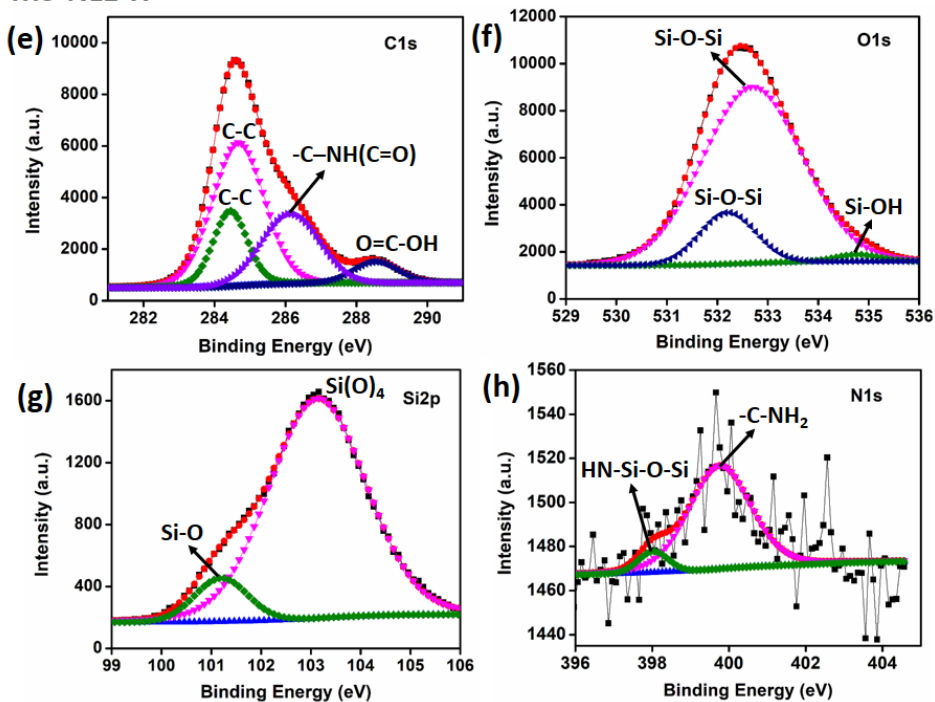
Fig. 2.15: Core level spectra of Neem bionanocomposites (a-d) MS-NLE-E and (e-h) MS-NLE-H.

2.3.13 Bionanocomposites active corrosion protection evaluation

Prior to self-healing evaluation, the nanocomposite inhibitors were evaluated for active anticorrosion performance in 3.5 wt.% NaCl solution at different pH after 15 days immersion in the absence and presence of the inhibitors. The effect of pH strongly influences the corrosion reactions and corrosion inhibition offered by the bionanocomposites through the release pattern and reactions of the bio-based inhibitor molecules in the electrolyte solution. The passive film of aluminum and its alloys is unstable in alkaline corrosive solutions, and the exposed matrix surface usually suffers a higher corrosion rate and possible active dissolution of intermetallic particles of the alloy[61] Similarly, acidic pH and high Cl- activity also destroys the passive layer formed.[62] With a slower release of the inhibitor molecules from the nanocontainers at acidic pH, (Fig. 2.10) the alloy surface remains exposed to the aggressive environment for a longer time than it experiences the protective effect of the inhibitor molecules. More attack on the alloy occurs even in the presence of the slow-released inhibitors (Fig. 2.16). As the pH of the solution increases, for neutral and alkaline solutions, the anodic dissolution reaction and the oxygen reaction at the cathode can be explained by the following reactions in equations 2.6-2.8. While the presence of the Cl- in neutral media are known to cause pitting corrosion in aluminium by the slow dissolution of the passive film, high pH promotes the formation of aluminate in the anodic reaction (equation 2.7) resulting in general corrosion:[63]

$$Al + 3OH^- \rightarrow Al(OH)_3(s) + 3e^- \qquad (2.6)$$

$$Al(OH)_3(s) + OH^-(aq) \rightarrow Al(OH)_4^-(aq) \qquad (2.7)$$

$$1/2O_2 + H_2O + 2e^- \rightarrow 2OH^- \qquad (2.8)$$
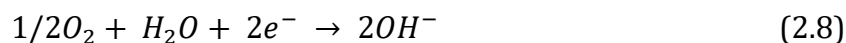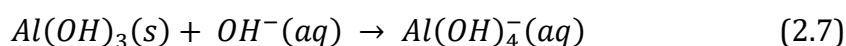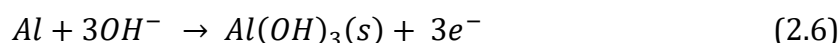
The increasing pH of the media in the presence of the inhibitor results in a fast release of the inhibitors at the initial 2 h of the reaction (Fig. 2.10) which appears to remain stable at alkaline pH. At high pH (>9) flavonoids are easily deprotonated which strongly influences the coordination to metal ions. Thus, in alkaline solution, the metal ions present in solution have a strong affinity for the deprotonated flavonoids resulting in the formation of stable complexes.[64,65] This provides an effective

corrosion protection of the electrode surface in the aggressive environments (Fig. 2.16 (f & i)).
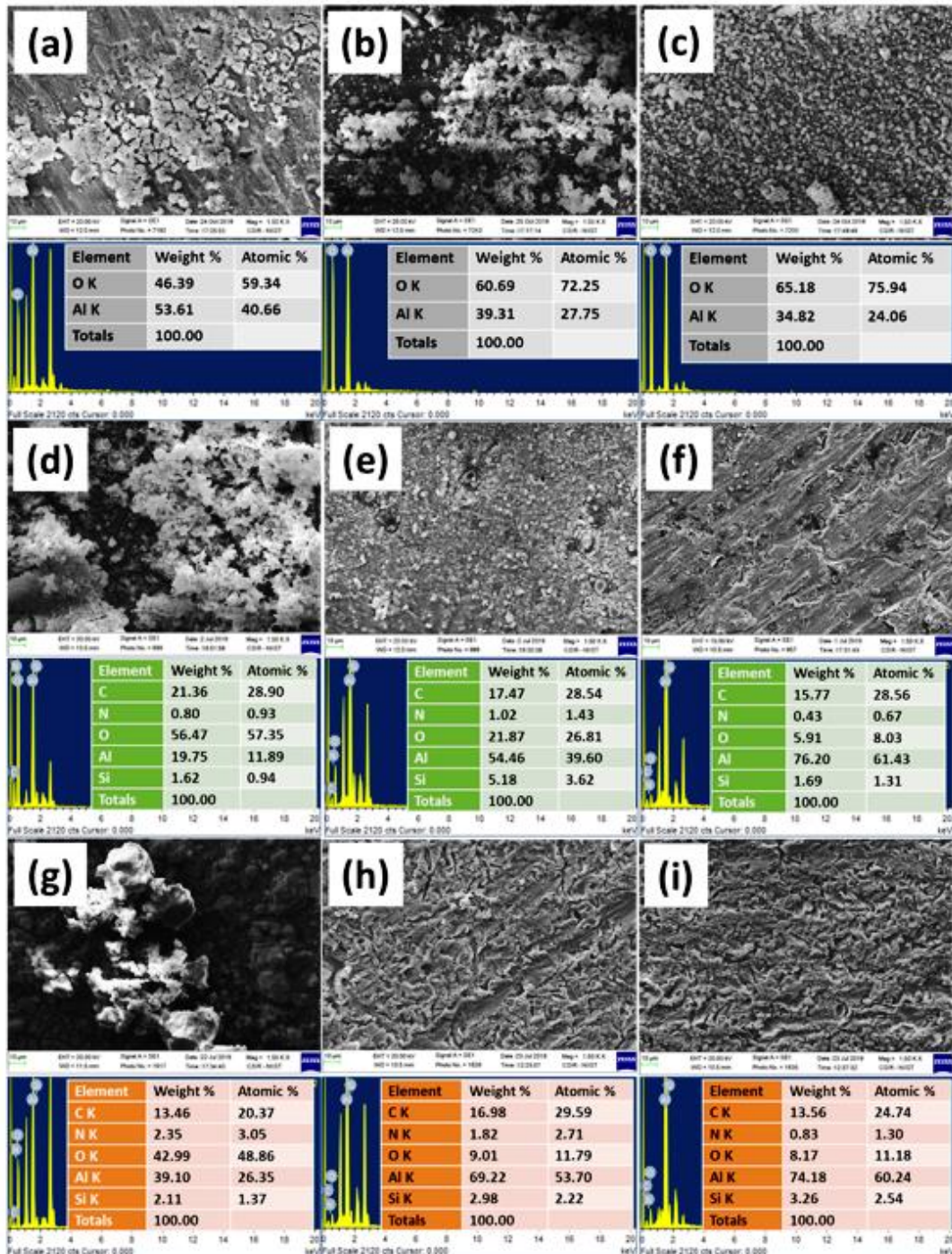
Fig. 2.16: SEM/EDS analysis of Al6061 after 15 days immersion in 3.5 wt.% NaCl at (a) pH 3.2 (b) pH 6-7, (c) pH 10 without the inhibitor. In the presence of 0.5 g/L MS-

NLE-E (d) pH 3.2 (e) pH 6-7, (f) pH 10. In the presence of 0.5 g/L MS-NLE-H (g) pH 3.2 (h) pH 6-7, (i) pH 10

2.3.14 Self-healing evaluation of the epoxy-based coatings

The average thicknesses of EP, NBC-1, and NBC-2 were similar (9.5 ± 2 μm) and estimated from the cross-sectional scanning electron microscopy images. Fig. 2.17 includes micrographs of the coated samples and their corresponding thickness measured via SEM.
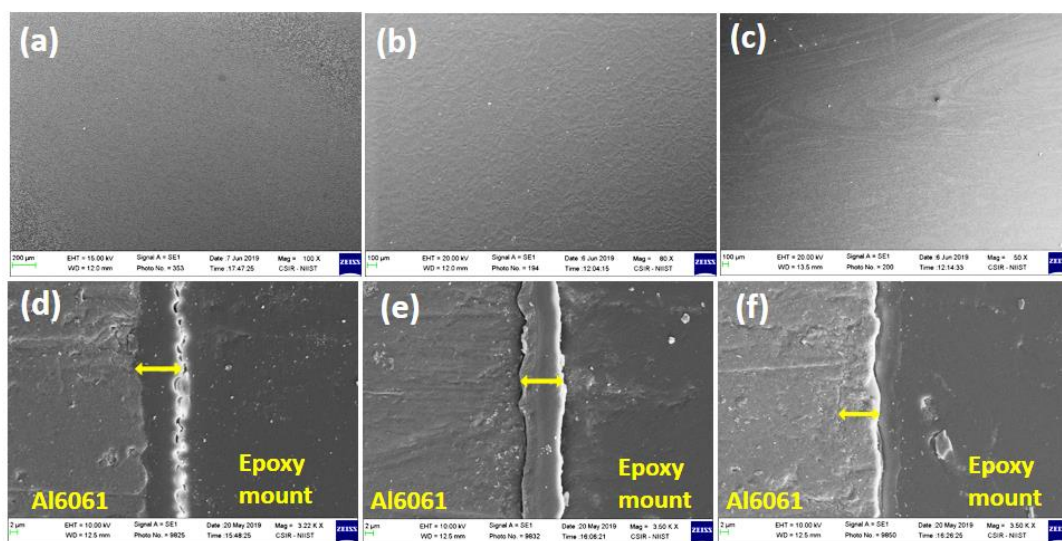
Fig. 2.17: SEM micrographs of (a) EP, (b) NBC-1, and (c) NBC-2 showing the coating surfaces and thickness (d-f) in the same order.

EIS measurement was performed to evaluate the active corrosion protection of the modified coatings in comparison with the unmodified epoxy coating. EP, NBC-1 and NBC-2 were scratched and immersed in 3.5 wt.% NaCl solutions for up to 48 h at pH 3.00, 6.49 (as prepared) and 10.00. The defect exposed the underlying alloy to the aggressive chloride environment. Fig. 2.18(a-f) represents the electrochemical impedance analysis of the scratched NBC coated Al6061 substrates after 48 h of immersion in 3.5 wt.% NaCl at different pH in comparison with the unloaded epoxy coating. Since best results of active corrosion protection and self-healing were achieved at pH 10, the impedance analysis of data obtained at pH 10 is discussed. Two

equivalent circuit models (Fig. 2.21d) were applied to appropriately analyze the impedance data and were fitted using ZSimpWin software until no further fitting improvement was achieved. The equivalent circuits both had two time constants described differently as $R_{sol}(Q_{coat}(R_{coat}(Q_{dl}R_{ct})))$ and $R_{sol}(Q_{coat}R_{coat})(Q_{dl}R_{ct})$ with a fit quality of chi-square values (χ^2) < 0.01. Interpretation of the circuit elements are as follows: R_{sol} is the solution resistance, and Q_{coat} represents the constant phase element of the scratched coating and R_{coat} the resistance of the scratch in the coating. Q_{dl} and R_{ct} corresponds to the double-layer constant phase element and charge transfer resistance, respectively. R_{coat} reflects the protective properties of the polymeric layer even in the presence of pores and cracks in the polymer-based coating. In the neem modified coatings, the values of the coating resistance is two orders of magnitude higher than the unmodified coating. The higher R_{coat} values of the modified coatings reflects the inhibiting property of the coating and the reduction in corrosion in the defects during the exposure time. R_{ct} values reflects the kinetics involved in the electrochemical reaction at the interfaces. Being scratched coatings, R_{ct} reveals the active corrosion inhibition occurrence within the scratched portion in the presence of the inhibitors. When R_{ct} values are high it implies slow electrochemical reactions occurred at the electrode surface which further implies corrosion inhibition at the exposed electrode surface in response to the presence and reactions of the released inhibitor molecules. The fitted values obtained from the equivalent circuits in Table 2.6 reveals R_{ct} values in the order EP<NBC-2<NBC-1 after 48 h immersion in the alkaline chloride solution.
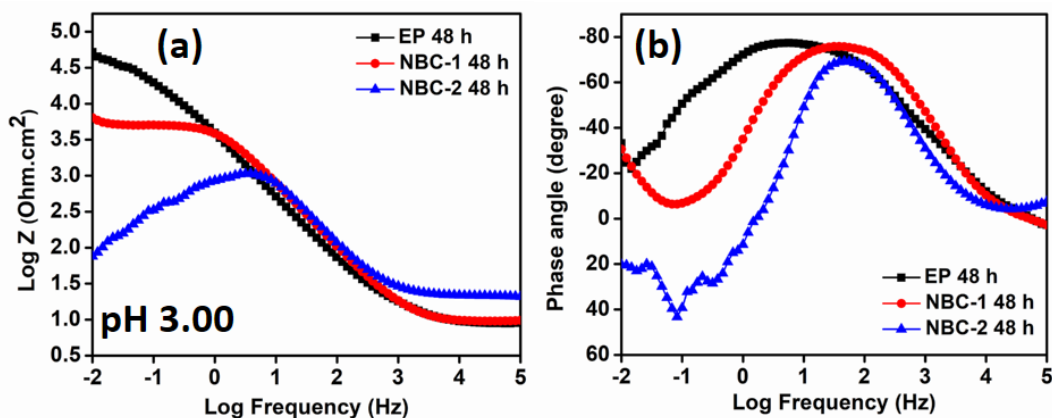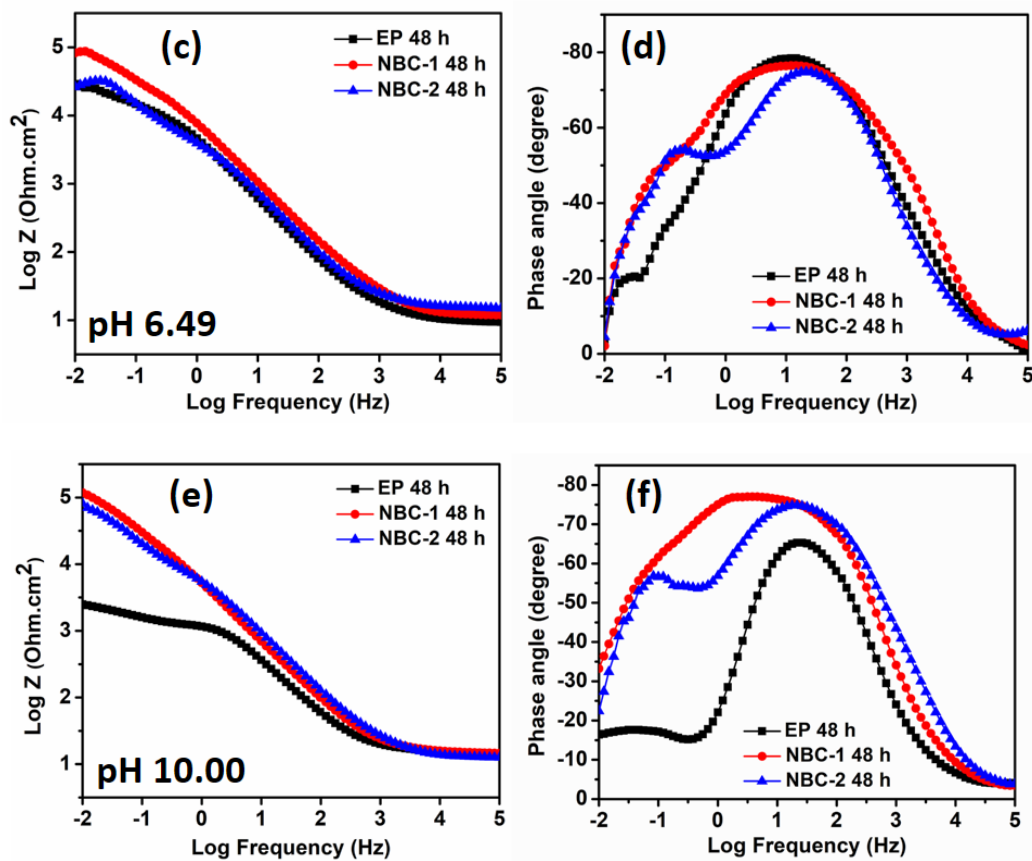
Fig. 2.18: (a-f) Bode and phase angle plots of scratched NBCs coated Al6061 substrates after 48 h of immersion in 3.5 wt.% NaCl at different pH in comparison with the unloaded epoxy coating.

Table 2.6: Impedance data from equivalent circuits (EC) for the scratched EP, NBC-1, and NBC-2 coatings after 48 h of immersion in 3.5 wt.% NaCl solution at pH 10.00.

EC Parameters	EP	NBC-1	NBC-2
R_{sol} (Ω cm^2)	15.38	15.36	12.77
Q_{coat} (S.sec^n)	7.666 x10^{-5}	5.301 x10^{-5}	6.752 x10^{-5}
n (0<n<1)	0.84	0.84	0.78
R_{coat} (Ω cm^2)	1408	168900	108500
Q_{dl} (S.sec^n)	3.663 x10^{-3}	1.464 x10^{-4}	4.703 x10^{-5}
n (0<n<1)	0.82	1	1
R_{ct} (Ω cm^2)	1647	5384	2633
χ^2	2.458 x10^{-3}	1.400 x10^{-3}	1.892 x10^{-3}

From the SEM analysis (Fig. 2.19) the width of the scratched portions decreased with immersion time in comparison to the unmodified epoxy coating. While from the EDS analysis the elemental distribution within the scratched portion, revealed chloride and oxygen-rich corrosion products, with the presence of Na and Al in greater proportions on the exposed surface of the unloaded epoxy coating compared to the EDS of the products in the presence of the released inhibitors. In the loaded coatings defect, reduced signals for Al, O, Na and Cl were observed with strong signals for C from the layer formed on the exposed metal surface within the scratch which correlates with protection originating from the inhibiting components of the modified coatings. The schematic of the active corrosion inhibition coatings containing the encapsulated biomass extract via pH-responsive self-healing is shown in Fig. 2.20. The resultant evolution modulus of impedance |Z| at 0.01 Hz for EP and NBC coatings for the study duration is represented in Fig. 2.21(a-c). The impedance at the lowest frequency (|Z|0.01 Hz) reflects the corrosion resistance of the coatings.[66,67] For the modified coatings there is an initial decline at 24 h in impedance modulus at the lowest frequency (|Z|0.01 Hz) and a subsequent increase up to 48 h. The time-dependent plots (Bode, phase angle and Nyquist) at pH 10 is presented in Fig. 2.22. [66,67]
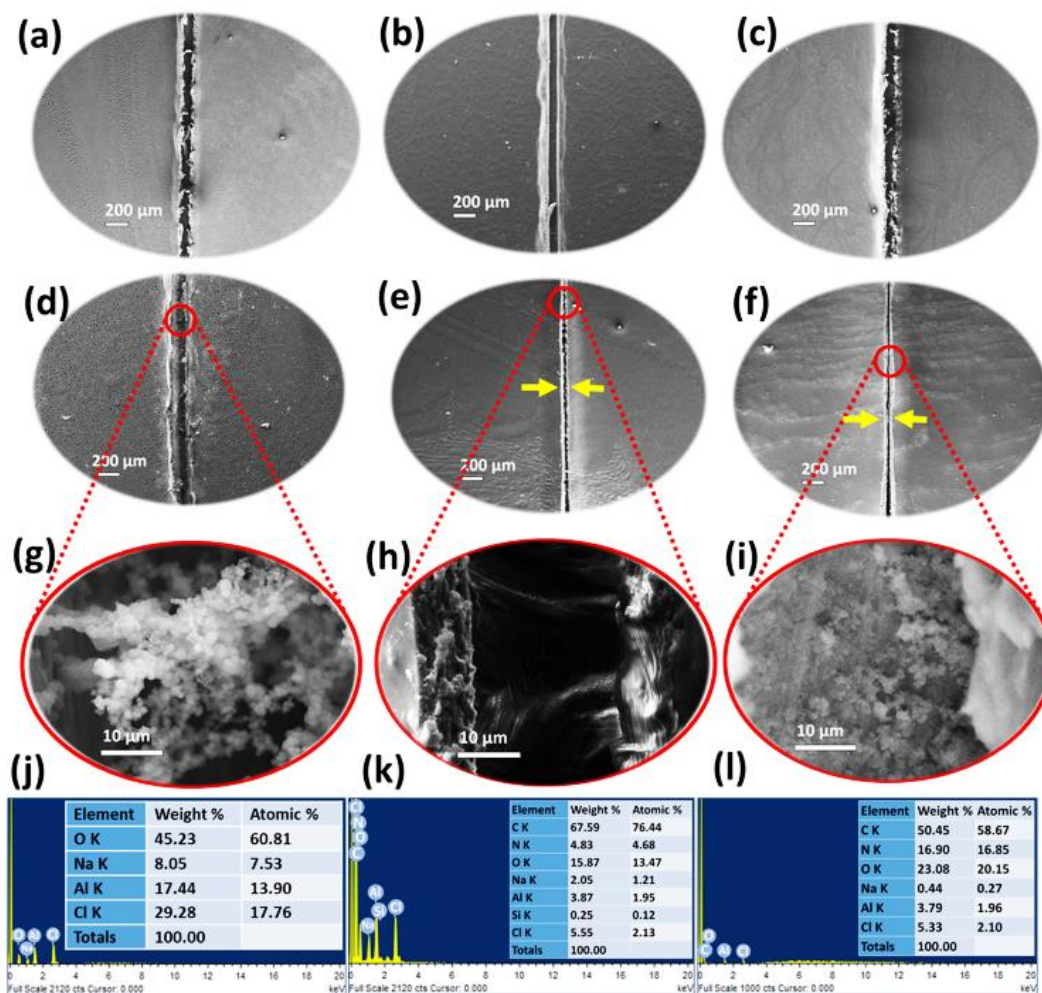
Fig. 2.19: SEM micrographs of the scratched studied coatings before (a-c) and after (d-f) 48 h immersion in the alkaline chloride media. (g) Corrosion product in the absence of the inhibitors. NBC-1 (h) and NBC-2 (i) protective layers showing the active corrosion protection via self-healing from the leached inhibitor in the scratched portion of the coatings. (j-l) corresponding EDS in the absence and presence of the inhibitors.
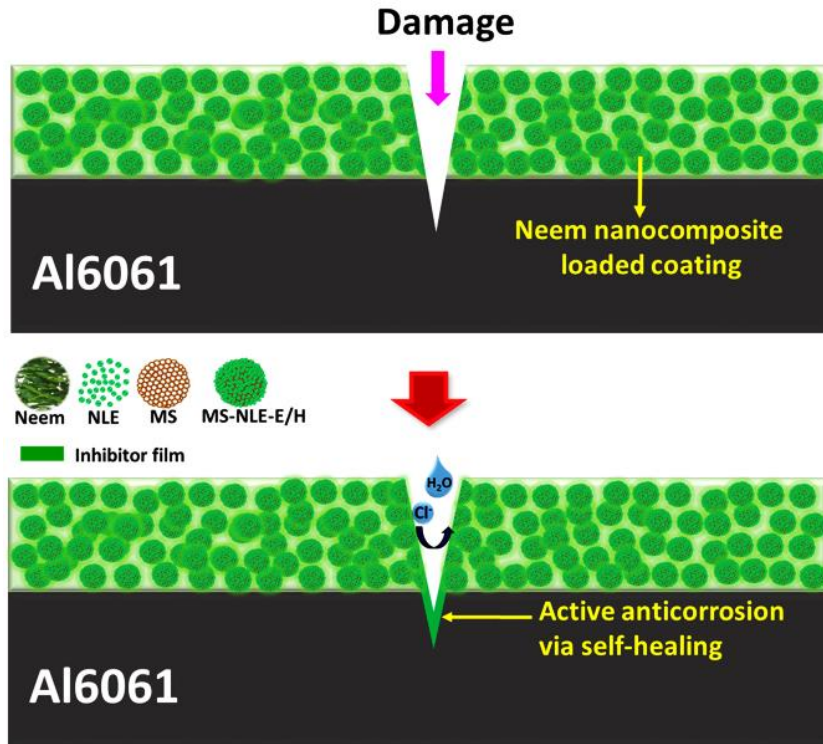
Fig. 2.20: Schematic of pH-responsive self-healing from the neem nanocomposite coatings.
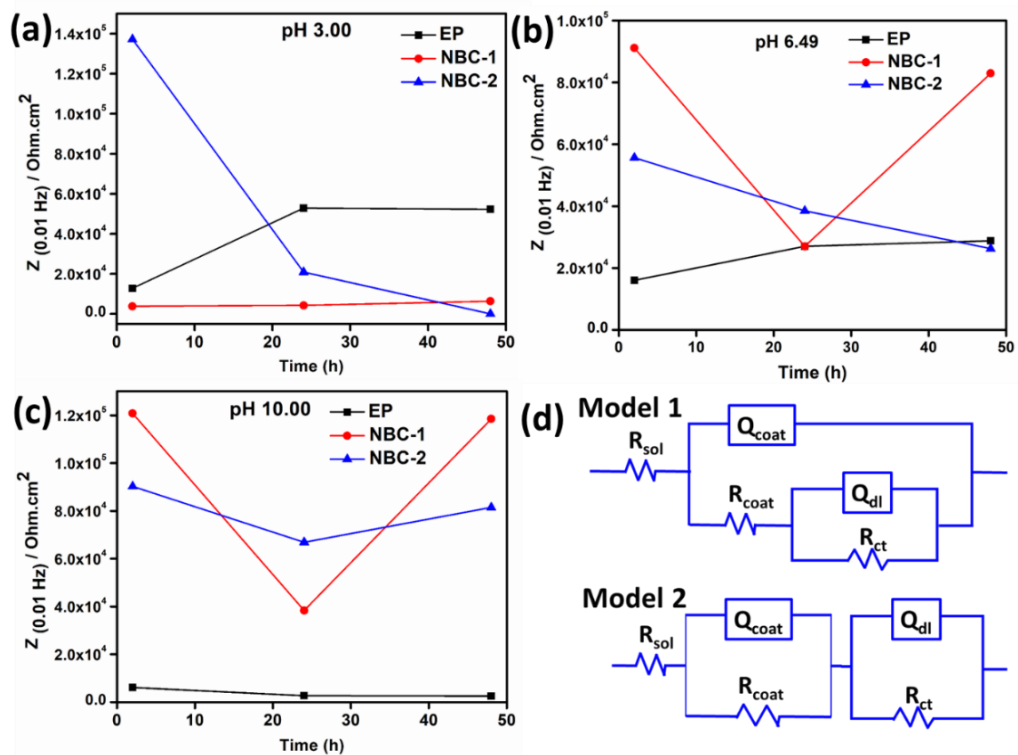
Fig. 2.21: (a-c) Evolution modulus of impedance |Z| at 0.01 Hz for NBC coatings; all scratched surfaces during 2-48 h immersion time at different pH. (d) Equivalent circuits used to fit the impedance data.
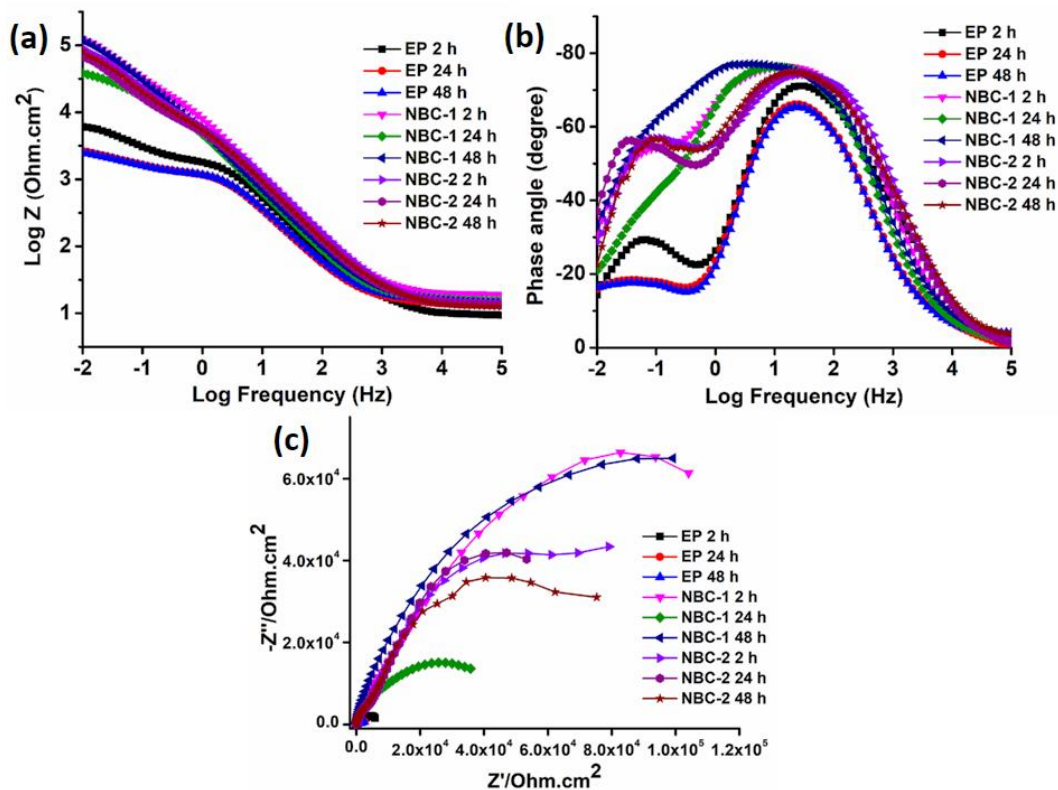
Fig. 2.22: (a) Bode (b) phase angle and (c) Nyquist plots of scratched NBCs coated Al6061 substrates between 2-48 h of immersion in 3.5 wt.% NaCl at pH 10 in comparison with the unloaded epoxy coating.

The polarization curves for the scratched coatings evaluated at different pH are presented in Fig. 2.23. The corresponding fitted parameters such as corrosion current densities (I_{corr}), and corrosion potential (E_{corr}) are presented in Tables 2.7-2.9. A decrease in I_{corr} is known to correspond to a decrease in corrosion rate. At pH 3.00 a poor performance in the modified defective coating is observed due to the slow release of the biomolecules at acidic pH but as the pH increases to pH 10.00, a remarkable decrease in I_{corr} values from 16.860 to 0.126 ($\mu A\ cm^{-2}$) occurs. This enhancement in anticorrosion capability is due to the release and adsorption of the active embedded components of the modified coatings offering better corrosion

resistance at the alkaline pH compared to the degrading natural oxide film formed in the scratched portion of the unmodified coating.
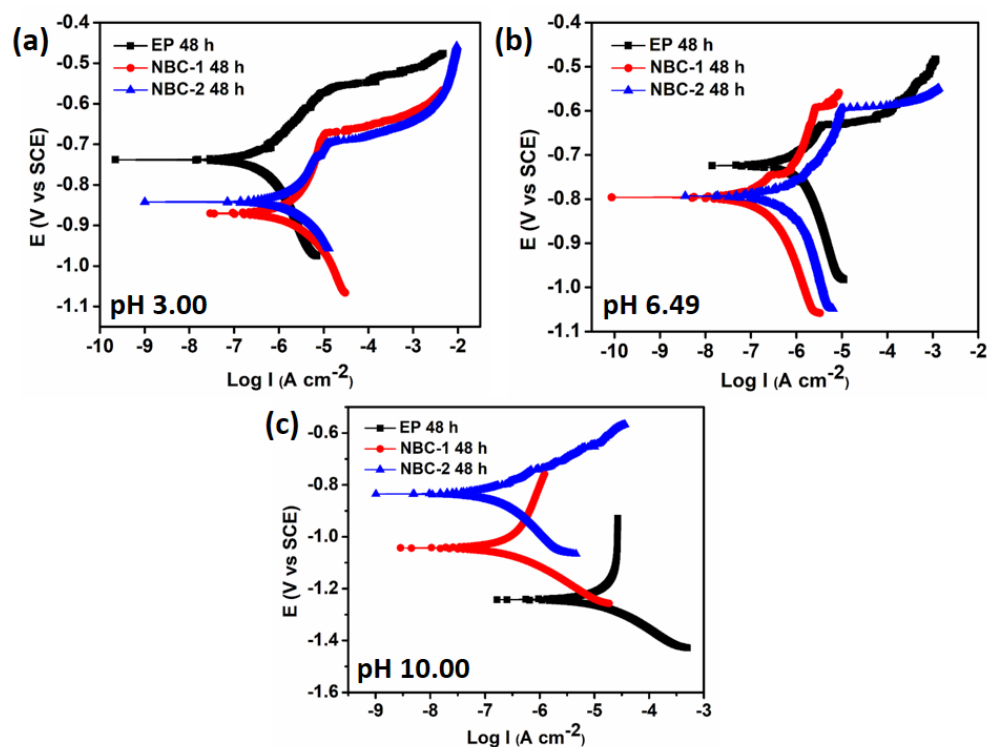
Fig. 2.23: Potentiodynamic Polarization curves of scratched epoxy-neem coated (EP, NBC-1, NBC-2) Al6061 substrates after 48 h of immersion in 3.5 wt.% NaCl at different pH (a) 3.00, (b) 6.49, (c) 10.00).

Table 2.7: Potentiodynamic polarization parameters obtained on the artificially scratched coatings after 48 h of immersion in 3.5 wt.% NaCl solution (pH 3.00).

Scratched coatings in 3.5 wt.% NaCl pH 3.00 after 48 h	E_{corr} (mV)	I_{corr} (μA cm^{-2})
EP	-738	0.466
NBC-1	-870	2.504
NBC-2	-842	2.398

Table 2.8: Potentiodynamic polarization parameters obtained on the artificially scratched coatings after 48 h of immersion in 3.5 wt.% NaCl solution (pH 6.49).

Scratched coatings in 3.5 wt.% NaCl pH 6.49 after 48 h	E_{corr} (mV)	I_{corr} (μA cm^{-2})
EP	-724	0.522
NBC-1	-796	0.217
NBC-2	-793	0.691

Table 2.9: Potentiodynamic polarization parameters obtained on the artificially scratched coatings after 48 h of immersion in 3.5 wt.% NaCl solution (pH 10.00).

Scratched coatings in 3.5 wt.% NaCl pH 6.49 after 48 h	E_{corr} (mV)	I_{corr} (μA cm^{-2})
EP	-1242	16.860
NBC-1	-1043	0.297
NBC-2	-835	0.126

2.3.15 Antimicrobial activity of the epoxy-based coatings

For qualitative assessment of antimicrobial activity, the antimicrobial activity of the prepared epoxy-based coatings was examined against the bacteria strain, *Pseudomonas nitroreducens* and fungi strain, *Aspergillus unguis* (NII-08123) using inhibition zone method. Neem extract has been reported to exhibit antibacterial and antifungal activity by *in vitro* and *in vivo* experiments due to the presence of compounds like azadirachtin, desactylimpin, quercetin, sitosterol, nimbin, nimbinin, nimbidin, nimbosterol and margisine, desactylimbin, triterpenes or the limonoids such as meliantriol[17] Other compounds reported to be antimicrobial in nature from the organic extracts of neem leaves include, Azadiradione, nimonol and epoxy azadradione.[18] The biological activity of active compounds in the neem plant covers a wide range of established functions aside from the antifungal and antibacterial activities.[68]

The capability of the loaded epoxy-based coatings on aluminium alloy 6061 substrates to inhibit microbial adhesion/propagation was investigated and the inhibition zones around the samples placed on the agar inoculated with the microbes as shown in Fig. 2.24 were measured. The antibacterial action of the synthesized coatings was observed after 24 h of incubation. In NBC-2 dual zones of bacterial inhibition were observed. The antibacterial action of the unmodified epoxy coating is due to the nature of the solvents used in the coating formulation while the increased diameter in the presence of neem extract loaded coatings reveals the that the additional action is most likely from the neem-based additives.

The antifungal action of the synthesized coatings was observed after 48 h of incubation and a gradual change in conidia pigmentation from green to slight yellow was seen. The areas of slight yellow pigmentation (changes in mycelial sporulation) were much larger than the clear zones measured. This may be due to a response against abiotic stress and limiting growth conditions.[69] All the epoxy coated samples showed antimicrobial activity against the microbes as shown in Fig. 2.24. Average values for zones of inhibition were between 25-39 mm (Table 2.10) and the bare alloy became the control sample which showed no zone of inhibition. The inhibitory effect is a probable synergy of the entire components of the coatings.

P. nitroreducens (bacteria) investigation after 24 h
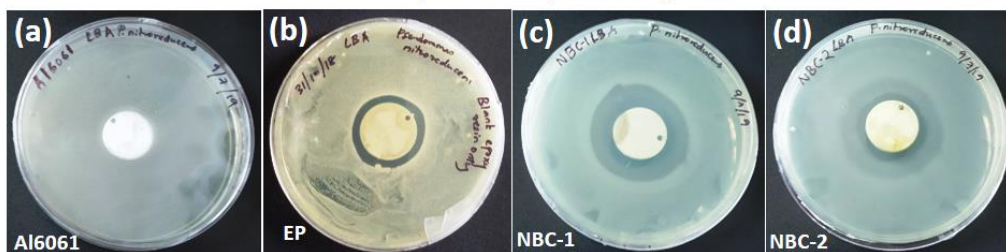
A. unguis (fungi) investigation after 48 h
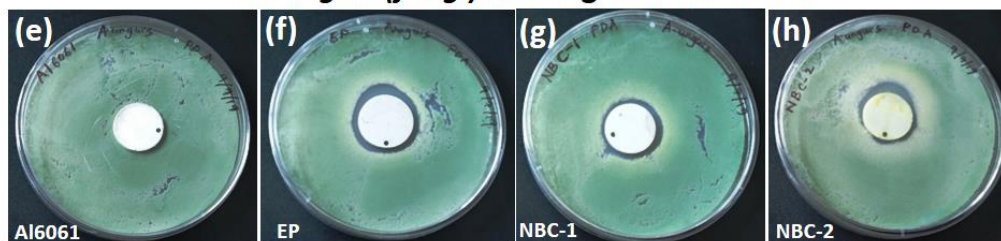
❖ **Mycelial pigmentation observed**

Fig. 2.24: Antimicrobial action of the studied substrates against *Pseudomonas nitroreducens* colony on LBA agar (a) Control - bare Al6061, (b) unloaded epoxy coated Al6061, (c) NBC-1, (d) NBC-2 and *Aspergillus unguis* (NII-08123) colony on PDA agar (e) Control - bare Al6061, (f) unloaded epoxy coated Al6061, (g) NBC-1, (h) NBC-2.

Table 2.10: Zone of inhibition for epoxy-neem coatings.

Microbes	Inhibition zone (mm)			
	Bare Al6061	EP	NBC-1	NBC-2
Bacteria (*P.nitroreducens*)	0	25	39	39
Fungi (*A. unguis*)	0	29	25	27

2.4   Conclusions

Organic inhibiting films generally do not provide reliable long term corrosion protection on their own. In order to ensure extended service lifetimes, the metal surfaces are treated to provide a consistent surface that is free of contamination and unfavorable phases. Thus, metal finishing processes provide the secondary role of corrosion protection.   Alkaline and acidic pretreatment baths reduces the heterogeneous nature of the metal surface. Irrespective of the nature of the alloy surface, significant corrosion inhibition was obtained from the neem leaves extract in 1 M HCl solution.

Furthermore, it has been demonstrated in this study that 'neem leaves crude extract' could be complexed with Si nanoparticles to form a hybrid bionanocomposites. The eventually obtained coatings exhibited anticorrosive properties and can be applied as a primer layer on aluminium alloy 6061. It was observed that the solvent type, surface area and presence of silanol groups were crucial factors for the natural product loading. MS carriers of nanometer size range can be used together with existing thermosetting polymeric coating materials to obtain functional film coatings for metallic surfaces. The studies revealed that the

potent anticorrosion effect of the crude vegetal extract is due to the coexistence of the polyphenol species and other active compounds within it. The impedance measurements revealed an increase of low-frequency impedance during immersion in the corrosive media which is related to the suppression of active corrosion processes of the corroded areas. Furthermore, all studied epoxy-based coatings exhibited both antibacterial and antifungal activity. Hence, it is believed that coatings formulated with the incorporation of bio-based renewable resources will rapidly expand into a wide number of applications. It is therefore pertinent that the raw materials selected as corrosion inhibitors have to be chosen carefully, to avoid competing with the food industry.

References

[1]   P. B. Raja, M. G. Sethuraman, *Mater. Lett.* **2008**, *62*, 113.

[2]   K. Xhanari, M. Finšgar, M. Knez Hrnčič, U. Maver, Ž. Knez, B. Seiti, *RSC Adv.* **2017**, *7*, 27299.

[3]   R. Twite, G. Bierwagen, *Prog. Org. Coatings* **1998**, *33*, 91.

[4]   T. A. S. F. ' A. (ASFA), *ARCHITECTURAL SURFACE FINISHING GUIDE*.

[5]   E. E. Oguzie, *Corros. Sci.* **2007**, *49*, 1527.

[6]   R. Rosliza, W. B. Wan Nik, *Curr. Appl. Phys.* **2010**, *10*, 221.

[7]   M. Pitchaipillai, K. Raj, J. Balasubramanian, P. Periakaruppan, *Int. J. Miner. Metall. Mater.* **2014**, *21*, 1083.

[8]   M. Dabalà, E. Ramous, M. Magrini, *Mater. Corros.* **2004**, *55*, 381.

[9]   A. Taguchi, F. Schüth, *Microporous Mesoporous Mater.* **2005**, *77*, 1.

[10]   P. Vijayan, M. AlMaadeed, *Express Polym. Lett.* **2016**, *10*, 506.

[11]   E. Abdullayev, V. Abbasov, A. Tursunbayeva, V. Portnov, H. Ibrahimov, G. Mukhtarova, Y. Lvov, *ACS Appl. Mater. Interfaces* **2013**, *5*, 4464.

[12]   A. Chenan, S. Ramya, R. P. George, U. Kamachi Mudali, *Ceram. Int.* **2014**, *40*, 10457.

[13]   K. Biswas, I. Chattopadhyay, R. K. Banerjee, U. Bandyopadhyay, *Biological activities and medicinal properties of neem (Azadirachta indica)*; 2002; Vol. 82.

[14]   M. A. Alzohairy, *Evidence-Based Complement. Altern. Med.* **2016**, *2016*, 1.

[15] M. B. Isman, O. Koul, A. Luczynski, J. Kaminski, *J. Agric. Food Chem.* **1990**, *38*, 1406.

[16] S. Chaudhary, *Front. Plant Sci.* **2017**, *8*.

[17] U. P. Singh, H. B. Singh, R. B. Singh, *Mycologia* **1980**, *72*, 1077.

[18] J. Dai, V. A. Yaylayan, G. S. Vijaya Raghavan, J. R. Parè, Z. Liu, *J. Agric. Food Chem.* **2001**, *49*, 1169.

[19] L. Valek, S. Martinez, *Mater. Lett.* **2007**, *61*, 148.

[20] P. Okafor, E. Ebenso, U. Ekpe, *Int. J. Electrochem. Sci.* **2010**, *5*, 978.

[21] R. A. Prabhu, T. V. Venkatesha, B. M. Praveen, K. G. Chandrappa, S. B. Abd Hamid, *Trans. Indian Inst. Met.* **2014**, *67*, 675.

[22] A. Nahlé, I. Abu-Abdoun, I. Abdel-Rahman, M. Al-Khayat, *Int. J. Corros.* **2010**, *2010*, 1.

[23] T. Sangeetha, M. Fredimoses, *E-Journal Chem.* **2011**, *8*, S1.

[24] G. Brahmachari, *ChemBioChem* **2004**, *5*, 408.

[25] R. Subapriya, S. Nagini, *Curr. Med. Chem. Agents* **2005**, *5*, 149.

[26] G. Pandey, K. K. Verma, M. Singh, *Int. J. Pharm. Pharm. Sci.* **2014**, *6*, 444.

[27] S. D. Toliwal, K. Patel, *Modified neem (Azadirachta indica Juss) oil based curing of acid functional acrylic copolymer resin for anticorrosive coating*; 2006; Vol. 65.

[28] A. B. Chaudhari, A. Anand, S. D. Rajput, R. D. Kulkarni, V. V. Gite, *Prog. Org. Coatings* **2013**, *76*, 1779.

[29] A. B. Chaudhari, P. D. Tatiya, R. K. Hedaoo, R. D. Kulkarni, V. V. Gite, *Ind. Eng. Chem. Res.* **2013**, *52*, 10189.

[30] R. Marathe, P. Tatiya, A. Chaudhari, J. Lee, P. Mahulikar, D. Sohn, V. Gite, *Ind. Crops Prod.* **2015**, *77*, 239.

[31] A. S. Karun, S. Hari, W. S. Ebhota, T. P. D. Rajan, U. T. S. Pillai, B. C. Pai, *Metall. Mater. Trans. A* **2017**, *48*, 279.

[32] R. Rosliza, W. B. Wan Nik, *Curr. Appl. Phys.* **2010**, *10*, 221.

[33] N. Saleema, D. K. Sarkar, R. W. Paynter, D. Gallant, M. Eskandarian, *Appl. Surf. Sci.* **2012**, *261*, 742.

[34] L. Cao, H. Zhang, C. Cao, J. Zhang, F. Li, Q. Huang, *Nanomaterials* **2016**, *6*, 126.

[35] Y. Zhu, J. Shi, H. Chen, W. Shen, X. Dong, *Microporous Mesoporous Mater.* **2005**, *84*, 218.

[36] C. Verma, E. E. Ebenso, I. Bahadur, I. B. Obot, M. A. Quraishi, *J. Mol. Liq.* **2015**, *212*, 209.

[37] C. Verma, L. O. Olasunkanmi, E. E. Ebenso, M. A. Quraishi, I. B. Obot, *J. Phys. Chem. C* **2016**, *120*, 11598.

[38] K. de Lira Mota, F. de Oliveira Pereira, W. de Oliveira, I. Lima, E. de Oliveira Lima, *Molecules* **2012**, *17*, 14418.

[39] S. Hernandez, S. Hassani, A. S. Nassef, In *Trends in oil and gas corrosion research and technologies: Production and transmission*; El-Sherik, A., Ed.; Woodhead Publishing: United Kingdom, 2017.

[40] N. Perez, *Electrochemistry and Corrosion Science*; Springer International Publishing: Switzerland, 2004.

[41] N. L. Sukiman, X. Zhou, N. Birbilis, A. E. Hughes, J. M. . . Mol, S. J. Garcia, X. Zhou, G. E. Thompson, In *Aluminium Alloys - New Trends in Fabrication and Applications*; Ahmad, Z., Ed.; InTech, 2012.

[42] H.-S. Lee, J. K. Singh, J. H. Park, *Constr. Build. Mater.* **2016**, *113*, 905.

[43] G. S. Frankel, *J. Electrochem. Soc.* **1998**, *145*, 2186.

[44] N. Birbilis, R. G. Buchheit, *J. Electrochem. Soc.* **2005**, *152*, B140.

[45] M. B. M. C. Felipe, D. R. Silva, C. A. Martinez-Huitle, S. R. B. Medeiros, M. A. M. Maciel, *Mater. Corros.* **2013**, *64*, 530.

[46] E. E. Oguzie, *Port. Electrochim. Acta* **2008**, *26*, 303.

[47] T. Balakrishnan, S. Sathiyanarayanan, S. Mayavan, *ACS Appl. Mater. Interfaces* **2015**, *7*, 19781.

[48] V. S. Sastri, *Corrosion inhibitors : principles and applications*; Wiley, 1998.

[49] S. Pappavinasam, In *Uhlig's corrosion handbook*; Revie, R., Ed.; John Wiley & Sons, Inc: Canada, 2000; pp. 1089–1105.

[50] G. F. Andrade, D. C. F. Soares, R. K. D. S. Almeida, E. M. B. Sousa, *J. Nanomater.* **2012**, *2012*, 1.

[51] M. Vallet-Regí, F. Balas, D. Arcos, *Angew. Chemie Int. Ed.* **2007**, *46*, 7548.

[52]   J. Andersson, J. Rosenholm, S. Areva, M. Lindén, *Chem. Mater.* **2004**, *16*, 4160.

[53]   K. B. Arun, S. Thomas, T. R. Reshmitha, G. C. Akhil, P. Nisha, *J. Funct. Foods* **2017**, *31*, 198.

[54]   C. P. Jaroniec, R. K. Gilpin, M. Jaroniec, *J. Phys. Chem. B* **1997**, *101*, 6861.

[55]   W. Cheng, J. Nie, L. Xu, C. Liang, Y. Peng, G. Liu, T. Wang, L. Mei, L. Huang, X. Zeng, *ACS Appl. Mater. Interfaces* **2017**, *9*, 18462.

[56]   T. Chen, Q. Zhang, J. Xu, J. Pan, Y.-T. Cheng, *RSC Adv.* **2016**, *6*, 29308.

[57]   P. J. Launer, B. Arkles, In *Silicon Compounds: Silanes & Silicones*; Gelest, Inc: Morrisville, PA, 2013; pp. 175–178.

[58]   H. Wu, P. Li, D. Pan, Z. Yin, Q. Fan, W. Wu, *PLoS One* **2016**, *11*, e0149632.

[59]   F. T. Martins, M. H. dos Santos, C. P. Coelho, L. C. A. Barbosa, G. C. Dias, M. P. Fracca, P. P. Neves, P. C. Stringheta, A. C. Doriguetto, *J. Pharm. Biomed. Anal.* **2011**, *54*, 451.

[60]   M. Bordbar, *RSC Adv.* **2017**, *7*, 180.

[61]   G. Venkatasubramanian, S. M. A, A. K. Jha, *Res. J. Chem. Sci.* **2013**, *3*, 74.

[62]   F.-Y. Ma, In *Pitting Corrosion*; InTech, 2012.

[63]   D. B. Blücher, J.-E. Svensson, L. G. Johansson, *J. Electrochem. Soc.* **2003**, *150*, B93.

[64]   Y. Liu, M. Guo, *Molecules* **2015**, *20*, 8583.

[65]   M. M. Kasprzak, A. Erxleben, J. Ochocki, *RSC Adv.* **2015**, *5*, 45853.

[66]   D. Borisova, D. Akçakayıran, M. Schenderlein, H. Möhwald, D. G. Shchukin, *Adv. Funct. Mater.* **2013**, *23*, 3799.

[67]   M. Wang, M. Liu, J. Fu, *J. Mater. Chem. A* **2015**, *3*, 6423.

[68]   G. Brahmachari, *ChemBioChem* **2004**, *5*, 408.

[69]   G. Zafra, A. E. Absalón, D. V. Cortés-Espinosa, *Brazilian J. Microbiol.* **2015**, *46*, 937.

Chapter 3

Smart Anticorrosive Bio-Coatings: Evaluation of Quercetin for Corrosion Protection of Al6061

Scratched coatings after corrosion test

Unscratched coatings after corrosion test
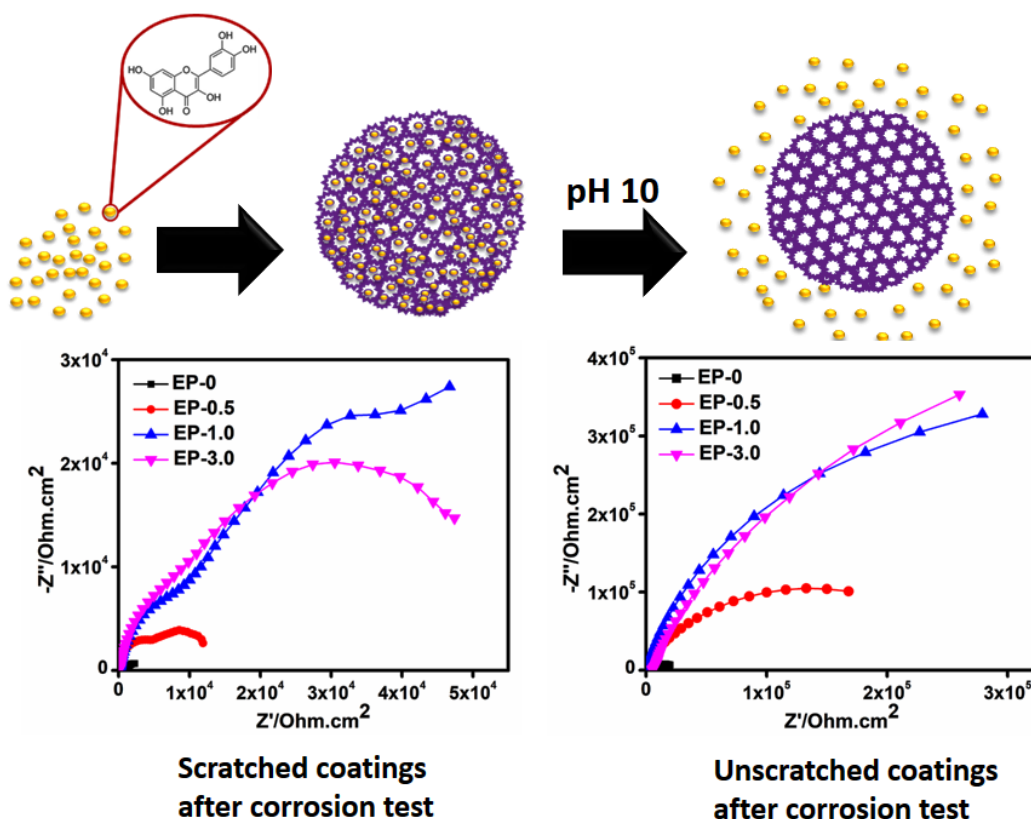
Abstract

The present investigation describes a new contribution to the development of active anticorrosive films. The "phytochemical" Quercetin (QCT), a known secondary metabolite of plants, loaded in silica nanocontainers as the natural organic inhibitor was utilized to obtain active anticorrosive coatings. With an artificial defect induced on the epoxy nanocomposite coating and subsequent corrosion reactions, active corrosion protection was triggered. The optimum performance was achieved from the 1.0 wt.% loaded coatings. The unscratched nanocomposite coatings were also examined and revealed enhanced corrosion protection in comparison with the unmodified epoxy coating. The anticorrosive action of the bio-coatings was controlled by the release and reactions of

the inhibiting component from the coating at pH 10. The corrosion protection offered by QCT was due to the chemical transformation experienced by QCT with pH influence involving possible autoxidation and polymerization processes. Both immersion and electrochemical corrosion tests were employed in the study to systematically evaluate the corrosion protection. Furthermore, a primary investigation was conducted to assess the antibacterial property of the bio-coatings which offered significant antibacterial protection to the aluminium alloy surfaces by inhibiting the growth of the biofilm-forming bacteria Pseudomonas nitroreducens. These findings encourage the exploration of bio-based coatings for enhanced anticorrosion protection of aluminium alloys.

3.1   Introduction

Phytochemicals extracted from plants provide comparable corrosion inhibition characteristics, due to the presence of organic compounds like alkaloids, tannins, saponins, carbohydrates, proteins, lignins, flavonoids, terpenoids, fatty acids, phenols, carotenoids, amino acids, etc. in them. The reaction centers include multiple bonds, aromatic rings, heteroatoms such as nitrogen, oxygen, and phosphorus, etc.[1–3]

Quercetin is a natural, nontoxic, and environmentally friendly inhibitor. A well-known flavonoid compound, belonging to the group of natural polyphenolic compounds, abundant in plants. It is an excellent free-radical scavenging antioxidant and one of the most effective antioxidants compounds.[4–6] Quercetin has dye properties and its chemical structure consisting of two phenyl rings and a heterocyclic ring contains multi-adsorption centres bound to the aromatic rings. It is of great interest in research because of its pharmacological importance.[7,8]   Corrosion control is a collective effort of appropriate substrate surface treatments, inhibitors, and coatings, etc. towards achieving the desired goal of protecting the metallic material from its aggressive environment. Nanotechnology has therefore provided the platform to explore the non-conventional composites of which ecofriendly bionanocomposite is of interest. Although there is a large number of publications on the use of natural inhibitors for corrosion protection of metals exposed to corrosive environments, research dedicated to the use of bio-based inhibitors embedded in coatings is rare.

Corrosion protection of the underlying metal due to inhibiting components within the coating occurs as a result of an interaction between the corrosion inhibitor and the corroding metal surface and its environment.[9–11] Since direct addition of corrosion inhibitors has almost always resulted in undesirable leaching of inhibiting molecules and subsequent reactions with the coating matrix.[12] The encapsulation of organic corrosion inhibitors into a host material as guest-host complexes with nanocontainers is an effective delivery system of organic inhibitors in coatings for active corrosion protection of metallic substrates and it is being widely explored.[12–14] In achieving these, silica nanostructures are most widely used as nanocontainers for inhibitor storage. In particular, Mesoporous silica nanoparticles (MSN) can host various bioactive compounds and drug molecules.[15,16] Several investigations have demonstrated the application of MSN for the release of corrosion inhibitors.[10,13,17,18]

The objective of the present work is to evaluate the application of silica nanoparticles without further functionalization as nanocontainers for loading bio-based inhibitor quercetin and to investigate the influence of pH conditions on quercetin release and reactions for corrosion inhibition. The efficiency of quercetin as a corrosion inhibitor when loaded in silica nanocontainers was examined in 3.5 wt.% NaCl solution at pH 3.00, 6.44-7.00 and 10.00. The pH-triggered release of the flavonoid quercetin as corrosion inhibitor from MSN is discussed. These local changes in pH can be used as an intrinsic stimulus for smart functional containers to release the corrosion inhibitors during corrosion occurrence.[14,19] Surface morphological changes, anticorrosion and antibacterial effects of the newly derived eco-friendly coatings provided insight into the extent of its protection efficiency.

3.2   Materials and methods

3.2.1   Materials

Quercetin dihydrate 98.0% and Cetyltrimethylammonium bromide (CTAB) were purchased from SD Fine Chemicals, Mumbai, India. Tetraethyl orthosilicate reagent grade 98% from Sigma-Aldrich, Germany. Ethanol 99.9% (Changshu Hongsheng Fine Chemicals Co., Ltd), and HCl 36% (Avantor Performance Materials India Ltd), 1-Butanol anhydrous 99.8% (Signa-Aldrich, USA). NaOH pellets purified (SD

Fine Chemicals, Mumbai, India). NaCl was purchased from Merck Specialties Private Limited, Mumbai, India. Ultrapure water of 18.2 MΩ·cm resistivity at 25°C (Evoqua water technologies, Inexus Biotech Pvt. Ltd. India) was used in the study. pH of solutions were adjusted with 0.1 M HCl or 2.0 M NaOH. Diglycidyl ether of bisphenol A (DGEBA) was purchased from Thermofisher scientific, India and commercially available HY951 obtained from Vantico, India was used as the hardener. All chemicals were used as purchased without further purification. The strain *Pseudomonas nitroreducens* was procured from NIIST culture collection, Thiruvanathapuram, Kerala.

3.2.2 Methods

3.2.2.1 Synthesis of the Inhibitor-Nanoparticle composite

Mesoporous silica nanocontainers were prepared following the procedure described by Cao et al. with slight modification[20] as discussed in Chapter 2 section 2.2.2.3. Quercetin (QCT) was dissolved in ethanol solution at 40 mg/mL following the loading process described by Zhu et al. with slight modification.[21] 0.5 g mesoporous silica nanoparticles (MSN) was added into 25 mL QCT-Ethanol solution at room temperature. The conical flask was sealed to prevent the evaporation of ethanol and the mixture was stirred for 24 h. MSN adsorbed with QCT was separated from this solution by centrifugation and dried under vacuum at 60°C for about 16 h. The loading process was repeated to ensure maximum loading of the inhibitor.

3.2.2.2 Substrate and coating preparation

Aluminium alloy 6061 substrates was obtained and cleaned as described in Chapter 2, section 2.2.2.5. 3.5 wt.% NaCl of analytical grade was the saline medium used throughout the study. QCT-loaded MSN was added to the epoxy (DGEBA) at 0.5, 1.0 and 3.0 wt.% concentration of the total mass of the hardener and the resin. Firstly, the nanocomposite was sonicated with 1-butanol using Ultrasonic cleaner, GT-1990QTS (China) for 15 mins. This was added to the epoxy and stirred with a magnetic stirrer at 1500 rpm until the entire mixture appeared well-homogenized. On addition of the hardener, a further timely stirring and sonication were observed before coating the alloy substrate. The epoxy to hardener ratio used was 2:1. The pretreated alloy samples were dip coated at 350 mm/min. After application, the freshly coated samples were left

for room temperature curing process for up to 7 days and preserved in a desiccator before use.

3.2.3 Characterizations

Most of the characterizations have been fully described in Chapter 2, section 2.2.3. Functional groups in the samples was determined with Perkinelmer FTIR, Model 2, Perkinelmer Singapore PTE LTD recorded in transmittance mode by ATR-FTIR. The crystalline structure of the composites was examined by X-ray diffraction (XRD) PANalytical, Netherlands with Cu Kα radiation at a 2θ range of 5-70°. SEM micrographs were recorded using Zeiss EVO 18 cryo-SEM Special Edition with variable pressure detector attached with EDS working at 10-30 kV after sputtering with gold. TEM micrographs were recorded using JEOL 2010 TEM operating at 300 kV. TGA was determined using STA7300 Thermal Analysis System, Hitachi, under argon atmosphere. N_2 adsorption-desorption method was adopted to characterize the mesoporous structure, pore size and volume and specific surface area of MSN and MSN-QCT using Micromeritics, Tristar II, USA. DLS and ζ-potential measurements were performed using Malvern Zetasizer Nano ZS90, Germany. UV-Visible spectrophotometer model UV-2401PC (SHIMADZU) was used for absorbance measurement and recording the spectra of the loaded nanoparticles in comparison with the inhibitor from 200-600 nm. Both Electrochemical impedance spectroscopy (EIS) and Potentiodynamic polarization (PP) studies were conducted for the anticorrosive systems with a conventional three-electrode cell using CH Instruments electrochemical workstation (CHI608E, CH Instruments Inc.). The EIS and PP measurements were performed as described in Chapter 2. The average coating thickness were estimated from the cross-sectional SEM images.

3.2.4 Antibacterial evaluation of the epoxy coatings

Epoxy-MSN-QCT coating was tested for antibacterial activity by an inhibition zone method. For culturing the bacteria (*Pseudomonas nitroreducens*), the culture media (Luria Bertani Broth and Luria Bertani Agar) and glassware were autoclaved at 121°C, 15 psi for 15 min prior to the experiments. After cooling, a loop of *Pseudomonas nitroreducens* strain was inoculated in 100 mL Luria Bertani Broth under sterile

conditions and incubated at 37°C, overnight. After the incubation, 100 μL of the culture was uniformly plated on the Luria Bertani Agar (LBA) petri plates using sterile L-rod. The bare alloy (control sample) and coated alloy samples was circular with a diameter of 2 cm and was placed in the center of petri plates in such a manner that both the bare alloy and the coatings were in contact with the culture. The plates were examined for possible clear zone formation after 24 h incubation at 37°C. The entire experiments were conducted in triplicates and to prevent any possible contamination it was carried out in a laminar hood. The presence of a clear zone around the investigated samples on the plates was recorded as an inhibition against the test bacteria.

3.3 Results and discussion

3.3.1 Nanocontainer and nanocomposite characterization

3.3.1.1 ATR-FTIR analysis

The ATR-FTIR spectra of QCT and MSN-QCT were recorded in order to investigate possible chemical interactions between the natural inhibitor and the mesoporous silica nanoparticles. In Fig. 3.1, hydroxyl groups are present in samples b, c, and d within 3550-3200 cm^{-1} in the spectra. Also, in Fig. 3.1(a) C-H stretching vibrations occurred at 2925 and 2854 cm^{-1} and C-H bending vibrations at 1474 cm^{-1} respectively from the templates. The bands at 1227 cm^{-1} represent Si-CH$_2$ and 961 cm^{-1} for silanol group (Si-OH). Si-O-Si show one or more very strong infrared bands in the region of 1130-1000 cm^{-1} and the band related with Si-O rocking in the region of 455 cm^{-1}[22] which has been observed in Fig. 3.1 (a-c). In Fig. 3.1(b), the band at 1630 cm^{-1} for water bending vibration is present after template depletion due to a more hydrophilic silanol-containing surface.[23]

In quercetin spectrum, the broad band characteristic of the phenolic hydroxyl bonding within 3550-3200 cm^{-1} is observed. Characteristic absorption for C=O occurs within 1600-1800 cm^{-1} and these accommodates the bands at 1660.41 and 1738.67 cm^{-1} for stretching of the C=O carbonyl functional group. While bands at 1606.04 and 1516.24 cm^{-1} for C=C aromatic bonds stretching, 1377.02 cm^{-1} for quercetin aromatic ring of the phenolic moiety of the quercetin molecule, 1316.88 cm^{-1} for =C-O-H of the phenolic group and 1262.51 cm^{-1} a band of medium intensity related to the stretching

C-O-C aryl ketone were recorded. Also, 1174.37 cm^{-1} represents the band attributed to the aromatic ring of quercetin, 1016.20 cm^{-1} attributable to the conjugation of the aryl ether with C=C-O of the aromatic ring of the quercetin, 932.99 cm^{-1} for aromatic group C-H stretching, 816.84 cm^{-1} for stretching of the catechol moiety. Similar bands for quercetin are reported.[24,25]

Bands between 620 cm^{-1} and 810 cm^{-1} in SiO$_2$ containing materials help to identify the kind of SiO$_2$.[22] The shoulder at 1227 cm^{-1} of Si-CH$_2$ is decreased and slightly shifted to 1220 cm^{-1}. Si-OH (silanol group) at 961.78 cm^{-1} also present. The absence of bands typical for alkyl C-H stretching frequencies at 2854 cm^{-1} and 2925 cm^{-1} in Fig. 3.1(b) after calcination, confirmed removal of the surfactant templates from MSN.[6] In MSN-QCT, slight shifts in wavenumbers were observed, which includes 1663.72 cm^{-1} for stretching of the C=O carbonyl functional group, 1610.04 cm^{-1} and 1513.95 cm^{-1} for C=C aromatic bonds stretching, 1384.21 cm^{-1} for quercetin aromatic ring of the phenolic moiety of the quercetin molecule, 1313.72 cm^{-1} for =C-O-H of the phenolic group, and the shoulder at 1244.75 cm^{-1} of Si-CH$_2$ decreased. While 967.59 cm^{-1} represents silanol group (Si-OH) and 943.70 cm^{-1} for aromatic C-H stretch. This confirms the incorporation of quercetin into the MSN. However, it should be noted that any FTIR spectrum mainly provides the structural information of the particles.[26]
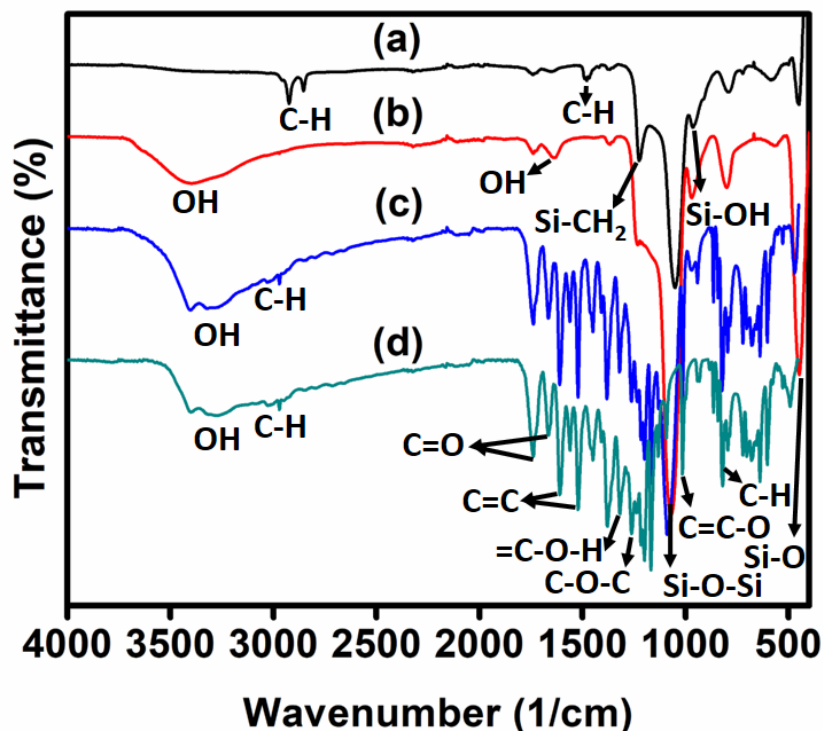
Fig. 3.1: ATR-FTIR spectra of (a) MSN before calcination, (b) MSN after calcination, (c) MSN-QCT, and (d) QCT.

3.3.1.2 XRD analysis

In Fig. 3.2, the broadened peak between 15° and 25° is attributed to amorphous MSN.[27] The crystalline nature of quercetin was confirmed by distinct peaks at 2 theta degrees corresponding to 10.76^{o}, 12.43^{o}, 13.63^{o}, 15.78^{o}, 16.06^{o}, 23.77^{o}, 24.31^{o} 26.41^{o}, and 27.10^{o}. Similar peaks have been reported for the flavonoid quercetin.[6,24] For the physical mixtures of MSN and QCT, the peaks obtained at 2 theta degrees matched with the peaks obtained for QCT, similar to earlier reports.[6] This reveals that the nanocomposite also had crystalline properties after the loading process. This also supports the presence of the corrosion inhibitor adsorbed reasonably to the MSN.
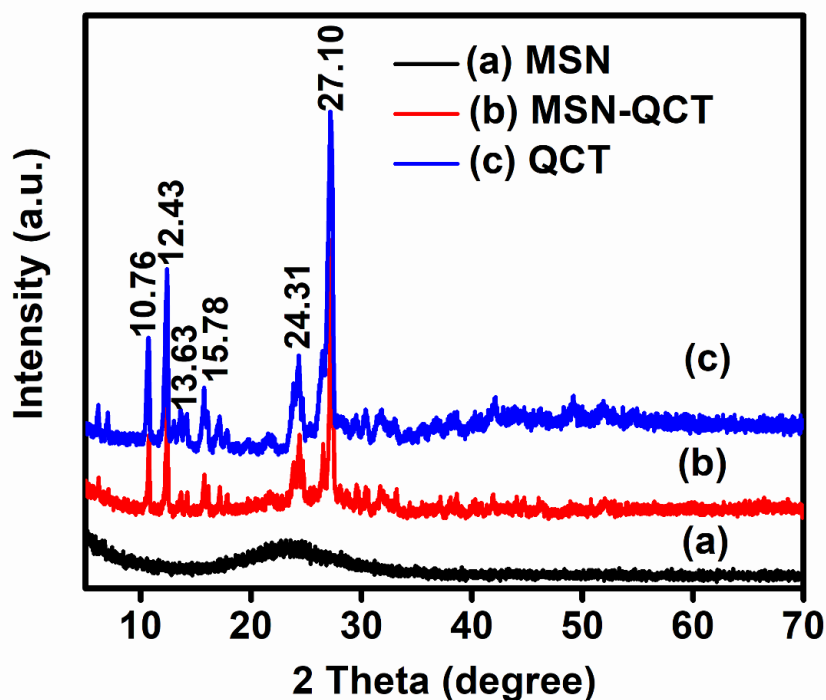
Fig. 3.2: XRD pattern of (a) MSN, (b) MSN-QCT, and (c) QCT.

3.3.1.3 Morphology and Size analysis

The SEM micrographs and corresponding EDS spectra and data in Fig. 3.3 represents the surface morphologies of the studied particles after their synthesis. The nanoparticles exhibit a roughened surface. Shape and surface preservation was maintained after loading with the inhibitor molecules; an indication of structural stability.[10] Elemental compositions reflect the constituents of both MSN and MSN-QCT after the synthesis protocols. The hydrodynamic particle size and particle size distribution of the synthesized MSN and MSN-QCT were determined by dynamic light scattering using water as the solvent. The hydrodynamic diameter (nm) obtained for the synthesized MSN was 212.58 and the zeta potential (mV) -26.7 ± 1.0 while for MSN-QCT, size (nm) was 372.00 and zeta potential (mV) -16.5 ± 3.7.

Element	Weight %	Atomic %
O K	57.94	70.75
Si K	42.06	29.25
Totals	100.00	

Full Scale 3578 cts Cursor: 0.000

Element	Weight %	Atomic %
C K	47.33	57.31
O K	39.40	35.82
Si K	13.27	6.87
Totals	100.00	

Full Scale 1808 cts Cursor: 0.000
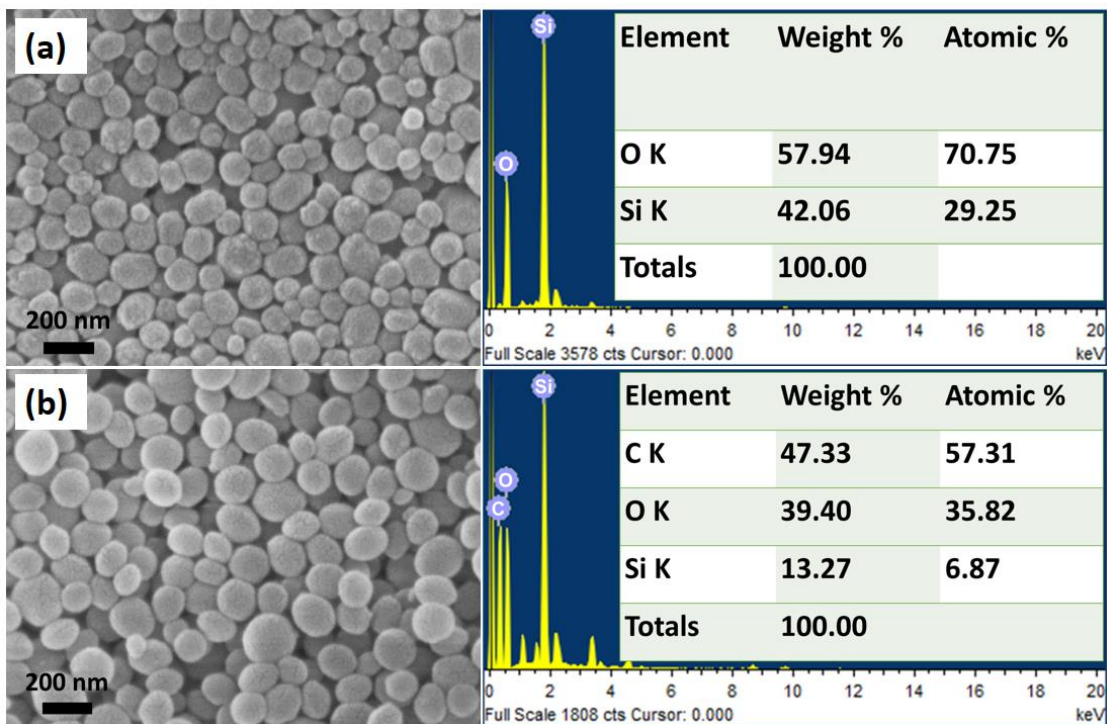
Fig. 3.3: SEM micrographs and EDS spectra of (a) MSN and (b) MSN-QCT.

The TEM micrographs in Fig. 3.4 (a-d) represents the morphologies of the studied nanoparticles in the order (a & b) empty calcined mesoporous silica nanoparticles (c & d) quercetin loaded MSN. The mesoporous nature of MSN allowed for loading via adsorption of the corrosion inhibitor. The nanocomposite complex is polydispersed and mostly spherical.
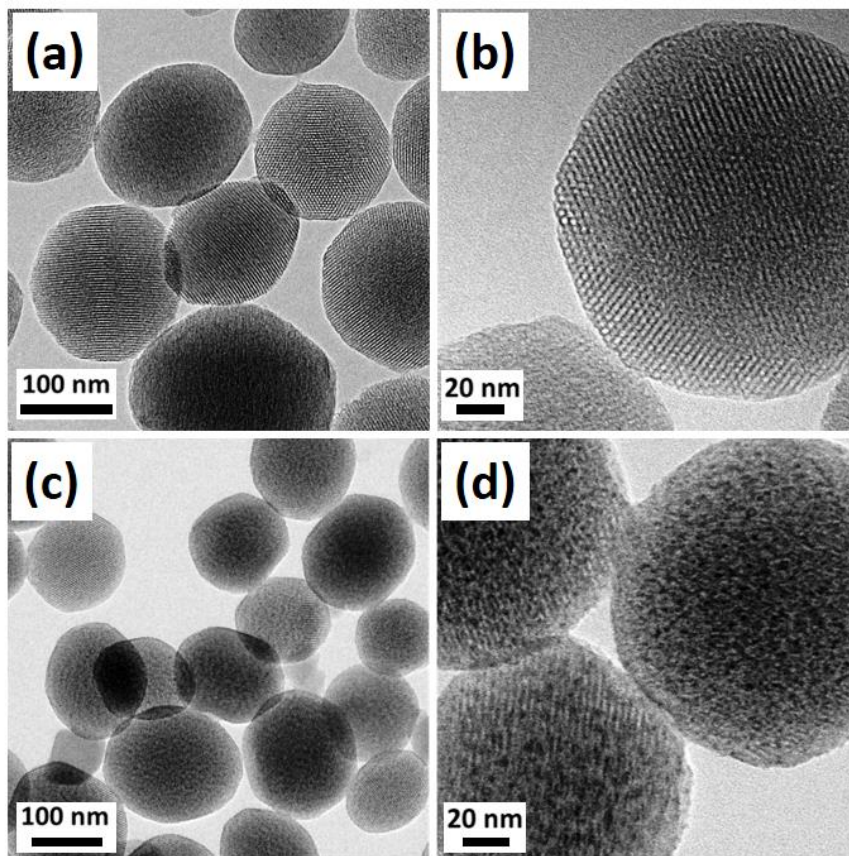
Fig. 3.4: TEM micrographs of (a, b) empty MSN and (c, d) MSN-QCT at different magnifications.

3.3.1.4 TG and DTA analysis

TG analysis measures the change in mass, thermal stability and thermal decomposition of materials.[28] The loading capacity of the composite corrosion inhibitor and its thermal stability were determined through this technique under inert conditions. Fig. 3.5 shows the mass loss/DTA curves of MSN and MSN-QCT under argon atmosphere. Both endothermic and exothermic reactions were observed. Synthesized MSN sample showed one major mass loss stage. 25% mass loss between 30 and 85°C is associated with removal of physisorbed water molecules on the external surface of the material. Then a 2% degradation in the temperature range of 180-450°C may be ascribed to the thermal degradation of slight hydrocarbon contamination. The first

derivative was at 62.43°C with an endothermic peak. MSN showed a residual mass of 71.56% at 900 °C.

MSN-QCT sample showed more than one distinct mass loss stages. The first 21.64 % mass loss between 30 and 121°C corresponding to the endothermic peak at 113.08°C is associated with desorption of physisorbed water molecules on the external surface of the material and possible residual organic solvent during the preparation. The first thermal degradation of the incorporated organic moiety anchored to the pore wall of MSN occurred with an endothermic peak at 324.07°C and a mass loss of 22.13% between 121-384°C. The next weight loss between 384-900°C corresponds to combustion of remaining carbon species and possible dehydroxylation of the silicate networks.[28] MSN-QCT showed a residual mass of 42.01% at 900°C. The DTA path of quercetin exhibited an evident endothermic event at 115.86°C determined by the loss (19.0%) of possible H_2O molecules from the crystal lattice of the hydrate form of quercetin. A second endothermic reaction, evident by a peak at 325.20°C, related to the melting of the flavonoid, and an exothermic event occurred at 347.22°C. The accompanying weight loss of about 14.56% is related to quercetin degradation process.[29,30]
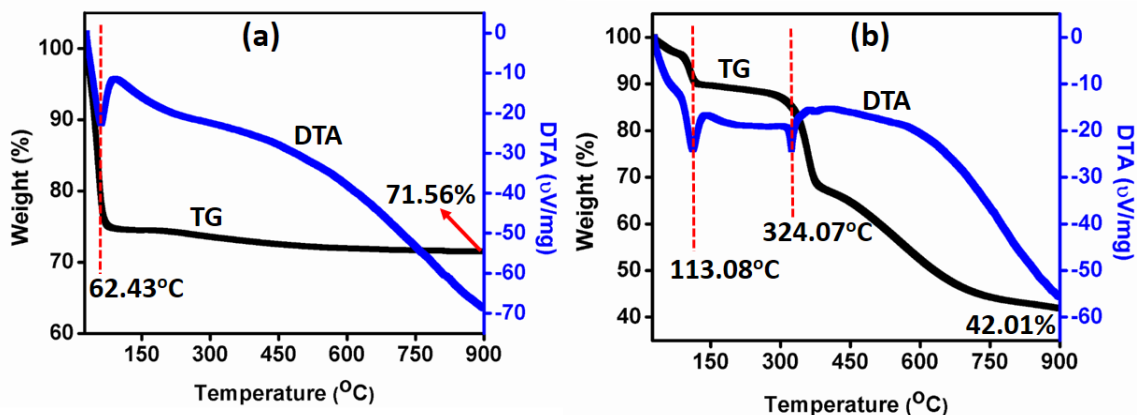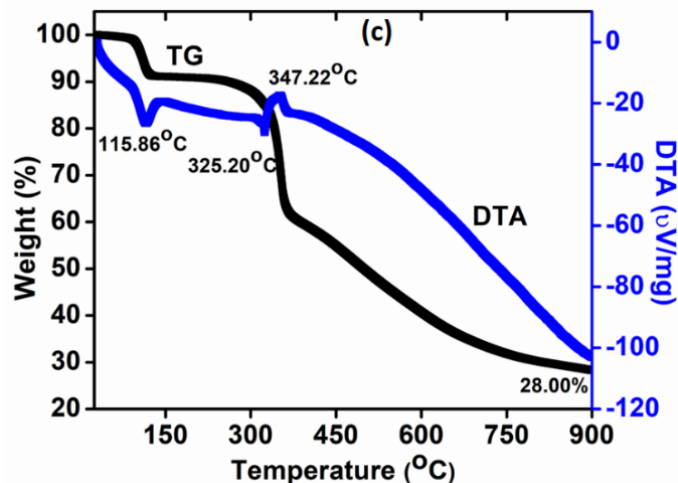
Fig. 3.5: TG and DTA curves of (a) MSN, (b) MSN-QCT, and (c) QCT.

3.3.1.5 Nitrogen adsorption/desorption analysis

N$_2$ adsorption/desorption analysis is concerned with pore spaces not filled with adsorbate during the adsorption process or spaces emptied by capillary action during the desorption process.[31] N$_2$ sorption provides an estimate on the loading efficiency by observing the change in porosity and reduction in the total pore volume of the nanoparticles. A decrease of the total pore volume can be assigned to the loaded inhibitor molecules in the mesopores of the silica network [13]. With the Brunauer-Emmett-Teller (BET) method, the specific surface area was calculated and with Barrett-Joyner-Halenda (BJH) method, the pore size distribution was determined from the adsorption branch of the isotherm. For the MSN samples, BET surface area was: 867.38 m^2/g, Total pore volume at P/P$_o$ = 0.98: 0.49 cm^3/g, Pore Diameter by BJH method: 2.98 nm. While for MSN-QCT, BET surface area sharply reduced to 13.72 m^2/g, Total pore volume at P/P$_o$ = 0.98: 0.04 cm^3/g and Pore Diameter by BJH method rather became larger at 19.01 nm. MSN-QCT presents a slightly different N$_2$ isotherm from MSN, where the step corresponding to the capillary condensation of nitrogen within the mesopores seems to vanish. The hysteresis loop was completely lost and surface area significantly reduced indicating maximum filling of spaces in MSN (Fig. 3.6) and changes in mesoporous structure characteristics. The loss of the hysteresis loop affirms that the pores were blocked by quercetin due to the heavy loading and change in pore size were

127

observed.[20] Higher average pore diameter after inhibitor loading has also been reported.[13]
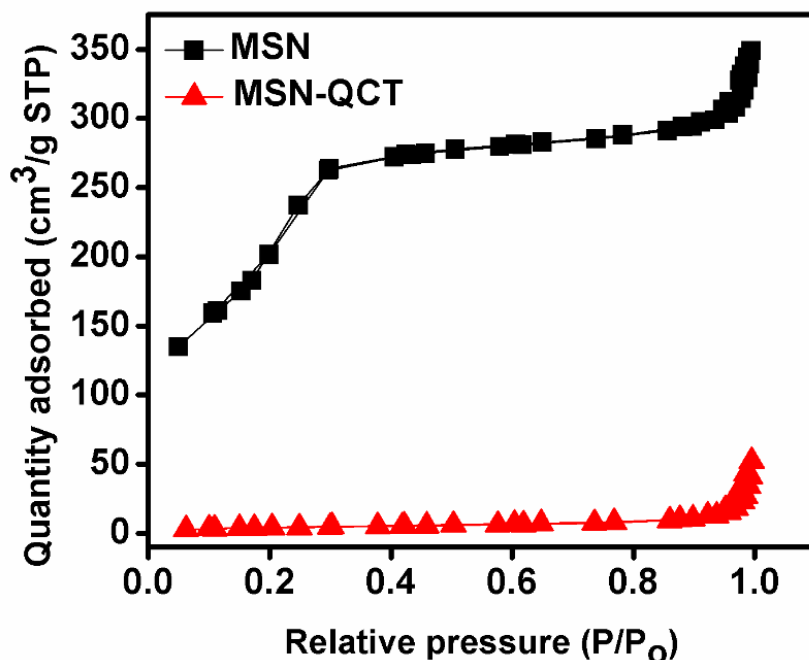
Fig. 3.6: Nitrogen adsorption/desorption isotherms for MSN and MSN-QCT.

3.3.1.6 UV-Visible analysis and Reaction kinetics of the inhibitor

Quercetin was successfully loaded into MSN by mixing the MSN with a saturated quercetin-ethanol solution followed by stirring for 24 h in an air-tight vial. Fig. 3.7(a) presents the UV-vis spectra of quercetin solution before and after the interactions with MSN. λ-max for quercetin is mainly at 257 and 374 nm. The UV-visible spectra (Fig. 3.7(a)) showed that the absorption maxima for quercetin was decreased after the interaction of quercetin molecules with MSN. Also, there were no new absorption bands and the position of the peaks was not changed. This decrease in the absorption intensity of quercetin after the interaction with MSN confirmed the decrease of the quercetin concentration in the solution as well as the successful loading and adsorption of the quercetin molecules in the pores and interiors of MSN. The loading of the organic inhibitor molecules in inorganic nanocontainers are made possible through weak non-covalent interactions such as physical adsorption, electrostatic interaction, hydrogen bonding and π-π stacking.[32,33]
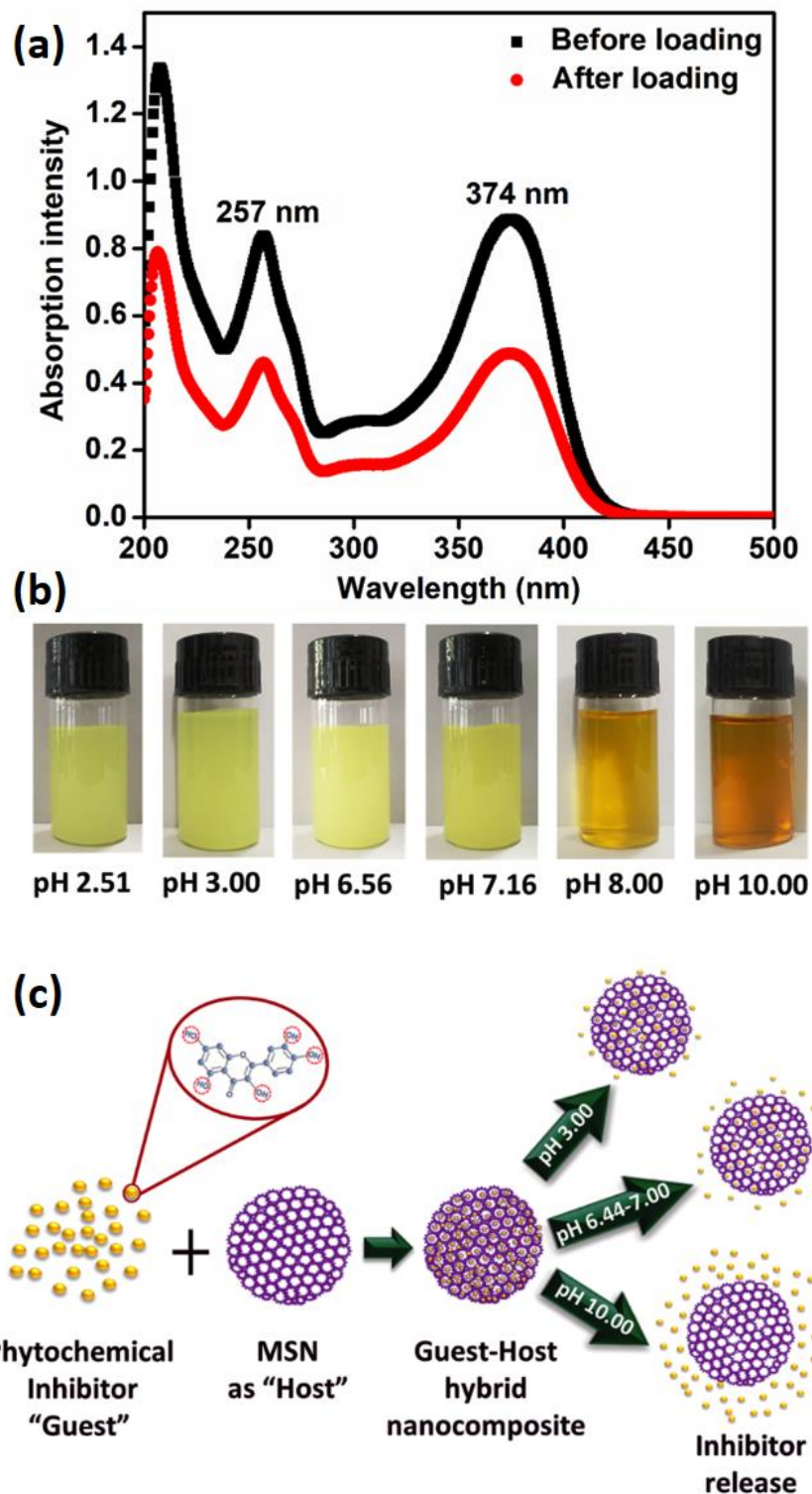
Fig. 3.7: (a) UV-visible spectra of QCT before and after interaction with MSN. (b) Gradual dissolution of MSN-QCT in the aqueous medium (3.5 wt.% NaCl) with pH

changes revealed from the turbidity of the solution alongside color changes (Concentration 0.5 g/L for optical photo clarity). (c) Graphic representation of loading quercetin into MSN and their release behaviors when exposed to different pH solutions of 3.5 wt.% NaCl.

The release of QCT entrapped in MSN was determined by UV-visible analysis. 5 mg of MSN-QCT was dispersed in 50 mL of 3.5 wt.% NaCl at pH values within 3.00-10.00 at room temperature and the resulting solution stirring at 500 rpm using a magnetic stirrer. NaCl solution with acidic pH was obtained by adding 0.1 M HCl drop by drop to NaCl solution while NaCl solution with alkaline pH was obtained by adding 2 M NaOH drop by drop to NaCl solution. The pH adjustments were monitored with a pH meter. Being a dense colored solution, known dilutions were made and 3 mL of the diluted solution were extracted using a micropipette at a specific time interval (4 h) for the analysis. Gradual dissolution of MSN-QCT in the aqueous medium at varying pH values revealed from the turbidity changes of the solution shows that MSN-QCT can drastically change its solubility and color in the aqueous medium during the transition from acidic to alkaline pH (Fig. 3.7(b)). Fig. 3.7(c) illustrates the inhibitor release in response to pH changes in the aggressive environment.

During the experimental time scale, certain observations were made regarding shifts in the absorbance peaks. For pH 3.00, at 4 h, the quercetin peaks at 257 and 374 nm shifted to 254 and 370 nm. For pH 7.00, at 4 h the quercetin peak at 374 nm shifted to 370 nm. For pH 10.00 at 4 h, the appearance of a new peak at 318 nm was observed displacing the peculiar quercetin absorption peaks (Fig. 3.8).
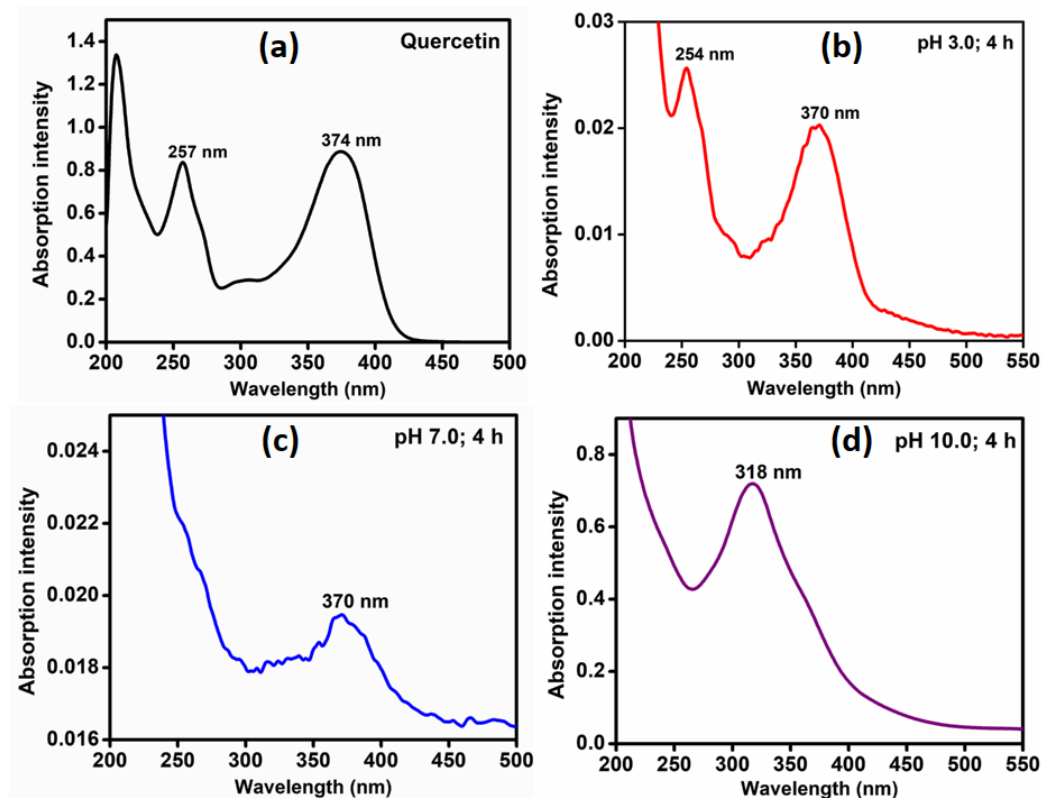
Fig. 3.8: UV-Visible spectra of (a) Quercetin in ethanol solution (b) pH 3.0, (c) pH 7.0, and (d) pH 10.0 of MSN-QCT in 3.5 wt.% NaCl during a given time scale showing shifts in the absorbance peaks. This is meant to provide insight into the possible reactions that occurred during interaction with time.

The appearance of new peaks indicates that the conjugation system in quercetin has decreased and is subsequently destroyed with the possible formation of an oxidative product[34] The release kinetics of inhibitors encapsulated into nanocontainers observed in aqueous nanocomposite suspensions with various pH values mimics the local pH changes which can be caused by the corrosion onset. pH value is known to significantly influence the electrochemical responses of polyphenols and hydroquinones[35] Significant changes in the appearance, as well as the physical and chemical states of their products, are due to oxidation reactions. The oxidation of quercetin in aqueous solution is reported to involve a two-electron process (equation 3.1) as the electrochemical behavior of quercetin is strongly dependent on solution pH.[7] QCT-H_2 represents quercetin, Q_o represents the oxidized form of quercetin.

$$QCT - H_{2\,(sol)} \rightarrow Q_{o\,(sol)} + 2H^+_{(sol)} + 2e^-_{(gas)} \tag{3.1}$$
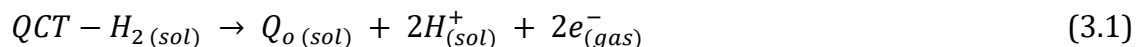
Under moderately alkaline conditions a dissociation of the quercetin molecule into the dianion A^{2-} occurs. The resultant oxidation products are unstable in the presence of air.[35] Since quercetin has five electroactive functional OH groups in its structure, the oxidation product of quercetin isn't a single product but it also consists of intermediates that undergo intramolecular rearrangements. As pH increases and with the passage of time, a reddish brown color develops in the solution due to the formation of oxidation products of quercetin such as quinone species. Also, depending on time evolution these may result in a further cleavage of the intermediates to generate quite smaller phenolic acids.[34,36] The compound(s) responsible for the appearance of the intensive color of reaction media and any isolated dry reaction products should include benzoquinone-like molecular fragments (chromophores), although the content may be small.[8] Thus, the complex variations observed in the absorption spectra indicated that the species existing at different pH may not be the simple result of deprotonation of the hydroxyl groups of QCT. At alkaline pH, stronger spectral changes in QCT support ionization of the OH group at C3 (C-ring) position. The reactivity of the flavonoid molecule at alkaline pH influencing its stability involves the C3-OH group in the C-ring; the catechol moiety in the B-ring; and the C2=C3 bond in the C-ring.[36] The reaction sequence indicating the formation of reactive quinone species of different concentrations and reactivity from quercetin as it undergoes intramolecular rearrangements is informative.[37]

3.3.2 Anticorrosion efficiency of MSN-QCT in the corrosive media

The nanocomposite was evaluated for its corrosion inhibiting action as the preliminary investigation prior to the coating evaluation. Changes in pH is a preferred trigger for corrosion protection systems due to the fact that, corrosion is usually accompanied by alkaline or acidic pH shift. Therefore, smart coatings containing inhibitor loaded containers may utilize the corrosion reaction to release the corrosion inhibitor.[13,38] The corrosion inhibiting properties of the synthesized MSN-QCT with respect to aluminum alloy 6061 were assessed by visual inspection of the metallic substrates after immersion for 15 days in different pH solutions of the NaCl.

Electrochemical impedance spectroscopy and potentiodynamic polarization were used for further analysis. During the potentiodynamic polarization analysis, after the corrosion potential of the working sample immersed in the test solution became nearly constant, cathodic and anodic polarization curves were measured at a scan rate of 1 mV/s from −250 mV to +250 mV of the OCP values.

The initial concentration of 0.5 g/L MSN-QCT in the electrolyte was investigated at different pH. The pH that triggered the most release of the inhibitor was pH 10.00. The photographs of the aluminium alloy samples after 15 days of immersion in the different electrolyte solutions (blank solution & MSN-QCT solution) are shown in Fig. 3.9. In the MSN-QCT free electrolyte (3.5 wt.% NaCl, sample a-c), the alloy surface is attacked by corrosion processes, irrespective of the pH showing pits and deposits of white corrosion products especially at pH 7.00 and 10.00. In the presence of MSN-QCT 0.5 g/L, the situation appears different but improved compared to the blank samples upon drying except for pH 3.00. At pH 3.00 in the presence of MSN-QCT, the surface appears to be heavily covered with dense deposits (panel d).

At pH 7.00, in the presence of MSN-QCT, the deposits were far less (panel e) and the solution was slightly darkened with respect to color change from the inhibitor and the duration of the study. At pH 10.0, the degree of corrosion of the alloy clearly decreases in the presence of MSN-QCT, as corrosion products are not visually seen scattered about the surface rather a reddish precipitate appeared on the top hanging portion same as in the solution and after drying (panel f). Visual analysis of the metallic substrates indicates a positive effect in using the nanocontainer/inhibitor systems, especially at alkaline pH environments.
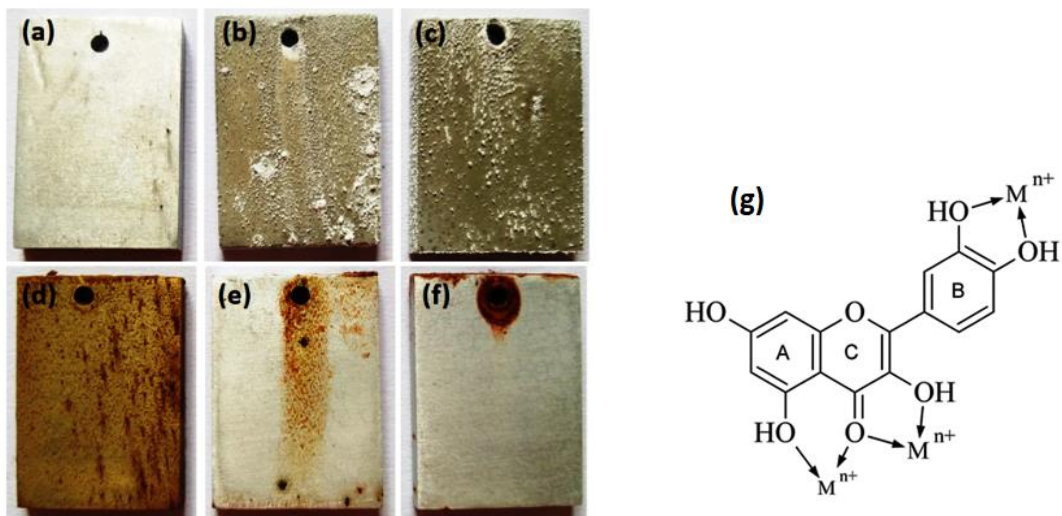
Fig. 3.9: Photographs of Al6061 surface after 15 days of immersion in 3.5 wt.% NaCl (a) pH 3.00, (b) pH 7.00 (c) pH 10.00 and 3.5 wt.% NaCl loaded with MSN-QCT (0.5 g/L) at (d) pH 3.00, (e) pH 7.00 (f) pH 10.00. (g) Possible chelating sites of quercetin coordinating with metal ions.[39]

Corresponding SEM/EDS analysis of the unwashed substrates after immersion in the different solutions without and with 0.5 g/L MSN-QCT is shown in Fig. 3.10. From the EDS analysis, the elemental distribution on the surface of the substrates in the absence of the inhibitor shows a lesser signal for Al and stronger signal for O which could be correlated to aluminium oxide/hydroxide formation. The reverse occurs in the presence of the inhibitor for the exposed aluminium alloy substrate surface where elements C and Si can also be identified from the inhibitor.
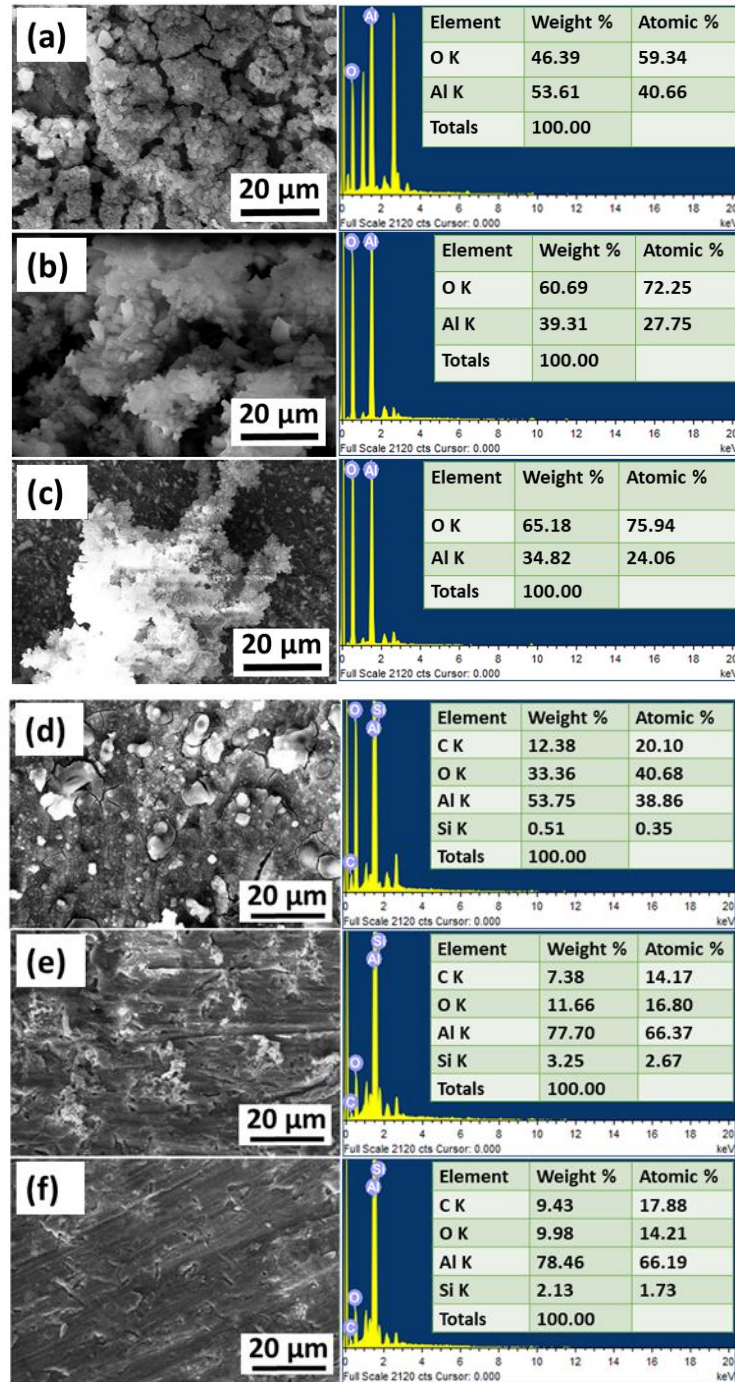
Fig. 3.10: SEM/EDS of Al6061 surface after 15 days of immersion in 3.5 wt.% NaCl without MSN-QCT (a) pH 3.00 (b) pH 7.00 (c) pH 10.00 and 3.5 wt.% NaCl loaded with MSN-QCT (0.5 g/L) at (d) pH 3.00 (e) pH 7.00 (f) pH 10.00.

The reaction products obtained were dried and analyzed with FTIR and XRD for more insight into the corrosion inhibition reactions. Significant differences were observed in the ATR-FTIR spectra and X-ray diffractogram especially for the resultant product at pH 10.00 (Fig. 3.11 & 3.12).
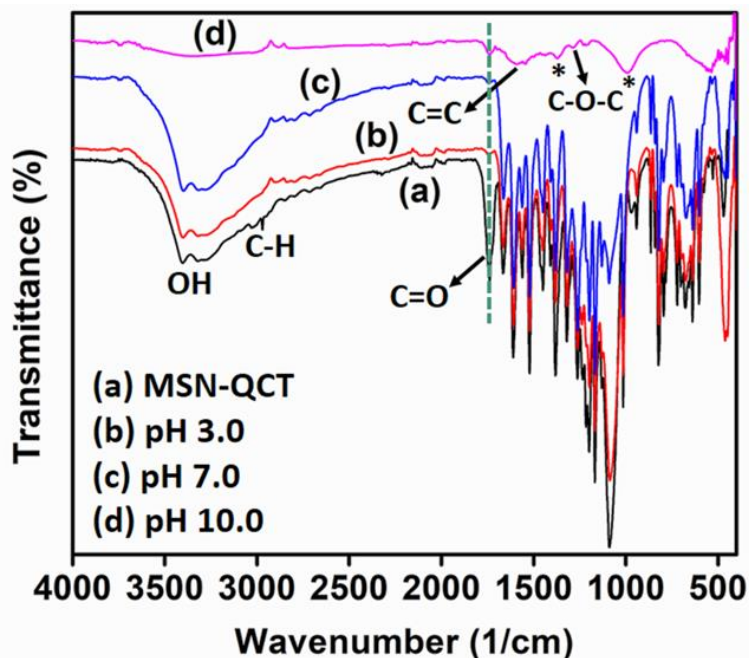
Fig. 3.11: Compared ATR-FTIR spectra of (a) MSN-QCT and the dried reaction products from the alloy surface obtained after 15 days immersion in 3.5 wt.% NaCl (b) pH 3.00, (c) pH 7.00 (d) pH 10.00. Differences in spectral pattern and intensity is observed. (*) at 1370 cm^{-1} is a shift from 1377 cm^{-1} of the Quercetin aromatic ring. (*) at 548 cm^{-1} for deformation band of alkenes. The C=O peak in MSN-QCT is almost completely reduced in all the reaction products; an indication of metal-flavonoid chelation due to metal-flavonoid complexing reactions.

In the ATR-FTIR spectra of Fig. 3.11 the spectrum of the product adsorbed on the alloy surface at pH 3.0 is much similar to that of MSN-QCT. The spectrum of the product at pH 7.0 reveals a reduction in the intensity of the Si-O-Si, and Si-O peaks compared to that of pH 3.0. Also the C=O peaks in MSN-QCT is almost completely reduced in all the pH-based spectra. The spectrum of reaction product at pH 10 is completely different from the others. At pH 10, the OH group is greatly reduced, the band at 1590 cm^{-1} represents stretching of C=C bonds of aromatic ring, 1370 cm^{-1} a shift from 1377 cm^{-1}

of the Quercetin aromatic ring. 1284 cm^{-1} represents C-O-C aryl ketone. Broadened bands at 990 cm^{-1} and 548 cm^{-1} represent deformation bands of alkenes. These findings suggest the formation of new products at alkaline pH capable of corrosion protection of the alloy.

Flavonoids easily chelate with metal ions creating complex compounds and the metal-flavonoid chelates are usually colored [40]. The color depends on the nature of flavonoid and the chelating metal ions in the complex formation. In this study, C=O position (Fig. 3.11) reveals the probable site for complexation with the metal ions. The possible coordination sites is either between 5-hydroxy and 4-carbonyl group or between 3-hydroxy and 4-carbonyl group. Similar results have been reported and with other flavonoids.[40–42] Hence the color changes in Fig. 3.9 indicate that complexes were formed with Al ion in all the pH studied but the maximum protection of the alloy was obtained at pH 10. The structure of quercetin showing possible chelating sites for coordinating to metal ions is shown in Fig. 3.9(g). In the X-ray diffractogram (Fig. 3.12) while additional peaks at 2 theta degrees of 45.50^o, 45.62^o and 56.59^o were observed for pH 10. A slight shift in the major QCT peak of 27.10 to 27.49 2θ degree was also observed. This difference in the XRD pattern of reaction products at pH 10 compared to the other pH derived products may be due to the changes occurring during the release of the inhibitor and its reaction at alkaline pH reflecting in differences in spectral patterns corresponding to probable formation of new products capable of reducing the formation of aluminium oxide/hydroxides. pH 3.0 and pH 7.0 showed strong similarities with the spectrum of MSN-QCT which is the encapsulated inhibitor in MSN.
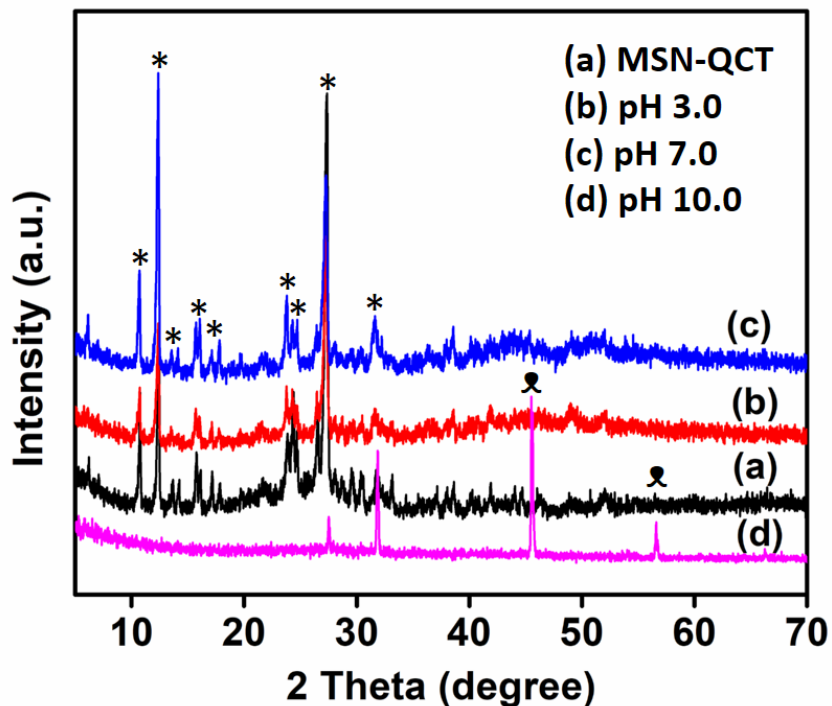
Fig. 3.12: Compared XRD patterns of (a) MSN-QCT and the dried reaction products from the alloy surface obtained after 15 days immersion in 3.5 wt.% NaCl (b) pH 3.00, (c) pH 7.00, and (d) pH 10.00. Peaks with (*) match with MSN-QCT peaks. The crystalline peaks with the symbol (*) corresponds with the crystalline peaks in MSN-QCT at 2 theta degrees of 10.76^o, 12.43^o, 13.63^o, 15.78^o, 16.06^o, 23.77^o, 24.31^o, 27.10^o and 31.57^o, 33.11^o.

Electrochemical impedance spectroscopy (EIS) was used to study the effect of the nanocomposite addition on the performance of coating film as well as provide information on the corrosion mechanism. It has effectively been used to monitor the active corrosion protection and failure processes of organic coatings.[14,43] With the nanocomposite as inhibitor the metallic substrates were immersed in 3.5 wt.% NaCl solutions containing the MSN-QCT powders (from a single MSN-QCT loading) and the pH was varied (pH 3.00, 6.44 & 10.00) for the initial EIS/Tafel analysis to determine the inhibitory action (Fig. 3.13). The samples were immersed in the respective solutions for 24 h. Bode and phase angle plots are larger and wider in the presence of 0.5 g/L MSN-QCT at pH 10.00 showing a single time constant while pH 3.00 & 6.44 show some

138

relaxation effects. pH-dependent inhibitor actions were observed in the following order: alkaline>near neutral>acidic. Acidic pH and high Cl ion activity tends to destroy the passive layer formed.[44] In alkaline solutions, the passive film of aluminum and its alloys is unstable and the matrix surface exposed to the solution suffers a higher corrosion rate. The oxidation activity of the inhibitor in the highly alkaline environment results in its release and dissolution and this promotes a passive film formation for protection of the matrix surface. In the absence of MSN-QCT, the alkaline NaCl solution results in a more negative E_{corr} value (-1248 mV; Table 3.1) of the bare alloy compared to the others. This negative shift in E_{corr} at higher pH may be due to the possible active dissolution of intermetallic particles of the alloy.[45]
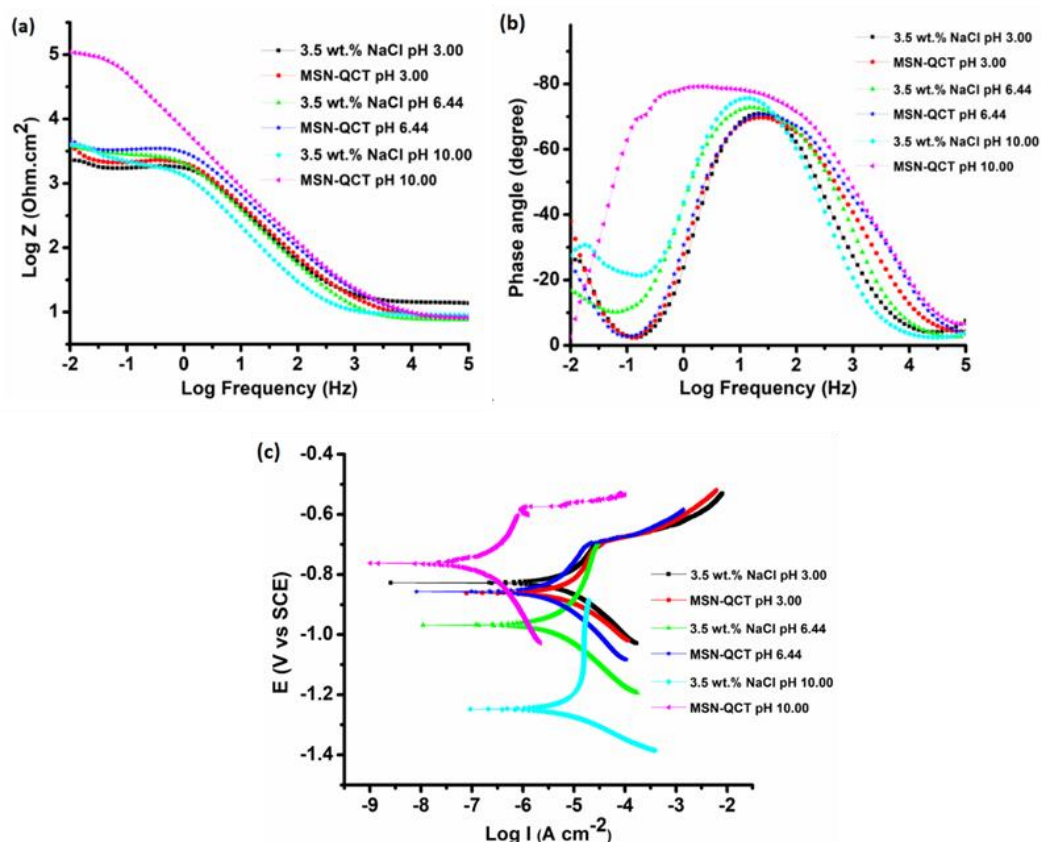
Fig. 3.13: (a) Bode and (b) phase angle plots, (c) Tafel plots for the aluminium alloy 6061 reactions at varying pH without and with 0.5 g/L MSN-QCT (single inhibitor loading) for 24 h in 3.5 wt.% NaCl solution.

Similarly, the corrosion current (I_{corr}) obtained for the bare alloy at pH 10.00 was the highest (8.941 µA cm^{-2}) compared to the other tested pH values (Table 3.1). However, in the presence of the MSN-QCT, 0.5 g/L, at pH 10.00 the displacement in the E_{corr} values to more positive potentials (-762 mV) implies oxidation reaction and passive layer formation this is also reflected in its lowest corrosion rate from the significant decrease in the I_{corr} values (0.207 µA cm^{-2}) (Table 3.1). A more positive potential is considered to have better pitting corrosion resistance [44]. pH 3.00 and 6.44 in the presence of MSN-QCT at the same concentration, shows a poor release of the inhibitor from the host shell in comparison to that of pH 10.00. Basic pH favored the release and reactions of the loaded QCT which inhibited dissolution of the metal which should normally occur at such high pH values. This confirms the successful protective action of QCT.

Table 3.1: Potentiodynamic polarization parameters obtained with MSN-QCT after 24 h immersion in 3.5 wt.% NaCl with pH changes.

Test solutions @ 24 h immersion	E_{corr} (mV)	I_{corr} (µA cm^{-2})
pH 3.00 (3.5 wt.% NaCl)	-828	8.176
pH 3.00 (with inhibitor 0.5 g/L)	-862	9.117
pH 6.44 (3.5 wt.% NaCl)	-968	4.791
pH 6.44 (with inhibitor 0.5 g/L)	-857	4.181
pH 10.00 (3.5 wt.% NaCl)	-1248	8.941
pH 10.00 (with inhibitor 0.5 g/L)	-762	0.207

3.3.3 Protective epoxy-MSN-QCT coatings

Incorporating inhibitor loaded particles in the coating provides active physical recovery although a complete coating recovery may not be obtained and is not obligatory but hindering corrosion activity in the damaged area is required.[9] In order to qualify the overall performance of the studied coatings with respect to the effect of the loaded particles; coatings without inducing any damage were also assessed along with scratched coatings. SEM micrographs of the prepared coatings had smoother

surfaces and no visible pores with the presence of the loaded nanoparticles (Fig. 3.14). With a higher magnification (insets), a dimpled pattern of the epoxy coatings were observed which can occur due to several reasons. In this case, when curing with the aliphatic amine hardener, the slow solvent volatilization during the curing process at low temperature is the probable reason. Similar results has been reported for curing of epoxies at low temperatures with aliphatic amine hardeners.[46] This results in a breath-figure pattern as observed in polymer surfaces but with the EDS analysis the underlying alloy is not exposed. The coating thickness of ~15.0 ±2.0 µm was obtained from the SEM cross-section of the coatings. The coatings were evaluated using EIS technique. The parameters of great interest while using the EIS technique are the impedance and phase angles. It is expected during active corrosion protection that the corrosion inhibitor will leach out of the coating matrix when triggered to react with the metallic surface, decreasing the electrochemical activity in the damaged site resulting in an increase in the total impedance of the system while passivating the metal surface.[47] The impedance spectra of the Al6061 coated with epoxy containing MSN-QCT in different concentrations after 48 h of immersion in 3.5 wt.% NaCl with the artificial defect are represented in the form of Bode (log frequency vs. log |Z|) and phase angle plots in Fig. 3.15 (a) and (b). The spectra of the blank coating (EP-0) and that of the lowest concentration of fillers (EP-0.5) can be divided into two frequency regions (high and low) showing 2-time constants. The spectra of higher filler concentrations (EP-1.0 and EP-3.0) are divided into three frequency regions (high, intermediate and low frequencies) showing 3-time constants all present from 2 h of immersion up to 48 h. Fig. 3.15(c) presents the Nyquist plots for the studied scratched coatings showing the increasing diameter of the capacitive loops with increasing filler concentration.
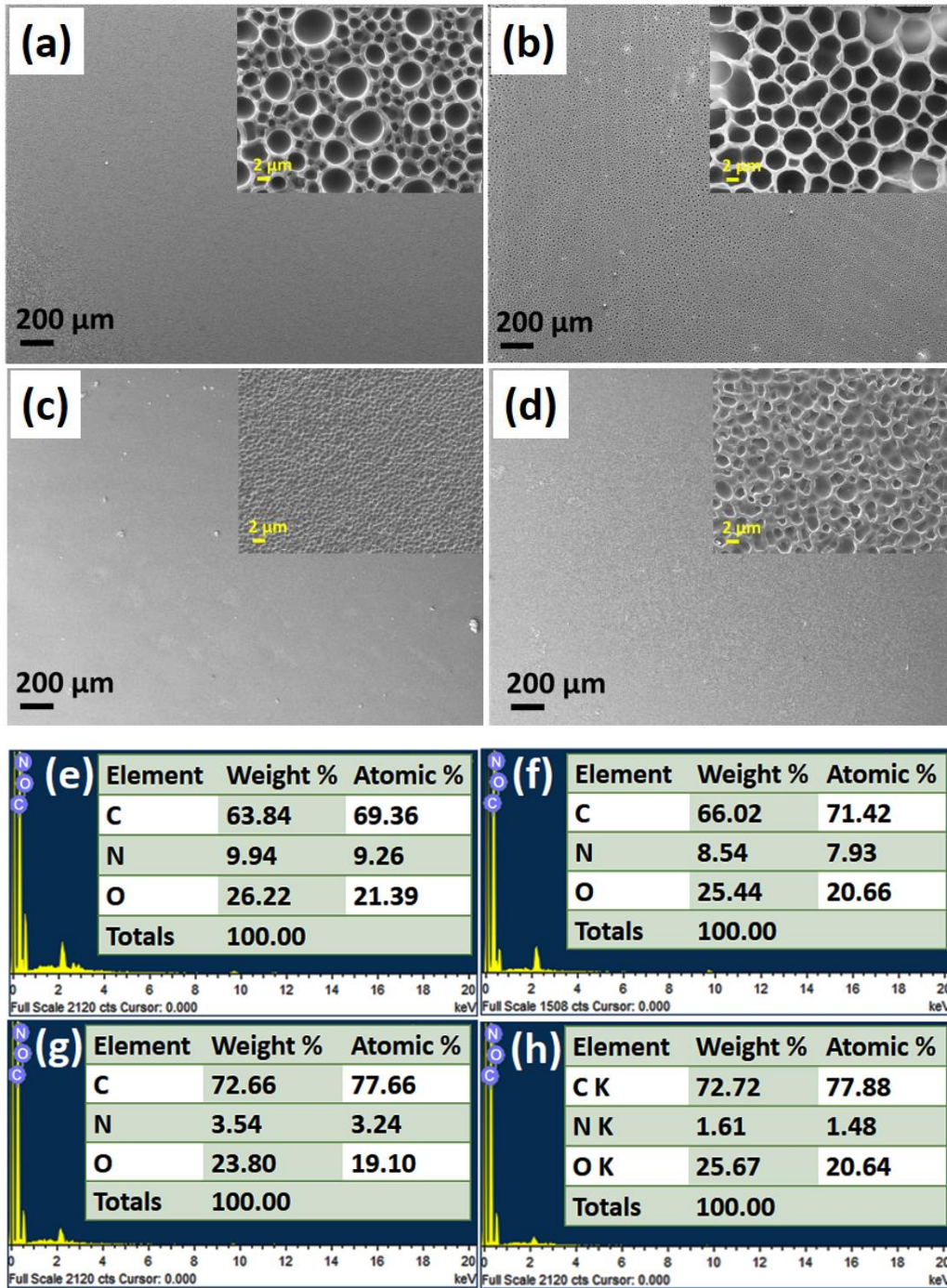
Fig. 3.14: SEM micrographs of (a) EP-0, (b) EP-0.5, (c) EP-1.0, and (d) EP-3.0 coatings and corresponding EDS of (e) EP-0, (f) EP-0.5, (g) EP-1.0, and (h) EP-3.0 coatings. Insets are 5.00K X magnification of the coatings showing the patterned nature of the coating.

The electrochemical response of a coating is usually represented at high frequencies and the relaxation processes occurring closer to the metal surface are usually studied from the lower frequencies. Furthermore, the corrosion process and mass transport of the corrosive species dominate the lower frequencies (1-0.01 Hz) of the EIS spectra.[10] To evaluate the resistive and capacitive behavior of each part of the coating systems, the EIS spectra (Fig. 3.15(a-c)) obtained after 48 h of immersion in 3.5 wt.% NaCl (pH 10.00) were fitted using equivalent circuits shown in Fig. 3.15(d). To determine the optimal models presented, EIS results were fitted to several different circuit models using ZSimpWin software until no further fitting improvement was achieved and all EIS data were considered in the fitting process (that is Bode, phase angle and Nyquist plots). The fitting provides quantitative parameters. The chosen circuits have a fit quality of chi-square values (χ^2) < 0.01. The fitting parameters for the coating response are summarized and presented in Table 3.2. Constant phase element (Q) represents the non-ideal capacitance caused by inhomogeneous nature of the interface.[48,49] R_{ct} is the charge transfer resistance is related to the kinetics of an electrochemical reaction at the interface.[10,48] R_{coat} represents the resistance of the coating layer and high R_{coat} values with the presence of fillers in the coating are indicative of better barrier properties.[10]

Active corrosion protection reflects the hindering of redox reactions as a result of inhibitor action.[50] In Fig. 3.15(d) Q_{dl} represents constant phase element equivalent to double layer capacitance at the metal-electrolyte interface as the phase angles were not equal to -90°. In the modified coatings R_{ct} is correlated to the active corrosion protection provided by the release of the inhibitor from the nanocontainers for the loaded coatings (EP-0.5-3.0). The protective layer formed increased the impedance of the loaded coatings and reduced the direct contact between corrosion inducing factors (water, oxygen, chloride ions etc.) and the metal substrate indicating a healing action. While with EP-0 there is an influence from the native aluminium oxide layer between the coating and the metal surface in the aggressive solution. Although the circuit model is the same for EP-0 and EP-0.5 (Model 1).

In Fig. 3.15(d), model 2 is the fitting circuit for EP-1.0 and EP-3.0 EIS spectra. The medium frequency resistance may be assigned to the interfacial oxide layer. Resistance of the oxide layer (R_{ox}) is a measure of the intermediate oxide barrier properties and if R_{ox} for modified coating is higher than the value for the unmodified one, this can be attributed to the inhibiting effect of the inhibitor, which prevents the propagation of cracks in the intermediate oxide layer by the suppression of the cathodic reaction. Similarly, the low values of C_{ox} or Q_{ox} in inhibitor modified coatings is attributed to the smaller area of the oxide directly exposed to the electrolyte.[48] Furthermore, higher R_{ct} values for modified coatings, implies that incorporation of inhibiting additives slows down the kinetics of the corrosion process by reducing the bare area of the metal surface. While lesser R_{ct} values for the unmodified coating implies higher area of the bare metal surface exposed and this is the consequence of the poor barrier properties of both polymer and oxide layers.[48,51]
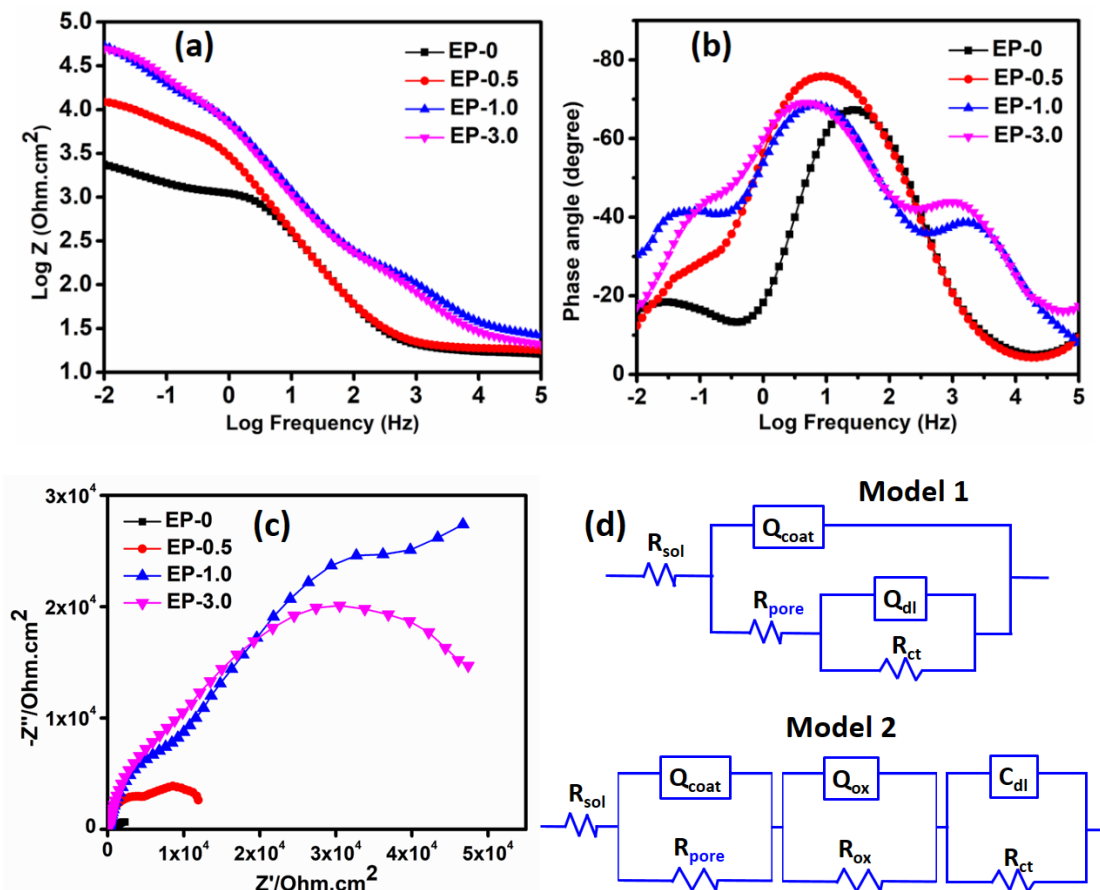
Fig. 3.15: (a) Bode plots showing the impedance and (b) phase angle plots as a function of frequency (c) Nyquist plots after 48 h of immersion in 3.5 wt.% NaCl (pH 10.00) of Al6061 substrates coated with epoxy modified with different concentrations of the MSN-QCT after making an artificial defect. (d) Equivalent circuits used to fit the experimental EIS data of scratched coatings EP-0 and EP-0.5 (model 1); EP-1.0 and EP-3.0 (model 2).

The SEM/EDS analysis in Fig 3.16 illustrates the scribed portion of the unloaded and loaded coatings after 48 h of immersion in 3.5 wt.% NaCl (pH 10.00). After the reaction time, the elemental distribution in the exposed marked area for EP showed a stronger signal for Al and a reduced bare area of the metal surface was observed for EP-1.0 which correlates with protection originating from the inhibiting components. As illustrated in Fig. 3.16 there is penetration of the electrolyte in the exposed region of the scratch, leaching and dissolution of QCT from the coating matrix. The dissolved QCT adsorbed on the exposed alloy surface and facilitated the inhibited electrochemical corrosion reactions. Related findings regarding release of inhibitors from carriers for corrosion protection have been reported.[52]

Element	Weight %	Atomic %
C K	12.15	19.66
N K	0.86	1.20
O K	32.91	40.00
Na K	3.05	2.58
Mg K	0.32	0.26
Al K	47.84	34.47
Si K	1.83	1.27
Cl K	1.03	0.56
Totals	100.00	

Element	Weight %	Atomic %
C K	41.50	58.41
N K	3.79	4.58
O K	10.71	11.32
Na K	18.02	13.26
Al K	0.25	0.16
Si K	0.02	0.01
Cl K	25.71	12.26
Totals	100.00	
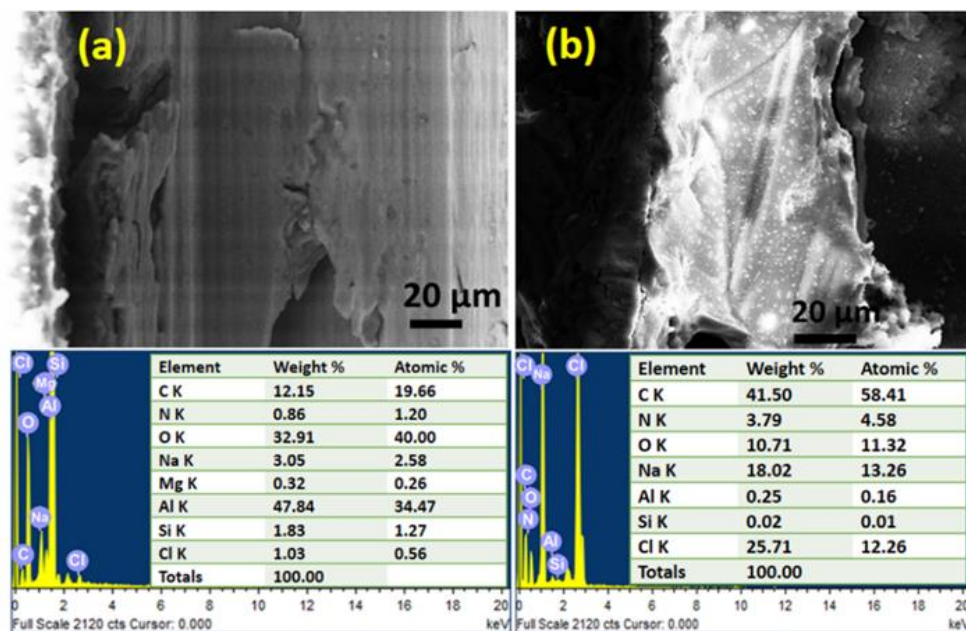
Fig. 3.16: SEM micrographs and EDS spectra within the scratched portion of both (a) EP and (b) EP-1.0 coatings after 48 h of immersion in 3.5 wt.% NaCl solution at pH 10.00.

Table 3.2: Impedance data obtained from equivalent circuits (EC) for artificially scratched EP-0, EP-0.5, EP-1.0, EP-3.0 coatings after 48 h of immersion in 3.5 wt.% NaCl solution at pH 10.00.

EC Parameters	Coating samples			
	EP-0	EP-0.5	EP-1.0	EP-3.0
R_{sol} (Ω cm^2)	17.34	19.11	25.55	18.92
Q_{coat} (S.sec^n)	5.908 x10^{-5}	5.878 x10^{-5}	8.597 x10^{-5}	6.281 x10^{-5}
n (0<n<1)	0.89	0.89	0.72	0.79
R_{coat} (Ω cm^2)	1235	7177	85280	54160
Q_{ox} (S.sec^n)	-	-	1.274 x10^{-5}	4.113 x10^{-5}
n (0<n<1)	-	-	0.78	0.68
R_{ox} (Ω cm^2)	-	-	107.2	162.6
C_{dl} (F)	-	-	2.826 x10^{-5}	3.972 x10^{-5}
Q_{dl} (S.sec^n)	3.748 x10^{-3}	7.835 x10^{-4}	-	-
n (0<n<1)	0.82	0.96	-	-
R_{ct} (Ω cm^2)	1634	6075	6376	5363
χ^2	2.9 x 10^{-3}	3.3 x 10^{-3}	3.0 x 10^{-4}	1.4 x 10^{-3}

Fig. 3.17 shows the EDS mapping of the exposed surfaces before and after 48 h of immersion in the alkaline chloride solution. In EP, the distributions of the elements mapped on the exposed substrates is shown. It is clear that Al & O are densely distributed in the scratched area as well as some contribution of C and N from the coating matrix after the immersion period. In EP-1.0 (MSN-QCT loaded coating) concentration of Al is reduced while C and O are reasonably distributed. Contributory distribution of Si from the nanocontainers is also observed. The complex film formation in the presence of the inhibitor provided corrosion protection for the underlying alloy.

Data obtained from fitting the circuit models (Table 3.2) showed that both R_{coat} and R_{ct} values were greater for all MSN-QCT loaded coatings compared to the unmodified coating, obviously demonstrating active corrosion protection. The unmodified coating was observed to be more degraded compared to the modified coatings due to the absence of inhibitors. Furthermore, addition of MSN-QCT into the epoxy coating appreciably increased the diameter of the Nyquist plots and also reflects in the magnitude of the low frequency impedance modulus ($|Z|_{0.01}$ Hz) against the reference epoxy coating as will be discussed in the later section.
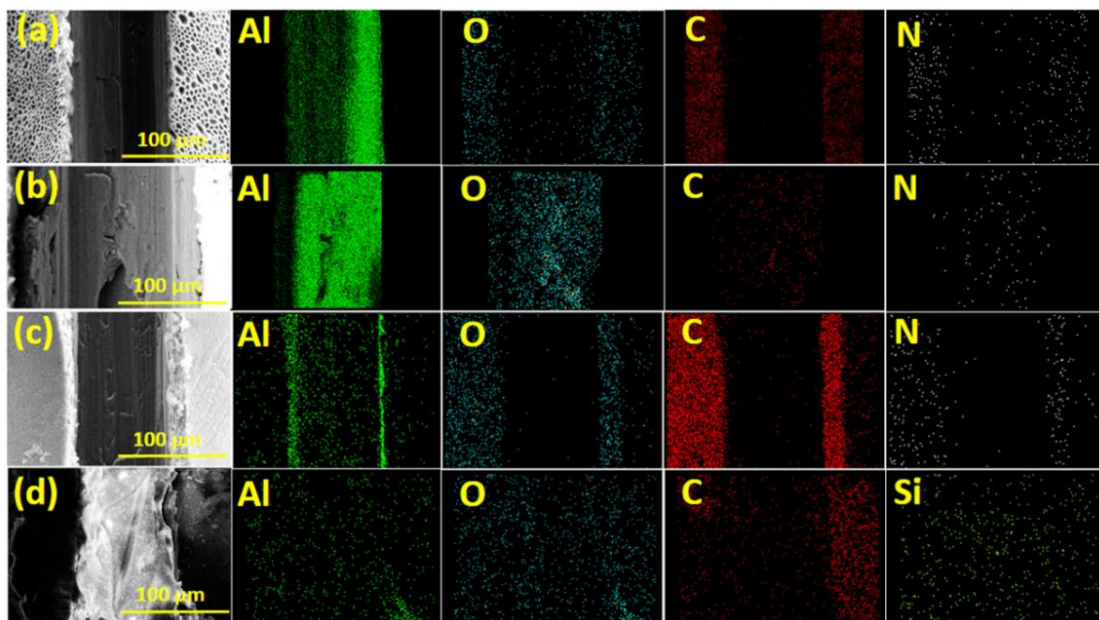
Fig. 3.17: EDS mapping of (a) EP originally scratched surface before immersion (b) EP scratched area only after immersion (c) EP-1.0 originally scratched surface before immersion (d) EP-1.0 after immersion in 3.5 wt.% NaCl solution at pH 10.00 for 48 h. The presence of Si is from the nanocontainers used in loading the inhibitor.

The unscratched coatings were also assessed under the same conditions since incorporated fillers meant for active corrosion responses can also deteriorate the integrity of the coating matrix. These are represented with Bode and phase angle plots in Fig. 3.18(a) and (b) as well as Nyquist plots in Fig. 3.18(c). The impedance data were analyzed by three different equivalent circuit models shown in Fig. 3.18(d) to interpret the evolution process. The corresponding fitting parameters are summarized in Table

3.3. EP-0 and EP-0.5 are characterized with two different models for the two-time constant cases. EP-1.0 and EP-3.0 fit model 3 which is used to simulate the one-time constant case where the Q_{coat} in parallel with R_{coat} is in series with $R_{solution}$. Although the phase angle of EP-1.0 (Fig. 3.18(b)) is observed to be higher and wider, the analyzed R_{coat} value for EP-3.0 is larger. Furthermore, as the concentration of the incorporated nanocomposite additives in the defect free epoxy coating increased, a high performance coating with excellent barrier properties was formed. From the EIS analysis, R_{coat} is extremely high for both EP 1.0 and EP-3.0 and the fitting of the EIS data corresponds with the characteristic Randles circuit (Model 3) which is possibly due to the resistance and constant phase element of the coating (Fig. 3.18(d)). Table 3.3 shows that the barrier effect increased with increasing filler concentrations in the defect free coatings analyzed in the salt solution at pH 10.00.
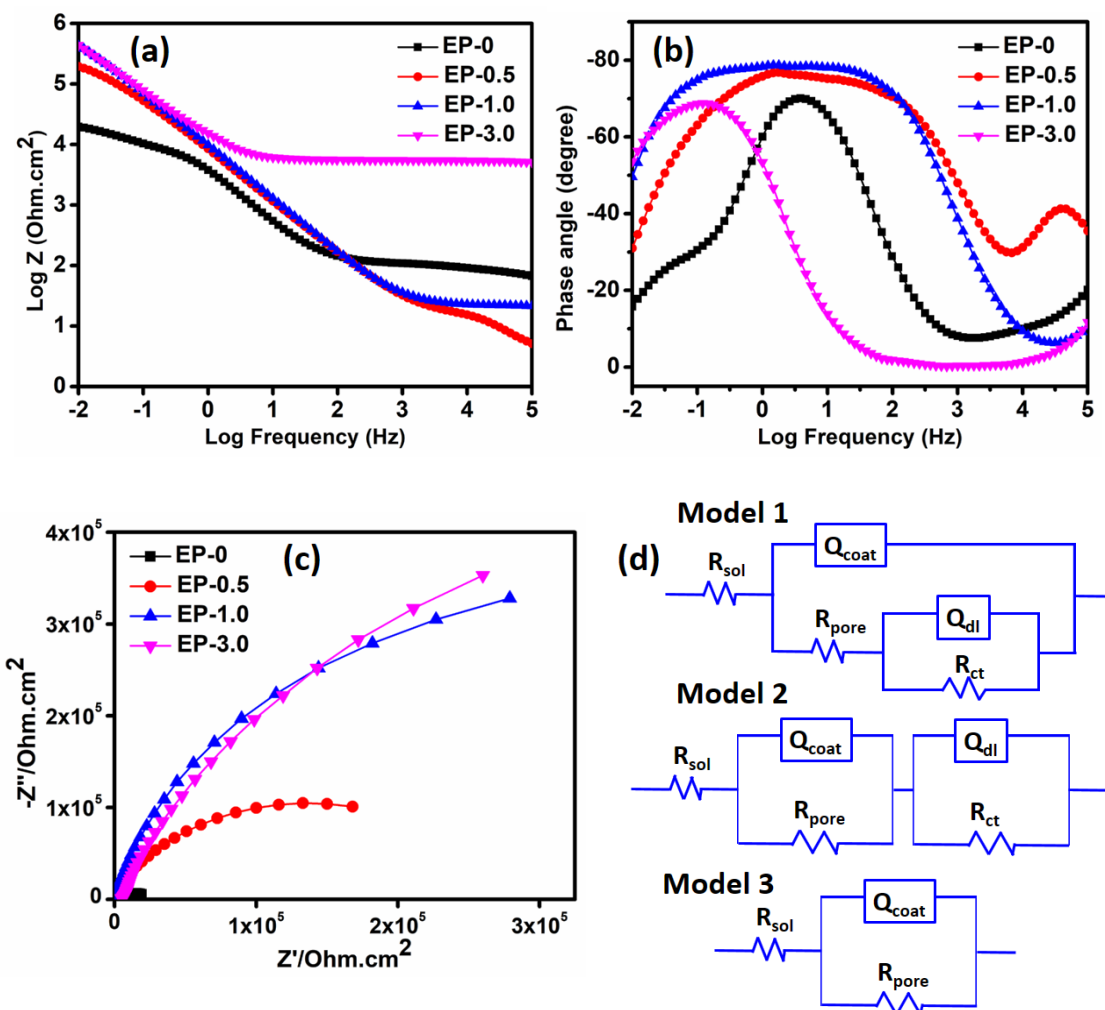
Fig. 3.18: (a) Bode plots showing the impedance and (b) phase angle plots as a function of frequency (c) Nyquist plots after 48 h of immersion in 3.5 wt.% NaCl (pH 10.00) without any artificial defect. (d) Equivalent circuits used to fit the experimental EIS data of unscratched coatings; EP-0 (model 1), EP-0.5 (model 2), EP-1.0 and EP-3.0 (model 3).

Table 3.3: Impedance data obtained from equivalent circuits (EC) for unscratched EP-0, EP-0.5, EP-1.0, EP-3.0 coatings after 48 h of immersion in 3.5 wt.% NaCl solution at pH 10.00.

EC Parameters	Coating samples			
	EP-0	EP-0.5	EP-1.0	EP-3.0
R_{sol} (Ω cm^2)	1.06×10^{-4}	3.053	22.32	5457
Q_{coat} (S.sec^n)	6.317×10^{-5}	2.252×10^{-6}	2.078×10^{-5}	1.86×10^{-5}
n (0<n<1)	0.36	0.89	0.88	0.82
R_{coat} (Ω cm^2)	131.2	12.8	8.979×10^5	1.293×10^6
Q_{dl} (S.sec^n)	2.978×10^{-5}	2.584×10^{-5}	-	-
n (0<n<1)	0.96	0.85	-	-
R_{ct} (Ω cm^2)	3.218×10^4	2.574×10^5	-	-
χ^2	2.69×10^{-3}	7.47×10^{-4}	1.80×10^{-3}	2.79×10^{-3}

Fig. 3.19 represents the evolution modulus of impedance |Z| at 0.01 Hz for both scratched (active) and unscratched (barrier performance) coatings with different concentrations of MSN-QCT during 48 h immersion in 3.5 wt.% NaCl (pH 10.00). In Fig. 3.19(a) only the defective unmodified coating shows a steady decrease in modulus of impedance at 0.01 Hz from 2-48 h. This decrease is due to the quick access of the electrolyte to the underlying metal through the defect. While the modified coatings rather show an increase in modulus of impedance for the first 24 h which can be related to the release of the corrosion inhibitor from the coating. The slight decrease with remaining time was insignificant. This action provided active protection effect in the

modified coatings. To provide additional insight into this trend, Bode and phase angle plots showing the time intervals for the modified scratched coatings is shown in Fig. 3.20. In Fig. 3.19(b), the modulus of impedance of the unmodified coating decreases after 24 h and the electrolyte gradually penetrates the coating through the pores reaching the underlying metal. Both EP-0.5 and EP-1.0 show an initial decrease in impedance at the low frequency and subsequent recovery after 24 h related to the effect of the inhibitor loaded in the coatings. The response of EP-3.0 may be due to the higher concentration of the loaded inhibiting components of the coating. The impedance at the lowest frequency ($|Z|_{0.01\,Hz}$) is known to be reflective of the corrosion resistance of the coatings.[10,14] These findings for increase in impedance modulus at the lowest frequency ($|Z|_{0.01\,Hz}$) for encapsulated inhibitor loaded coatings is in good agreement with other studies.[10,53] Fig. 3.19(c) reveals that both active and barrier protection were achieved from the scratched and unscratched coatings respectively. Hence the embedded inhibiting components did not appear to deteriorate the coating barrier properties at the concentrations evaluated.
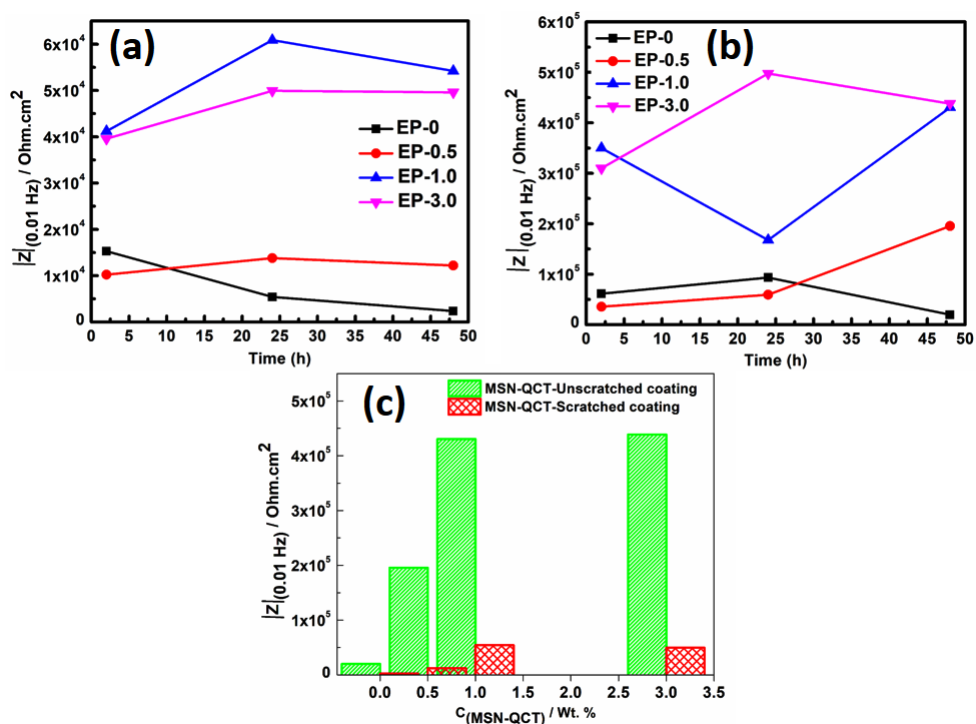
Fig. 3.19: Evolution modulus of impedance |Z| at 0.01 Hz for MSN-QCT coatings; (a) active (scratched) and (b) barrier performance coatings (unscratched) during 2-48 h

immersion. (c) Impedance |Z| measured at 0.01 Hz after 48 h immersion in 3.5 wt.% NaCl (pH 10.00) for both scratched (active) and unscratched coatings with different concentrations of MSN-QCT.
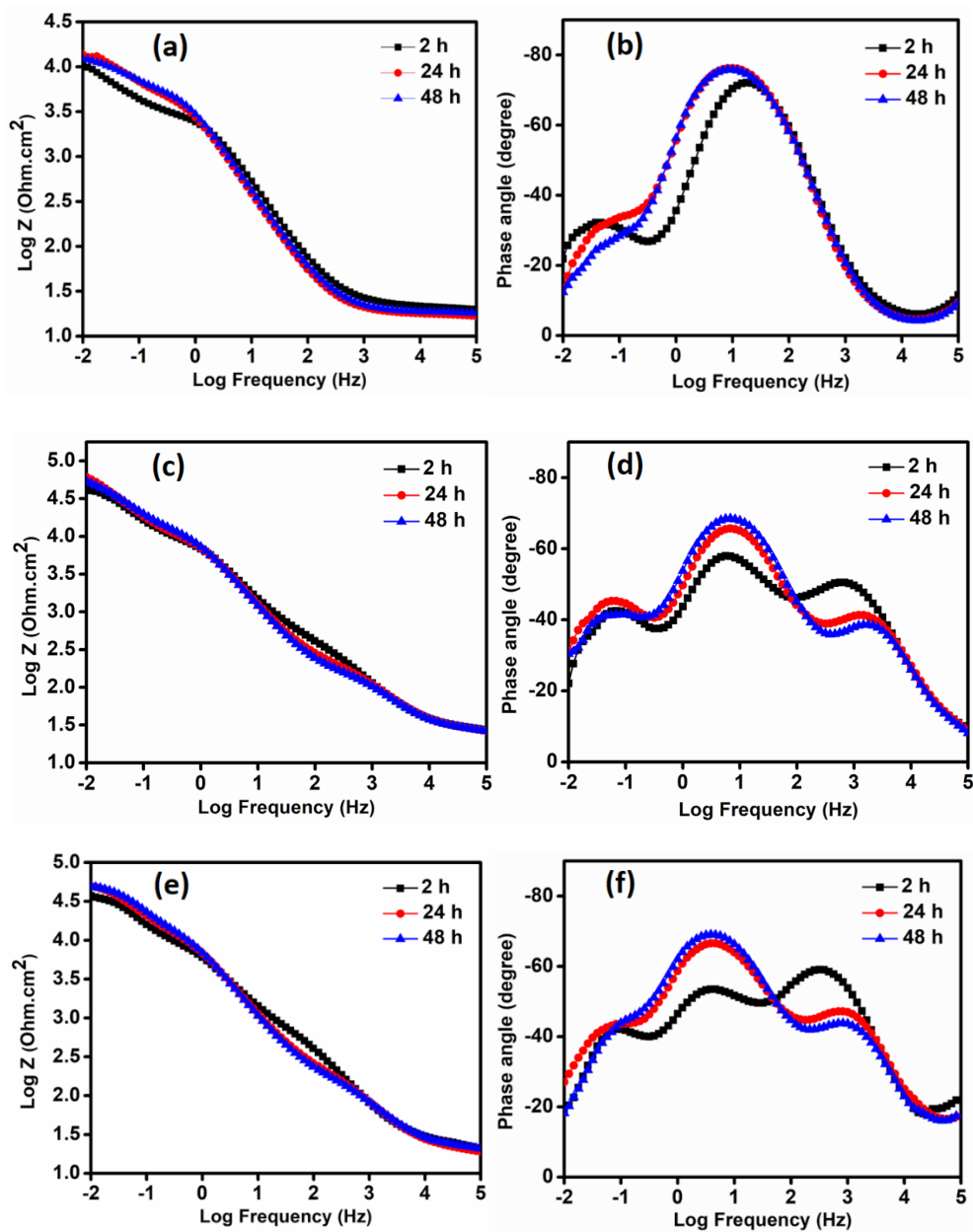
Fig. 3.20: Bode and phase angle plots for immersion in 3.5 wt.% NaCl (pH 10) solution after making an artificial scratch. (a, b) EP-0.5 (c, d) EP-1.0 (e, f) EP-3.0 to show the active anticorrosion effect with time.

The polarization curves for both scratched and scratch-free coatings are represented in Fig. 3.21(a) and (b). The corresponding fitted parameters such as corrosion current densities (I_{corr}), and corrosion potential (E_{corr}) are presented in Tables 3.4 and 3.5. The decrease in I_{corr} values from 22.750 to 0.339 ($\mu A\ cm^{-2}$) corresponds to a decrease in corrosion rates from EP-0 to EP-3.0 of the defected coatings. This enhancement in anticorrosion capability is due to the release of the active embedded components of the modified coatings which offer better corrosion resistance relative to the degrading natural oxide film formed in the defected unmodified coating. Similarly, with the defect-free coatings, I_{corr} values also decrease from 2.371 to 0.049 ($\mu A\ cm^{-2}$) for EP-0 to EP-3.0 providing lesser corrosion rates from the modified coatings. As E_{corr} increases in both defected and defect-free coatings, it indicates that attack on the underlying alloy becomes difficult due to adsorption of inhibiting components; which form a protective covering on the alloy surface thereby slowing down the corrosion rate.
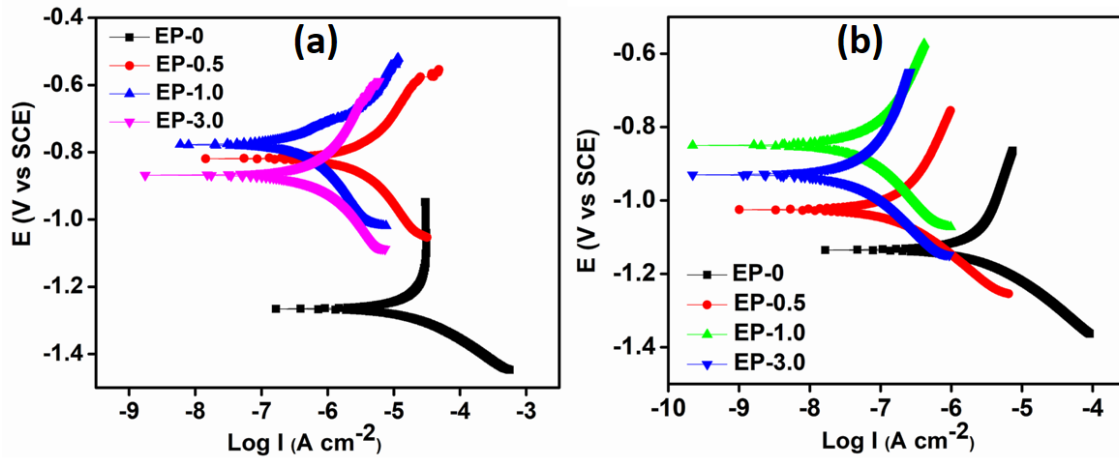
Fig. 3.21: Polarization curves after 48 h of immersion in 3.5 wt.% NaCl (pH 10.00) of Al6061 substrates coated with epoxy modified with different concentrations of the MSN-QCT; (a) with an artificial defect (b) without any artificial defect.

Table 3.4: Potentiodynamic polarization parameters obtained on the artificially scratched coatings after 48 h of immersion in 3.5 wt.% NaCl solution.

Coatings in 3.5 wt% NaCl pH 10 after 48 h (With artificial defect)	E_{corr} (mV)	I_{corr} (μA cm^{-2})
EP-0	-1266	22.750
EP-0.5	-819	3.087
EP-1.0	-777	0.339
EP-3.0	-868	0.720

Table 3.5: Potentiodynamic polarization parameters obtained on the unscratched coatings after 48 h of immersion in 3.5 wt.% NaCl solution.

Coatings in 3.5 wt% NaCl pH 10 after 48 h (Without artificial defect)	E_{corr} (mV)	I_{corr} (μA cm^{-2})
EP-0	-1135	2.371
EP-0.5	-1025	0.159
EP-1.0	-850	0.062
EP-3.0	-930	0.049

3.3.4 Antibacterial action of the epoxy-based coatings

The antibacterial action of the synthesized coatings was observed after 24 h of incubation. The capability of the loaded epoxy-based coatings on aluminium alloy 6061 substrates to inhibit bacteria adhesion/proliferation was investigated as shown with the agar disc method. Interestingly, the optical images (Fig. 3.22) reveal that all the epoxy coated samples showed antibacterial property against *P. nitroreducens*. The presence of a clear zone around the coating samples on the plates was recorded as an inhibition against the test bacterial strain. Hence the bare alloy became the control sample which had no zone of inhibition. In order to identify the cause of antibacterial activity in the unmodified epoxy coating, further experimentations were conducted to identify the specific component(s) in the coating responsible for its antibacterial activity. Both the hardener and the diluent showed zones of inhibition against the test

bacterial strain. Although the zones of inhibition obtained from evaluating quercetin alone were larger. Therefore, the inhibitory effect is a synergy of the entire components of the coating (Fig. 3.23).
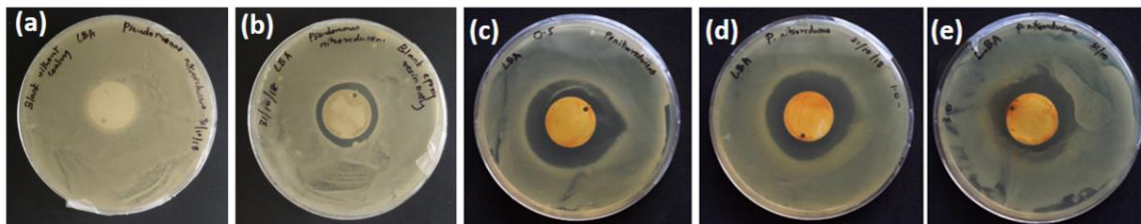
Fig. 3.22: Antibacterial activity of the epoxy coatings against *Pseudomonas nitroreducens*; (a) Control - bare Al6061, (b) unloaded epoxy coated Al6061, (c-e) 0.5, 1.0, 3.0 wt.% MSN-QCT DGEBA coating in the presence of *Pseudomonas nitroreducens* showing the zones of inhibition.

The unmodified epoxy coating contained only the diluent butanol and the hardener HY951 (identified as Triethylenetetramine; TETA). To identify the cause of antibacterial activity, 50 μL of butanol was loaded on to a paper disc (2 cm diameter) and placed on LBA plate containing *P. nitroreducens*. In parallel, 50 μL of HY951 was loaded on to a paper disc (2 cm diameter) and placed on LBA plate containing *P. nitroreducens*. Both the plates were incubated at 37°C overnight. From the results (Fig. 3.23 (a) & (b)), it was observed that HY951 and butanol presented a synergistic effect on the antibacterial activity in the blank epoxy coating. Similarly, 50 μL of a mixture of QCT in butanol was loaded on to a paper disc (2 cm diameter) and placed on LBA plate containing *P. nitroreducens* to ascertain the antibacterial efficiency of QCT (Fig. 3.23(c)) which revealed a larger zone of inhibition. Therefore, in addition to the effect of the hardener and diluent, the antibacterial action of the MSN-QCT loaded coatings was due to diffusion of QCT through the synthesized coatings as observed during the study.
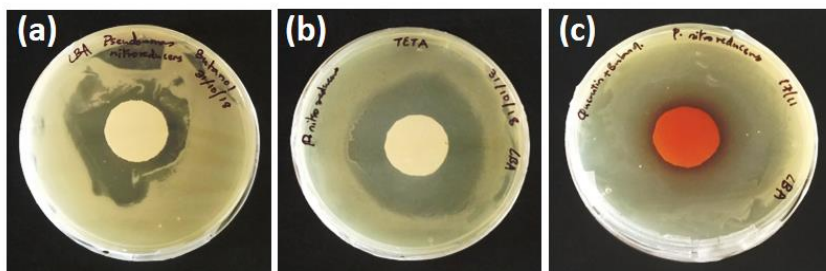
Fig. 3.23: Antibacterial activity of (a) 1-butanol, (b) HY951 (TETA), and (c) QCT/butanol against *Pseudomonas nitroreducens* showing the zones of inhibition. Concentration of QCT in butanol was 3.0 wt.% of the total mass of the hardener and the resin (same as those used in preparing the coatings).

3.4 Conclusions

It has been demonstrated in this study that the low-cost bio-based corrosion inhibitor 'Quercetin' could be loaded into mesoporous silica nanoparticles to form an effective hybrid nanocomposite with corrosion inhibiting properties. In the aggressive chloride environment, pH changes aided the understanding of the performance of the nanocomposite inhibitor which had significant corrosion inhibiting action at an alkaline pH. That is, pH 10 provided a decrease in the corrosion rate due to the chemical changes of quercetin in the basic medium over time. Being a flavonoid, the chemical modifications in the alkaline aqueous solution involves an oxidation reaction that affects the aromatic rings. These chemical changes resulted in structural rearrangements and the formation of possible intermediate products. Active corrosion protection occurred due to the release and reactions of the organic inhibitor in the alkaline chloride medium and the formation of a protective film in the scratched area. The barrier performance of the unscratched coatings was also influenced by the action of the embedded particles. Either way, the loaded coating performance surpassed the unmodified coating throughout the study in the aggressive chloride environment. In addition, the coatings showed antibacterial properties against *P. nitroreducens* with an enhanced zone of inhibition in the presence of MSN-QCT loaded coatings. Inhibitor loaded coatings are practically required for active corrosion protection systems of metallic substrates which is very important for industrial applications.

155

References

[1]   J. Buchweishaija, *Tanzania J. Sci. 35*, 77.

[2]   M. Sangeetha, S. Rajendran, T. S. Muthumegala, A. Krishnaveni, *ZAŠTITA Mater.* **2011**, *52*, 3.

[3]   M. A. Quraishi, A. Singh, V. K. Singh, D. K. Yadav, A. K. Singh, *Mater. Chem. Phys.* **2010**, *122*, 114.

[4]   W. Bors, W. Heller, C. Michael, M. Saran, In *Methods in enzymology, Vol. 186*; CA Rice, E. V. and L. P., Ed.; Academic Press Inc.: New York, 1990; pp. 343–355.

[5]   L. C. Pirvu, In *Developments in Corrosion Protection.*; Mahmood Aliofkhazraei, Ed.; IntechOpen: UK, 2014; pp. 181–197.

[6]   K. E.A. AbouAitah, A. A. Farghali, *J. Nanomed. Nanotechnol.* **2016**, *07*.

[7]   H. R. Zare, M. Namazian, N. Nasirizadeh, *J. Electroanal. Chem.* **2005**, *584*, 77.

[8]   I. Zenkevich, A. Eshchenko, S. Makarova, A. Vitenberg, Y. Dobryakov, V. Utsal, *Molecules* **2007**, *12*, 654.

[9]   J. Tedim, S. K. Poznyak, A. Kuznetsova, D. Raps, T. Hack, M. L. Zheludkevich, M. G. S. Ferreira, *ACS Appl. Mater. Interfaces* **2010**, *2*, 1528.

[10]   D. Borisova, D. Akçakayıran, M. Schenderlein, H. Möhwald, D. G. Shchukin, *Adv. Funct. Mater.* **2013**, *23*, 3799.

[11]   T. H. Tran, A. Vimalanandan, G. Genchev, J. Fickert, K. Landfester, D. Crespy, M. Rohwerder, *Adv. Mater.* **2015**, *27*, 3825.

[12]   S. Amiri, A. Rahimi, *J. Polym. Res.* **2014**, *21*, 566.

[13]   D. Borisova, H. Möhwald, D. G. Shchukin, *ACS Nano* **2011**, *5*, 1939.

[14]   M. Wang, M. Liu, J. Fu, *J. Mater. Chem. A* **2015**, *3*, 6423.

[15]   S. K. Natarajan, S. Selvaraj, *RSC Adv.* **2014**, *4*, 14328.

[16]   M. Vallet-Regí, F. Balas, D. Arcos, *Angew. Chemie Int. Ed.* **2007**, *46*, 7548.

[17]   A. Keyvani, M. Yeganeh, H. Rezaeyan, *Prog. Nat. Sci. Mater. Int.* **2017**, *27*, 261.

[18]   X. Ma, L. Xu, W. Wang, Z. Lin, X. Li, *Corros. Sci.* **2017**, *120*, 139.

[19]   M. L. Zheludkevich, J. Tedim, M. G. S. Ferreira, *Electrochim. Acta* **2012**, *82*, 314.

[20]   L. Cao, H. Zhang, C. Cao, J. Zhang, F. Li, Q. H.- Nanomaterials, undefined 2016, *mdpi.com*.

[21] Y. Zhu, J. Shi, H. Chen, W. Shen, X. D.-M. and Mesoporous, undefined 2005, *Elsevier*.

[22] P. J. Launer, B. Arkles, In *Silicon Compounds: Silanes & Silicones*; Gelest, Inc: Morrisville, PA, 2013; pp. 175–178.

[23] K. Möller, J. Kobler, T. Bein, *Adv. Funct. Mater.* **2007**, *17*, 605.

[24] Y. Qi, M. Jiang, Y.-L. Cui, L. Zhao, X. Zhou, *Nanoscale Res. Lett.* **2015**, *10*, 408.

[25] I. C. C. M. Porto, T. G. Nascimento, J. M. S. Oliveira, P. H. Freitas, A. Haimeur, R. França, *Eur. J. Oral Sci.* **2018**, *126*, 146.

[26] J.-T. Zhang, J.-M. Hu, J.-Q. Zhang, C.-N. Cao, *Prog. Org. Coatings* **2004**, *51*, 145.

[27] T. Chen, Q. Zhang, J. Xu, J. Pan, Y.-T. Cheng, *RSC Adv.* **2016**, *6*, 29308.

[28] E. Vunain, N. N. Opembe, K. Jalama, A. K. Mishra, R. Meijboom, *J. Therm. Anal. Calorim.* **2014**, *115*, 1487.

[29] G. S. Borghetti, J. P. Carini, S. B. Honorato, A. P. Ayala, J. C. F. Moreira, V. L. Bassani, *Thermochim. Acta* **2012**, *539*, 109.

[30] E. P. Porcu, M. Cossu, G. Rassu, P. Giunchedi, G. Cerri, J. Pourová, I. Najmanová, T. Migkos, V. Pilařová, L. Nováková, P. Mladěnka, E. Gavini, *Int. J. Pharm.* **2018**, *541*, 224.

[31] Ş. GÜNAYDIN, A. YILMAZ, *TURKISH J. Chem.* **2015**, *39*, 317.

[32] S. Tang, X. Huang, X. Chen, N. Zheng, *Adv. Funct. Mater.* **2010**, *20*, 2442.

[33] A. Chenan, S. Ramya, R. P. George, U. Kamachi Mudali, *Ceram. Int.* **2014**, *40*, 10457.

[34] A. Zhou, S. Kikandi, O. A. Sadik, *Electrochem. commun.* **2007**, *9*, 2246.

[35] R. Sokolová, Š. Ramešová, I. Degano, M. Hromadová, M. Gál, J. Žabka, *Chem. Commun.* **2012**, *48*, 3433.

[36] Z. Jurasekova, C. Domingo, J. V. Garcia-Ramos, S. Sanchez-Cortes, *Phys. Chem. Chem. Phys.* **2014**, *16*, 12802.

[37] V. Stepanic, A. C. Gasparovic, K. G. Troselj, D. Amic, N. Zarkovic, .

[38] C. Zea, R. Barranco-García, B. Chico, I. Díaz, M. Morcillo, D. de la Fuente, *Int. J. Corros.* **2015**, *2015*, 1.

[39] M. M. Kasprzak, A. Erxleben, J. Ochocki, *RSC Adv.* **2015**, *5*, 45853.

[40]   D. Malesev, V. Kuntic, *J. Serbian Chem. Soc.* **2007**, *72*, 921.

[41]   K. Pyrzynska, A. Pękal, *Crit. Rev. Anal. Chem.* **2011**, *41*, 335.

[42]   M. Symonowicz, M. Kolanek, *Biotechnol Food Sci* **2012**, *76*, 35.

[43]   W. Wang, W. Li, L. Song, W. Fan, C. Xiong, X. Gao, X. Zhang, X. Liu, *J. Electrochem. Soc.* **2017**, *164*, C635.

[44]   F.-Y. Ma, In *Pitting Corrosion*; Bensalah, N., Ed.; InTech, 2012.

[45]   G. Venkatasubramanian, S. M. A, A. K. Jha, *Res. J. Chem. Sci.* **2013**, *3*, 74.

[46]   D. Liu, W. Zhao, S. Liu, Q. Cen, Q. Xue, *Surf. Topogr. Metrol. Prop.* **2017**, *5*, 024003.

[47]   Y. Gonzalez-Garcia, S. J. Garcia, J. M. C. Mol, In *Active Protective Coatings,*; Springer, Dordrecht, 2016; pp. 203–240.

[48]   A. Latnikova, D. Grigoriev, M. Schenderlein, H. Möhwald, D. Shchukin, *Soft Matter* **2012**, *8*, 10837.

[49]   M. Behzadnasab, S. M. Mirabedini, M. Esfandeh, R. R. Farnood, *Prog. Org. Coatings* **2017**, *105*, 212.

[50]   F. Maia, J. Tedim, A. D. Lisenkov, A. N. Salak, M. L. Zheludkevich, M. G. S. Ferreira, *Nanoscale* **2012**, *4*, 1287.

[51]   H. Zhao, J. Ding, H. Yu, *ChemistrySelect* **2018**, *3*, 11277.

[52]   H. Qian, D. Xu, C. Du, D. Zhang, X. Li, L. Huang, L. Deng, Y. Tu, J. M. C. Mol, H. A. Terryn, *J. Mater. Chem. A* **2017**, *5*, 2355.

[53]   B. Qian, M. Michailidis, M. Bilton, T. Hobson, Z. Zheng, D. Shchukin, *Electrochim. Acta* **2019**, *297*, 1035.

Chapter 4

Biogenic Ag Nanoparticles of Neem Leaves Extract; its Structural Evaluation and Antimicrobial Investigations
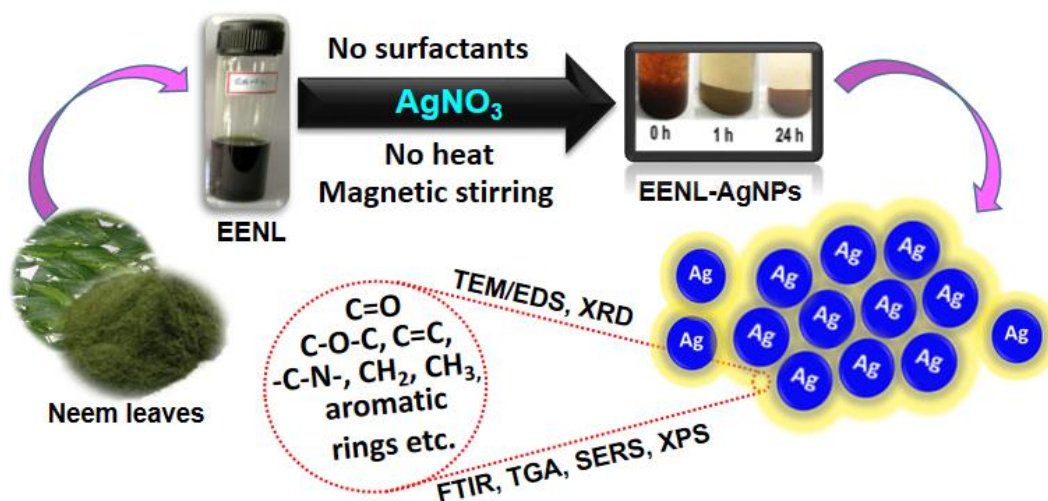
Abstract

Silver nanocrystals have been successfully fabricated by the bioreduction route using the ethanolic extract of Azadirachta indica (Neem) leaves as the reducing and capping agent without the solvent interference. The silver nanocrystals were grown in a single-step method, at room temperature, and without the influence of external energy or surfactants. As a function of the ratio of silver ions to reducing agent molecules, the nanoparticles were characterized by UV-Vis spectroscopy and transmission electron microscopy (TEM). The nanoparticles were roughly spherical and polydispersed with diameters less than 40 nm as determined with High-resolution transmission electron microscopy (HRTEM). Fast Fourier Transform analysis (FFT) and X-ray diffraction (XRD) analysis elucidated the crystalline nature of the nanoparticles. The presence of participating functional groups was determined with FTIR. The SERS activity of the silver nanoparticles was explored using 30 µM solution of Rhodamine B as the Raman probe molecule. The bioreduction process was monitored through SERS fingerprinting detecting vibrational energies of metal-ligand bonds. It was possible to detect the SERS spectral pattern of the probe

molecules on the Ag nanoparticles without the use of any aggregating analytes. Thus, the formation of probable intra and inter-particle hot-spots is attributed to evaporation-induced aggregation. Furthermore, the effect of stirring and precursor salt concentration influenced the kinetics involved in the fabrication process. The thermal stability of the lyophilized nanoparticles prepared from 0.1 M AgNO$_3$ was evaluated with TGA and had a residual mass of 60% at 600°C. XPS studies was used to validate the compositional and chemical-state information. The biomass capped silver nanoparticles provided antimicrobial activity by inhibiting the growth of biofilm-forming bacteria like Pseudomonas nitroreducens, and the fungi Aspergillus unguis - NII 08123.

4.1   Introduction

Metal nanoparticles have been investigated extensively over the years. Several reduction processes have been applied in the preparation of stable silver nanoparticles, such as chemical reduction in aqueous media with and without stabilizers, radiation chemical reduction, thermal decomposition in organic solvents, Langmuir-Blodgett films, microwave irradiation, photolytic, sonochemical, electrochemical reduction, bioreduction etc. The peculiarity of silver nanoparticles is due to its unique antibacterial, optical, electrical, catalytic properties etc. and also its response as substrates for surface-enhanced Raman spectroscopy (SERS).[1,2] The use of biomaterials is aimed at reducing toxicity in manufacturing and applications. It is believed that natural vegetative resources are still very much underutilized. Biomaterials such as plants can be suitably scaled up for large-scale synthesis of nanoparticles. The bio-fabrication process reduces the synthesis steps, environmental risks and cost[3] alongside the intensive use of synthetic reactants and solvents. Furthermore, the importance of this biological synthesis is that of yielding nanoparticles capped with biological entities, which have improved biocompatibility and can be used in many biomedical applications.[4] Thus, we are interested in using materials that will contribute to the health and environmental protection towards biocompatible and biodegradable value-added products.

But a comparatively better option to the use of whole plants is that of plant biomass and extracts in the fabrication of metal nanoparticles. However, the use of

plant biomass proffers difficulty in purification of as-synthesized metal nanoparticles prior to their applications. Functional groups (e.g. hydroxyl groups) play key reductive roles in the formation of metal nanomaterials while the strong interaction between biomolecules and metal nanomaterials influences their stability. Also, higher reduction rates of metal precursors with facile shape control of the metal nanoparticles have been observed.[5] The biomass-related process for synthesizing silver nanoparticles is simple and emerging as a competitive method to the conventional physical and chemical methods. The use of silver nanoparticles has gained recognition in several sectors. Previous studies such as Shankar et al.[6] on the synthesis of silver nanoparticles from aqueous extracts of Neem leaves by bioreduction method described another useful application of the widely acknowledged and viable plant. This led to various other studies on the synthesis of silver nanoparticles from the same aqueous extract of Neem leaves,[7–9] etc. and has been mainly applied in the biomedical sector for inhibiting the growth of some microorganisms. Neem, the popular age-long sustainable medicinal plant referred to as the 'village dispensary' and recognized by US National Academy of Sciences as 'Neem - a tree for solving global problems' contains over 140 active phytochemicals in the entire plant subdivided into isoprenoids and non-isoprenoids.[10–12] But the field of nanotechnology has allowed our aptitude to formulate, model and characterize nanostructured materials in new ways resulting in the recent development encouraging highly desirable properties. These nanomaterials are uniquely functional due to their large surface area to volume ratios, size and shape effects and also quantum effects.[13]

The importance of the present work lies in the fabrication of silver nanocrystals from the ethanolic extract of Neem leaves and its response in SERS interrogation providing a correlation with other characterizations for the reducing, capping and stabilizing properties of the crude extract during and after the nanoparticle synthesis. Furthermore, exploring its antimicrobial activity by inhibiting the growth of *Pseudomonas nitroreducens*, and *Aspergillus unguis* - NII 08123 as estimated by the zones of inhibition. In this study, the prepared silver nanocrystals from the ethanolic extract of Neem leaves (EENL) is referred to hereafter as EENL-AgNPs. The SERS activity in the absence of aggregating agents but in the presence of a model analyte is reported including characteristics of

Raman spectra of the plant extract. XPS enabled determination of the compositions and chemical species of EENL-AgNPs in their near-surface regions. To the best of our knowledge, neither silver nanoparticles synthesized by bioreduction of Neem nor Neem extracts have been reported to inhibit the growth of *Pseudomonas nitroreducens*, and *Aspergillus unguis* - NII 08123. The approach herein contributes to inexpensive, facile and green route to nanocrystalline silver fabrication, highlighting its antimicrobial responses.

4.2 Materials and methods

4.2.1 Materials

Neem leaves were collected from healthy trees within CSIR-NIIST. Silver nitrate (99.0%) ACS reagent was purchased from Sigma-Aldrich and used as received. Rhodamine B was purchased from Alfa Aesar, England and KBr for IR spectroscopy was purchased from Spectrochem Pvt. Ltd., Mumbai, India. Ethanol (99.9%) was procured from Changshu Hongsheng Fine Chemicals Co., Ltd, China. Ultrapure deionized (DI) water of 18.2 MΩ·cm resistivity at 25°C (Milli-Q purifier system, Merck, Germany) was used in preparing the standard solutions. The strains *Pseudomonas nitroreducens* and *Aspergillus unguis* - NII 08123 were procured from NIIST culture collection, Thiruvanathapuram, Kerala.

4.2.2 Methods

4.2.2.1 Preparation of EENL

Ethanolic extract of Neem leaves (EENL) was prepared by applying the procedure described in Rodríguez-León et al.[14] with some modifications. All the same, a brief is provided here. 10 g of dried Neem leaves were put in a flask, and 100 mL of an ethanol/water solution (70:30 v/v) was added. The mixture was magnetically stirred for one day at room temperature (T = 25°C), filtered three times with Whatman no. 1 filter paper to obtain the ethanolic extract.

4.2.2.2 Biosynthesis of silver nanoparticles

10 mL of EENL (10% w/v) and 90 mL of each silver nitrate solution (a) 1×10^{-3} M, (b) 3×10^{-3} M, (c) 5×10^{-3} M, (d) 10×10^{-3} M and (e) 0.1 M were mixed by dropwise addition of the reducing agent. Each solution was kept on magnetic stirring at 500 rpm. After complete addition, further stirring for 15 min was observed and the mixture was allowed to stand for 24 h away from light. Thereafter, each mixture was centrifuged and washed severally with DI water and

the available residue was transferred to a freeze dryer. Finally, the obtained powder was subjected to XRD, FTIR, TGA and XPS.

4.2.3 Physicochemical and morphological characterizations

UV-Visible spectrophotometer model UV-2401PC (SHIMADZU) was used for absorbance measurements. 0.2 mL each of the samples were diluted up to 5 mL with DI water prior to each measurement. The UV-visible spectra of the resulting diluents were monitored as a function of silver salt concentration and reaction time at a resolution of 1.0 nm for a range of 200-800 nm. DLS and ζ-potential measurements were performed using Malvern Zetasizer Nano ZS90, Germany. For transmission electron microscopy (TEM) analysis, purification by centrifuging was done for up to seven times to reduce the quantity of biomaterial capping the nanoparticles, then few drops of the obtained silver nanoparticles were placed onto a carbon-coated copper grid and allowed to evaporate for 2-3 days. Micrographs from TEM and the live Fast Fourier Transform (FFT) analysis were obtained using (JEOL 2010) operated at 300 kV. Elemental composition of the prepared metal nanoparticles was determined with an energy dispersive spectrometer (EDS) Technai G^2 30LaB$_6$, ST attached to the transmission electron microscope. To evaluate the crystalline nature of the silver nanoparticles, X-ray Diffraction (XRD) analysis was undertaken using XRD, PANalytical, Netherlands with Cu Kα radiation at a 2θ range of 10-90°. The presence of participating functional groups was determined using Fourier Transform Infrared Spectroscopy (FTIR), (IRPrestige-21 SHIMADZU) in transmittance mode by KBr pellet method. The spectral pattern and SERS measurements of the fabricated silver nanoparticles were performed under a confocal Raman microscope (α-300R, S/N 100-1200-896 WITec Wissenschaftline Instrument & Technologie GmbH, Germany) with a laser beam of excitation wavelength 633 nm and 7 mW powers, directed to the sample through 20× objective with 600 g/mm grating and a Peltier cooled CCD detector. Stokes shifted Raman spectra were collected in the range of 400-3000 cm^{-1} with 1 cm^{-1} resolution and an integration time of 2 seconds and 20 accumulations. Prior to every measurement in solid-phase detection, a drop of the colloidal solution was drop cast onto a clean glass slide and the solvent was allowed to evaporate at ambient temperature and calibration with a silicon standard (Raman peak centered at 520 cm^{-1}) was performed. *WI-Tec Project plus* (v 2.1) software package

was used for data evaluation. The SERS analysis was investigated with a probe molecule. In the presence of the probe molecule; Rhodamine B (RB), the samples were prepared by mixing the probe molecule with Ag colloids in a ratio of 1:9 (v/v) while varying the concentration of the probe molecule for optimum SERS enhancement. SERS spectra for dried sample were obtained from different locations. Thermogravimetric analysis (TGA) of the bioreduced silver nanoparticles was carried out on thermal analyzer (STA 7300 Thermal Analysis System, Hitachi) within the temperature range of 30°C to 600°C at a heating rate of 10°C/min under an inert atmosphere of argon. The TGA experiments were performed to monitor the % weight loss of the nanoparticles and its thermal stability. The surface chemistry of EENL-AgNPs were analyzed using X-ray photoelectron spectroscopy (XPS, PHI 5000 Versa Probe II, ULVAC-PHI Inc., USA) equipped with micro focused (200 μm, 15 KV) monochromatic Al-Kα X-Ray source (hν = 1486.6 eV). Both survey spectra and narrow scan (high-resolution spectra) were recorded. Survey scans were recorded with an X-ray source power of 50 W and pass energy of 187.85 eV. High-resolution spectra of the major elements were recorded at 46.95 eV pass energy.

4.2.4 Evaluation of antimicrobial activities of EENL-AgNPs

The EENL-AgNPs were tested for both antibacterial and antifungal activities by the Disc diffusion method. *Pseudomonas nitroreducens* and *Aspergillus unguis* - NII 08123 were taken as the test bacteria and fungus. For bacterial culturing, the culture media (Luria Bertani Broth and LB Agar) and glass wares were autoclaved at 121°C, 15 psi for 15 min, before the experiments. After cooling, a loop of *Pseudomonas nitroreducens* strain was inoculated in 100 mL Luria Bertani Broth under sterile conditions and incubated at 37°C, overnight. After the incubation, 100 μL of the culture was uniformly plated on the Luria Bertani Agar petri plates using sterile L-rod. The sterilized circular paper disc of 15 mm diameter was placed in the center of petri plates in contact with the culture and 50 μL of EENL-AgNPs was pipetted onto it. Blank sterilized discs was used as control in the absence of EENL-AgNPs while $AgNO_3$ of same concentration was also investigated. The plates were examined for possible clear zone formation after 24 h incubation at 37°C. The zone of inhibition (halo formation) observed was measured. The experiments were carried out in triplicates.

For the antifungal activity, the fungus culture media (Potato Dextrose Agar) and glass wares were autoclaved at 121°C, 15 psi for 15 min, prior to the experiments. The fungus, *Aspergillus unguis* - NII 08123 was cultured on Potato Dextrose Agar slants for 72 h. The sporulated culture was treated with sterile 0.85% NaCl solution to dislodge the spores to form a spore suspension according to the modified protocol of De Lira Moto.[15] 75 μL of the spore suspension was uniformly plated on sterile Potato Dextrose Agar plates using sterile L-rod. 50 μL of EENL-AgNPs was pipetted onto the sterilized paper disc 15 mm diameter and placed in the center of petri plates in contact with the culture. In the absence of EENL-AgNPs, AgNO$_3$ of the same concentration was also investigated. The plates were examined for possible clear zone formation after 72 h incubation at 30°C. The zone of inhibition (halo formation) was detected and measured. The entire antimicrobial experiment was done in triplicates. Concentrations of the lyophilized EENL-AgNPs studied were 1 mg/mL and 5 mg/mL with DI water as the dispersant.

4.3   Results and discussion

4.3.1 Characterization of the bio-reduced silver nanoparticles

4.3.1.1 Bio-reduction reaction

Extracts of Neem leaves and bark have been reported to possess better metal chelating properties. This property can be attributed to their endogenous chelating agents, primarily phenolic compounds with properly oriented functional groups, capable of chelating metal ions.[16] Furthermore, in a quantitative estimation of total flavonoid reported by Ghimeray et al.[16] Neem leaves were found to have higher flavonoid content than the bark of the Neem plant. The nature and quantity of phytochemicals extracted from Neem differ depending upon the type of extracting solvent and methodology adopted. Higher concentrations of more bioactive flavonoid compounds can be obtained with ethanol extract especially with 70% ethanol due to its higher polarity than pure ethanol. The active phyto-compounds in the leaves extracted with ethanol include quercetin, rutin, lupeol, ellagic acid, β-sitosterol, ferulic acid,[17,18] azadirachtin[19] etc. Nanoparticles of silver were generated via bio-reduction method in the presence of EENL. The Liquid-phase synthesis has the main advantage of forming plenty of nanoparticles (NPs), with a greater degree of control over particle size.[20] The formation of silver

nanoparticles (AgNPs) starts almost immediately, as shown in Fig. 4.1 with a significant color shift of the solution towards a light yellow, thus suggesting that the chemical reaction took place and that the seeds are available in the solution. As the concentration of the silver ions increases in solution, precipitation occurs. Fig. 4.1 is a pictorial illustration of the room temperature synthesis of the nanocrystals with the aid of the renowned bio-resource.
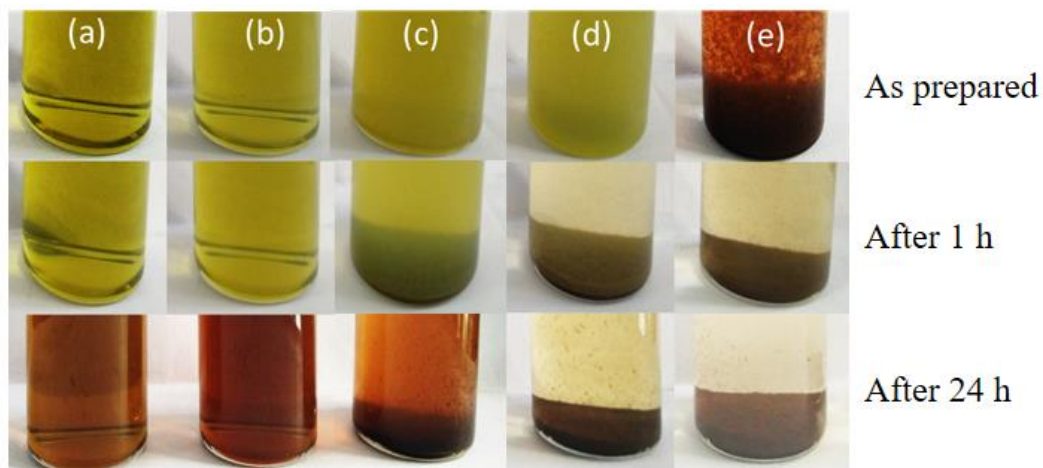
Fig. 4.1: Visual appearance from photo images of EENL-AgNPs showing color changes corresponding to growth during the reaction time. Vials correspond to EENL-AgNPs prepared from varying silver salt concentrations: (a) 1×10^{-3} M, (b) 3×10^{-3} M, (c) 5×10^{-3} M, (d) 10×10^{-3} M and (e) 0.1 M.

The color changes observed due to the strong absorption of visible light from excitation of the nanoparticles surface plasmons[14] was confirmed by the UV-Visible experiments. Metallic nanoparticles experience color changes depending on size in the nanoscale region. For nanospheres with d ~ 15 nm, only the transverse plasmon peak will be observed but if the radius of the sphere is increased up to d ~ 30 nm, the transverse plasmon absorption peak may shift slightly. A further increase will be a significant red shift.[21] Furthermore, the population of nanoparticles depends on the concentration of the silver salt. More yield of the nanoparticles is obtained within 24 h with increasing silver salt concentration because there is more of the reacting material available for the nanoparticle growth.[14] The yield of nanoparticle obtained was influenced by the combined effect of increasing salt concentration with uniform stirring for which precipitation occurred almost immediately after preparation at higher silver salt concentrations

as shown in Fig. 4.1(e). Best results were obtained with the highest silver salt concentration 0.1 M AgNO$_3$ thus, it was chosen as optimal concentration for the current study to evaluate other reaction parameters and make necessary comparisons.

4.3.1.2 UV-Visible analysis

The formation of EENL-AgNPs in solution was confirmed with UV-Visible spectroscopy, via the surface plasmon resonance (SPR) bands. The morphology, dielectric environment of the synthesized nanoparticles and its composition influences the SPR bands.[22] These surface plasmons are collective excitation of electrons near the surface which signifies standing waves on a surface. Mie's theory describes their interaction with light where smaller nanoparticles absorb light at shorter wavelengths and at longer wavelengths, larger nanoparticles absorb light. It is important to note that at a size of a few nanometers a system contains several hundred atoms such that discontinuities are no longer observed and the shift in wavelength with size appears smooth. However, surface plasmon obey somewhat complex rules, and their wavelength in some cases increases and in others decreases with size.[23] The metal reduction depends on the chemicals compounds in the plant extract and the concentration of the metal salt in the solution. The spectrum of the silver nanoparticles obtained contains strong plasmon bands within 416 - 450 nm, representing the reduction of Ag$^+$ ions to Ag^0 in the extract solution. The appearance of the absorption band is caused by 4d→5s, p inter-band transitions.[1] Silver nanoparticles exhibit a surface plasmon resonance absorption that is dependent on many factors including the dielectric constants of both the metal and the surface, the inter-particle distance, the shape and size of the particles[22]. Beer-Lambert's law explains that from an absorbance spectrum, the peak height of a surface plasmon band is proportional to the concentration of the reacting species in the system.[24] In Fig. 4.2(a), peak height increases with increase in silver salt concentration in the reaction system. The red shift also observed with increase in silver salt concentration may be due to the influence of concentration on nanoparticle growth resulting in increased sizes of the nanoparticles on aggregation and subsequent precipitate formation. With large metal nanoparticles, the dipolar localized surface plasmon resonance (LSPR) peak

undergoes significant broadening due to radiation damping and is red-shifted by the LSPR peaks of multipolar modes.[25] To exclude the influence of the extracting solvent UV-visible analysis of the solvent was carried out (Fig. 4.2(b-d)) and no absorbance peaks were observed.
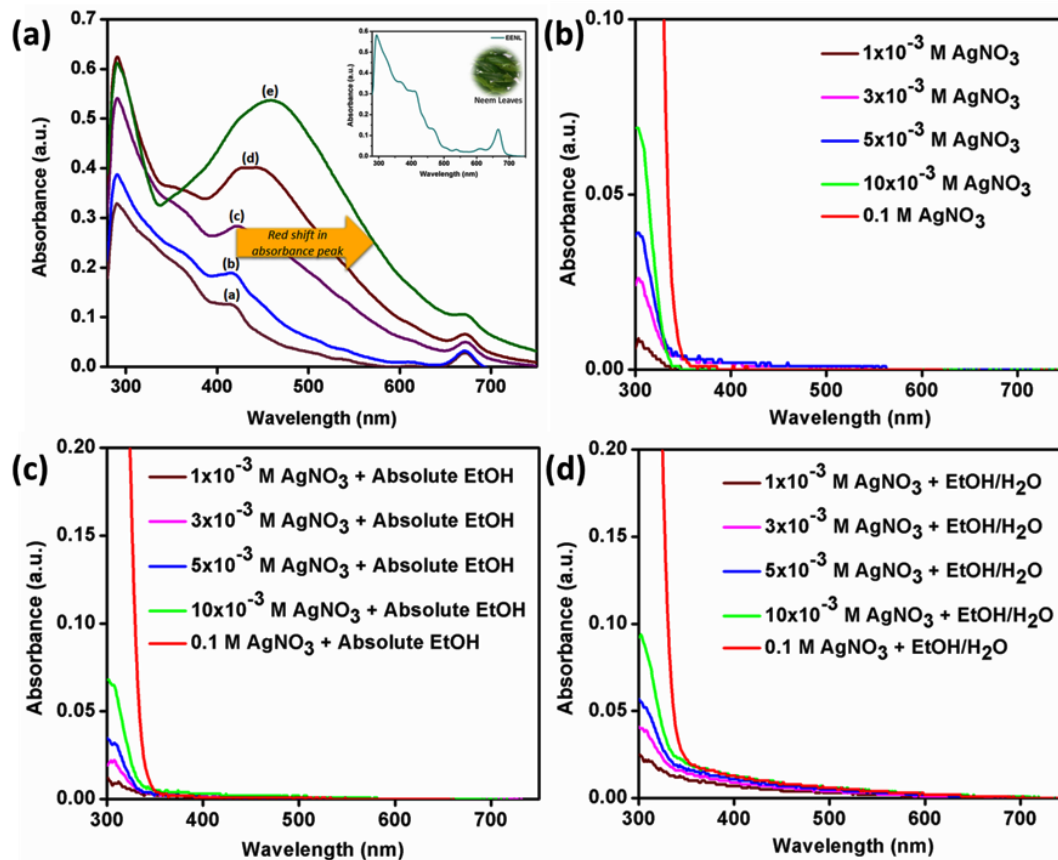
Fig. 4.2: (a). Kinetics of the reaction process via UV-Visible spectra of EENL-AgNPs from varying concentrations (a) 1×10^{-3} M, (b) 3×10^{-3} M, (c) 5×10^{-3} M, (d) 10×10^{-3} M and (e) 0.1 M of the silver salt within 24 h. Red shift observed. For comparison, inset shows the plot of the biomass extract alone (EENL). (b) UV-Visible spectra of $AgNO_3$ without reducing agent. (c) UV-Visible spectra of $AgNO_3$ with absolute ethanol. (d) UV-Visible spectra of $AgNO_3$ with ethanol/water (70/30).

4.3.1.3 FTIR analysis

The FTIR spectrum (Fig. 4.3(a)) for the biomass extract revealed prominent transmittance located at 3269.05 cm^{-1} for, hydrogen-bonded OH stretch indicating the presence of hydroxyl group, 2939.34 and 2874.80 cm^{-1} for C-H stretch of alkanes, 1587.86 cm^{-1} for C=C of aromatic group, 1395.02 for C-H bend of alkanes (CH$_3$) and 1073.09 cm^{-1} attributed to secondary alcohols, C-O stretch. Along with

small peaks of 1716.95 cm^{-1} for normal C=O stretch of ketones and 1202.17 cm^{-1} for alcoholic C-O stretch. These bands support the presence of polyphenols. Furthermore, bands within 1563-700 cm^{-1} can also be attributed to vibrations involving C-N stretching such as 1249 and 1170 cm^{-1} for C-N stretch. A band at 1395 cm^{-1} is assigned for C-H bending. While bands within 1620-1590, 1570-1515, and 1550-1510 cm^{-1} are assigned to N-H bending in amides and also the interaction between N-H bending and C-N stretching of the C-N-H group. In comparison with the silver nanoparticles after the reduction process (Fig. 4.3(b)), the peaks became shortened and certain shifts were observed but the presence of similar functionalities exists. The hydrogen-bonded OH stretch shifted to 3446.34 cm^{-1}, the C-H stretch of alkanes shifted to 2923.01 cm^{-1}, 1596.42 cm^{-1} are assigned to C=C of the aromatic group and the peak at 1716.95 cm^{-1} for normal C=O stretch of ketones rather intensified. Shifts also occurred in the fingerprint region where 1451.01 cm^{-1} represents C-H bend of alkanes (CH$_3$) and 1363.14 cm^{-1} for N=O of the aliphatic nitro group. 1202.17 cm^{-1} for alcoholic C-O stretch and 1073.09 cm^{-1} secondary alcohols, C-O stretch were observed in both spectra. These results from FTIR suggests that the water soluble phenolic compounds present in the ethanolic extract acted as the reducing, capping and stabilizing agents for the fabricated nanoparticles. The strong transmittance bands in the extract molecules is much lessened with the formation of the nanoparticles which may be attributed to the strong interaction between the silver ions and the biomass during the reduction process.
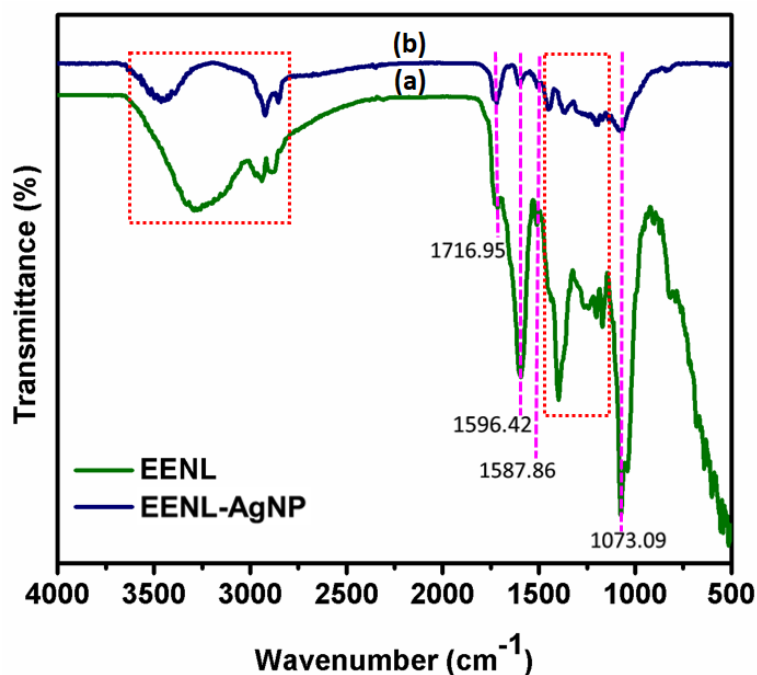
Fig. 4.3: FTIR spectra of (a) EENL and (b) EENL-AgNPs prepared from 0.1 M AgNO$_3$.

4.3.1.4 TEM analysis of fabricated nanoparticles

The TEM micrographs in Fig. 4.4(a) reveals a predominantly spherical morphology with the population of smaller sized nanoparticles from the lowest concentration and with an increase in AgNO$_3$ concentration, the growth of the nanoparticles may have occurred as the size is increased (Fig. 4.4(b)). The EDS spectra in Fig. 4.4(a & b) confirmed that the nanoparticles are composed mainly of silver and elemental contributions from the TEM grid includes the presence of Cu. A trace amount of oxygen is present which may be attributed to the presence of the biomolecules capping the nanoparticles on the grid. The presence of the capping layer of biomolecules can be seen clearly in Fig. 4.4(c) as a light-colored layer coating the nanoparticles. Similar results have been reported[3,14,26] when employing biomass extracts as reducing and capping agents in noble metal nanoparticle fabrications. The crystalline nature of the bioreduced silver nanoparticles in Fig. 4.4 is exposed via high-resolution transmission electron microscope (HRTEM) (Fig. 4.4(d)) along with its corresponding live FFT plot (Fig. 4.4(e)) disclosing more than one crystalline nature of the nanostructured material. The spots in the corresponding FFT (Fig. 4.4(e)) were indexed to the (111) and

(200) diffractions planes of Ag (observed interplanar distance $d_1 = 2.32$ Å, $d_2 = 2.00$ Å respectively). Also, indexed to (111) diffraction plane of AgO respectively (observed $d_3 = 2.73$ Å).
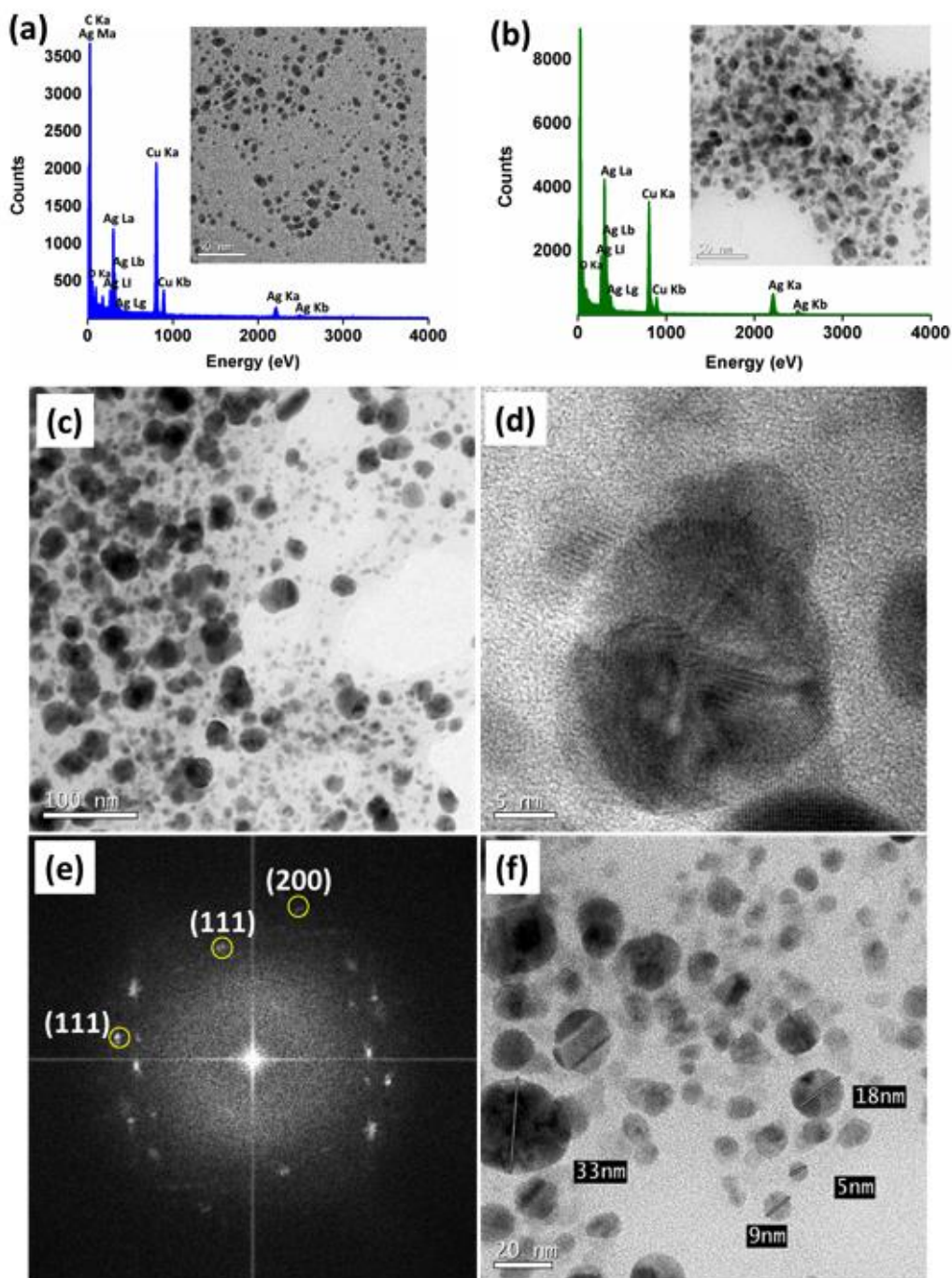
Fig. 4.4: TEM micrographs/EDS spectra of EENL-AgNPs prepared with (a) 1×10^{-3} M and (b) 0.1 M concentrations of the silver salt after reaction time of 24 h. (c) TEM micrograph of EENL-AgNPs prepared with 0.1 M AgNO$_3$ after a reaction time of 24 h, (d) HRTEM micrograph of (c) with (e) its corresponding live FFT plot showing

the Miller indices. (f) TEM micrograph of EENL-AgNPs prepared from 0.1 M AgNO$_3$ showing particle sizes.

4.3.1.5 XRD analysis of the nanocrystals

The X-ray diffraction (XRD) profile is a useful tool for the characterization of microstructures of nanocrystalline solids in which small crystallite size and lattice microstrain can cause broadening of the diffraction peaks.[27] Silver nanoparticles obtained by reducing 1×10^{-3} M AgNO$_3$ with the extract yielded sizes within 4 - 20 nm measured during TEM analysis. After purification by centrifuging, only a minute quantity settled out as the size enhanced thermodynamic instability. Thus obtaining sufficient quantity for powder XRD was a challenge. But with an increase in silver ion concentration to 0.1 M, more of the nanoparticles precipitated in a single reaction and was sufficient for powder XRD analysis. From the XRD analysis, the numerical parameter, full width at half maximum (FWHM) can be used to estimate particle size dispersion, alongside shape and represents the width of an absorbance spectrum.[24] The crystallite sizes were calculated using the Debye–Scherer equation[28] to be about 8 - 27 nm for EENL-AgNPs prepared from 0.1 M AgNO$_3$ which corroborates the sizes measured during TEM analysis to be within 5 - 33 nm (Fig. 4.4(f)).

The diffraction lines were broadened (Fig. 4.5(a)) and the widths of the diffraction lines are related to the size, size distribution, strain and defects in the nanocrystals. When the sizes of nanocrystals decrease (<100 nm), the line width is usually broadened attributable to the loss of long range order relative to the bulk[21] and strain.[28] The experimental diffraction angles at 2θ and the standard diffraction angles also at 2θ are in agreement and presented in Table 4.1. XRD has advantages over TEM for grain size measurement based on the fact that average grain size is determined by a larger area of the sample while TEM imaging is localized within a small region of the sample, and does not exclude the problem of grain overlap.[27] The wide angled XRD pattern of the fabricated silver nanoparticles in Fig. 4.5(a) shows four well-resolved diffraction peaks at 38.196, 44.129, 64.389, 77.332 indexed to (111), (200), (220) and (311) reflections of crystalline cubic silver (JCPDS 00-004-0783). A crystalline peak at 32.084 2θ value, indexed to (111) reflection of cubic AgO (JCPDS 01-076-1489) was detected when

analyzed using X'Pert Highscore Plus software. The presence of cubic AgO crystals has been reported when synthesizing silver nanoparticles from extracts of plant materials[26]. Furthermore, the experimental diffraction angles at 2θ and the standard diffraction angles at 2θ are in agreement and presented in Table 4.2. In addition, some unassigned peaks, noted with stars in the diffractogram suggests the crystallization of bio-organic phase on the surface of the silver nanoparticles which agreed with previous reports utilizing extracts of biomass for the fabrication of silver nanoparticles.[26]

Table 4.1: Experimental and standard diffraction angles of silver nanocrystals with d-spacings.

S/N	hkl	Experimental diffraction angle, 2θ [degrees]	d-spacing (Å)	Standard diffraction angle, 2θ [degrees] JCPDS 00-004-0783 (Cubic silver)	d-spacing (Å)
1.	111	38.196	2.354	38.117	2.359
2.	200	44.129	2.050	44.279	2.044
3.	220	64.389	1.445	64.428	1.445
4.	311	77.332	1.232	77.475	1.231

Table 4.2: Experimental and standard diffraction angles of silver (II) oxide (AgO) nanocrystals with d-spacing.

S/N	hkl	Experimental diffraction angle, 2θ [degrees]	d-spacing (Å)	Standard diffraction angle, 2θ [degrees] JCPDS 01-076-1489 (Cubic silver (II) oxide)	d-spacing (Å)
1.	111	32.083	2.787	32.167	2.780

4.3.1.6 XPS analysis of EENL-AgNPs

The X-ray Photoelectron Spectroscopy (XPS) was employed to determine the compositions and chemical species of EENL-AgNPs in their near-surface regions (Fig. 4.5(b-f)). The binding energy was calibrated by referencing the C 1s

peak at 284.6 eV using XPS data. From the general survey scan (Fig. 4.5(b)), EENL-AgNPs sample contains Ag, C, O, and N. The deconvolution analysis of XPS raw spectra allowed us to ascertain the presence of all Ag species present in support of the HRTEM and XRD results which showed the presence of Ag and AgO. From the deconvoluted high resolution Ag 3d spectrum (Fig. 4.5(c)), the peak fitting showed the Ag species existing in the sample. The Ag 3d core level spectrum is usually resolved into two spin-orbit components, Ag $3d_{5/2}$ and Ag $3d_{3/2}$. The binding energies of Ag $3d_{3/2}$ and Ag $3d_{5/2}$ at 374.2 eV and 368.2 eV, respectively and the splitting of the 3d doublet of Ag of 6 eV, indicates the existence of AgNPs at their Ag^0 state. While the additional peaks at binding energies of 374.3 and 369.4 eV, were an indication of the presence of AgO. Same Ag 3d binding energy for AgO has been reported.[29] The oxide phase appeared probably due to the presence of certain proteins in the biomass that lead to a partial oxidation of the Ag.

The deconvoluted C 1s spectrum (Fig. 4.5(d)) shows several carbon species which is expected at binding energies 284.6, 288.8, 287.3 and 286.1 eV corresponding to C-C, O-C=O, C=O,[30] and C–NH(C=O) of the carbon atom nearest the amido nitrogen,[31] The deconvoluted O 1s spectrum (Fig. 4.5(e)) shows three oxygen species at binding energies 532.7, 533.5 and 531.3 eV corresponding to O-C=O oxygen double bond in carboxylic acid,[32] C-O and -C=O of the biomass molecules present on the surface of the AgNPs meant to stabilize them and O due to AgO.[33] While the deconvoluted N 1s spectrum (Fig. 4.5(f)) shows two nitrogen species at binding energies 399.1 and 400.8 eV corresponding to C–NH_2[34] and H-N-C=O of amide-N, aromatic-N, and amine-N of proteins.[35] The functional groups present on EENL-AgNPs infer the biomass capping.
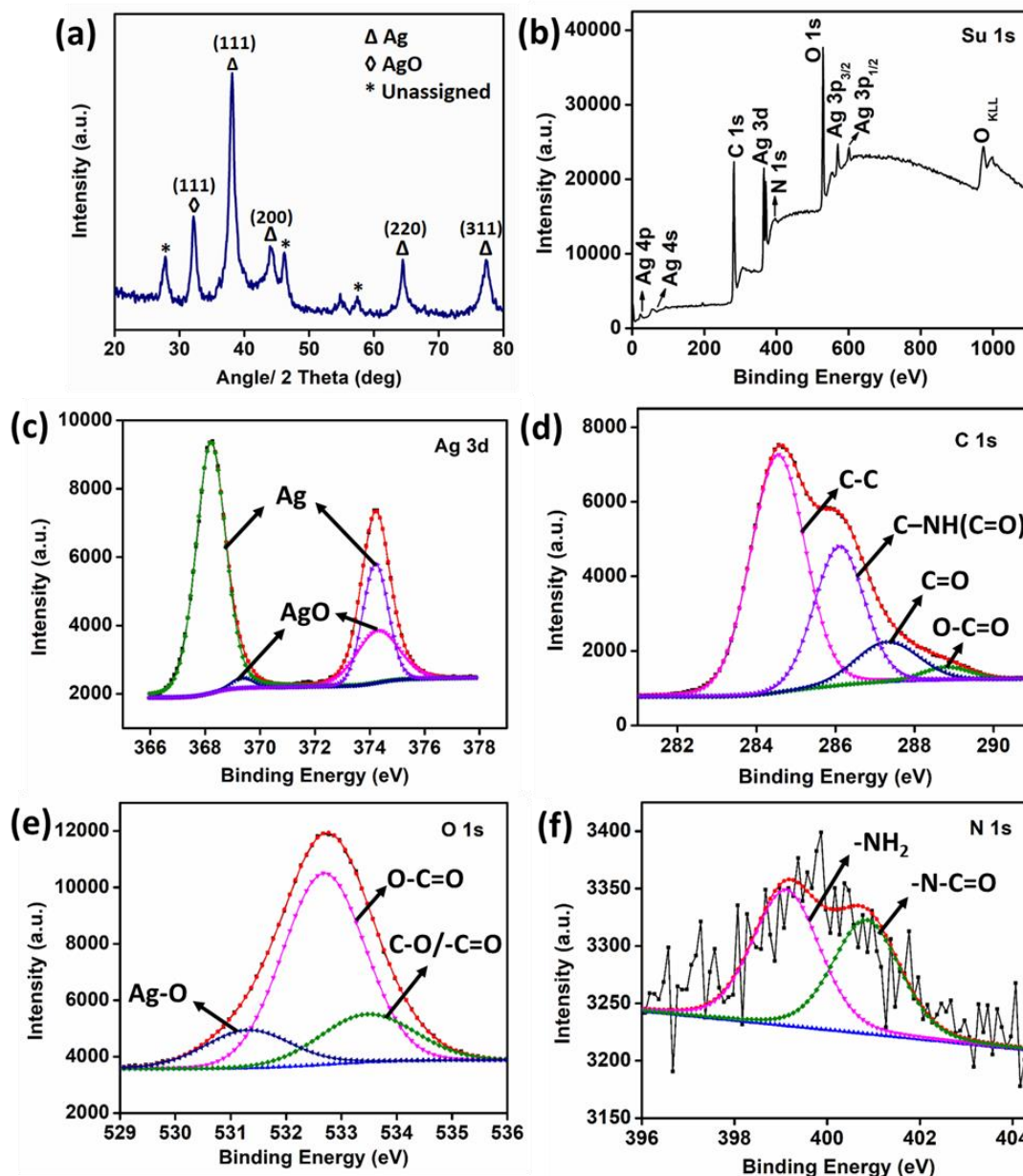
Fig. 4.5: (a). XRD pattern of EENL-AgNPs prepared from 0.1 M AgNO₃. Representative XPS spectra taken for EENL-AgNPs showing (b) XPS general survey spectrum (c) High-resolution Ag 3d spectrum, (d) high-resolution C 1s spectrum, (e) high-resolution O 1s spectrum, (f) high-resolution N 1s spectrum.

4.3.1.7 Surface-Enhanced Raman Scattering (SERS) analysis

The non-invasive technique does not involve specific sample preparation. The effectiveness of Raman spectroscopy is influenced by the intensity of the local electric field ''seen'' by the molecule amongst other factors.[36] Thus the manifest features in SERS are ultrahigh sensitivity and specificity of which the SERS signal sensitivity, in particular, is dependent on the size and shape of the nanoparticles.[4]

In this study, the SERS response for the biomolecules adsorbed onto the surface of EENL-stabilized colloidal AgNPs synthesized from 0.1 M AgNO$_3$ salt was investigated with the aid of confocal Raman microscopy. The vibrational properties of the adsorbed biomolecules on AgNPs is capable of providing structural information of the molecules and its local interactions. It is of the essence that when examining nanoparticles, the nature of surface plasmons, the particular metal in use and the resultant size and shape of the nanoparticles can be defined as a sea of electrons having a particular resonance that contributes to the electromagnetic mechanism. An electromagnetic enhancement occurs as a result of the increasing electromagnetic field encountered by the molecule on the surface of the metal[37] leading to excitation of plasmon absorption in the surrounding area of the nanoparticle. The enhancement of the Raman spectra of molecules in the surface region of metal nanoparticles is due to this local field effect. Certain factors are known to contribute to the total SERS enhancement effect depending on the experimental conditions. These includes electromagnetic enhancement ensuing from excitation of the metal, charge transfer from metal to adsorbate (chemical enhancement), resonant Raman spectroscopy in which excitation corresponds to an electronic transition in the molecule, and an off-resonance enhancement referred to as excitation to virtual states due to metal-adsorbate interaction.[22]

Achieving colloids of suitable sizes and shapes for strong SERS is not always an easy task. The bioreduction conditions are determined by the functional groups present in the plant extracts, while the concentration of the metal salt and necessary temperature are the factors that can be controlled.[38] After drop casting and evaporation, the contact line of the droplet is pinned, this induces convective flow within the droplet toward the contact line. The volume of the droplet reduces resulting in an increase in the concentration of species within the droplet, which in turn induced aggregation mechanically.[39] The biomass extract (EENL) responded to the laser excitations producing intensities corresponding to the presence of δ(CC) aliphatic chains, υ(CC) alicyclic, aliphatic chain vibrations, aromatic rings, υ(C-O-C) asymmetric, aromatic azo, δ(CH$_2$),δ(CH$_3$) asymmetric, amides, υ(C=C), carboxylic acid, υ(C=O), υ(C-(NO$_2$)) etc. as shown in Fig. 4.6(a). Peak assignments are presented in Table 4.3.

Table 4.3: Raman bands and corresponding assignments of EENL.

Raman bands Assignments (Raman shift cm⁻¹)	Assignments
167.50, 232.08	Lattice vibrations
326.68	δ(CC) aliphatic chains
654.17, 684.18	υ(CC) alicyclic, aliphatic chain vibrations
812.97 - 972.16	υ(C-O-C), υ(CC) alicyclic, aliphatic chain vibrations
1001.79, 1021.55, 1046.62	Aromatic rings
1076.26	υ(C-O-C) asym
1190.61	υ(CC) alicyclic, aliphatic chain vibrations
1344.48	υ(C-(NO$_2$))
1399.18, 1438.70	Aromatic azo, δ(CH$_2$),δ(CH$_3$) asym
1488.46	Aromatic ring
1572.81	Aromatic/hetero ring, υ(C=C)
1607.38	υ(C=C)
1676.90	Carboxylic acid
1746.43	υ(C=O)

As regards a colloid droplet, the convective flow deposits the suspended particles onto the substrate[39] and aggregation is an essential criterion for achieving high SERS intensity.[39] Rhodamine B (RB) was chosen as the model Raman reporter to verify the SERS enhancement effect. SERS was observed for molecules on or nearby the surface of nano-metals that can support localized surface plasmon resonances. Aggregation of nanoparticles was mechanically forced by droplet evaporation from the colloids prepared from 0.1 M AgNO$_3$. The circular stain formed on the glass slide after the solvent evaporation with areas of high concentration of silver nanoparticle aggregates was interrogated by SERS for the detection and identification of the functional groups. Peaks with intensities < 200

cm^{-1} represent lattice vibrations in crystals. Significant SERS peaks obtained within 150 - 450 cm^{-1} correspond to υ(X metal-O), for the vibrational energies of metal-ligand bonds a region of the infrared that is experimentally difficult to detect. These vibrations are frequently Raman active.[40] After purification and removal of loosely bound biomolecules and by-products, in the presence of the dye probe, SERS response for firmly adsorbed biomolecules were realized corresponding to δ(CC) aliphatic chains, υ(CC) alicyclic, aliphatic chain vibrations, aromatic rings, amides, υ(C-O-C) asymmetric, aromatic rings, δ(CH$_2$),δ(CH$_3$) asymmetric and υ(C=C). Peak assignments of EENL-AgNPs@0.1 M AgNO$_3$ are presented in Table 4.4. The SERS spectra of the silver nanoconstruct (with 30 μM RB) excited at 633 nm is shown in Fig. 4.6(b). Certain differences in the wave numbers and intensities of the bands were observed in the spectral pattern which may be due to the orientation of the adsorbed extract molecules on the Ag nanoparticles. Therefore, SERS studies confirmed the presence of the capping biomolecules on the nanoparticles.
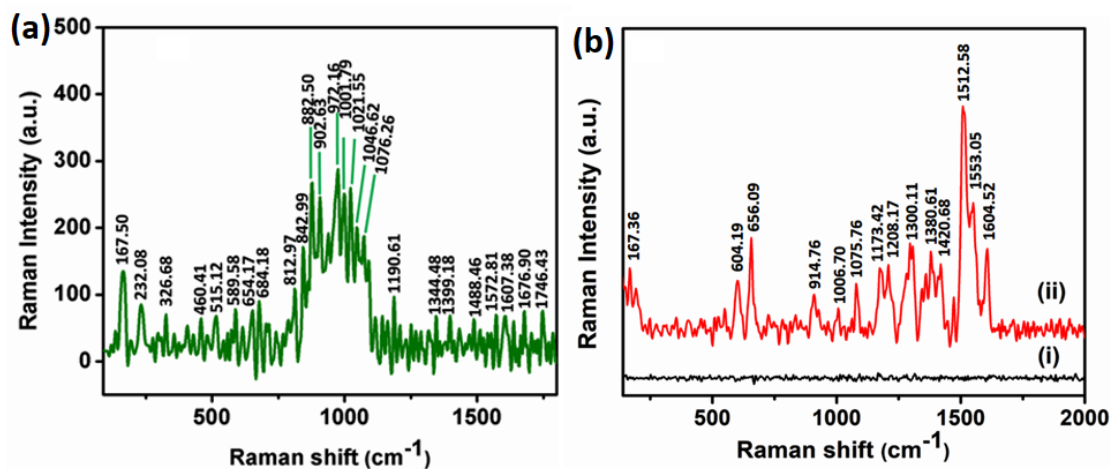
Fig. 4.6: (a) Raman spectra of EENL and (b(i)) Raman spectra of RB. (ii) SERS spectra of biomolecules fabricated on silver nanoparticles (EENL-AgNPs@0.1 M AgNO$_3$) with 30 μM RB yielding the optimum enhancement. Raman spectra were taken at an excitation wavelength of 633 nm and an acquisition time of 2s and plotted as average intensities excited at 633 nm (n=10; number of accumulations).

Table 4.4: SERS bands and corresponding assignments of EENL-AgNPs@0.1 M AgNO$_3$ after interaction with the probe molecule.

Raman bands Assignments (Raman shift cm^{-1})	Assignments
81.14, 104.02	Lattice vibrations
167.50	υ(Xmetal-O)
604.19, 656.09	υ(CC) alicyclic, aliphatic chain vibrations
914.76	υ(C-O-C), υ(CC) alicyclic, aliphatic chain vibrations
1006.70	Aromatic rings
1075.76, 1173.42	υ(C-O-C) asym, υ(CC) alicyclic, aliphatic chain vibrations
1300.11, 1380.61	υ(CC) alicyclic, aliphatic chain vibrations, δ(CH$_3$)
1420.68	δ(CH$_2$) δ(CH$_3$) asym
1512.58, 1533.05	υ(C=C)
1604.52	υ(C=C)

4.3.2 Effect of AgNO$_3$ concentration on the fabrication of EENL-AgNPs

The impact of AgNO$_3$ concentration on the synthesis of AgNPs was examined in the range (a) 1x10^{-3} M, (b) 3x10^{-3} M, (c) 5x10^{-3} M, (d) 10x10^{-3} M and (e) 0.1 M with respect to reaction time extending up to 48 h as detailed in Fig. 4.7(a-e). The intensity of plasmon band enhanced with the increase of Ag$^+$ ion concentration and broadened as a red shift occurred. The intensity boost of absorption band with distinct SPR peaks results from the increase of metal particle size, combined with the band shift[41] and an increase in contact or incubation time for completion of the reaction.[42] The incubation time strongly influences the stability of the synthesized nanoparticles.[42] The yield of nanoparticles at higher salt concentrations also increased due to the availability of more material for the nanoparticle growth.[14,41] Color changes occurred according to different AgNO$_3$ concentrations in the reactions (Fig. 4.1). The color intensity of the reaction mixture also increased with increase in the AgNO$_3$ concentration that reacted with the extract molecules as the incubation reaction time increased.[41] Nanoparticle

precipitation occurred for higher salt concentrations even before the completion of 24 h. Similar results have been reported with the fabrication of AgNPs from aqueous extracts of *Jatropha curcas* seeds,[43] Banana peels,[44] etc.
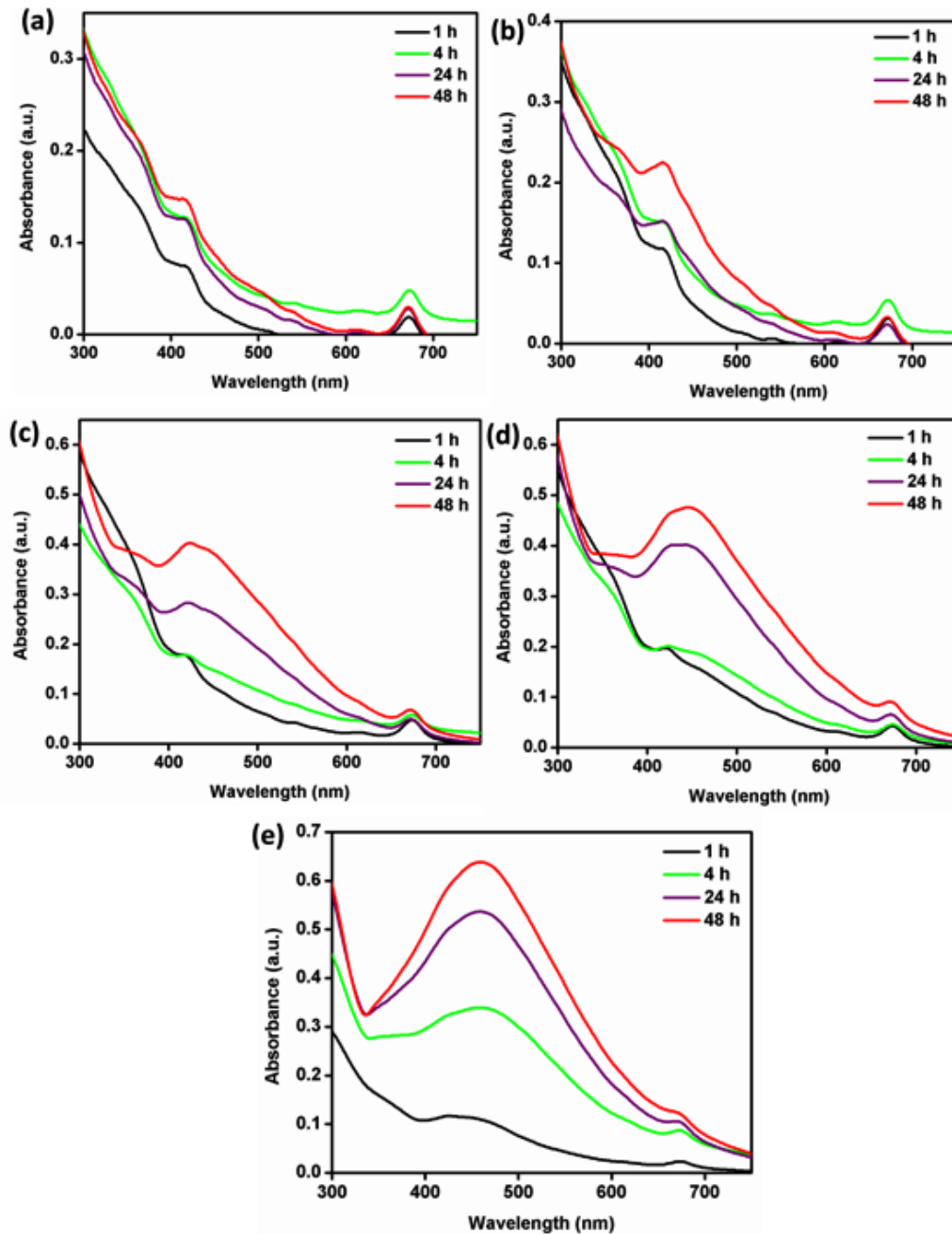
Fig. 4.7: UV-Visible spectra of EENL-AgNPs as a function of Ag^+ ion concentration within 1 - 48 h time limits. Concentrations involved are: (a) 1×10^{-3} M, (b) 3×10^{-3} M, (c) 5×10^{-3} M, (d) 10×10^{-3} M and (e) 0.1 M. Increase in absorbance values with subsequent SPR peak broadenings observed as the reaction time increases.

4.3.3 Effect of stirring on the kinetics of fabrication of EENL-AgNPs

The kinetics of the reaction in terms of rate of the reaction during the nanocrystal formation was investigated. To achieve this, a different set of nanoparticles were prepared without uniform stirring, lesser stirring speed and time and SPR peak intensities were lower as shown in Fig. 4.8(a). The original set of reactions (Fig. 4.8(b)) were uniformly stirred at 500 rpm and after complete addition of the reducing agent, an extended stirring time of 15 min was observed. For the reactions represented in Fig. 4.8(a), color change and precipitation were slower. This implies that probably reactant materials may not have completely reacted. For those in Fig. 4.8(b), the solution turned darker at a faster rate and flakes of silver were visible in the solution. With the extended stirring time increase in the probability of collision occurred between the particles leading to particles aggregation being much more evident with increasing precursor salt concentration. Furthermore, from the UV-Vis spectra in Fig. 4.8(b), the SPR peaks broadened, became more intense and shifts towards longer wavelengths occurred. Thus, in comparison with Fig. 4.8(a), broadening of the SPR peaks in Fig. 4.8(b) may be due to stirring uniformity and speed with increasing stirring time allowing faster nucleation to occur as the particles became more polydispersed.
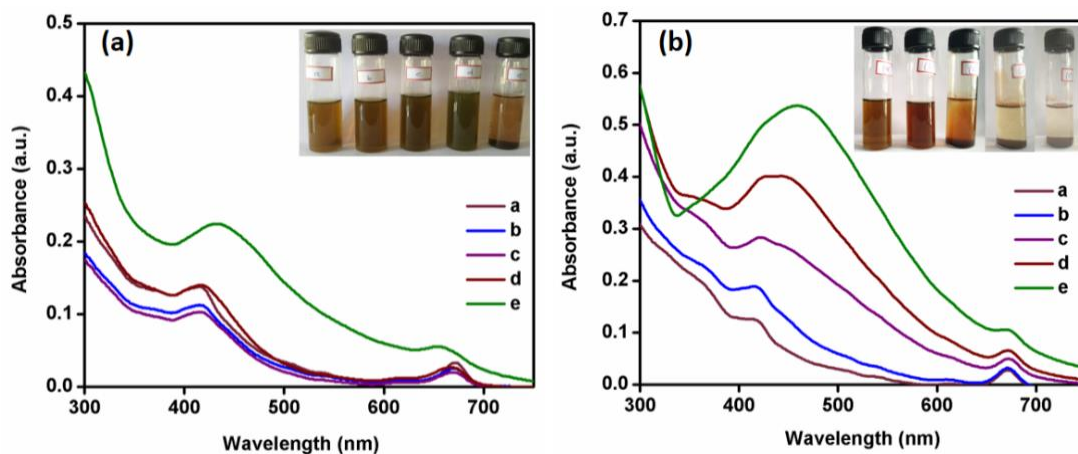
Fig. 4.8: UV-Vis spectra of different concentrations of EENL-AgNPs during (a) uncontrolled kinetics and (b) controlled kinetics @ 24 h. Inset are photo images of the colloidal solutions of silver nanoparticles after 24 h.

4.3.4 Stability of EENL-AgNPs

Ag nanoparticles of small sizes are generally unstable because of their high surface energy, this makes the Ag particles prone to aggregation. The formation of the capping layer due to EENL on the surface of the Ag nanoparticles contributes to addressing problems associated with the colloidal stability of bioreduced Ag nanocrystals. Hydrodynamic particle sizes of the fabricated nanoparticles were determined from DLS measurements and the stability of the prepared colloidal EENL-AgNPs in water was investigated using ζ-potential measurements (section 3.6.1) and Fig. 4.9. Likewise the thermal stability of the lyophilized nanocrystals was determined with TGA measurements in section 3.4.2 and Fig. 4.10.

4.3.4.1 Particle size analysis

Hydrodynamic particle size distribution and zeta potential of aqueous dispersions of EENL-AgNPs were measured by dynamic laser light scattering using Malvern Zetasizer Nano ZS90, Germany. For particle size measurement scattering angle at 90° was used. Very dilute colloidal solutions were used and aggregation was reduced by sonication before the analysis. The stability of nanoparticles depends on both size and surface charge of the nanoparticles. The DLS data measurements of all the studied concentrations indicate that the sizes of the particles varied. The average (hydrodynamic) particle size distributions were between 96.0 - 170.9 nm and zeta potential within -13.4 ± 3 mV to -34.2 ± 7 mV. The sizes obtained with DLS are larger than those observed with TEM and XRD. This observation is made in all concentrations studied. While the dimension in TEM image is consistent with XRD, the inconsistency here may be attributed to weak adhesion of two or more colloidal particles in solution which results in the evidently larger sizes detected in the DLS measurements.[45] The size distribution plots and zeta potential (ζ) of EENL-AgNPs are presented in Fig. 4.9. ζ values of ±30 mV corresponds to long-term stability, good colloidal nature and high dispersity of particles in suspensions. Dissociation of acidic groups on the surface of a particle will give rise to a negatively charged surface resulting in negative-negative repulsion while a basic surface will take on a positive charge.[46] Negative ζ value have been reported for biogenic AgNPs from plant biomass.[47]
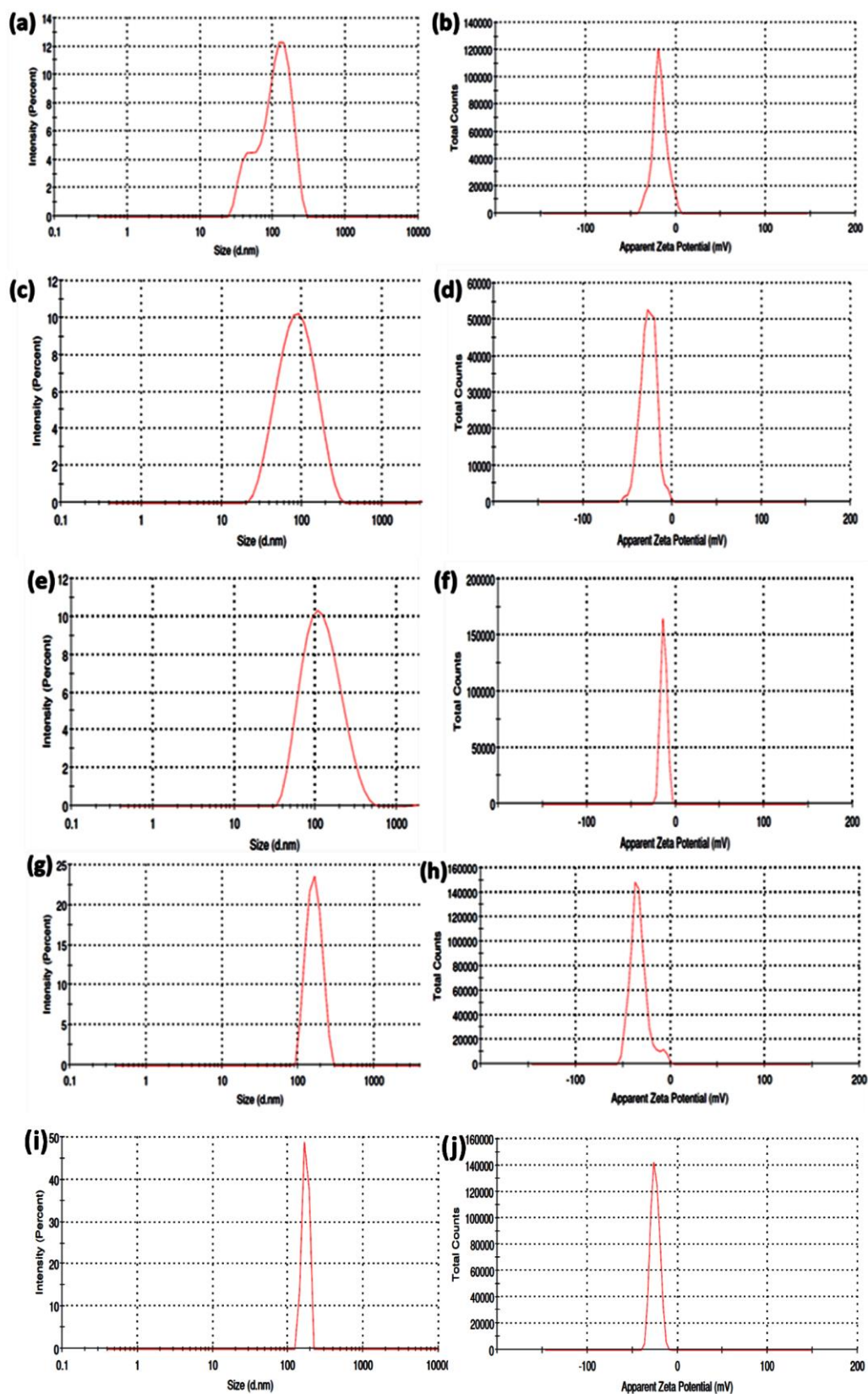
Fig. 4.9: DLS and Zeta potential plots of 1 mM (a & b), 3 mM (c & d), 5 mM (e & f), 10 mM (g & h), 0.1 M (i & j) EENL-AgNPs.

4.3.4.2 Thermogravimetric analysis

TGA analysis of the freeze dried nanocrystals determines its thermal stability. Fig. 4.10 shows the thermograms of EENL and EENL-AgNPs@0.1 M AgNO$_3$. An initial weight loss between 1 - 3% at 110°C for EENL and EENL-AgNPs@0.1 M AgNO$_3$ attributed to evaporation due to the presence of water molecules in both samples. Thereafter, there was a steady weight loss until 500°C of about 82% for EENL due to decomposition of the organic matter. While the weight loss amounting to 37% for EENL-AgNPs@0.1 M AgNO$_3$ at the same temperature was due to desorption of bioorganic components present on the surface of silver nanoparticles, which was expected to be responsible for the reduction and stabilization of the aqueous silver ions to silver nanoparticles. This supports that the bioactive molecules were capped on the AgNPs and were degraded completely at high temperatures, leaving a residual mass of 60% at 600°C. The high thermal stability of EENL-AgNPs@0.1 M AgNO$_3$ can be attributed to the presence of inorganic metal as silver nanoparticles.
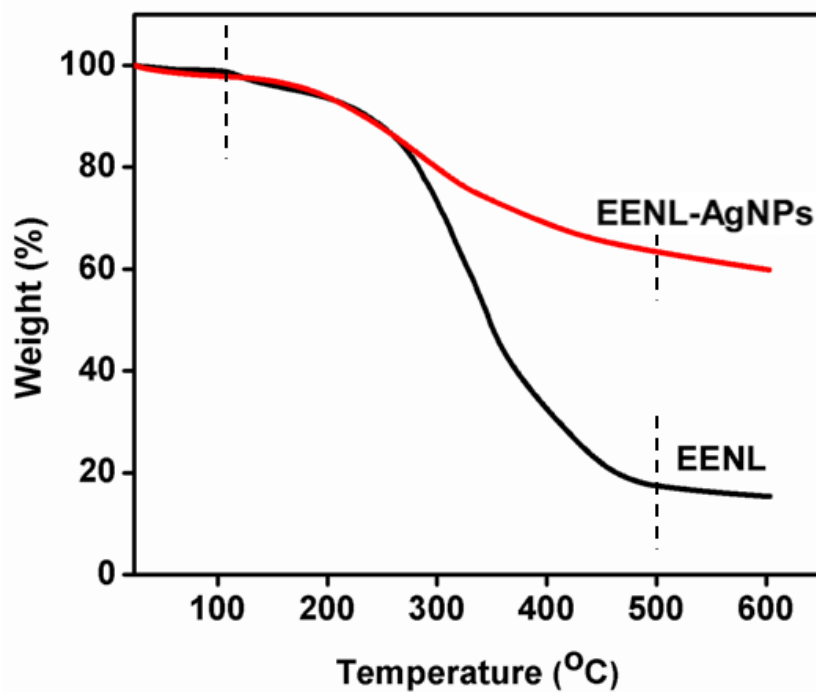
Fig. 4.10: TGA curves of EENL and lyophilized EENL-AgNPs@0.1 M AgNO$_3$.

4.3.5 Antimicrobial activities of EENL-AgNPs

Neem extract exhibits antibacterial and antifungal activity by *in vitro* and *in vivo* experiments due to the presence of compounds like desactylimbin, triterpenes or the limonoids such as meliantriol, azadirachtin, desactylimpin, quercetin, sitosterol, nimbin, nimbinin, nimbidin, nimbosterol and margisine.[48] Other compounds like Azadirachtin, Azadiradione, nimonol and epoxy azadradione were also obtained from the organic extracts of Neem leaves which were reported to be antimicrobial in nature.[49] Silver nanoparticles (both synthetic and bio-derived) exhibit broad-spectrum biocidal activity towards many different microbial strains. It is a potent antibacterial agent towards *E. coli*,[9,41,50] *S. aureus*,[9,19,41,50] *P. aeruginosa*,[51] *Listeria monocytogenes, Staphylococcus saprophyticus, Pseudomonas putida*[41] etc. It is also a viable antifungal agent for *A. terreus*,[52] *Humicola insolens, Fusarium dimerum, Mucor indicus* and *Trichoderma reesei*[53] etc. Recently, antifungal activities of silver nanoparticles were reported in some *Aspergillus* species.

These include *Aspergillus* section *Flavi* (*Aspergillus flavus, Aspergillus nomius* and *Aspergillus. parasiticus*) and two of section *Circumdati* (*Aspergillus ochraceus* and *Aspergillus melleus*).[54] In this work, the antimicrobial activity of the prepared silver nanoparticles was examined against *Pseudomonas nitroreducens* and *Aspergillus unguis* (NII-08123) strains. *Pseudomonas nitroreducens* is a biofilm producing bacteria that can react with metal surfaces altering the chemistry of the protective layer and enhancing biocorrosion.[55] *Aspergillus unguis* (NII-08123) is a filamentous fungus isolated from the soil.[56] It is known to occur mainly in tropical and sub-tropical soils and has been isolated from marine and aquatic habitats.[57] *Aspergillus unguis* (NII-08123) observed on the PDA were heavily sporulated by forming green spores within 72 h of incubation.

The results showed that for the microbial strains, the introduction of silver nanoparticles affected the growth kinetics and the antimicrobial effect was found to be dose dependent. The diameter of the zone of inhibition for the bacterial strain was measured to be 19.5 mm and 25 mm for 1 mg/mL and 5 mg/mL impregnated discs respectively (Fig. 4.11(a)). While for the fungal strain, the diameter of the zone of inhibition was measured to be 21 mm for 5 mg/mL impregnated disc and for the 1 mg/mL impregnated disc, the zone of inhibition was not significant (Fig

4.11(b)). After 72 h incubation, it was observed that the fungal spores grew on the surface of the blank disc (control), whereas the fungal spores did not grow on the discs impregnated with EENL-AgNPs. The 5 mg/mL impregnated disc showed a significant zone of inhibition and formation of yellow spores beyond the clear zone, indicating the inhibition of sporulation. The antimicrobial activity of AgNPs on Gram-negative bacteria is concentration dependent and associated with the formation of 'pits' within the cell wall of the bacteria giving rise to the accumulation of AgNPs in the bacterial membrane following cell death.[58]

Further suggestions involve free radicals derived from the surface of AgNPs resulting in free radical-induced membrane damage.[50] Both the bactericidal activity and the antifungal activity was sustained during the period of exposure. The capping compounds on the silver nanoparticles from the Neem extract is a possible contribution to the antibacterial and antifungal activity of the silver nanoparticles. The Neem extract has a wide range of established biological activities.[59]
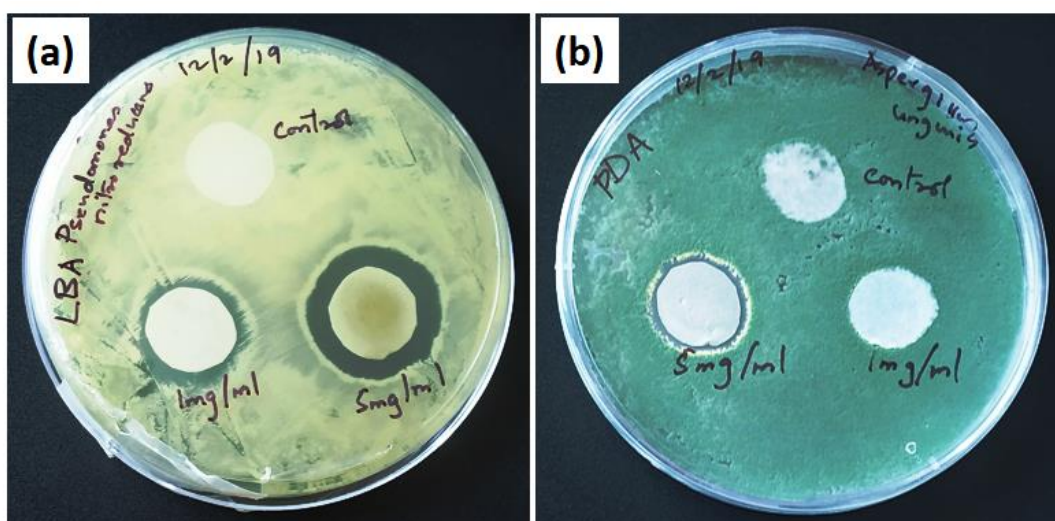
Fig. 4.11: Antimicrobial action of the lyophilized EENL-AgNPs@0.1 M AgNO$_3$ showing zones of inhibition at different nanoparticle concentrations against (a) *Pseudomonas nitroreducens* colony on LBA agar (reverse side) and (b) *Aspergillus unguis* (NII-08123) colony on PDA agar.

In comparison, the effect of silver nitrate on the microbes was investigated (Fig 4.12). The average diameter of the zone of inhibition for the bacterial strain

was 24 mm for 1 mg/mL and 28 mm for 5 mg/mL impregnated discs (Fig. 4.12(b-c)). With the fungal strain, the average diameter of the zone of inhibition was measured to be 25 mm for the 1 mg/mL impregnated disc and 27 mm for 5 mg/mL impregnated disc (Fig. 4.12(e-f)). Effective microbial growth-inhibition of silver nitrate has been well documented. Silver nitrate is highly cytotoxic since it affects mitochondrial fibroblast function.[60] The efficiency of silver nitrate is obtained in the form of metallic silver since ancient times. It is also established that higher concentrations of $AgNO_3$ kills bacteria effectively than AgNPs. But nanoparticles may be synthesized by bacteria at lower concentrations of $AgNO_3$. AgNPs and silver metal in water solutions both release silver in the form of Ag^+ ions, which act as antimicrobial agents in the same manner as $AgNO_3$. Interestingly, the reaction of all these species against bacteria is thought to be basically the same, although the rate of inactivation may vary widely, possibly due to the rate of Ag^+ release.[61]
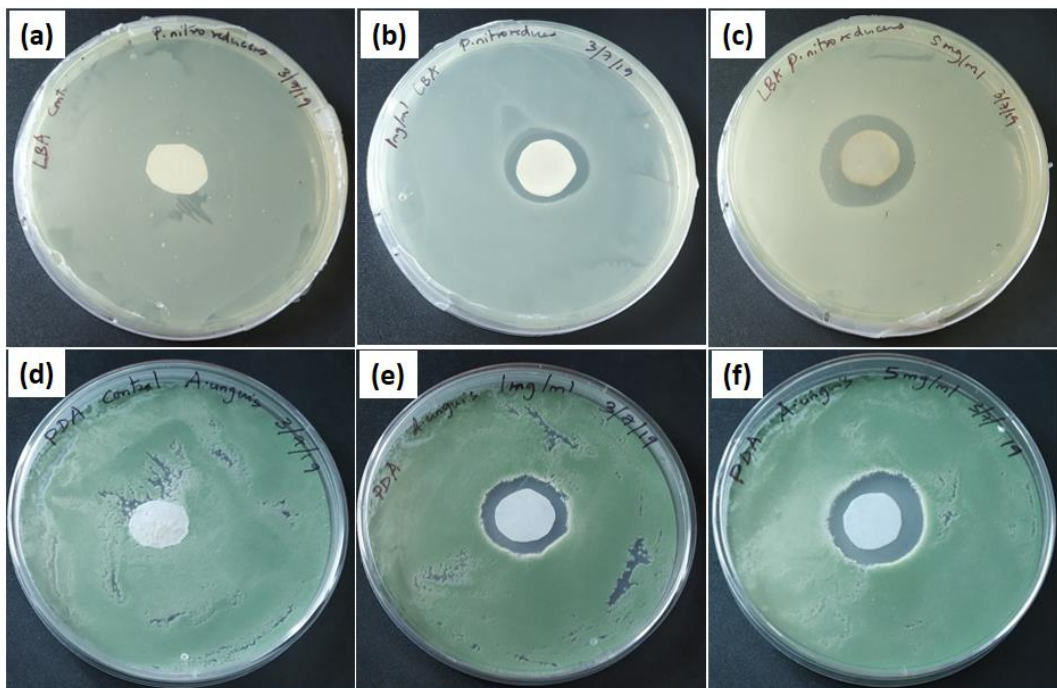
Fig. 4.12. Antimicrobial action of $AgNO_3$ (1 mg/mL and 5 mg/mL) showing zones of inhibition against (a) *Pseudomonas nitroreducens* colony on LBA agar and (b) *Aspergillus unguis* (NII-08123) colony on PDA agar.

4.4   Conclusions

The present study demonstrated a facile approach of biogenic synthesis of nanostructured silver crystals via ethanol extract of Neem leaves. Other reported syntheses of silver nanoparticles, utilized an aqueous extract of the biomass and required the application of a form of energy such as heating during the synthesis protocol. In contrast, this approach is undemanding and consumed no energy. The reduction of noble metal salts by the combination of phytochemicals in the plant biomass without an additional stabilizing agent is explored for the fabrication and subsequent accumulation of nano-metal colloids. The influence of the extracting solvent was excluded as no absorbance peaks were observed. An increase in both silver salt concentration and uniform stirring influenced the rate of precipitation of the nanocrystals in the colloidal solution which were observed to be SERS responsive when probed with Rhodamine B without any external aggregating agents. The nanoparticles were composed mainly of silver and the XRD pattern confirmed the cubic phases of the silver nanocrystals. Uniform stirring and extended stirring time allowed faster nucleation to occur as the particles became more polydispersed. With data obtained from different characterization techniques (UV–Vis spectroscopy, TEM, FTIR, XRD, SERS TGA and XPS) it can be deduced that the metal ions initially present in metal salts are reduced by bioreducing agents present in the whole extract, which played the multifunctional role of aggregating, capping, and stabilizing the nanocrystals to grow into defined sizes and shape. The nature of the bioreducing agents and reaction conditions employed played essential roles in controlling the morphology and activity of the nanocrystals. Furthermore, the ability of EENL-AgNPs to induce significant toxicity to the test microbes offers a noteworthy opportunity to utilize bioreduced AgNPs in the formulation of antimicrobial coatings. The significant contributions from these results support the multifunctional role of extracts of dried plant biomass in the synthesis of nanocrystalline silver particles showcasing its increasing antimicrobial potentials.

References

[1]   H. J. Hah, S. M. Koo, S. H. Lee, *J. Sol-Gel Sci. Technol.* **2003**, *26*, 467.

[2]   T. Premkumar, K. E. Geckeler, *New J. Chem.* **2014**, *38*, 2847.

[3]   S. Yn Lee, S. Krishnamurthy, C.-W. Cho, Y.-S. Yun, *ACS Sustain. Chem. Eng* **2016**.

[4]   T. S. Sreeprasad, T. Pradeep, In *Springer Handbook of Nanomaterials*; Robert Vajtai, Ed.; Springer Berlin Heidelberg: Berlin, Heidelberg, 2013; pp. 303–388.

[5]   J. Huang, L. Lin, D. Sun, H. Chen, D. Yang, Q. Li, *Chem. Soc. Rev.* **2015**, *44*, 6330.

[6]   S. S. Shankar, A. Rai, A. Ahmad, M. Sastry, *J. Colloid Interface Sci.* **2004**, *275*, 496.

[7]   A. Tripathy, A. M. Raichur, N. Chandrasekaran, T. C. Prathna, A. Mukherjee, *J. Nanoparticle Res.* **2010**, *12*, 237.

[8]   P. Banerjee, M. Satapathy, A. Mukhopahayay, P. Das, *Bioresour. Bioprocess.* **2014**, *1*, 3.

[9]   A. Verma, M. S. Mehata, *J. Radiat. Res. Appl. Sci.* **2016**, *9*, 109.

[10]   K. Biswas, I. Chattopadhyay, R. K. Banerjee, Biological activities and medicinal properties of neem (Azadirachta indica)Biswas, K., Chattopadhyay, I., & Banerjee, R. K. (2002). Biological activities and medicinal properties of neem (Azadirachta indica). Department of Physiology, 82(11). *Curr. Sci.* **2002**, *82*, 1336–1345.

[11]   N. D. Vietmeyer, *Neem: a tree for solving global problems.*; National Academy Press, Washington D.C, 1992.

[12]   R. Subapriya, S. Nagini, *Curr. Med. Chem. Agents* **2005**, *5*, 149.

[13]   D. R. Baer, P. E. Burrows, A. A. El-Azab, *Prog. Org. Coatings* **2003**, *47*, 342.

[14]   E. Rodríguez-León, R. Iñiguez-Palomares, R. Navarro, R. Herrera-Urbina, J. Tánori, C. Iñiguez-Palomares, A. Maldonado, *Nanoscale Res. Lett.* **2013**, *8*, 318.

[15]   K. de Lira Mota, F. de Oliveira Pereira, W. de Oliveira, I. Lima, E. de Oliveira Lima, *Molecules* **2012**, *17*, 14418.

[16]   A. K. Ghimeray, C. Jin, B. K. Ghimire, D. H. Cho, *J. Biotechnol.* **2009**, *8*, 3084.

[17]   S. Susmitha, K. K. Vidyamol, P. Ranganayaki, R. Vijayaragavan, *Glob. J. Pharmacol.* **2013**, *7*, 316.

[18]   G. Pandey, K. K. Verma, M. Singh, *Int. J. Pharm. Pharm. Sci.* **2014**, *6*, 444.

[19]   P. V. Quelemes, M. L. G. Perfeito, M. A. Guimarães, R. C. dos Santos, D. F. Lima, C. Nascimento, M. P. N. Silva, M. J. dos S. Soares, C. D. Ropke, P. Eaton, J. de

Moraes, J. R. S. A. Leite, *J. Ethnopharmacol.* **2015**, *175*, 287.

[20]   P. Christian, F. Von der Kammer, M. Baalousha, T. Hofmann, *Ecotoxicology* **2008**, *17*, 326.

[21]   J. Z. Zhang, *Optical Properties and Spectroscopy of Nanomaterials*; World Scientific Publishing Co. Pte. Ltd., 2009.

[22]   K. G. Stamplecoskie, J. C. Scaiano, V. S. Tiwari, H. Anis, *J. Phys. Chem. C* **2011**, *115*, 1403.

[23]   E. Roduner, *Chem. Soc. Rev.* **2006**, *35*, 583.

[24]   A. L. Nogueira, R. A. F. Machado, A. Z. De Souza, F. Martinello, C. V. Franco, G. B. Dutra, *Ind. Eng. Chem. Res.* **2014**, *53*, 3426.

[25]   R. El-dessouky, M. Georges, H. M. E. Azzazy, In *Functional Nanoparticles for Bioanalysis, Nanomedicine, and Bioelectronic Devices*; Hepel, M., et al, Ed.; American Chemical Society: Washington, DC, 2012; Vol. 1, pp. 358–404.

[26]   A. A. Abdelhamid, M. A. Al-Ghobashy, M. Fawzy, M. B. Mohamed, M. M. S. A. Abdel-Mottaleb, *ACS Sustain. Chem. Eng.* **2013**, *1*, 1520.

[27]   S. C. Tjong, H. Chen, *Mater. Sci. Eng. R Reports* **2004**, *45*, 1.

[28]   T. Theivasanthi, M. Alagar, *Nano Biomed. Eng.* **2012**, *4*.

[29]   A. M. Ferraria, A. P. Carapeto, A. M. Botelho do Rego, *Vacuum* **2012**, *86*, 1988.

[30]   F. A. Permatasari, A. H. Aimon, F. Iskandar, T. Ogi, K. Okuyama, *Sci. Rep.* **2016**, *6*, 21042.

[31]   D. Pappas, A. Bujanda, J. D. Demaree, J. K. Hirvonen, W. Kosik, R. Jensen, S. McKnight, *Surf. Coatings Technol.* **2006**, *201*, 4384.

[32]   V. Duc Chinh, G. Speranza, C. Migliaresi, N. Van Chuc, V. Minh Tan, N.-T. Phuong, *Sci. Rep.* **2019**, *9*, 5667.

[33]   S. Agnihotri, S. Mukherji, S. Mukherji, *Nanoscale* **2013**, *5*, 7328.

[34]   A. P. Carapeto, A. M. Ferraria, A. M. Botelho do Rego, *Nanomaterials* **2019**, *9*, 780.

[35]   L. Torres-González, R. Díaz-Ayala, C. Vega-Olivencia, J. López-Garriga, *Sensors* **2018**, *18*, 4262.

[36]   A. Moores, F. Goettmann, The plasmon band in noble metal nanoparticles: An introduction to theory and applications. *New J. Chem.* **2006**, *30*, 1121–1132.

[37]   G. P. Glaspell, C. Zuo, P. W. Jagodzinski, *J. Clust. Sci.* **2005**, *16*, 39.

[38]   L. Zeiri, *J. Raman Spectrosc.* **2007**, *38*, 950.

[39]   M. R. Barmi, C. Andreou, M. R. Hoonejani, M. Moskovits, C. D. Meinhart, *Langmuir* **2013**, *29*, 13614.

[40]   D. A. Skoog, F. J. Holler, S. R. Crouch, *Principles of instrumental analysis. 7th Edition*; Cengage Learning, USA: Boston, 2018.

[41]   M. P. Patil, J. Palma, N. C. Simeon, X. Jin, X. Liu, D. Ngabire, N.-H. Kim, N. H. Tarte, G.-D. Kim, *New J. Chem.* **2017**, *41*, 1363.

[42]   M. S. Akhtar, J. Panwar, Y.-S. Yun, *ACS Sustain. Chem. Eng.* **2013**, *1*, 591.

[43]   H. Bar, D. K. Bhui, G. P. Sahoo, P. Sarkar, S. Pyne, A. Misra, *Colloids Surfaces A Physicochem. Eng. Asp.* **2009**, *348*, 212.

[44]   A. Bankar, B. Joshi, A. R. Kumar, S. Zinjarde, *Colloids Surfaces A Physicochem. Eng. Asp.* **2010**, *368*, 58.

[45]   K. Möller, J. Kobler, T. Bein, *J. Mater. Chem.* **2007**, *17*, 624.

[46]   Malvern Instruments, *Zetasizer Nano Ser. Tech. note MRK654-01* 1.

[47]   S. Mukherjee, D. Chowdhury, R. Kotcherlakota, S. Patra, V. B, M. P. Bhadra, B. Sreedhar, C. R. Patra, *Theranostics* **2014**, *4*, 316.

[48]   U. P. Singh, H. B. Singh, R. B. Singh, *Mycologia* **1980**, *72*, 1077.

[49]   J. Dai, V. A. Yaylayan, G. S. Vijaya Raghavan, J. R. Parè, Z. Liu, *J. Agric. Food Chem.* **2001**, *49*, 1169.

[50]   J. S. Kim, E. Kuk, K. N. Yu, J.-H. Kim, S. J. Park, H. J. Lee, S. H. Kim, Y. K. Park, Y. H. Park, C.-Y. Hwang, Y.-K. Kim, Y.-S. Lee, D. H. Jeong, M.-H. Cho, *Nanomedicine Nanotechnology, Biol. Med.* **2007**, *3*, 95.

[51]   P. Senthilkumar, S. Rashmitha, P. Veera, C. Ignatious, C. SaiPriya, A. Samrot, *J. Pure Appl. Microbiol.* **2018**, *12*, 969.

[52]   R. Choudhury, M. Majumder, D. N. Roy, S. Basumallick, T. K. Misra, *Int. Nano Lett.* **2016**, *6*, 153.

[53]   M. Vivek, P. S. Kumar, S. Steffi, S. Sudha, *Avicenna J. Med. Biotechnol.* **2011**, *3*, 143.

[54]   K. P. Bocate, G. F. Reis, P. C. de Souza, A. G. Oliveira Junior, N. Durán, G. Nakazato, M. C. Furlaneto, R. S. de Almeida, L. A. Panagio, *Int. J. Food Microbiol.* **2019**, *291*, 79.

[55]   C. C. Beech IB, *Biofilms on corroding materials. In Biofilms in medicine, industry and environmental biotechnology : characteristics, analysis and control. Piet Lens, V. O'Flaherty, A. P. Moran, P. Stoodley, T. Mahony (Eds.)*; IWA

Pub, 2003.

[56] K. P. Rajasree, G. M. Mathew, A. Pandey, R. K. Sukumaran, *J. Ind. Microbiol. Biotechnol.* **2013**, *40*, 967.

[57] C. W. DODGE, *Medical mycology. Fungus diseases of men and other mammals.*; London, H. Kimpton, 1936.

[58] I. Sondi, B. Salopek-Sondi, *J. Colloid Interface Sci.* **2004**, *275*, 177.

[59] G. Brahmachari, *ChemBioChem* **2004**, *5*, 408.

[60] E. Hidalgo, R. Bartolomé, C. Barroso, A. Moreno, C. Domínguez, *Skin Pharmacol. Physiol.* **1998**, *11*, 140.

[61] R. Li, J. Chen, T. C. Cesario, X. Wang, J. S. Yuan, P. M. Rentzepis, *Proc. Natl. Acad. Sci.* **2016**, *113*, 13612.

Chapter 5

Smart Core-Shell Hybrid Nanocomposite Coatings with Multifunctional Characteristics
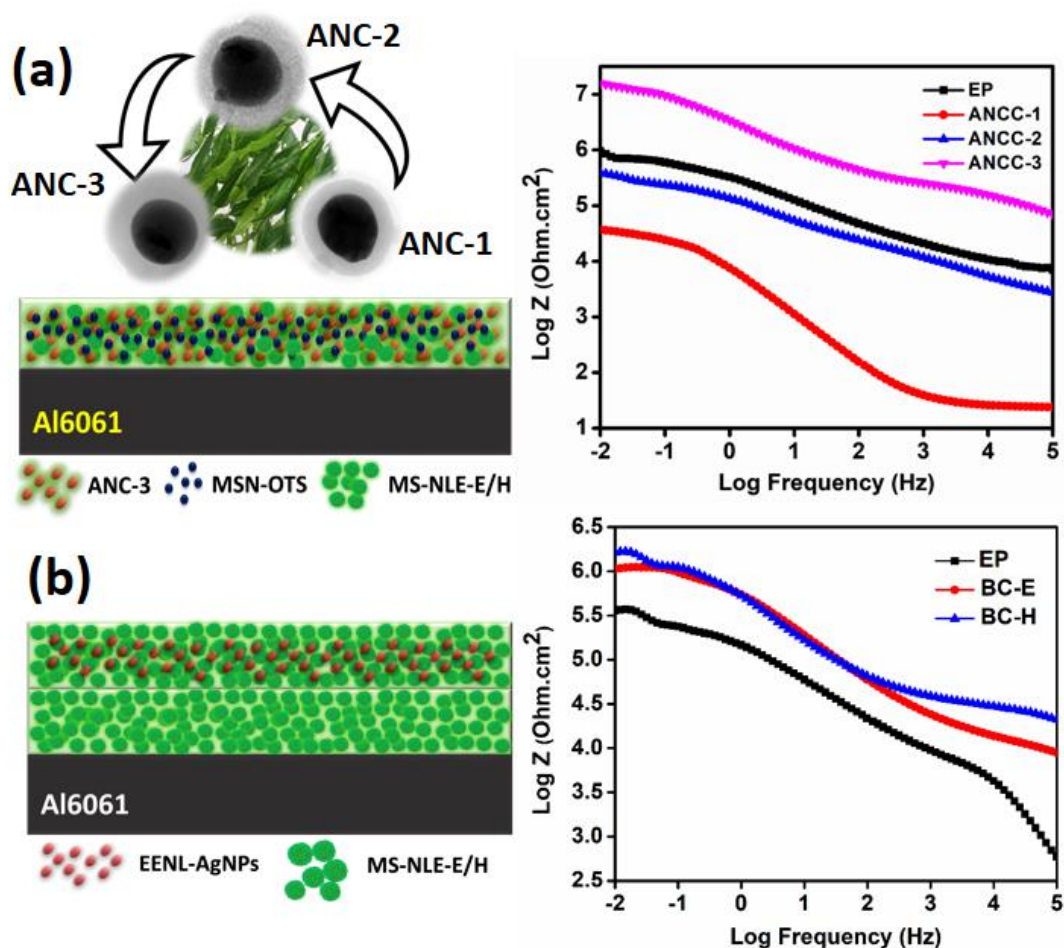
Abstract

This study describes the evaluation of silver nanocomposites for both anticorrosive and antimicrobial performances in fabricated epoxy-based coatings. Neem biomass extract was utilized as the reducing agent in the preparation of the silver nanoparticles. A combination of Tetraethylorthosilicate and Octyltriethoxysilane were used as surface modifiers to impart stability, control surface reactivity through functionalization, and improve the dispersibility of the nanoparticles in the epoxy matrix. The one-pot synchronous process produced stable, near-spherical silver-core

nanocomposites. The mesoporous silica shell allowed the incorporation of the biomass extract as a corrosion inhibitor. The presence of the corrosion inhibitor in the nanocomposite provided enhanced anticorrosion performance compared to the unloaded epoxy coatings. The antimicrobial effect of silver nanoparticles in the core was influenced by the confinement of the silver nanoparticles in the matrix restricting its release in sufficient amounts. Direct dispersal of silver nanoparticles in the epoxy matrix without functionalization resulted in poor anticorrosion performance due to promoted conductivity from the silver particles in the epoxy resin. A hybrid of the silver nanoparticles with the bio-based corrosion inhibitor leveraged the anticorrosion performance of the coatings and improved the antimicrobial performance of the nanocomposite coatings by inhibiting the growth of Pseudomonas nitroreducens and Aspergillus unguis species.

5.1   Introduction

Nanosilver encounters certain challenges for antimicrobial surface coatings due to easy aggregation, difficulty to be controllably immobilized on surfaces, potential toxicity (concentration dependent), lack of controllability in synthesis and processing, and burst release of silver ions.[1,2] For these reasons, polymeric materials are good candidates to form composite coatings with nanosilver due to their great structure tailorability, flexibility, and various methods available for polymer immobilization. Polymer components in antimicrobial coatings serve various chemical and physical functions. Firstly, as stabilizers for nanosilver synthesis preventing aggregation in solutions or on surfaces. Secondly, as linkers for nanosilver, which is directly loaded or in situ synthesized in antimicrobial composite coatings. Thirdly, as a matrix to control silver ion release. These functions are closely related to fabrication methods of the composite coatings.[2,3]

The peculiarity of silver nanoparticles is its wide range of antimicrobial properties, its response as substrates for surface-enhanced Raman spectroscopy, large available surface area to volume ratio, high catalytic activity, good electric double layer capacitance etc. these factors have made silver nanoparticles a choice material in the biomedical sector, new-generation sensors, electronics, biotechnology sector, and optical devices formulations amongst others.[4–6] The bioreduction process of silver nanoparticles reduces the synthesis steps,

194

environmental risks, cost[7] and intensive use of synthetic reactants and solvents. The biological synthesis yields nanoparticles capped with biological entities, which has improved biocompatibility and enhanced the biomedical applications.[8] Hydroxyl groups are known to play key reductive roles in the formation of metal nanomaterials while the strong interaction between biomolecules and metal nanomaterials influences their stability.[9,10] The application of biomaterials is aimed at reducing toxicity and biomaterials such as plants can be suitably scaled up for large-scale synthesis of nanoparticles.[11] Furthermore, the biological entities in biomass extracts have contributed immensely to corrosion protection of metals and alloys.[12–19]

In the present study, the silver nanoparticles were synthesized and functionalized in two different ways (in situ surface functionalization and the seeded functionalization techniques) while employing the neem leaves extract as the bio-reducing agent. The products, core-shell nanocomposites were further utilized to fabricate coatings which were assessed for anticorrosive and antimicrobial efficiency. Exploring green alternatives for conventional chemical additives to coatings for corrosion protection and antimicrobial activities on metals and alloys is a welcomed approach. The combination of organic and inorganic phases in coating formulations has realized superior properties for corrosion protection. The constructive modification of high-performance industrially relevant polymers like epoxy, when loaded with diverse nanoparticles, contributes to its wide area of significant applications.

5.2 Materials and methods

5.2.1 Materials

Ammonium hydroxide (28 % NH_3) was purchased from Alfa Aesar, England and Octyltriethoxysilane (OTS 97%) was purchased from Sigma-Aldrich, USA. All other materials/chemicals used have been described in the previous chapters and were used without additional purification.

5.2.2 Methods

5.2.2.1 Seeded functionalization technique – Ravine model

The bio-reduced silver nanoparticles (EENL-AgNPs) prepared in Chapter 4 section 4.2.2.2 were functionalized following the process described by Lismont et al.[20] In brief, 4 mg/mL of the fabricated AgNPs was sonicated for 20 min. 125 μL of

tetraethylorthosilicate (TEOS) was added and the mixture was further sonicated for 2 minutes. In a separate flask, 250 µL of the ammonia solution was added into 3 mL of ethanol and mixed. The EENL-AgNPs-TEOS was injected into the ammonia-ethanol mixture and stirred for 25 min to allow SiO_2 shell thickness. After 25 min, 40 mL of ethanol was added to stop the reaction. The particles were centrifuged at 10000 rpm for 10 min and washed with ethanol. The simultaneous nucleation and aggregation of silica shell growth onto the silver nanoparticles are described in Fig. 5.1.
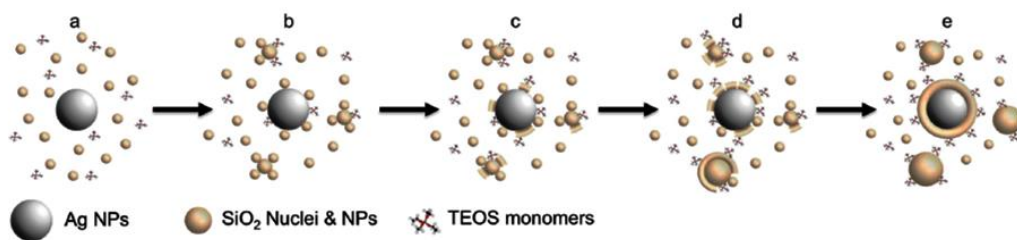
Fig. 5.1: Schematic of the functionalization of the bio-reduced AgNPs via the seeded functionalization technique to yield Ag@SiO_2 core-shell nanoparticles. (a) The appearance of primary SiO_2 nuclei, (b) slow aggregation onto AgNPs surface, (c) initial formation of ravine structure, (d) fresh SiO_2 nuclei filling the ravines, and (e) final wrapping of AgNPs.[20]

5.2.2.2 One-pot synchronous Synthesis

Neem leaves crude ethanolic extract was prepared as described in Chapter 2 section 2.2.2.1. The core-shell silver-mesoporous silica nanoparticles (Ag@MSN) were synthesized using Silver nitrate as a precursor, by a facile one-pot process following the procedure described in Han et al.[21] with modifications. Ethanolic extract of Neem leaves (NLE) was used as the reducing agent and a ratio of TEOS:OTS as the silica precursors. CTAB was used as the stabilizer and template and sodium hydroxide as a basic catalyst. In brief, 0.20 g of CTAB was dissolved in the solution containing 96 mL of water and 2.4 mL of 0.5 M NaOH was added. After stirring at 80°C for 30 min, 0.6 mL of NLE (EENL) was added followed by 2.0 mL of 0.1 M aqueous silver nitrate solution. Then 1.0 g of TEOS:OTS (0.8:0.2) was added with stirring for 2 h. The products were purified by centrifuging at 10000 rpm for 10 min,

washed with ethanol and water (3x) and dried at 50°C in vacuum for 24 h. The as-prepared product after vacuum drying is designated hereafter as ANC-1.

5.2.2.3 Mesoporous silica nanoparticles templated by Octyltriethoxysilane (MSN-OTS)

Mesoporous silica nanoparticles templated by Octyltriethoxysilane was prepared following the method described by Chen[22] with modifications. In the process, 20 mL of ethanol, 3 mL of deionized water and 0.628 mL of ammonium hydroxide were premixed and stirred at 30°C for 10 min. 2 mL of TEOS was mixed with 0.8 mL of OTS and stirred separately. The silane mixture was added to the ethanol mixture dropwise whilst stirring at 500 rpm and allowed to react for 2 h at 30°C. The product was centrifuged at 10000 rpm for 10 min, washed three times with ethanol and vacuum dried at 40°C for 24 h.

5.2.2.4 Loading of NLE onto Ag@MSN core-shell nanoparticles

The template was removed from ANC-1 by calcination at 550°C for 6 h and designated as ANC-2. Afterward, ANC-2 was loaded with NLE following the process described in Chapter 2, section 2.2.2.4. After being centrifuged and dried under vacuum at 50°C, ANC-3 was obtained. The products ANC-1, ANC-2, and ANC-2 were subjected to XRD, FTIR, TGA, and N_2 adsorption-desorption techniques.

5.2.2.5 Substrate and nanocomposite coating preparation

The test substrate aluminium alloy 6061 was obtained and prepared as described in Chapter 2 section 2.2.2.5. Key coating components (DGEBA, HY951, and 1-butanol) are the same as those used in previous chapters. Two different coating formulations were prepared. Firstly, coatings prepared with the core-shell silver nanoparticles/nanocomposites designated as ANCCs. 1 wt.% each of ANCs, MSN-OTS, and MS-NLE-E were sonicated for 15 min in butanol. The mixture was blended with the epoxy and stirred for 20 min. the hardener was added and the coating was stirred briefly and sonicated within 5 min. Samples were dip-coated at 700 mm/min and allowed to air dry for some days prior to preservation in a desiccator before use. The coatings obtained were designated as ANCC-1, ANCC-2, and ANCC-3 while EP represents the unloaded epoxy coating. Secondly, the bilayer coatings prepared with 2 wt.% MS-NLE-E/H as the base coat and a blend of 2 wt.% MS-NLE-E/H and 5 mg EENL-AgNPs as the topcoat. The base coat was air dried for 24 h. The topcoat was then applied, air-dried, then oven-dried at 50°C for 24 h and preserved in a

desiccator before use. The coatings prepared were designated as BC-E and BC-H while EP represents the unloaded epoxy coating.

5.2.3 Physicochemical and morphological characterizations

The nanocomposites were characterized using transmission electron microscopy (TEM), scanning electron microscopy (SEM), X-ray Diffraction (XRD) analysis, thermogravimetric analysis (TGA), N_2 adsorption-desorption analysis, and ATR-FTIR as described in Chapter 2, section 2.2.3. Similarly, the electrochemical impedance spectroscopy (EIS) and Potentiodynamic polarization (PP) studies were conducted for the anticorrosive systems with the conventional three-electrode cell, CH Instruments electrochemical workstation CHI608E, CH Instruments Inc. as described in Chapter 2, section 2.2.3. The substrates were dip-coated using Spectrodip Instruments dip coater (Chennai, India).

5.2.4 Antimicrobial evaluation

The procedure for coating evaluation in the presence of the test microbes is the same procedure described in Chapter 2, section 2.2.4. While the procedure for the nanocomposite evaluation is described in Chapter 4, section 4.2.4. Deionized water, 1-butanol, and the hardener HY951 were the solvents used for the nanocomposite microbial assessment.

5.3 Results and Discussion

5.3.1 SEM/EDS analysis of the nano-constructs

The morphological characterizations of Ag@SiO$_2$ prepared via seeded functionalization technique and that of MSN-OTS obtained from mesoporous silica nanoparticles templated with octyltriethoxysilane is presented in Fig. 5.2. The nanoparticles were spherical in shape. In the core-shell nanoparticles, the silica shell is meant to enhance the colloidal stability and control the distance between core particles within assemblies through shell thickness.[23] MSN-OTS was prepared as an additive to improve interfacial adhesion, particle dispersion and promote intimate polymer filler interaction for the coatings to be fabricated with the nanoparticles prepared in this chapter.
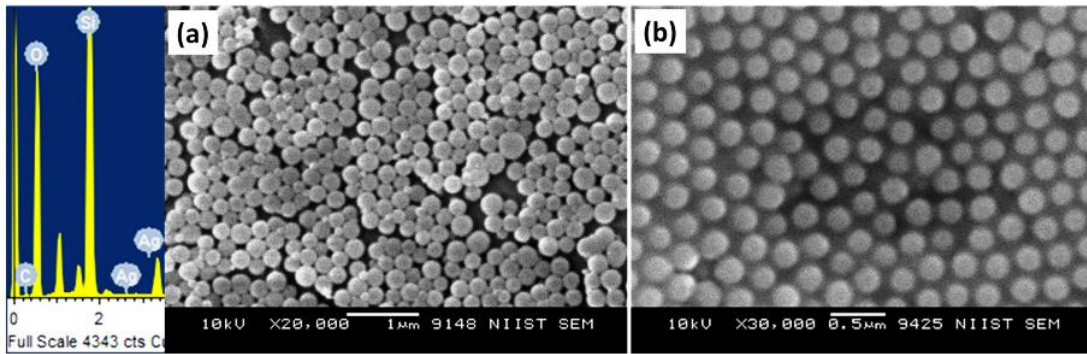
Fig. 5.2: (a) SEM/EDS of Ag@SiO$_2$ and (b) SEM micrograph of MSN-OTS.

5.3.2 TEM analysis of the nano-constructs

The TEM micrographs in Fig. 5.3 presents the morphology of Ag@SiO$_2$, MSN-OTS, and ANC-1, ANC-2, and ANC-3. The spherical morphology of Ag@SiO$_2$ (Fig. 5.3(a-b)) is that of a large shell and small core. MSN-OTS (Fig. 5.3(c)) appears to be a distorted spherical nanoparticle with sizes within 56-114 nm measured with TEM. While in Fig. 5.3(d-f) the distorted spherical Ag@MSN were mainly composed of the large core, small shell silver nanoparticles for ANC-1, ANC-2 and ANC-3 respectively. Generally, the silica shell stabilizes small particles against coalescence as well as acts as a selective membrane to control the rate of chemical reactions involving the metal cores.[24] But with the passage of time, it was observed that AgNPs slowly etched away when the nanoparticles were kept in the coating solution for a while (Fig 5.3(b)) due to the oxidation of silver in the presence of ammonia forming soluble [Ag(NH$_3$)$_2$]$^+$ complex.[25] The ammonia solution was used as the catalyst for the hydrolysis of the TEOS precursor and was found to attack the silver nanomaterials through the following reaction in equation 5.1[25,26] which constituted a drawback in the initial AgNPs coating evaluation that will be discussed in the later section.

$$4Ag + \ O_2 + \ 8NH_3 . H_2O \ \rightarrow 4Ag(NH3)_2^+ + 4OH^- + 6H_2O \qquad (5.1)$$
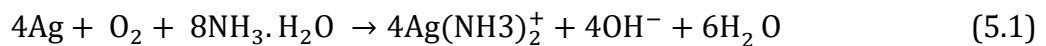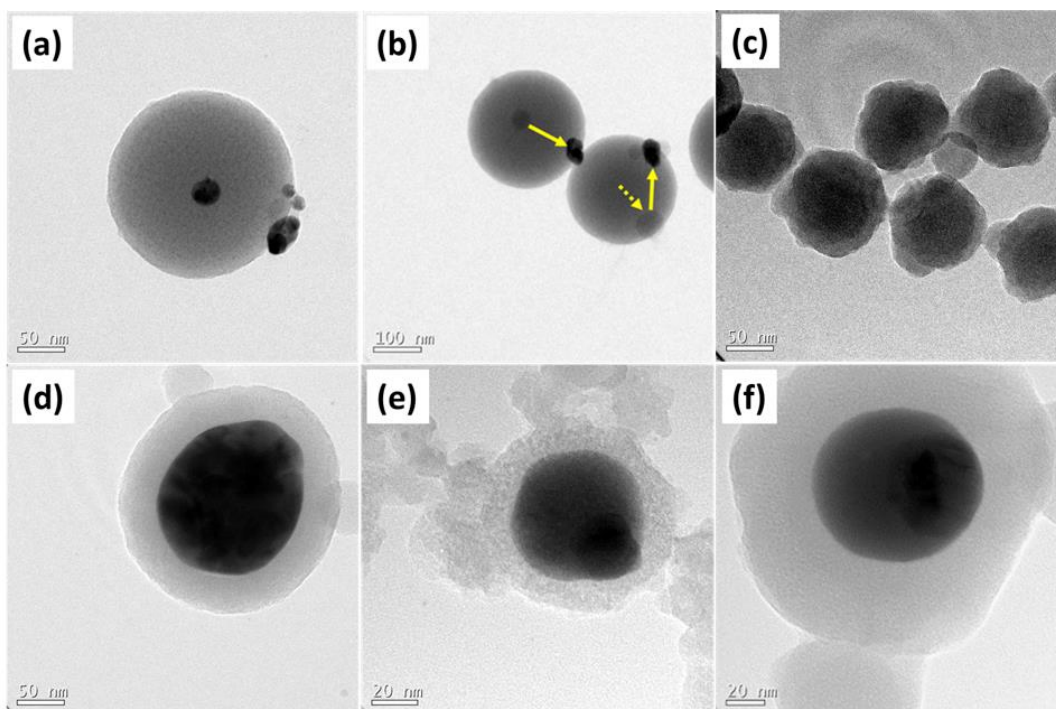
Fig. 5.3: TEM micrographs of (a & b) Ag@SiO$_2$, (C) MSN-OTS, (d) ANC-1, (e) ANC-2, and (f) ANC-3.

To overcome the etching occurrence of the silver nanoparticles, the one-pot synchronous route was applied using NaOH as the basic catalyst. Ag@MSN was obtained and designated as ANC-1 (Fig. 5.3(d)). After calcination and template removal, ANC-2 (Fig. 5.3(e)) and after loading NLE as a corrosion inhibitor into the porous silica shell obtained, ANC-3 (Fig. 5.3(f)). The photo images of Ag@MSN nanocomposites ANC-1, ANC-2 and ANC-3 are presented in Fig. 5.4. The sizes of the cores obtained were within 92-123 nm and the shells were within 32-40 nm. The schematic detailing the preparation of the core-shell-based nanocomposites is presented in Fig 5.5.
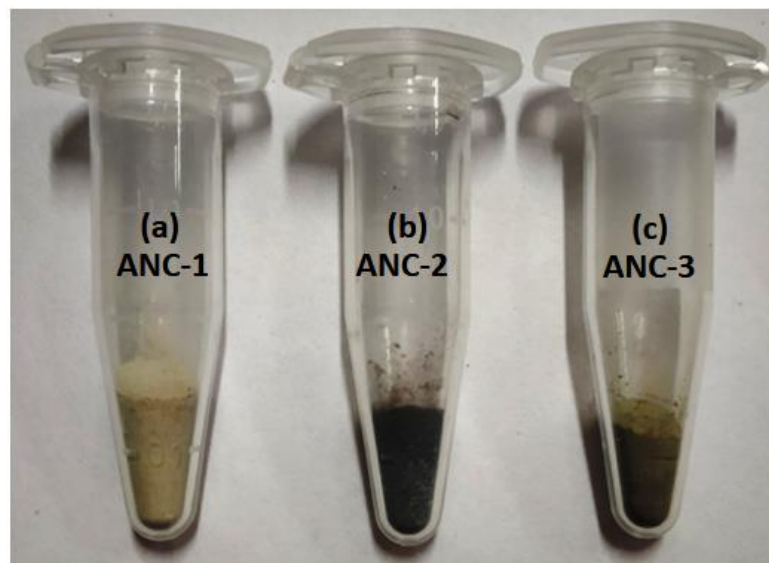
Fig. 5.4: Photo images of Ag@MSN nanocomposites (a) ANC-1, (b) ANC-2, and (c) ANC-3.
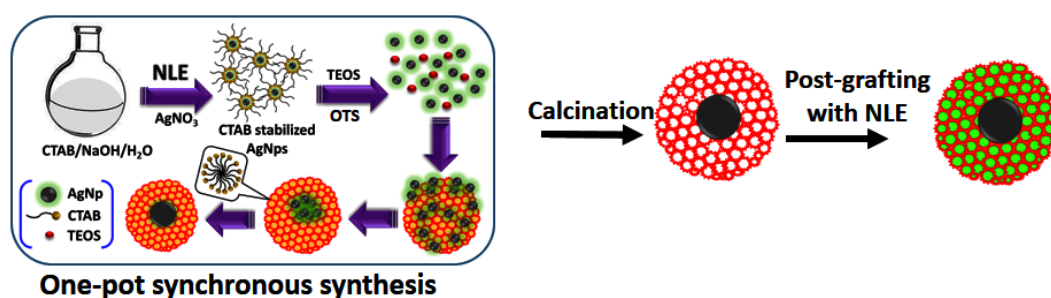
Fig. 5.5: Schematic of the detailed preparation of the Ag@MSN (ANC-1, ANC-2, and ANC-3).

5.3.3   XRD analysis

Fig. 5.6 represents the diffractograms of the studied samples which was used in the coating formulation. Amorphous SiO_2 is characterized by a broad hump between 15° and 25°.[27] To analyze the crystallinity samples, X'Pert Highscore plus software was used and peaks in ANC-1 at 44.576 and 64.657 2θ values were indexed to (200) and (220) reflections of cubic Ag (JCPDS 01-087-0597). Peaks at 31.220, 55.293, and 81.758 2θ values were indexed to (200), (222), and (422) reflections of cubic AgBr (JCPDS 01-079-0149) while the peak at 73.460 2θ value was indexed to (226) reflection of tetragonal AgO (JCPDS 01-084-1108).

In ANC-2, the peaks at 38.509, 44.675, 64.874, and 76.773 2θ values were indexed to (111), (200), (220), and (311) reflections of cubic Ag (JCPDS 01-087-0597). The peak at 31.429 2θ value was indexed to (200) reflection of cubic AgBr (JCPDS 01-079-0149) while the peak at 86.392 2θ value was indexed to (611) reflection of tetragonal AgO (JCPDS 01-084-1108). In ANC-3, the peak at 38.332 2θ value and a slightly shifted peak at 45.016 2θ value, were indexed to (111) and (200) reflections of cubic Ag (JCPDS 01-087-0597). The peak at 31.403 2θ value was indexed to (200) reflection of cubic AgBr (JCPDS 01-079-0149) and the peak at 55.769 2θ value was indexed to (141) reflection of tetragonal AgO (JCPDS 01-084-1108). The experimental diffraction angles at 2θ and the standard diffraction angles at 2θ were observed to be in agreement and are presented in Tables 5.1-5.3. The unassigned peaks in Fig. 5.6 are crystalline peaks for powdered x-rays of biomass extracts discussed in Chapter 2, section 2.3.11.
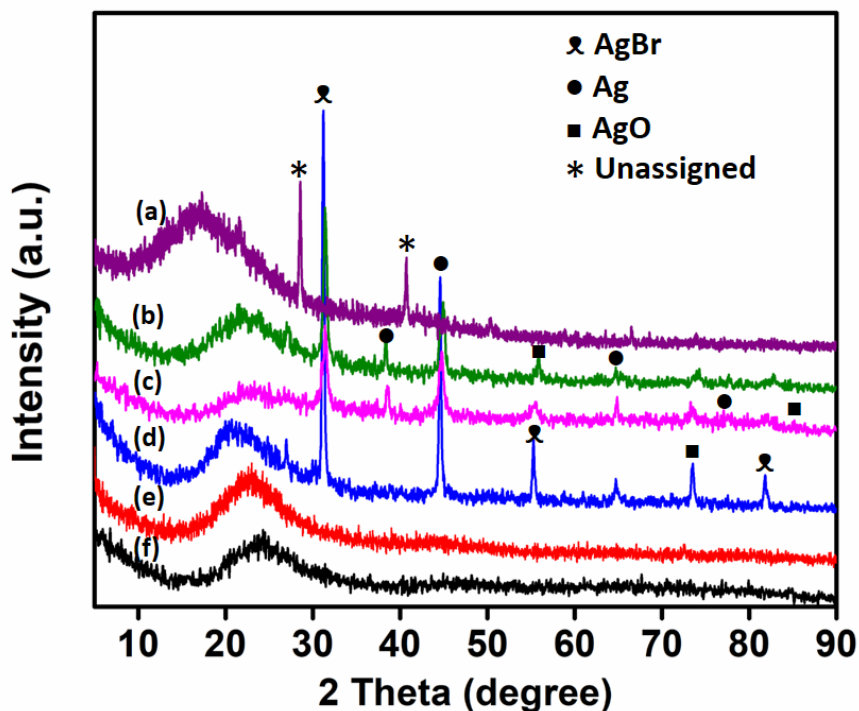
Fig. 5.6: XRD diffractograms of (a) NLE, (b) ANC-3, (c) ANC-2, (d) ANC-1, (e) MS-NLE-E, and (f) MSN-OTS.

Table 5.1: Experimental and standard diffraction angles of Ag nanoparticles in all Ag@MSN with d-spacings.

S/N	hkl	Experimental diffraction angle, 2θ [degrees]	d-spacing (Å)	Standard diffraction angle, 2θ [degrees] JCPDS 01-087-0597 (Cubic silver)	d-spacing (Å)
1.	111	38.509	2.336 (ANC-2)	38.114	2.359
2.	111	38.332	2.346 (ANC-3)	38.114	2.359
3.	200	44.576	2.031 (ANC-1)	44.299	2.043
4.	200	44.675	2.027 (ANC-2)	44.299	2.043
5.	200	*45.016	2.012 (ANC-3)	44.299	2.043
6.	220	64.657	1.440 (ANC-1)	64.443	1.444
7.	220	64.874	1.436 (ANC-2)	64.443	1.444
8.	311	76.773	1.241 (ANC-2)	77.400	1.232

Table 5.2: Experimental and standard diffraction angles of silver bromide (AgBr) nanoparticles in all Ag@MSN with d-spacing.

S/N	hkl	Experimental diffraction angle, 2θ [degrees]	d-spacing (Å)	Standard diffraction angle, 2θ [degrees] JCPDS 01-079-0149 (Cubic silver (II) oxide)	d-spacing (Å)
1.	200	31.220	2.862 (ANC-1)	30.944	2.887
2.	200	31.429	2.844 (ANC-2)	30.944	2.887
3.	200	31.403	2.846 (ANC-3)	30.944	2.887
4.	222	55.293	1.660 (ANC-1)	55.040	1.667
5.	422	81.758	1.177 (ANC-1)	81.606	1.178

Table 5.3: Experimental and standard diffraction angles of silver (II) oxide (AgO) nanoparticles in all Ag@MSN with d-spacing.

S/N	hkl	Experimental diffraction angle, 2θ [degrees]	d-spacing (Å)	Standard diffraction angle, 2θ [degrees] JCPDS 01-084-1108 (Cubic silver (II) oxide)	d-spacing (Å)
1.	226	73.460	1.289 (ANC-1)	73.369	1.289
2.	611	86.392	1.125 (ANC-2)	86.618	1.123
3.	141	55.769	1.647 (ANC-3)	55.951	1.642

5.3.4 ATR-FTIR analysis

The FTIR spectra in Fig. 5.7 represents NLE, ANC-1, ANC-2, ANC-3, and MSN-OTS. The spectrum for NLE shows bands for the presence of N-H and O-H overlap and C=O stretching of amides. C-H stretching vibrations at 2924 and 2854 cm^{-1} amongst others discussed in details in Chapter 2 section 2.3.1. In ANC-1, the stretching vibration of C-H at 2922 and 2852 cm^{-1}, Si-O-Si at 1030 cm^{-1}, Si-O at 433 cm^{-1} and Si-OH at 962 and 786 cm^{-1}, were present due to the template within the matrix. After calcination (ANC-2) all organic related bands were removed and bands corresponding to only Si-O-Si at 1055 cm^{-1}, Si-OH at 972 and 794 cm^{-1}, and Si-O at 449 cm^{-1} were present. After loading NLE (ANC-3), the bands corresponding to the presence of organic functional groups of NLE were observed at similar positions which confirms the adsorption of the neem phytochemicals onto the porous shell of the core-shell nanoparticle.
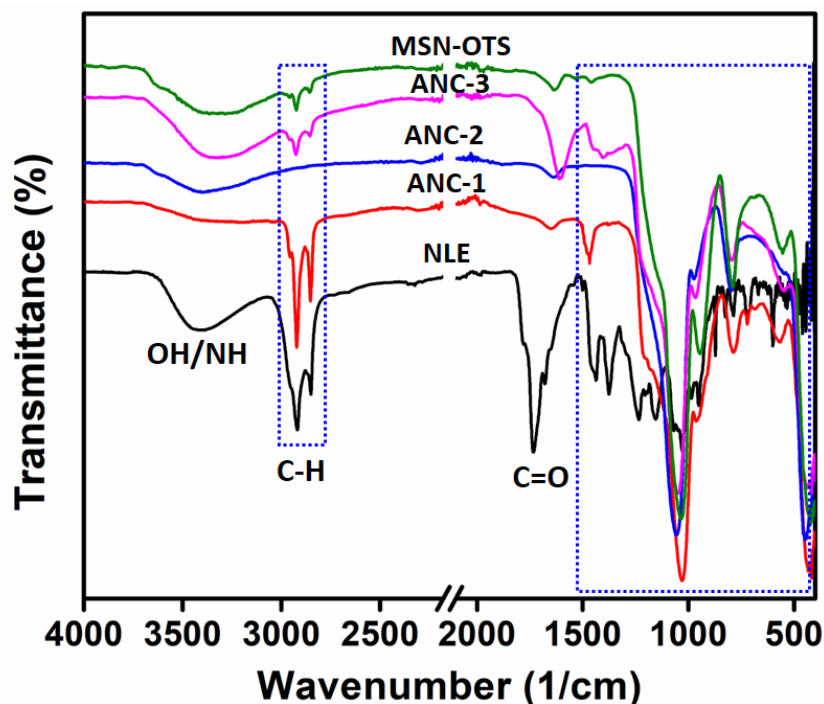
Fig. 5.7: ATR-FTIR spectra of NLE, ANC-1, ANC-2, ANC-3 and MSN-OTS.

5.3.5 N$_2$ adsorption-desorption analysis

The physical properties of the core-shell silver nanocomposites; ANC-2 and ANC-3 such as specific surface area, pore volume, and pore diameter were measured by N$_2$ adsorption-desorption technique. The extent of modification is presented in Table 5.4. The surface area of ANC-2 after calcination was found to be 393.26 m^2/g and decreased to 119.59 m^2/g (ANC-3) after loading the neem phytochemical. The decrease evidence that the porous shell is covered by the organic moieties. A decrease in the pore volume from 0.69 cm^3/g to 0.46 cm^3/g is evidence that the organic material is within the pores of the silica matrix. The extent of decrease is also influenced by the size of the bonded groups. The increase in average pore diameter was also observed after the loading. Furthermore, an open-loop structure was observed in the N$_2$ adsorption/desorption isotherms for ANC-2 and ANC-3 as shown in Fig. 5.8. The shape of the hysteresis loops of the core-shell nanocomposites before (ANC-2) and after (ANC-3) loading the neem phytochemical appears to fit the IUPAC classification of H3 and H4 hysteresis which contain a characteristic step-down in the desorption branch associated with the hysteresis loop closure. Materials that give rise to this type of loops from the isotherms may arise due to some complexities,

in this case, the presence of the solid core within the porous matrix may be a contributing factor. In ANC-2 the forced close phenomenon is observed where there is a steep region of the desorption branch leading to the lower closure point near a relative pressure of 0.4 to 0.5. In ANC-3 it is the unclosed loop phenomenon. Similar unclosed hysteresis loop structures of materials have been reported and are attributed to a pore network effect.[28]
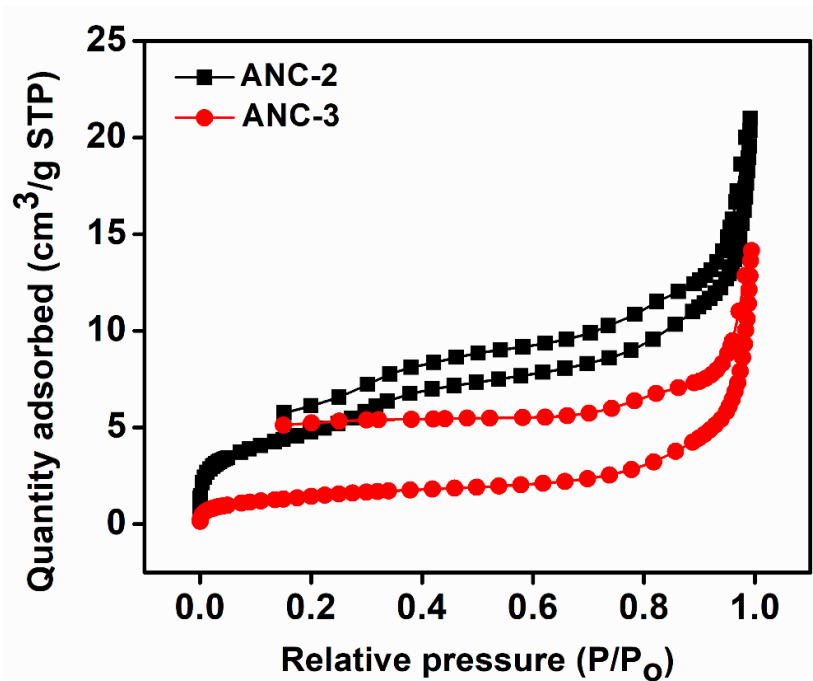
Fig. 5.8: N2 adsorption/desorption isotherms for ANC-2 and ANC-3.

Table 5.4: N2 Adsorption-desorption analysis of ANC-2 and ANC-3.

S/No.	Samples	BET surface area (m²/g)	Total pore volume at P/Po = 0.98 (cm³/g)	Pore Diameter by BJH (nm)
1.	ANC-2	393.26	0.69	7.31
2.	ANC-3	119.59	0.46	18.84

5.3.6 TG analysis

The changes in weight of the samples monitored with increasing temperature by thermogravimetry enabled the determination of the amount of organic moieties

loaded in the porous matrix of the silica shell. The weight loss evaluated in the temperature range of 25-600°C in argon atmosphere are shown in Table 5.5 and plotted in Fig. 5.9. The weight losses were recorded in distinct regions and the steps involve the thermodesorption of physisorbed water and the decomposition of organic components in the samples. The residual masses were considered at 600°C. Weight loss for NLE is evident that it comprises mostly of organic biomolecules in which 80.6% was decomposed between 150-600°C as earlier described in Chapter 2, section 2.3.8. Since ANC-1 comprised of the template, 45.9% was decomposed between 150-600°C. After template removal, ANC-2 had the least weight loss at the temperature of decomposition of organic compounds. The weight loss of ANC-3 between 150-600°C was 18.0% which confirms that NLE was successfully adsorbed onto ANC-2. The decreased weight loss for the samples between 25-150°C is indicative of the hydrophobic character of the samples. The residual masses at 600°C for ANC-2 and MSN-OTS were the highest at 83.5% due to the residual silicate network in the samples after the analysis and also the presence of inorganic silver in ANC-2.

Table 5.5: TG analysis of ANC-1, ANC-2, ANC-3, MSN-OTS, and NLE.

Samples	Weight Loss (%w/w)		Residues (% w/w)
	25-150°C	150-600°C	600°C
(a) NLE	4.1	80.6	15.3
(b) ANC-1	5.6	45.9	48.5
(c) ANC-2	12.7	4.5	83.5
(d) ANC-3	10.8	18.0	71.2
(e) MSN-OTS	9.7	6.6	83.5
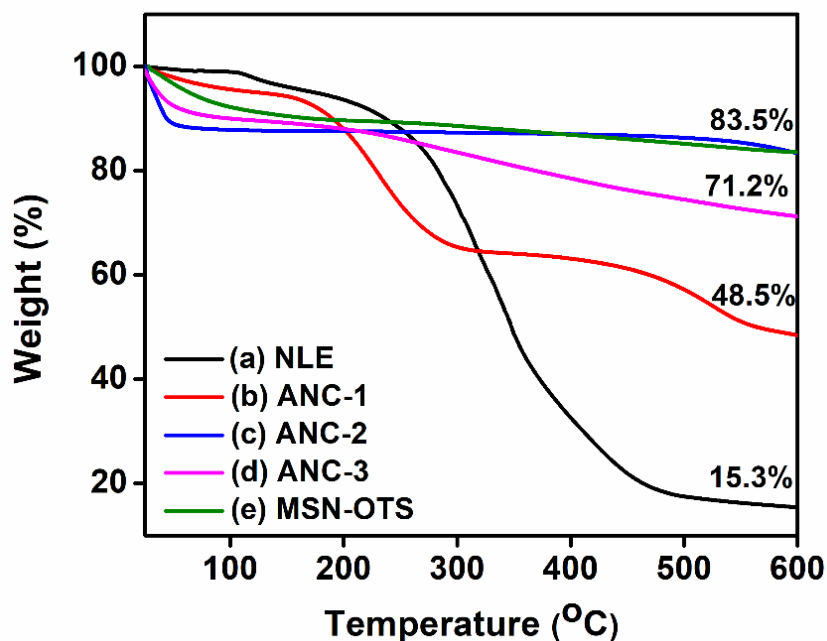
Fig. 5.9: TGA curves obtained at a heating rate of 10°C/min under argon atmosphere for (a) NLE, (b) ANC-1, (c) ANC-2, (d) ANC-3, and (e) MSN-OTS.

5.3.7 AgNPs-epoxy nanocomposite coatings anticorrosion evaluation

Coatings may contain many ingredients with specific functionalities but key considerations for designing corrosion-resistant coatings should be centered on protection, component design, and function as well as coating formulation.[29] The protective performance of epoxy coatings can be improved by the addition of secondary particles relatively miscible with the epoxy polymer. The incorporation of nanoparticles into epoxy resins fills available cavities, bridges cracks, and enables crack deflection and bowing.[30] This decreases porosity and zigzags the diffusion path for damaging species. With nanoparticles, coating defects in the form of holes from local shrinkage during curing are filled. The nanoparticles prevent epoxy disaggregation during curing and enable interconnection between molecules through its bridging effect. As a result, a reduction in total free volume as well as an increase in the cross-linking density of the epoxy resin is achieved ensuing a more homogenous coating.[31]

5.3.7.1 Epoxy-ANCC evaluation

The SEM micrographs and its corresponding EDS spectra of the coatings prepared using the core-shell nano-constructs are presented in Fig. 5.10. The

average thicknesses of the coatings EP, ANCC-1, ANCC-2, and ANCC-3 estimated from the cross-sectional scanning electron microscopy images (Fig. 5.11) was 30 ±3 μm.

Element	Weight %	Atomic %
C K	55.29	60.66
N K	23.91	22.49
O K	20.19	16.63
Si K	0.41	0.19
Br L	0.06	0.01
Ag L	0.15	0.02
Totals	100.00	

Element	Weight %	Atomic %
C K	65.01	70.30
N K	15.19	14.09
O K	18.71	15.19
Si K	0.85	0.39
Ag L	0.25	0.03
Totals	100.00	

Element	Weight %	Atomic %
C K	69.77	74.98
N K	6.58	6.07
O K	23.28	18.79
Si K	0.36	0.17
Totals	100.00	
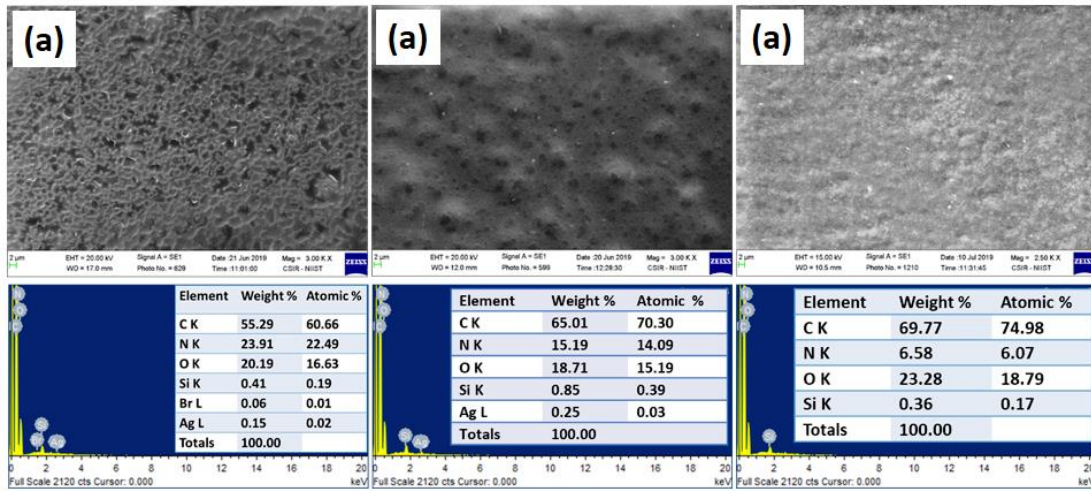
Fig. 5.10: SEM micrographs of (a) ANCC-1, (b) ANCC-2, and (c) ANCC-3 showing the nature of the coating surfaces and the corresponding EDS spectra.
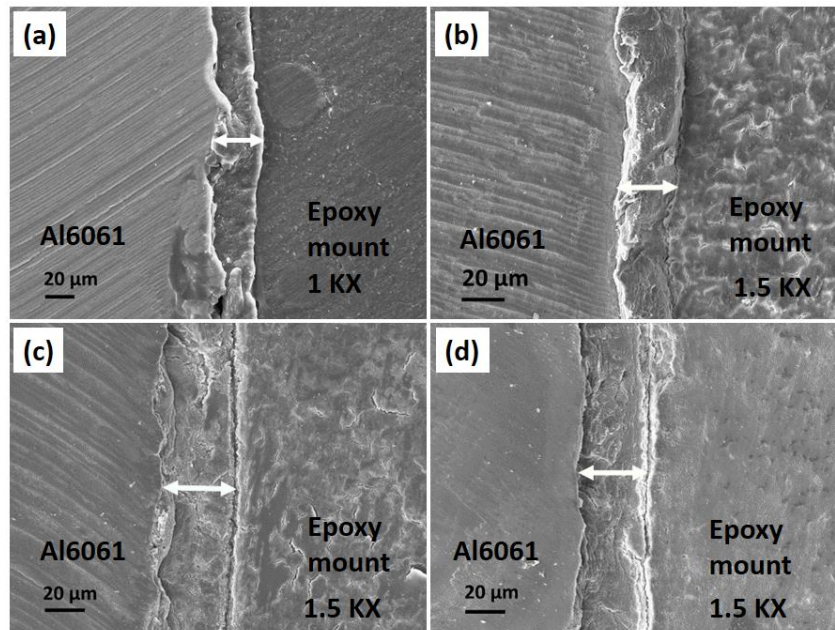
Fig. 5.11: Cross-sectional SEM micrographs of (a) EP, (b) ANCC-1, (c) ANCC-2, and (d) ANCC-3 for which coating thickness was determined.

The ANC-based coatings were evaluated for its anticorrosive performance via electrochemical impedance spectroscopy and potentiodynamic polarization techniques. Data collection was set at intervals for up to 48 h and changes in R_{coat},

Q_{coat}, R_{ct}, Q_{dl} and W over the hours of data collection for the working electrode in 3.5 wt.% NaCl were observed. Amongst the ANC-based coatings studied in comparison to the unloaded epoxy coatings, ANCC-3 had the best anticorrosive performance evidenced from the Bode and phase angle plots shown in Fig. 5.12. The schematic of the hybrid coating containing more of the neem extract inhibitor which was encapsulated in the porous silica shell is shown in Fig. 5.12(c). The impedance data were analyzed from two equivalent circuit (EC) models for the coatings (Fig. 5.12(d)) after 48 h immersion in 3.5 wt.% NaCl solution and presented in Table 5.6. Model 1 fits EP, ANCC-2 & ANCC-3 while Model 2 fits ANCC-1. The variations observed is due to the behavior of the different components of the coatings in the corrosive environment. Furthermore, the potentiodynamic polarization data meant to corroborate the findings from the Impedance analysis is presented in Table 5.7. The least corrosion current density (I_{corr}) determined from the Tafel plot (Fig. 5.12(e)) is that of ANCC-3 which offered better corrosion protection to the aluminium alloy substrate.

Fig. 5.12: (a) Bode plots and (b) Phase angle plots of the Ag@MSN coatings; ANCCs (c) Schematic of ANCC-3 (d) Equivalent circuits used for the impedance fitting (e) Tafel plots of the Ag@MSN coatings; ANCCs.

Table 5.6: Impedance data from equivalent circuit (EC) for EP, ANCC-1, ANCC-2 & ANCC-3 after 48 h immersion in 3.5 wt.% NaCl solution.

Coatings	R_{sol} (Ω cm^2)	Q_{coat} (S.sec^n)	n (0<n<1)	R_{coat} (Ω cm^2)	Q_{dl} (S.sec^n)	n (0<n<1)	R_{ct} (Ω cm^2)	W (S.sec^{-5})	χ^2
EP	5737	1.11 x10^{-6}	0.45	1.09 x10^6	4.21 x10^{-5}	0.98	88.42	5.57 x10^{-8}	3.08 x10^{-3}
ANCC-1	25.5	2.57 x10^{-5}	0.86	3.19 x10^4	1.32 x10^{-3}	1	1.83 x10^4	-	3.08 x10^{-3}
ANCC-2	547.3	2.32 x10^{-6}	0.39	6.98 x10^4	2.92 x10^{-7}	0.81	3.13 x10^5	1.93 x10^{-5}	1.45 x10^{-3}
ANCC-3	0.01	1.87 x10^{-9}	0.66	2.35 x10^5	9.84 x10^{-8}	0.56	2.13 x10^7	3.96 x10^{-5}	2.68 x10^{-3}

Table 5.7: Potentiodynamic polarization parameters obtained from ANCCs after 48 h immersion in 3.5 wt.% NaCl solution.

S/N	Coatings	E_{corr} (V)	I_{corr} (μA cm^{-2})
1.	EP	-1.330	0.0369
2.	ANCC-1	-0.698	0.2466
3.	ANCC-2	-1.040	0.0652
4.	ANCC-3	-1.150	0.0016

5.3.7.2 Bilayer nanocomposite coatings anticorrosion evaluation

The bilayer coating was meant to accommodate EENL-AgNPs within the coating without further functionalization. But simultaneously control the conductivity of silver nanoparticles in the epoxy coating by ensuring a base coat containing the encapsulated corrosion inhibitor was underneath. Furthermore, the encapsulated corrosion inhibitor was also blended with the silver nanoparticles in the topcoat. This created a zigzag diffusion path for the corrosive species and overcame the fast deterioration of the coating film in the presence of unfunctionalized silver nanoparticles. Knowing that leached silver ions in solution can combine with chloride ions to precipitate silver chloride. The coating thickness

of the bilayer coatings determined from the SEM cross-sectional area presented in Fig. 5.13 was measured to be 60 ±7 μm.

In Fig. 5.14(a) Bode and phase angle plots obtained from the electrochemical analysis is presented and the schematic of the bilayer coatings loaded with the different nanoparticles in Fig. 5.14(b). The equivalent circuit in Fig. 5.14(c) was applied to appropriately analyze the impedance data of the different coatings. The circuit was observed to have three time constants described as $R_{sol}(Q_{coat}(R_{coat}(Q_{dl}(R_{ct}(C_xR_x)))))$. Where R_{sol} is the solution resistance, Q_{coat} and R_{coat} correspond to the constant phase element of the coating and resistance of pores in the coating respectively. Q_{dl} and R_{ct} represents double-layer constant phase element and charge transfer resistance, respectively. C_x and R_x may be attributed to oxides or the presence of chemical species.

R_{coat} and R_{ct} values of BC-E and BC-H were increased compared to the unloaded epoxy coating of similar thickness. This implied slow electrochemical reactions occurred at the electrode surface which is attributed to corrosion inhibition. Although it appears that BC-E out-performed BC-H. The fitted values are detailed in Table 5.8. Likewise, the potentiodynamic polarization data obtained from the Tafel plots in Fig. 5.14(d) meant to corroborate the impedance data revealed a decreased corrosion current density (I_{corr}) for the bilayer coatings in comparison with the unloaded epoxy coating.
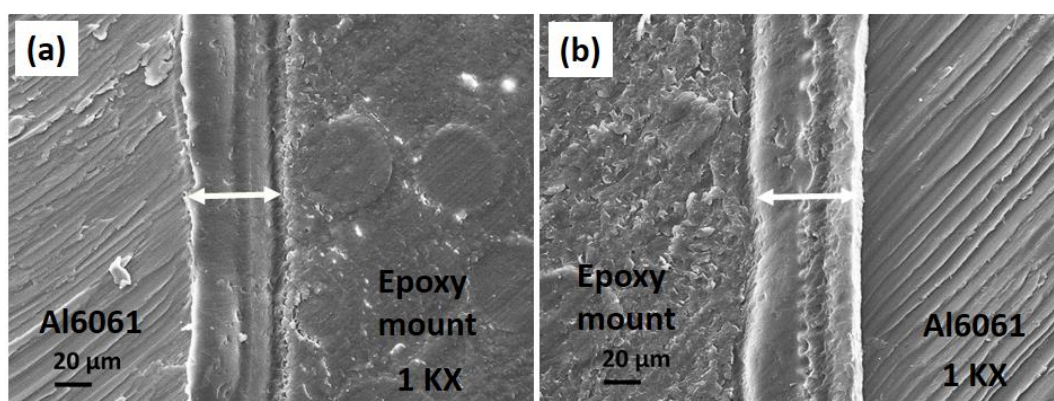
Fig. 5.13: Cross-sectional SEM micrographs of (a) BC-E and (b) BC-H for which coating thickness was determined.

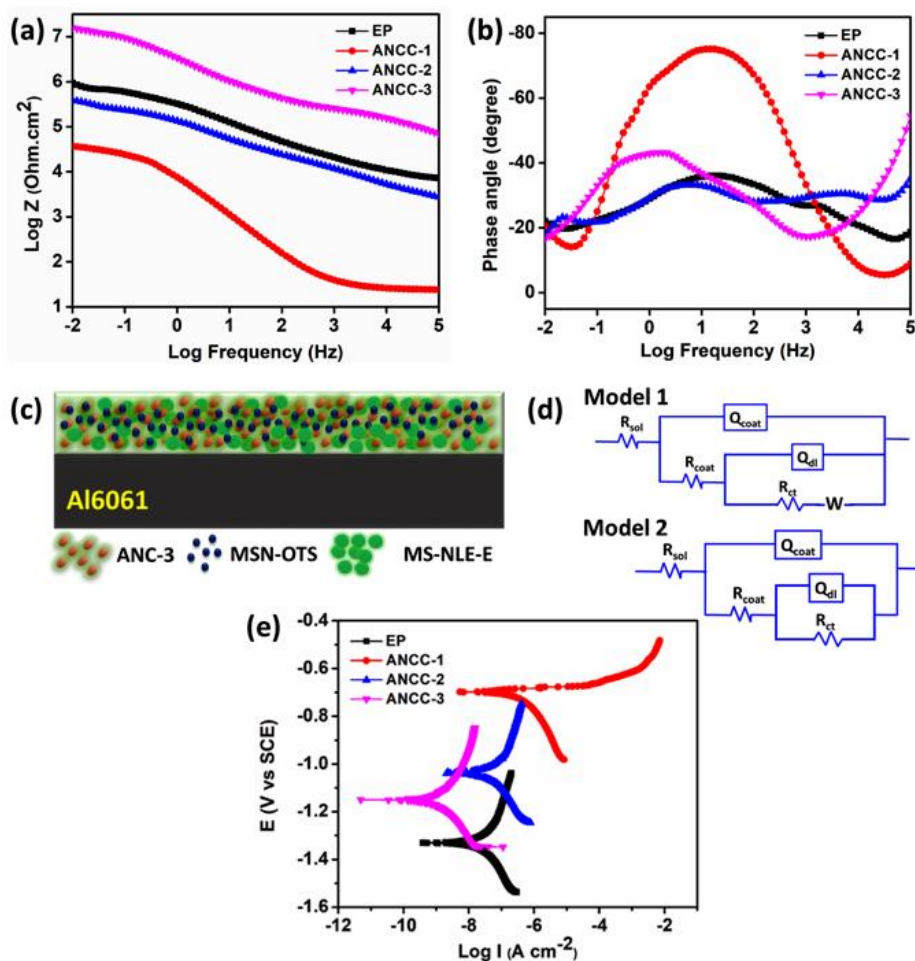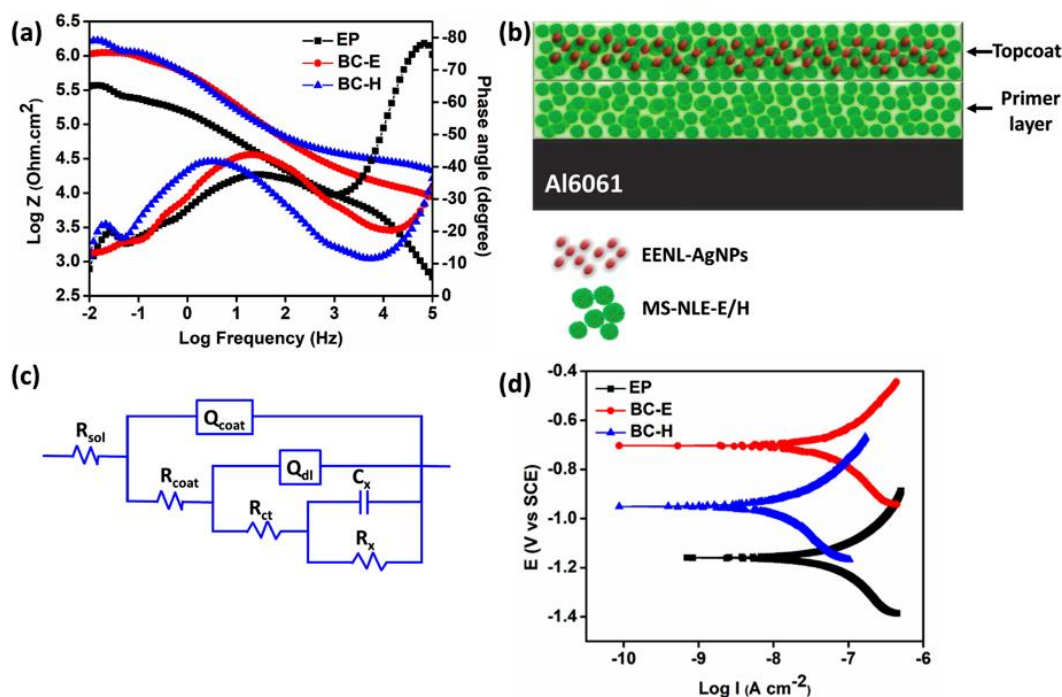**Fig. 5.14:** (a) Bode plots and Phase angle plots of the bilayer coatings (b) Schematic of BC-E and BC-H (d) Equivalent circuit used for the impedance fitting (e) Tafel plots of the bilayer coatings.

Table 5.8: Impedance data from the equivalent circuit (EC) for EP, BC-E, and BC-H after 24 h immersion in 3.5 wt.% NaCl solution.

EC Parameters	EP	BC-E	BC-H
R_{sol} (Ω cm^2)	70.28	0.010	0.025
Q_{coat} (S.sec^n)	2.662×10^{-9}	6.696×10^{-9}	1.377×10^{-9}
n (0<n<1)	1	0.69	0.75
R_{coat} (Ω cm^2)	5.831×10^3	1.352×10^4	3.168×10^4
Q_{dl} (S.sec^n)	1.672×10^{-6}	4.531×10^{-7}	5.575×10^{-7}
n (0<n<1)	0.54	0.57	0.58
R_{ct} (Ω cm^2)	2.953×10^5	1.259×10^6	1.666×10^6
C_x (F)	4.197×10^{-5}	5.602×10^{-5}	1.966×10^{-5}
R_x (Ω cm^2)	1.497×10^5	$*9.762 \times 10^{14}$	6.784×10^5
χ^2	6.5×10^{-4}	1.3×10^{-3}	1.9×10^{-3}

Table 5.9: Potentiodynamic polarization parameters from the bilayer coatings after 24 h immersion in 3.5 wt.% NaCl solution.

S/N	Coatings	E_{corr} (V)	I_{corr} (μA cm^{-2})
1.	EP	-1.159	0.0668
2.	BC-E	-0.703	0.0567
3.	BC-H	-0.951	0.0153

5.3.8 Nanocomposite antimicrobial evaluation

5.3.8.1 Nanocomposite antimicrobial evaluation in solution

All the nanoparticles and nanocomposites prepared for fabrication of the anticorrosive coatings were evaluated for the possible antimicrobial action if any in the solvents first. Since coating formulations contain various solvents such as the diluent and the hardener, the need to determine their antimicrobial efficiency, as well as their influence on the antimicrobial property of the nanocomposites, was considered important. In Fig. 5.15, the results showed that the solvents (a) butanol and (b) HY951 (TETA) affected the growth kinetics of the bacteria as mentioned in earlier chapters evident from the zones of inhibition. The investigations in water had no inhibiting effect on the microbes. In the presence of the Ag@MSN nanocomposites; (d) ANC-1, (g) ANC-2 and (e) ANC-3, the zones of bacterial inhibition enlarged indicative of a possible release of the silver ions and/or due to the neem biomolecules.

In Fig. 5.16, after 48 h, the antifungal action of the nanocomposites and solvents were observed between 48-120 h of incubation. In the presence of water, there were no apparent detrimental effects of the dispersed nanocomposites on the fungal growth which was evident everywhere even on the sterilized filter paper. In the presence of butanol, delayed pigmentation was observed. While TETA showed a large zone of inhibition alongside changes in mycelial sporulation (a change from green to yellowish pigmentation) around the zone of inhibition. The delayed pigmentation observed in the butanol dispersed nanocomposites heightened up to 120 h which implies that abiotic stress and limiting growth conditions were exerted on the fungal strains affecting pigment production.
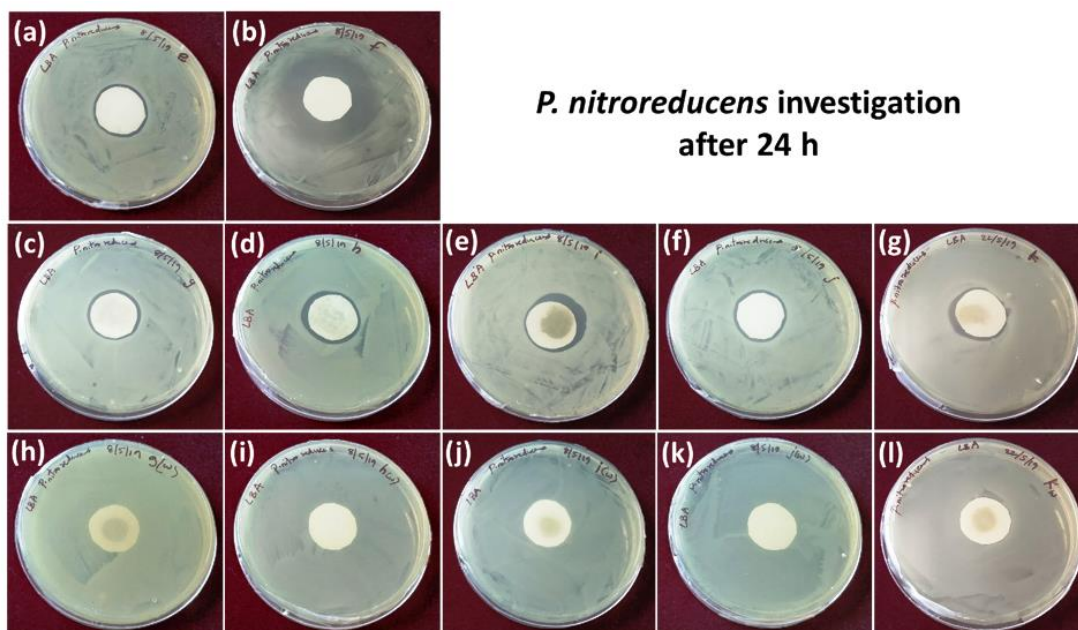
Fig. 5.15: Antibacterial action of the nanocomposites in solvents after 24 h against *Pseudomonas nitroreducens* colony on LBA agar (a) butanol (b) TETA (c-g) MS-NLE-E, ANC-1, ANC-3, MSN-OTS, ANC-2 respectively dispersed in butanol (h-l) MS-NLE-E, ANC-1, ANC-3, MSN-OTS, ANC-2 respectively dispersed in deionized water.
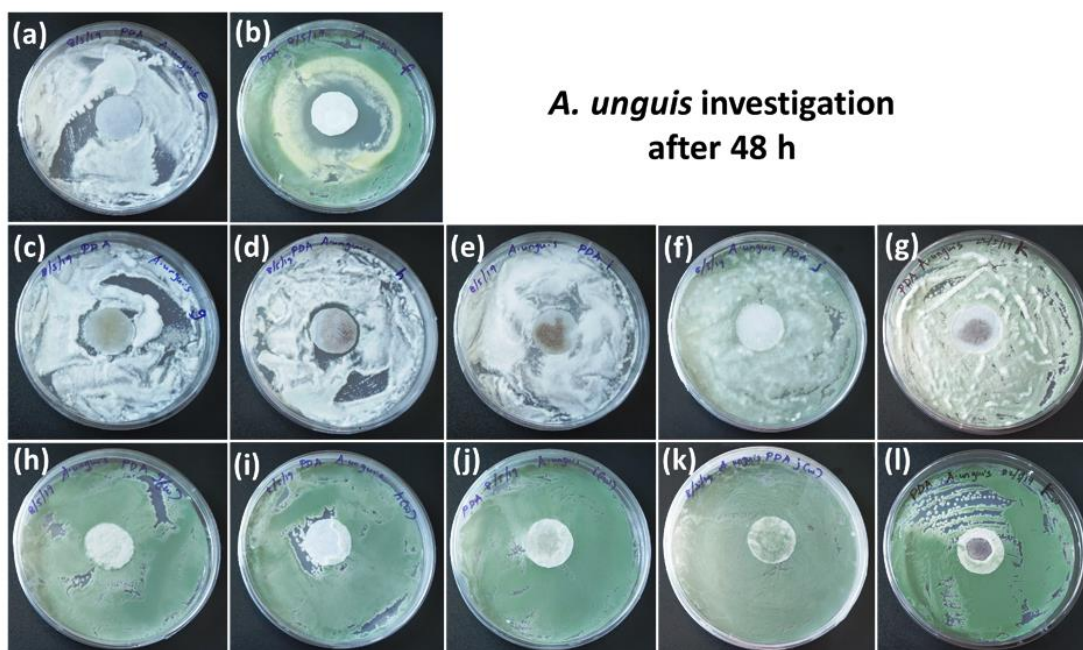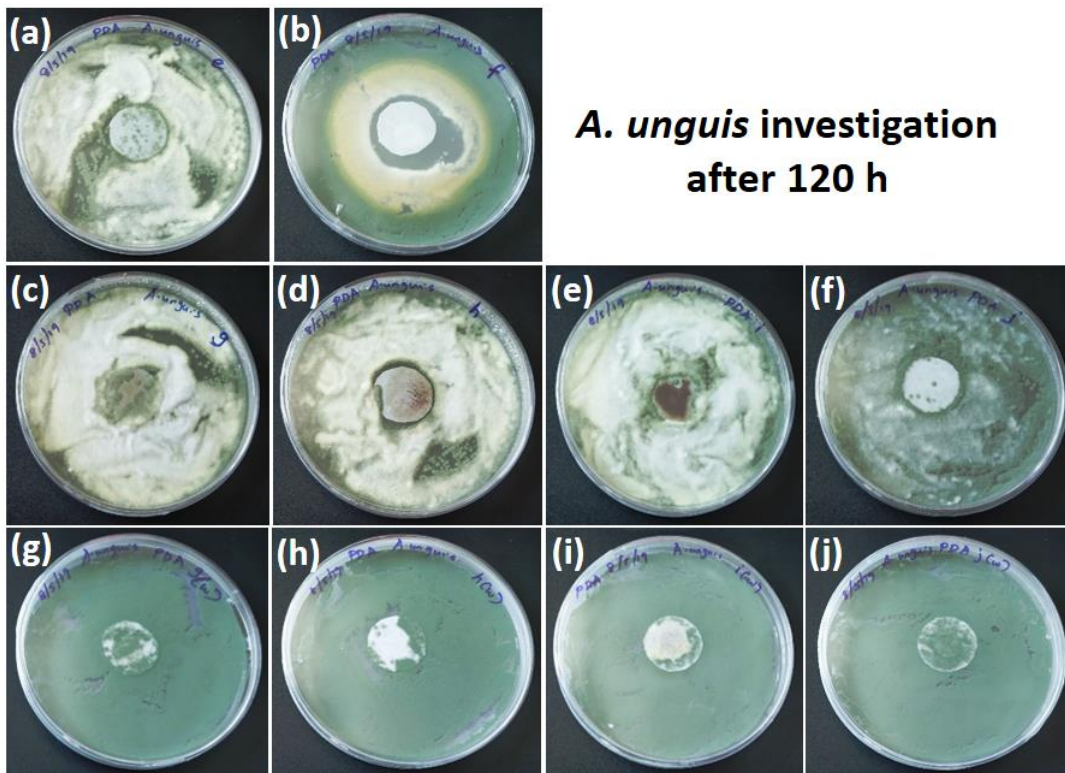
Fig. 5.16: (Top images) Antifungal action of the nanocomposites in solvents after 48 h against *Aspergillus unguis* colony on LBA agar (a) butanol (b) TETA (c-g) MS-NLE-E, ANC-1, ANC-3, MSN-OTS, ANC-2, respectively dispersed in butanol (h-l) MS-NLE-E, ANC-1, ANC-3, MSN-OTS, ANC-2, respectively dispersed in deionized water. Also, (Bottom images) Antifungal action of the nanocomposites in solvents after 120 h against *Aspergillus unguis* colony on LBA agar (a) butanol (b) TETA (c-f) MS-NLE-E, ANC-1, ANC-3, MSN-OTS, respectively dispersed in butanol (g-j) MS-NLE-E, ANC-1, ANC-3, MSN-OTS, respectively dispersed in deionized water.

5.3.8.2 AgNPs nanocomposite antimicrobial evaluation in coatings

Due to the solid nature of noble metal nanoparticles, the polymer chains stretch around them and in the absence of specific interactions smaller particles are more trapped than the larger sized ones. In the core-shell nanocomposite coatings this confinement of AgNPs limited the release of Ag ions in sufficient amount to combat the micro-organisms as shown in Fig. 5.17. For this reason, EENL-AgNPs/neem nanocomposite blend in the topcoat of the bilayer coating was made and found effective to combat the microbes (Fig. 5.18) and simultaneously provided enhanced corrosion resistance as described in the previous sections. But the antimicrobial activity of AgNPs is concentration-dependent, therefore composite

films of higher filler loading is required to achieve an enhanced and sustained antimicrobial effect. The 5 mg EENL-AgNPs used in the bilayer coatings fabrication appeared to be insufficient for an enhanced inhibition performance on the microbes. Furthermore, the antimicrobial activity of AgNPs is size and shape dependent, it is probable that the large cores may have a limiting effect on the release and inhibiting activity compared to smaller sized AgNPs.
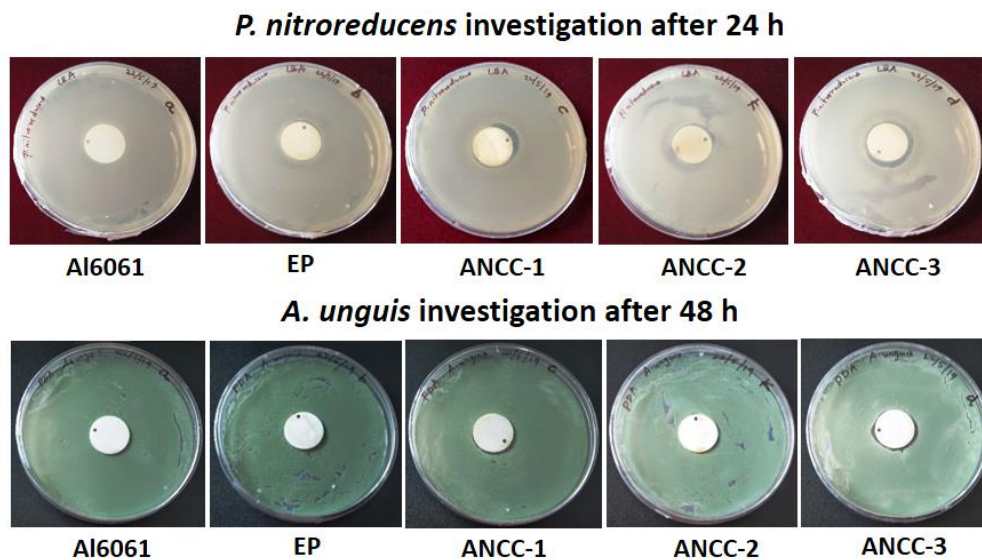

Fig. 5.17: Antimicrobial action of epoxy-ANCC coatings against *Pseudomonas nitroreducens* colony and *Aspergillus unguis* colony on LBA agar.
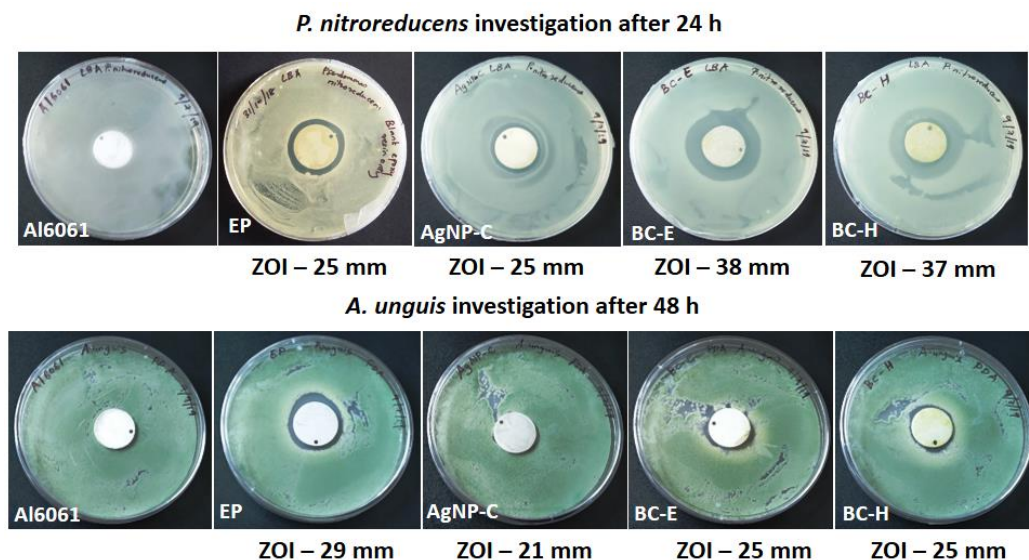

Fig. 5.18: Antimicrobial action of the bilayer coatings against *Pseudomonas nitroreducens* colony and *Aspergillus unguis* colony on LBA agar.

5.4 Conclusions

The one-pot synchronous fabrication of functionalized silver nanoparticles in comparison with the seeded functionalization technique, produced stable larger cores and thinner shells of silver-silica nanoparticles. The cost-effective approach of synthesizing silver nanoparticles from the ethanol extract of neem leaves by bio-reduction method and an in situ functionalization of the same is demonstrated. The crude biomass extract containing a mixture of phytochemicals was effective as a reducing agent, corrosion inhibitor and antimicrobial agent. The one-pot synthesis templated with CTAB yielded mixed nanoparticles of silver confirmed from the XRD studies. Also, the possibility of post-grafting biomass-based corrosion inhibitors into the porous silica shell surrounding the silver core was evidenced from the reduction in surface area and pore volume. The protective effect of the nanocomposite coatings was influenced by both the functionalization outcome of the fabricated nanoparticles and the presence of the loaded neem biomolecules as a corrosion inhibitor. Furthermore, the antimicrobial properties of the bilayer coatings were more evident compared to the epoxy-ANCCs. The nanoparticle/polymer mixtures enable the fabrication of novel films that have tailored structures and functionalities.

References

[1]   I. Sur, D. Cam, M. Kahraman, A. Baysal, M. Culha, *Nanotechnology* **2010**, *21*, 175104.

[2]   L. Guo, W. Yuan, Z. Lu, C. M. Li, *Colloids Surfaces A Physicochem. Eng. Asp.* **2013**, *439*, 69.

[3]   C. Zhao, L.-Y. Li, M.-M. Guo, J. Zheng, *Chem. Pap.* **2012**, *66*, 323.

[4]   P.-Y. Silvert, R. Herrera-Urbina, K. Tekaia-Elhsissen, *J. Mater. Chem.* **1997**, *7*, 293.

[5]   Y. A. Krutyakov, A. A. Kudrinskiy, A. Y. Olenin, G. V Lisichkin, *Russ. Chem. Rev.* **2008**, *77*, 233.

[6]   N. L. Pacioni, C. D. Borsarelli, V. Rey, A. V. Veglia, In *Silver Nanoparticle Applications, Engineering Materials*; Springer, Cham, 2015; pp. 13–46.

[7]   S. Y. Lee, S. Krishnamurthy, C.-W. Cho, Y.-S. Yun, *ACS Sustain. Chem. Eng.* **2016**, *4*, 2651.

[8]   T. S. Sreeprasad, T. Pradeep, In *Springer Handbook of Nanomaterials*; R. Vajtai,

Ed.; Springer Berlin Heidelberg: Berlin, Heidelberg, 2013; pp. 303–388.

[9] J. Y. Song, B. S. Kim, *Bioprocess Biosyst. Eng.* **2009**, *32*, 79.

[10] S. Kaviya, J. Santhanalakshmi, B. Viswanathan, J. Muthumary, K. Srinivasan, *Spectrochim. Acta Part A Mol. Biomol. Spectrosc.* **2011**, *79*, 594.

[11] V. Sanchez-Mendieta, A. Rafael Vilchis-Nestor, In *Noble Metals*; Su, Y.-H., Ed.; InTech: Europe, 2012; pp. 391–408.

[12] O. K. Abiola, Y. Tobun, *Chinese Chem. Lett.* **2010**, *21*, 1449.

[13] K. P. Vinod Kumar, M. Sankara Narayanan Pillai, G. Rexin Thusnavis, *J. Mater. Sci.* **2011**, *46*, 5208.

[14] A. Lecante, F. Robert, P. A. Blandinières, C. Roos, *Curr. Appl. Phys.* **2011**, *11*, 714.

[15] C. O. Akalezi, C. K. Enenebeaku, C. E. Ogukwe, E. E. Oguzie, *Environ. Pollut.* **2012**, *1*.

[16] S. B. Ulaeto, U. J. Ekpe, M. A. Chidiebere, E. E. Oguzie, *Int. J. M aterials Chem.* **2012**, *2012*, 158.

[17] N. C. Ngobiri, E. E. Oguzie, Y. Li, L. Liu, N. C. Oforka, O. Akaranta, *Int. J. Corros.* **2015**, *2015*, 1.

[18] K. Xhanari, M. Finšgar, M. Knez Hrnčič, U. Maver, Ž. Knez, B. Seiti, *RSC Adv.* **2017**, *7*, 27299.

[19] S. B. Ulaeto, A. V. Nair, J. K. Pancrecious, A. S. Karun, G. M. Mathew, T. P. D. Rajan, B. C. Pai, *Prog. Org. Coatings* **2019**, *136*, 105276.

[20] M. Lismont, C. A. Páez, L. Dreesen, *J. Colloid Interface Sci.* **2015**, *447*, 40.

[21] L. Han, H. Wei, B. Tu, D. Zhao, *Chem. Commun.* **2011**, *47*, 8536.

[22] Y. Chen, *Design, Synthesis, Multifunctionalization and Biomedical Applications of Multifunctional Mesoporous Silica-Based Drug Delivery Nanosystems*; Springer Theses; Springer Berlin Heidelberg: Berlin, Heidelberg, 2016.

[23] Y. Kobayashi, H. Katakami, E. Mine, D. Nagao, M. Konno, L. M. Liz-Marzán, *J. Colloid Interface Sci.* **2005**, *283*, 392.

[24] T. Ung, L. M. Liz-Marzán, P. Mulvaney, *Langmuir* **1998**, *14*, 3740.

[25] Z. Li, L. Jia, Y. Li, T. He, X.-M. Li, *Appl. Surf. Sci.* **2015**, *345*, 122.

[26] Y. Yin, Y. Lu, Y. Sun, Y. X.-N. Letters, U. 2002, *Nano Lett.* **2002**, *2*, 427.

[27] T. Chen, Q. Zhang, J. Xu, J. Pan, Y.-T. Cheng, *RSC Adv.* **2016**, *6*, 29308.

[28] L. Qi, X. Tang, Z. Wang, X. Peng, *Int. J. Min. Sci. Technol.* **2017**, *27*, 371.

[29] P. Roberge, *Corrosion engineering: principles and practice*; The McGraw-Hill Companies, Inc.: New York, 2008.

[30] M. H. Nazari, X. Shi, In *Industrial Applications for Intelligent Polymers and Coatings*; Hosseini M, M. A. S. H., Ed.; Springer International Publishing: Cham, 2016; pp. 373–398.

[31] X. Shi, T. A. Nguyen, Z. Suo, Y. Liu, R. Avci, *Surf. Coatings Technol.* **2009**, *204*, 237.

Chapter 6

Summary and Future perspectives

The first chapter in this research dealt with an overview of smart coatings. The area of "smart" or "intelligent" coatings is, in reality, a hot topic with a wide area of application due to the achievable multifunctionality. Coatings exhibiting smart characteristics are in hot demand especially when dual to multiple functionalities can now be achieved in most categories due to novel coating formulations aimed at maximizing its potential. The categories of smart coatings with anticorrosive properties centered on self-healing coatings and the use of micro to nanocontainers capable of being loaded with active agents, having trigger responsive qualities. Secondly, leading approaches for self-cleaning coatings involving high superhydrophobicity with extreme repellency to varying corrosive droplets which are maintained irrespective of the metal substrate and also UV stability. Thirdly, active corrosion-sensing coatings approach involving the inclusion of fluorescent or color indicators responsive to varying environmental triggers such as pH, ion or redox indicators etc. Fourthly, anti-fouling coatings with self-cleaning, water-resistant and superhydrophobic surfaces with low-surface free energy, low micro-roughness, and ultra-smooth topology to prevent fouling settlements when biocides are not utilized. As well as encouraging ecofriendly biocides.

Smart coatings and materials have been categorized into high-performance materials, property-changing materials and energy-exchanging materials. All aimed at exploiting the best properties of the individual constituents in both passive and active modes. Smart coatings containing nanoparticles are more versatile and ongoing efforts are devoted to the up-scaling of various nanocontainer production and evaluation. In addition, due to the wide use of plants in the area of corrosion protection, biomass derived phytochemicals as corrosion inhibitors were considered in the fabrication of smart coatings for the first time.

In chapter 2, metal finishing processes are key steps which provide the secondary role of corrosion protection. Alkaline and acidic pretreatment baths reduced

the heterogeneous nature of the metal surface and provided a consistent surface that was free of contamination and unfavorable phases. Although three different treatments were investigated which altered the nature of the alloy surface, significant corrosion inhibition was still obtained from the neem leaves extract in 1 M HCl solution. Furthermore, it was demonstrated that whole vegetal extract of neem leaves could be complexed with silica nanoparticles resulting in a hybrid bionanocomposite. It was also observed that the solvent type, surface area and presence of silanol groups in the mesoporous silica nanocarrier were crucial factors for the natural product loading. The eventually obtained coatings exhibited anticorrosive properties and were applied as a primer layer on aluminium alloy 6061. The impedance measurements revealed an increase of low-frequency impedance during immersion in the corrosive media which was related to the suppression of active corrosion processes within the defective areas of the coating. In addition, all studied epoxy-based coatings exhibited both antibacterial and antifungal activity towards the test microbes; *P. nitroreducens* and *A. unguis.*

In chapter 3, it has been demonstrated that Quercetin could be loaded into mesoporous silica nanoparticles to form an effective hybrid nanocomposite with corrosion-inhibiting properties. In the aggressive chloride environment, pH 10 provided a decrease in the corrosion rate due to the chemical changes of quercetin in the basic medium over time. Being a flavonoid, the chemical modifications in the alkaline aqueous solution involves an oxidation reaction that affects the aromatic rings. These chemical changes resulted in structural rearrangements and the formation of possible intermediate products. Active corrosion protection occurred due to the release and reactions of quercetin in the alkaline chloride medium and the formation of a protective film in the scratched area. Also, the barrier performance of the unscratched coatings was influenced by the action of the embedded particles. Either way, the loaded coating performance surpassed the unmodified coating throughout the study in the aggressive chloride environment and also displayed enhanced antibacterial properties against *P. nitroreducens.*

In chapter 4, a facile approach of biogenic synthesis of nanostructured silver crystals via ethanol extract of Neem leaves was studied. The approach was

undemanding and consumed no energy. The reduction of noble metal salts by the combination of phytochemicals in the plant biomass without an additional stabilizing agent was explored for the fabrication and subsequent accumulation of nano-metal colloids. The influence of the extracting solvent was excluded as no absorbance peaks were observed. An increase in both silver salt concentration and uniform stirring influenced the rate of precipitation of the nanocrystals in the colloidal solution which were observed to be SERS responsive when probed with Rhodamine B without any external aggregating agents. The nanoparticles were composed mainly of silver and the XRD pattern confirmed the cubic phases of the silver nanocrystals. Therefore, the metal ions initially present in metal salts were reduced by bioreducing agents present in the whole extract, which played the multifunctional role of aggregating, capping, and stabilizing the nanocrystals to grow into defined sizes and shape. The nature of the bioreducing agents and reaction conditions employed played essential roles in controlling the morphology and activity of the nanocrystals. The bioreduced silver nanoparticles induced significant toxicity to the test microbes; *P. nitroreducens* and *A. unguis* offering an opportunity to utilize bioreduced AgNPs in the formulation of antimicrobial coatings.

In chapter 5, the one-pot fabrication system was utilized with bio-reductants for the fabrication of core-shell silver nanoparticles. The study demonstrated bioreduction of the silver nanoparticles and an in-situ functionalization of the same. The fabricated nanocomposite coatings displayed enhanced anticorrosive properties only when the neem extract inhibitor was loaded into the silica shell. The core-shell silver nanocomposite showed poor antimicrobial properties due to core confinement. This shortcoming was overcome with a blend of spiked bioreduced silver nanoparticles and neem nanocomposites in a dual-layered coating which enabled both anticorrosive and antimicrobial properties of the fabricated coatings.

Overall, phytochemicals were investigated in different aggressive chloride solutions and were also encapsulated for investigating self-healing. Antimicrobial properties of the biomass derived nanoparticles and corrosion inhibitors were assessed and yielded significant zones of inhibition. The phytochemicals in both crude extract of

neem leaves and quercetin provided notable corrosion inhibiting properties in aggressive chloride solution and in epoxy-based coatings.

Future perspectives

- Superhydrophobic bio-based smart anticorrosive coatings.
- The repeatable healing action of the self-healing coatings.
- Bio-waste regenerated smart coatings.
- Hybrid anticorrosive coatings with intrinsic/extrinsic dual-response healing action.
- Antimicrobial nanoconstructs from a variety of waste biomass.

List of Publications

1. **Sarah B. Ulaeto**, Anju V. Nair, Jerin K. Pancrecious, Akhil S. Karun, Gincy Marina Mathew, T.P.D. Rajan, and B. C. Pai (2019). Smart Nanocontainer-Based Anticorrosive Bio-Coatings: Evaluation of Quercetin for Corrosion Protection of Aluminium Alloys. *Progress in Organic Coatings, 136, 105276.*

2. **Sarah B. Ulaeto**, Gincy Marina Mathew, Jerin K. Pancrecious, Jyothi B. Nair, T.P.D. Rajan, K. K. Maiti and B. C. Pai. Biogenic Ag Nanoparticles of Neem Extract; its Structural Evaluation and Antimicrobial Effects against *Pseudomonas nitroreducens* and *Aspergillus unguis* - NII 08123. *ACS Biomaterials Science & Engineering, 2019, (in press*).

3. Jerin K. Pancrecious, J. P. Deepa, V. Jayan, **Sarah Bill Ulaeto**, T.P.D. Rajan and B. C. Pai (2018). Nanoceria induced grain refinement in electroless Ni-B-CeO$_2$ composite coating for enhanced wear and corrosion resistance of Aluminium alloy. *Surface and Coatings Technology, 356, 29-37*.

4. Jerin K. Pancrecious, **Sarah Bill Ulaeto**, R. Ramya, T.P.D. Rajan & B. C. Pai (2018). Metallic composite coatings by electroless technique - a critical review. *International Materials Review, 63(8), 488-512*.

5. **Sarah B. Ulaeto,** Ramya Rajan, Jerin K. Pancrecious, T.P.D. Rajan, & B. C. Pai (2017). Developments in smart anticorrosive coatings with multifunctional characteristics. *Progress in Organic Coatings, 111, 294-314*.

6. **Sarah B. Ulaeto**, Lincy V. S., Gincy Marina Mathew, Jerin K. Pancrecious, Akhil S. Karun, and T. P. D. Rajan. Bio-responsive Strategy for Anticorrosion: Evaluating *A. indica* Anticorrosive Efficacy in Self-healing Epoxy Coatings. (*Manuscript to be submitted)*.

7. **Sarah B. Ulaeto**, Gincy Marina Mathew, Jerin K. Pancrecious, and T. P. D. Rajan Ag-based Anticorrosive Hybrid Coatings for Protection of Aluminium Alloys. (*Manuscript to be submitted*).

8. **Sarah B. Ulaeto**, Jerin K. Pancrecious, and T.P.D. Rajan. Aluminium Alloy Corrosion in Chloride Environments: Effect of Surface Preparations and Influence of Neem Extract Inhibitor. (*Manuscript to be submitted*).

9. **Sarah B. Ulaeto**, Jerin K. Pancrecious, and T.P.D. Rajan Advances in Corrosion Inhibitors for Protection of Metals and Alloys: A Review. (*Under Revision*).

Invited Book Chapters

1. **Sarah B. Ulaeto**, Ajekwene Kingsley Kema, Gincy Marina Mathew and T. P. D. Rajan. Nanocoatings for Anticorrosion: An Introduction. Chapter 24 in *"Corrosion Protection at the Nanoscale"* by Elsevier (2019) (*In press*), ISBN 978-0-12-819359-4.

2. **Sarah B. Ulaeto,** Suja P., Jerin K. Pancrecious, T.P.D. Rajan and B. C. Pai (2019). Intelligent Coatings for Anticorrosive Applications. Chapter 5 in "*Phenomena and Theories in Corrosion Science: Methods of Prevention"* pp. 219-254. Nova Science Publishers. ISBN: 978-1-53615-252-4.

3. **Sarah B. Ulaeto,** Jerin K. Pancrecious, T. P. D. Rajan and B. C. Pai. (2019). Smart Coatings. Chapter 17 in "*Noble Metal-Metal Oxide Hybrid Nanoparticles: Fundamentals and Applications"* pp. 341-372. Woodhead Publishing. ISBN: 978-0-12-814134-2, eBook ISBN: 978-0-12-814135-9.

4. **Sarah B. Ulaeto,** Jerin K. Pancrecious, Ramya Rajan, T. P. D. Rajan and B. C. Pai. (2018). Role of Nanodispersoids on Corrosion Inhibition Behavior of Smart Polymer Nanocomposite Coatings. Chapter 15 in "*Advanced Polymeric Materials for Sustainability and Innovations"* pp. 321-366. Apple Academic Press. ISBN 9781771886338 - CAT# N11991

List of Conference Presentations

1. **Sarah B. Ulaeto,** Gincy Marina Mathew, Jerin K. Pancrecious, T.P.D. Rajan. Antifouling: Ecofriendly Contributions from Bionanoparticles and Bio-coatings. NHBT 2019 at The Residency Tower, Trivandrum, Kerala, India during Nov. 20-24, 2019 (Poster presentation).

2. **Sarah B. Ulaeto,** Jerin K. Pancrecious, Gincy Marina Mathew, T.P.D. Rajan. Hybrid Nanocomposite Coatings for Corrosion Protection of Aluminium Alloys. NMD-ATM 2019 at Uday Samudra, Kovalam, Trivandrum, Kerala, India during Nov. 13-16, 2019 (Poster presentation).

3. **Sarah B. Ulaeto**, Anju V. Nair, Jerin K. Pancrecious, T. P. D. Rajan, B. C. Pai. Smart Release Bionanocomposite Coatings for Corrosion Protection of Aluminium Alloys. CORCON 2019 at CIDCO Convention Centre, Mumbai, India during Sept. 23-26, 2019 (Poster presentation).

4. **Sarah B. Ulaeto**, Jerin K. Pancrecious, T.P.D. Rajan, B. C. Pai. Host-Guest Interactions for Corrosion Protection of A6061 Alloy. Research Scholars Symposium IIM 2019, CSIR-NIIST, Trivandrum, Kerala, India on April 3, 2019 (Oral presentation).

5. **Sarah B. Ulaeto**, Anju V. Nair, Jerin K. Pancrecious, T. P. D. Rajan, B. C. Pai. Bionanocomposite Coatings Tailored for Corrosion Protection of Aluminium Alloys. ICAMPS, Trivandrum, Kerala, India during Oct. 25-27, 2018, (Poster presentation).

6. **Sarah B. Ulaeto**, Anju V. Nair, Jerin K. Pancrecious, T. P. D. Rajan, B. C. Pai. Green Nanocomposite for Corrosion Protection of Al-Mg-Si Alloy. ICMST, Oct. 10-13 2018, ISRO ATF Guest House, Veli, Trivandrum, Kerala, India (Oral presentation).

7. **Sarah B. Ulaeto,** Jerin K. Pancrecious, T.P.D. Rajan and B. C. Pai. Investigation on Self-Healing Nanocomposite Coating for Corrosion Protection of Al-Mg-Si Alloy. IIM Research Scholars Symposium, CSIR-NIIST, Trivandrum, Kerala, India on April 6, 2018 (Oral presentation).

8. **Sarah B. Ulaeto**, Jerin K. Pancrecious, T.P.D. Rajan and B. C. Pai. Electrochemical Behaviour and Corrosion Inhibiting Effects of Green Nanosilver Modified Epoxy Coatings. ADMAT SKYMat 2017, Kovalam, Kerala, India during Dec. 14-16, 2017 (Poster presentation).

9. **Sarah B. Ulaeto**, Jerin K. Pancrecious, T.P.D. Rajan, and B. C. Pai. Studies on corrosion protection of aluminium alloy surfaces by eco-friendly green inhibitors. NMD ATM 2017, International Symposium, BITS, Pilani-K K Birla Goa Campus, Goa, India during Nov. 11-14, 2017 (Oral Presentation).

10. **Sarah B. Ulaeto**, Jerin K. Pancrecious, Ramya Rajan, T.P.D. Rajan, and B. C. Pai. Extract-mediated Fabrication and Characterization of Silver Nano Crystals Initiated from *A. Indica* Leaves for Anticorrosive Coatings. CSMAT-2017 Munnar, Kerala, India during Mar. 9-11, 2017.

11. **Sarah B. Ulaeto**, Jerin K. Pancrecious, Ramya Rajan, and T.P.D. Rajan. Barrier Effects of Natural Extract Mediated Inhibition of Epoxy Coated Aluminium Alloy. LMCMP-2017 at CSIR-NIIST, Trivandum, Kerala, India on Mar. 3, 2017 (Poster presentation).

12. **Sarah B. Ulaeto**, Ramya Rajan, Jerin K. Pancrecious, and T.P.D. Rajan. Influence of natural inhibitors on the corrosion behavior of AA6061 aluminium alloys. CORCON 2016, at The Leela Ambiance Convention Hotel, New Delhi during Sept. 18-21, 2016 (Oral presentation).

Awards & Honours

1. **Best Poster Award** for the Presentation entitled "Smart Release Bionanocomposite Coatings for Corrosion Protection of Aluminium Alloys". Authored by **Sarah B. Ulaeto,** Anju V. Nair, Jerin K. Pancrecious, T.P.D. Rajan, B. C. Pai. CORCON 2019 Conference. Sep 23 - 26, 2019, Mumbai, India.

2. **Best Poster Award** for the presentation entitled "Bionanocomposite Coatings Tailored for Corrosion Protection of Aluminium Alloys.**"** Authored by **Sarah B.**

Ulaeto, Anju V. Nair, Jerin K. Pancrecious, T.P.D. Rajan, B. C. Pai. During ICAMPS, Oct. 25-27, 2018, Trivandrum, Kerala, India.

3. **Best Poster Award** for the presentation entitled "Extract-mediated Fabrication and Characterization of Silver Nano Crystals Initiated from *A. Indica* Leaves for Anticorrosive Coatings". Authored by **Sarah B. Ulaeto**, Jerin K. Pancrecious, Ramya Rajan, T.P.D. Rajan, and B. C. Pai. During CSMAT-2017 Munnar, March 9-11, 2017.

4. **Prof. BrahmPrakash Best Paper Award-2017** by IIM Trivandrum Chapter, Trivandrum, Kerala, India for the article "Developments in smart anticorrosive coatings with multifunctional characteristics" *Progress in Organic Coatings* (2017), *111, 294-314*. Authored by **Sarah B. Ulaeto,** Ramya Rajan, Jerin K. Pancrecious, T.P.D. Rajan, and B. C. Pai.